Dosimetry in intraoperative radiotherapy for glioblastoma using the INTRABEAM source

David Santiago Ayala Alvarez

Department of Physics
McGill University
Montreal, Quebec, Canada

A thesis submitted to McGill University in partial fulfillment of the requirements of the degree of
Doctor of Philosophy

 August 2024

Acknowledgements

I would like to express my gratitude to those who have supported me in the completion of this project. Firstly, I am deeply thankful to my supervisor, Prof. Jan Seuntjens, for his continuous support, guidance, and trust throughout this journey. His expertise and insightful feedback have been invaluable in shaping this research and my academic growth. Prof. Jan not only provided academic direction but also ensured I had the necessary funding during my studies and provided opportunities for presenting my work at conferences, for which I am very grateful.

I extend my sincere thanks to Dr. Peter Watson for his significant contributions to this project. His expertise in INTRABEAM dosimetry, provision of initial models, and continuous support were crucial to the success of this research. His guidance and willingness to share knowledge have greatly enhanced the quality of this work. Dr. Watson has also opened doors and opportunities for me to collaborate and present my work outside of the university. I appreciate Dr. Marija Popovic's invaluable assistance in the clinical aspects of this research. Her help in accessing the INTRABEAM system for measurements, facilitating access to randomized patient data, and providing clinical insights have been essential. My heartfelt gratitude goes to Michael Evans, whose expertise as a Radiation Safety Officer was crucial for the experimental aspects of this work. His assistance in accessing treatment rooms, providing tools for radiation dosimetry and safety, and offering insights into the interpretation of experimental results have been invaluable. I really appreciate and acknowledge the contributions of Dr. Veng Jean Heng, whose friendly assistance in Monte Carlo, treatment planning with `Brems`, and data analysis have been very helpful. Similarly, I thank Dr. Valerie Panet-Raymond for her support in the clinical approaches of my project for radiation oncology patients who may benefit from our research.

I am grateful to the staff and physicists at McGill University Health Centre who facilitated various aspects of this research, particularly in transporting the INTRABEAM system and assisting with experimental setups. Thank you to the engineers Joe Larkin and Bhavan Siva, who built an accessory for measurements with the INTRABEAM arm without the inclusion of applicators.

Thank you to Margery Knewstubb and Tatjana Nisic for their administrative support.

I also thank my colleagues and friends from the Medical Physics Unit for their support and for making this journey more enjoyable. Particularly, although there are more, I want to thank Veng, Felix, Chris, Morgan, Julien, Liam, and Yujing, who were working with me for the entire duration of my PhD.

Finally, I would like to express my deepest gratitude to my family. To my parents, Antonio and Beatriz, and my brother Esteban, thank you for your love and constant motivation throughout my academic journey and life in general. And to my wife, Lili, thank you for being by my side and making sacrifices to help me achieve my dreams. Thank you for your friendship and your constant support through all these years.

Abstract

This thesis focuses on improving the dosimetry of the INTRABEAM system for intraoperative radiotherapy (IORT) in brain cancer treatment, particularly within the context of the INTRAGO clinical trial for glioblastoma multiforme (GBM). The INTRABEAM system, which uses a miniature X-ray source to deliver localized radiation during surgery, presents unique dosimetric challenges due to its low-energy photon spectrum and steep dose gradients. Current clinical practices, based on the TARGIT dosimetry protocol, have shown limitations in accurately estimating doses to organs at risk (OARs) in complex anatomical sites like the brain.

The research presented here addresses these challenges through a comprehensive characterization of the INTRABEAM system using Monte Carlo (MC) simulations and experimental validation. The study begins with a detailed analysis of the bare INTRABEAM probe, deriving parameters based on the AAPM Task Group 43 (TG-43) formalism, a standardized method for calculating dose distributions in water around brachytherapy sources. This analysis reveals significant anisotropy and steep radial dose gradients in water. The work is then extended to include the spherical applicators used in clinical practice, providing a complete set of TG-43 parameters for all available applicator sizes, enabling fast and accurate 3D dose calculations within existing brachytherapy treatment planning frameworks.

A critical evaluation of different dosimetry formalisms for IORT in GBM treatment is presented, comparing the current clinical standard (TARGIT method) with more accurate approaches. These include the V4.0 calibration method, the C_Q method, which uses an MC-calculated factor to convert measurements made in water with an air-kerma calibrated ionization chamber into absorbed dose in water, and MC simulations in both water and heterogeneous media. The findings reveal significant discrepancies between these methods, with the TARGIT approach consistently underestimating doses to OARs. Notably, while the TARGIT method suggested no violations of OAR dose constraints, the more accurate methods identified multiple instances where constraints were exceeded.

The thesis concludes with a comprehensive evaluation of the TG-43 formalism for INTRABEAM IORT dosimetry in GBM treatment. This study, involving a cohort of 20 patients from the INTRAGO trial, compares TG-43 calculations with the TARGIT method and MC simulations in both water and heterogeneous media. The results demonstrate good agreement between TG-43 and MC simulations in water, with a 98.0% gamma pass rate using 1%/1mm criteria. However, MC simulations in heterogeneous media reveal larger deviations, particularly near bony structures, highlighting the potential limitations of water-based calculations in complex anatomical sites.

These findings have significant implications for clinical practice, suggesting the need for more accurate dosimetry methods in IORT for GBM treatment. The research shows the potential benefits of implementing TG-43 or MC-based dose calculations in treatment planning, which could lead to improved OAR sparing and more effective treatments. The thesis also identifies several avenues for future research, including the integration of intraoperative imaging, the development of real-time treatment planning systems, and further investigation of the radiobiological effects of low-energy X-rays used in INTRABEAM IORT.

In conclusion, this thesis provides a comprehensive analysis of INTRABEAM dosimetry for IORT in GBM treatment, offering insights that could lead to improved treatment accuracy and potentially better outcomes for patients. The work establishes a foundation for future advancements in IORT dosimetry and highlights the importance of continued research in this field.

Résumé

Cette thèse vise à améliorer la dosimétrie du système INTRABEAM pour la radiothérapie peropératoire (IORT) dans le traitement du glioblastome multiforme (GBM), dans le cadre de l'essai clinique INTRAGO. Le système INTRABEAM, utilisant une source miniature de rayons X, présente des défis dosimétriques uniques dus à son spectre de basse énergie et ses forts gradients de dose. Les pratiques actuelles, basées sur le protocole TARGIT, montrent des limites dans l'estimation précise des doses aux organes à risque (OAR) dans le cerveau.

La recherche aborde ces défis par une caractérisation complète du système INTRABEAM via des simulations Monte Carlo (MC) et une validation expérimentale. L'étude commence par l'analyse de la sonde INTRABEAM, dérivant les paramètres du formalisme TG-43, une méthode standardisée pour calculer les distributions de dose dans l'eau autour des sources de curiethérapie. Ce travail est étendu aux applicateurs sphériques cliniques, fournissant des paramètres TG-43 pour toutes les tailles d'applicateurs, permettant des calculs de dose 3D plus précis.

Une évaluation critique compare la méthode TARGIT avec des approches plus précises, incluant la méthode V4.0, la méthode C_Q, qui utilise un facteur calculé par MC pour convertir les mesures effectuées dans l'eau avec une chambre d'ionisation étalonnée en kerma dans l'air en dose absorbée dans l'eau, et des simulations MC dans l'eau et les milieux hétérogènes. Les résultats révèlent que TARGIT sous-estime systématiquement les doses aux OAR, identifiant des dépassements de contraintes non détectés par TARGIT.

La thèse se conclut par une évaluation complète du formalisme TG-43 pour la dosimétrie IORT INTRABEAM dans le traitement du GBM. Cette étude, impliquant une cohorte de 20 patients de l'essai INTRAGO, compare les calculs TG-43 avec la méthode TARGIT et les simulations MC à la fois dans l'eau et dans des milieux hétérogènes. Les résultats démontrent une bonne concordance entre les calculs TG-43 et les simulations MC dans l'eau, avec un taux de réussite gamma de 98,0% utilisant des critères de 1%/1mm. Cependant, les simulations MC dans des milieux hétérogènes révèlent des écarts plus importants, particulièrement près des struc-

tures osseuses, soulignant les limitations potentielles des calculs basés sur l'eau dans des sites anatomiques complexes.

Ces résultats ont des implications significatives pour la pratique clinique, suggérant le besoin de méthodes dosimétriques plus précises dans la IORT pour le traitement du GBM. La recherche montre les avantages potentiels de l'implémentation de calculs de dose basés sur TG-43 ou MC dans la planification du traitement, ce qui pourrait conduire à une meilleure protection des OAR et à des traitements plus efficaces. La thèse identifie également plusieurs pistes pour de futures recherches, incluant l'intégration de l'imagerie peropératoire, le développement de systèmes de planification de traitement en temps réel, et une investigation plus approfondie des effets radiobiologiques des rayons X de basse énergie utilisés dans la IORT INTRABEAM.

En conclusion, cette thèse fournit une analyse complète de la dosimétrie INTRABEAM pour la IORT dans le traitement du GBM, offrant des perspectives qui pourraient conduire à une amélioration de la précision du traitement et potentiellement à de meilleurs résultats pour les patients. Le travail établit une base pour de futures avancées en dosimétrie IORT et souligne l'importance de la poursuite de la recherche dans ce domaine.

Contents

Acknowledgements **i**

Abstract **iii**

Résumé **v**

List of figures **xiii**

List of tables **xxi**

List of abbreviations **xxv**

Preface **xxvii**

Contribution to original knowledge xxvii

Contribution of authors xxviii

1 Introduction **1**

1.1 Cancer and radiotherapy 1

1.2 Radiotherapy modalities 2

1.2.1 External beam radiotherapy 3

1.2.2 Brachytherapy 4

1.2.3 Intraoperative radiotherapy 5

1.2.4 Electronic brachytherapy 6

1.3 INTRABEAM system 6

1.4 Glioblastoma and the INTRAGO trial 10

1.5 Challenges in INTRABEAM dosimetry 12

1.6 Thesis objectives 13

1.7 Thesis outline . . . 14
References . . . 14

2 Radiation physics and dosimetry 19
2.1 Preface . . . 19
2.2 Radiation physics . . . 20
2.2.1 Photon interactions in matter . . . 20
2.2.2 Electron interactions in matter . . . 24
2.3 Dosimetric quantities and concepts . . . 26
2.3.1 Fluence . . . 26
2.3.2 Kerma . . . 27
2.3.3 Absorbed dose . . . 28
2.3.4 Charged particle equilibrium . . . 29
2.4 Experimental dosimetry . . . 29
2.4.1 Absolute, reference, and relative dosimetry . . . 29
2.4.2 Ionization chambers . . . 31
2.4.3 Solid-state detectors . . . 32
2.5 Brachytherapy dosimetry . . . 34
2.5.1 TG-43 dosimetry protocol . . . 34
2.5.2 Application to electronic brachytherapy . . . 37
2.5.3 Effects of tissue heterogeneities: TG-186 formalism . . . 39
2.6 INTRABEAM dosimetry . . . 42
2.6.1 TARGIT dosimetry method . . . 42
2.6.2 Zeiss V4.0 method . . . 43
2.6.3 C_Q method . . . 45
2.7 Monte Carlo methods . . . 46
2.7.1 Basics of Monte Carlo simulations . . . 46
2.7.2 Variance reduction techniques . . . 48
2.7.3 EGSnrc code system . . . 50
References . . . 52

3 INTRABEAM source modeling and initial TG-43 parameter calculations 59
3.1 Preface . . . 59

3.2 INTRABEAM source modeling . . . 60
3.2.1 Geometry and materials . . . 60
3.2.2 Beam characteristics . . . 61
3.2.3 Monte Carlo simulation parameters . . . 62
3.2.4 TG-43 parameter calculation methods and setup . . . 64
3.3 Monte Carlo model validation . . . 65
3.3.1 Experimental setup and measurements . . . 65
3.3.2 Comparison with Monte Carlo simulations . . . 68
3.4 Results and validation . . . 69
3.4.1 Monte Carlo model validation . . . 69
3.4.2 Radial dose function . . . 71
3.4.3 2D anisotropy function . . . 72
3.5 Discussion of initial findings . . . 73
Appendix . . . 75
References . . . 77

4 TG-43 parameters for INTRABEAM with spherical applicators 81
4.1 Preface . . . 81
4.2 Abstract . . . 82
4.3 Introduction . . . 83
4.4 Materials and Methods . . . 84
4.4.1 INTRABEAM source and spherical applicators . . . 84
4.4.2 Radiation transport parameters . . . 85
4.4.3 TG-43 parameters . . . 86
4.4.4 Source calibration . . . 88
4.4.5 Validation of the MC model . . . 89
4.5 Results and Discussion . . . 89
4.5.1 Uncertainty analyses . . . 89
4.5.2 Validation of the MC model . . . 91
4.5.3 Photon fluence spectra, air-kerma rates and dose-rate conversion coefficients. . . . 93
4.5.4 Radial dose function . . . 95
4.5.5 2D anisotropy function . . . 96

4.6 Conclusion . . . 97
Appendix . . . 99
References . . . 104

5 Dosimetry formalisms in IORT of glioblastoma 109
5.1 Preface . . . 109
5.2 Abstract . . . 110
5.3 Introduction . . . 110
5.4 Methods and Materials . . . 111
5.4.1 Study Design . . . 111
5.4.2 INTRABEAM Dosimetry . . . 112
5.4.3 IORT Treatment Planning Platform and Cumulative Dose Assessment . . . 113
5.5 Results . . . 116
5.5.1 Dosimetric Analysis . . . 116
5.5.2 Uncertainty Estimation . . . 117
5.6 Discussion . . . 119
5.7 Conclusion . . . 122
References . . . 123

6 Evaluation of the TG-43 formalism for INTRABEAM IORT dosimetry 127
6.1 Preface . . . 127
6.2 Abstract . . . 128
6.3 Introduction . . . 128
6.4 Materials and Methods . . . 129
6.4.1 Study design and data collection . . . 129
6.4.2 Dosimetry formalisms . . . 130
6.4.3 EBRT treatment planning . . . 131
6.4.4 Validation of TG-43 dose calculations . . . 133
6.4.5 TPS and OAR dose calculations . . . 133
6.4.6 Data analysis . . . 134
6.5 Results . . . 134
6.5.1 Validation of TG-43 dose calculations . . . 134
6.5.2 IORT-only OAR dose distributions . . . 138

6.5.3 Absolute dose metric differences . . . 138
6.5.4 Combined EBRT+IORT dose distributions . . . 139
6.5.5 Calculation times . . . 140
6.6 Discussion . . . 140
6.7 Conclusion . . . 145
References . . . 146

7 Summary and future directions 151
7.1 Summary . . . 151
7.1.1 Key findings . . . 151
7.1.2 Implications for clinical practice . . . 152
7.1.3 Limitations of the study . . . 153
7.2 Future research directions . . . 154
7.2.1 Integration of imaging and treatment planning . . . 154
7.2.2 Expansion of clinical applications and radiobiology studies . . . 155
7.2.3 Advanced modeling and quality assurance . . . 155
7.2.4 Comparative studies and treatment optimization . . . 155
7.3 Conclusion . . . 156
References . . . 156

List of figures

Figure 1.1 Illustration of the therapeutic window and therapeutic ratio concepts in radiotherapy. The curves show the relationship between radiation dose and both tumor control probability (TCP, solid line) and normal tissue complication probability (NTCP, dashed line). The therapeutic window (shaded region) represents the dose range where tumor control can be achieved while maintaining acceptable normal tissue complications. The therapeutic ratio is maximized at the dose where the separation between TCP and NTCP is greatest, indicated by the vertical dotted line. 3

Figure 1.2 The INTRABEAM system. Left: INTRABEAM source with a spherical applicator mounted on the articulated arm and floor stand. The floor stand (dimensions 74 cm $\times$ 194 cm $\times$ 150 cm, W $\times$ H $\times$ L) provides flexibility of movement with millimeter precision in six dimensions. Right: Schematic cross-section of the x-ray source (dimensions 7 cm $\times$ 1 1cm $\times$ 17 cm) showing internal components involved in electron beam generation and transport. The source probe has an outer diameter of 3.2 mm and length of 100 mm, with a 0.5 μm thick gold target at its tip. Key components are labeled, including the internal radiation monitor, cathode gun, accelerator section, beam deflector, electron beam path, and gold target. Figure reproduced from [19] under the Creative Commons Attribution License (CC BY). 8

Figure 1.3 A 4 cm diameter spherical applicator used with the INTRABEAM system for intraoperative radiotherapy in breast and brain tumors. 8

Figure 1.4 Comparison of dose distributions in an axial CT slice for different treatment delivery techniques: (a) EBRT plan showing a relatively uniform dose distribution typical of high-energy (6 MV) external beam delivery, (b) IORT calculated in water medium demonstrating the characteristic steep dose gradient and an approximately spherically symmetric distribution shaped by the applicator, and (c) IORT calculated with tissue heterogeneity corrections showing subtle variations in dose distribution due to tissue interfaces. The steep dose gradient in IORT (b,c) illustrates how spherical applicators modify the bare probe's output, creating an approximately spherical high-dose region that conforms to the surgical cavity while rapidly falling off to spare surrounding tissues. Isodose lines represent percentage of prescription dose (60 Gy for EBRT, 20 Gy at applicator surface for IORT) as indicated in the color map. Note that while tissue heterogeneity effects are minimal for EBRT at 6 MV, they become more pronounced for IORT due to the increased photoelectric effect at lower energies (50 kVp). 9

Figure 2.1 Relative predominance of photon interactions as a function of photon energy and absorber atomic number. The lines represent regions where the two neighboring effects are equally probable. Note the dominance of the photoelectric effect at low energies, especially for higher-Z materials, while Compton scattering predominates in the intermediate energy range for most materials of clinical interest. The horizontal band indicates the range of atomic numbers (Z=1-20) present in brain and surrounding tissues, including elements from hydrogen to calcium. The vertical band shows the energy range relevant to INTRABEAM IORT (1-50 keV), from the photon transport cutoff energy to the maximum tube potential. The overlap of these bands, primarily in the photoelectric effect region, illustrates why tissue composition significantly influences dose distributions in INTRABEAM IORT. Figure adapted from [3]. 22

Figure 2.2 Coordinate system used for brachytherapy dosimetry calculations as defined in the TG-43 formalism. The origin is at the center of the active source, with the z-axis aligned along the long axis of the source. Figure reproduced from [15]. 35

Figure 2.3 Mass-energy absorption coefficients for various materials relative to those for water for energies from 5 to 200 keV. Figure reproduced from [25]. . . 40

Figure 2.4 Zeiss Water Phantom components: (1) water tank, (2) rotary stage, (3) cable holder, and (4) positioning unit. The phantom design allows for precise depth dose and isotropy measurements using a non-waterproof ionization chamber. Figure reproduced from [35] 44

Figure 3.1 Schematic representation of the INTRABEAM source geometry used in MC simulations. The image on top shows the overall probe structure. The inset provides a magnified cross-sectional view of the source tip, detailing the beryllium window, gold target, and biocompatible layers. Note that the inset is not to scale. Figure adapted from [2] 61

Figure 3.2 Visualization of the modeled electron beam structure in the INTRABEAM source. The image shows the two concentric rings representing the electron impact pattern on the gold target, with radii ranging from 0.6 to 0.8 mm. This model accounts for the internal beam deflection system used to achieve a more isotropic dose distribution. 62

Figure 3.3 Energy fluence spectrum of the INTRABEAM bare probe measured in air at the probe surface. The spectrum shows prominent characteristic x-ray peaks from the gold target (Au L lines) and the nickel layer (Ni K lines), superimposed on a bremsstrahlung continuum that extends up to the maximum electron energy of 50 keV. 63

Figure 3.4 Coordinate system employed for TG-43 parameter calculations of the INTRABEAM source. The origin is located at the source tip, with $\theta = 0^\circ$ oriented along the source long axis, pointing away from the source. Figure reproduced from [2]. 64

Figure 3.5 Schematic diagram of the PTW 34013 parallel-plate ionization chamber. The inset provides details of the measuring volume. This chamber design is optimized for soft X-ray measurements, with a small sensitive volume to minimize perturbation effects. Figure reproduced from [21]. 66

Figure 3.6 Schematic representation of the PTW microDiamond TN60019 detector. The compact design allows for high spatial resolution measurements that are useful for characterizing the steep dose gradients of the INTRABEAM source. Figure reproduced from [21]. 66

Figure 3.7 Micro-CT projection image of the PTW microDiamond TN60019 detector, revealing its internal components. The image was acquired using a MEDISO NanoScan SdC at the McGill University Health Centre, with an x-ray tube setup of 35 kVp and 1 mAs. This image was used to confirm the dimensions for the modeled geometry. 67

Figure 3.8 Experimental setups for INTRABEAM dosimetry. (a) Measurements with the PTW 34013 ionization chamber in a Zeiss water phantom. The chamber is positioned in a plastic holder below the source. (b) Measurements with the PTW TN60019 microDiamond detector in a Wellhöfer water phantom using an automated 3D scanning system. The red circle indicates an in-house accessory used to bypass the INTRABEAM interlock system for bare probe measurements. Figure reproduced from [2]. 67

Figure 3.9 Comparison of MC-calculated and measured depth doses using the PTW 34013 ionization chamber. (a) Depth-dose curves for the INTRABEAM source normalized at 10 mm depth. MC calculations are compared with measurements from two different INTRABEAM sources (*Source 1* and *Source 2*). The inset shows the measurement geometry, where z indicates the distance from the source tip along the probe's longitudinal axis. (b) Local relative differences between MC simulations and measurements for both sources. Figure reproduced from [2]. 69

Figure 3.10 Comparison of MC-calculated and measured depth doses using the PTW TN60019 microDiamond detector with INTRABEAM *Source 1*. (a) Depth-dose curves for the INTRABEAM source normalized at 10 mm depth. Results from two microDiamond detectors are shown. The inset shows the measurement geometry, where z indicates the distance from the source tip along the probe's longitudinal axis, identical to the ionization chamber measurements. (b) Local relative differences between MC simulations and measurements for both detectors. Figure reproduced from [2]. . 70

Figure 3.11 Radial dose function of the INTRABEAM source compared to the Xoft source operated at 50 kV (data from Hiatt et al. (2015) [20]) and common brachytherapy sources ^{192}Ir, ^{125}I, and ^{103}Pd (data from Rivard et al. (2004) [25]). The inset shows the geometry for the radial dose function calculation, where r indicates the radial distance from the source tip, measured perpendicular to the probe's longitudinal axis ($\theta = 90°$). The INTRABEAM exhibits a steeper gradient near the source compared to conventional radionuclide sources. Figure reproduced from [2]. 71

Figure 3.12 2D anisotropy function for the INTRABEAM source. (a) Color map representation of the anisotropy function using the ring-shaped source model. (b) Anisotropy function curves at various distances from the source tip for the ring-shaped source model (solid lines) and the spotted-shaped source model (dotted lines). The inset shows the geometry for the anisotropy calculations, where r indicates the radial distance from the source tip and θ represents the polar angle measured from the probe's longitudinal axis. Figure reproduced from [2]. 72

Figure 4.1 Rendering of the spherical applicators models for the MC simulations. In (a), a picture of the 40 mm diameter applicator is compared with its simulation geometry shown in (b). In (c), the 15 mm applicator rendering is presented as an example of the smallest applicators, with sphere diameters from 15 to 30 mm, which include an aluminium filter. (d) shows the reference coordinate system used for determining the TG-43 parameters for the INTRABEAM source. 85

Figure 4.2 Dose calculation uncertainties due to geometry variations of the Al filter construction within tolerance values. The curves shown were calculated at 10 mm from the applicator surface for the smallest applicators of diameters 15 to 30 mm. 91

Figure 4.3 Depth-dose curves along the source longitudinal axis for the INTRABEAM system with spherical applicators ranging in diameter from 15 mm to 50 mm in steps of 5 mm. The curves are normalized at 10 mm from the applicator surface. The distances shown are measured from the source tip. The MC calculated data (marks only) are compared to the data provided by the manufacturer (Carl Zeiss) in the calibration file (solid lines). 92

Figure 4.4 Deviations from MC simulations to calibration data provided by the source manufacturer (Carl Zeiss), expressed as local relative differences, for the INTRABEAM source with each of the eight spherical applicators. 93

Figure 4.5 MC calculated anisotropy of the spherical applicators alone (after subtracting the bare probe anisotropy), at 10 mm from the applicators' surface, along the angular range $\theta = 0^\circ$ to 130°. The applicator anisotropy was calculated according to the manufacturer specifications (Carl Zeiss) relative to $\theta = 0^\circ$ and subtracting the bare probe anisotropy. 94

Figure 4.6 Photon fluence spectra scored in air at 50 cm from the source axis in an annular volume for (a) the INTRABEAM bare probe and (b) the INTRABEAM source with spherical applicators. 95

Figure 4.7 Radial dose functions for the INTRABEAM system with the available spherical applicators. The subscript "p" indicates that a point-source approximation was used in the calculations. The enhanced penetration of the smallest applicators is attributed to the beam pre-hardening throughout the added aluminium filter. 97

Figure 4.8 2D anisotropy function of the INTRABEAM source with the 40 mm diameter applicator calculated at several distances from the source tip in the polar angle range $\theta = 0^\circ$ to 160°. 98

Figure 4.9 2D anisotropy function curves calculated at 10 mm from the surface of the INTRABEAM spherical applicators in the polar angle range $\theta = 0^\circ$ to 160°. 99

Figure 5.1 Maximal point dose to planning risk volumes (PRV) obtained for the EBRT-only and for the combined EBRT + IORT plans, using the IORT obtained according to the TARGIT, the Zeiss V4.0, the C_Q, the MC to water (MC_w), and the MC to tissue (MC_{het}) dosimetry formalisms. Circles represent individual cases, and the coloured boxes enclose the interquartile range (Q1–Q3) of the median. The dose constraints are shown in dashed red for reference. *Abbreviations:* $D_{0.03cc}$ = maximal dose received by a volume greater than 0.03 cm^3; EBRT = external beam radiotherapy; IORT = intraoperative radiotherapy; OAR = organ at risk. 118

Figure 6.1 Global dose difference distribution between TG-43 and MC_w calculations for a representative patient. (a) Axial, (b) coronal, and (c) sagittal views of the dose difference maps. (d) Histogram of global dose differences. The colorbar represents the percentage difference relative to the prescription dose. Isodose lines for 2%, 5%, 10%, 20%, and 40% of the prescription dose are shown for both TG-43 (solid gray) and MC_w (dashed black) calculations. 135

Figure 6.2 Gamma analysis results for TG-43 vs MC_w dose distributions using 1%/1mm criteria for a representative patient. (a) Axial, (b) coronal, and (c) sagittal views of the gamma index distribution. (d) Histogram of gamma index values. The colorbar represents the gamma index, with values below 1 indicating agreement within the specified criteria. 136

Figure 6.3 Local dose difference distribution between TG-43 and MC_w calculations for a representative patient. (a) Axial, (b) coronal, and (c) sagittal views of the local dose difference maps. (d) Histogram of local dose differences. The colorbar represents the percentage difference relative to the local TG-43 dose. Isodose lines for 2%, 5%, 10%, 20%, and 40% of the prescription dose are shown for both TG-43 (solid gray) and MC_w (dashed black) calculations. 137

Figure 6.4 Distribution of near maximum doses ($D_{0.03\mathrm{cc}}$) to OARs for IORT plans calculated using four different dosimetry models: TG-43, TARGIT, $\mathrm{MC_w}$, and $\mathrm{MC_{het}}$. The boxplots show the median (horizontal line), interquartile range (box), and range (whiskers) of doses for each OAR and model. Individual data points are overlaid to show the spread of the data. The red dashed line represents the OAR dose constraint where applicable. Statistical significance of differences between models is indicated by asterisks: * $p \leq 0.05$, ** $p \leq 0.01$, *** $p \leq 0.001$, **** $p \leq 0.0001$, ns (not significant). 139

Figure 6.5 Absolute dose differences in near maximum dose ($D_{0.03\mathrm{cc}}$) between TARGIT, $\mathrm{MC_w}$, and $\mathrm{MC_{het}}$ models compared to the TG-43 reference model for IORT plans. The absolute dose difference is calculated as a percentage of the prescription dose. The boxplots show the median (horizontal line), interquartile range (box), and range (whiskers) of dose differences for each OAR and model comparison. Individual data points are overlaid to show the spread of the data. The dashed line at 0% represents no difference from the TG-43 model. 141

Figure 6.6 Distribution of near maximum doses ($D_{0.03\mathrm{cc}}$) to OARs for combined EBRT and IORT plans. The figure compares EBRT alone with combined EBRT+IORT using four different IORT dosimetry models: TG-43, TARGIT, $\mathrm{MC_w}$, and $\mathrm{MC_{het}}$. The boxplots show the median (horizontal line), interquartile range (box), and range (whiskers) of doses for each OAR and treatment scenario. Individual data points are overlaid to show the spread of the data. The red dashed line represents the OAR dose constraint where applicable. 142

List of tables

Table 3.1 Material specifications of the INTRABEAM source probe. 60

Table 3.2 Radial dose function data, $g_p(r)$, for the INTRABEAM source calculated using the TG-43 point-source model. Type A uncertainties are included. . . 75

Table 3.3 2D anisotropy function data, $F(r, \theta)$, for the INTRABEAM source using the ring-shaped source model. 'NA' indicates points inside the source where $F(r, \theta)$ is not determined. 76

Table 4.1 Summary of the characteristics of the MC method used to obtain the TG-43 parameters. 87

Table 4.2 Uncertainty budget for the MC calculation of the dose rate at the reference point, $\dot{D}_i(10\,\mathrm{mm},\, \pi/2)$, for all spherical applicators. Since the Al filter is not present in the applicators with diameters 35 to 50 mm, the corresponding uncertainty cells were marked as 'NA'. 90

Table 4.3 Uncertainty on the calibration dose rate data at 10 mm from the spherical applicators' surface, along the source probe axis, due to positioning tolerances. 90

Table 4.4 Total photon fluence, Φ, fluence averaged energy, $\bar{E}_\Phi$, fluence averaged transfer coefficient, $\overline{(\mu_{\mathrm{tr}}/\rho)}_{\mathrm{air},\Phi}$, and air-kerma rate, $\dot{K}_{50cm}$, calculated from the photon fluence spectra at 50 cm from the source tip (at θ = 90°), absorbed-dose rate to water at the reference point of 10 mm from the applicator surface, $\dot{D}(10\,\mathrm{mm},\, \pi/2)$, and dose-rate conversion coefficient, χ, for the INTRABEAM bare probe and all spherical applicators. The data shown were calculated for the system operated at a current of 40 μA. . . . 96

Table 4.5 MC calculated radial dose function data, $g_{\mathrm{p}}(r)$, for the INTRABEAM bare probe and with spherical applicators. The TG-43 point-source model has been used. Points located inside the applicator, for which $g_{\mathrm{p}}(r)$ is not determined, are indicated by 'NA'. 100

Table 4.6 MC calculated 2D anisotropy function data, $F(r,\theta)$, for the INTRABEAM source with the 15 and 20 mm diameter spherical applicators. Points located inside the applicators, for which $F(r,\theta)$ is not determined, are indicated by 'NA'. 101

Table 4.7 MC calculated 2D anisotropy function data, $F(r,\theta)$, for the INTRABEAM source with the 25, 30 and 35 mm diameter spherical applicators. Points located inside the applicators, for which $F(r,\theta)$ is not determined, are indicated by 'NA'. 102

Table 4.8 MC calculated 2D anisotropy function data, $F(r,\theta)$, for the INTRABEAM source with the 40, 45 and 50 mm diameter spherical applicators. Points located inside the applicators, for which $F(r,\theta)$ is not determined, are indicated by 'NA'. 103

Table 5.1 Summary of the relevant MC characteristics and input parameters used in this study. 114

Table 5.2 Mass density and elemental composition of tissues evaluated in this study. . 115

Table 5.3 Maximal point dose to planning risk volumes (PRV) calculated with the dose distributions obtained with the reference TARGIT, the Zeiss V4.0, the C_{Q}, the MC to water (MC_{w}), and the MC to tissue (MC_{het}) formalisms. The data shown correspond to the mean, in Gy, and the number of cases that exceeded the dose constraint (n_{exc}) in a cohort of eight patients. Data exceeding the constraints are shown in bold. 116

Table 5.4 Maximal point dose ($D_{0.03\mathrm{cc}}$) to planning risk volumes (PRV) calculated with the dose distributions obtained with the EBRT-only plan, and with the EBRT combined with the IORT obtained with the reference TARGIT, the Zeiss V4.0, the C_{Q}, the MC to water (MC_{w}), and the MC to tissue (MC_{het}) dosimetry formalisms. The data shown correspond to the mean, in Gy, and the number of cases that exceeded the dose constraint (n_{exc}) in a cohort of eight patients. Data exceeding the constraints are shown in bold. 117

Table 5.5 Uncertainty on the dose rate estimated at 10 mm from the surface of each spherical applicator, along the source axis, for the TARGIT, V4.0, C_Q, MC_w, and MC_{het} formalisms. 119

Table 6.1 Summary of the relevant MC characteristics and input parameters used in this study. 132

Table 6.2 Near maximum dose ($D_{0.03cc}$) to OARs calculated with the IORT plans in a cohort of 20 patients. 138

Table 6.3 Near maximum dose ($D_{0.03cc}$) absolute dose differences between the TARGIT, MC_w, and MC_{het} IORT dose calculation models and the TG-43 reference model in a cohort of 20 patients. 140

Table 6.4 Near maximum dose ($D_{0.03cc}$) to OARs calculated with the combined EBRT and IORT plans in a cohort of 20 patients. 142

List of abbreviations

AAA	Analytical Anisotropic Algorithm
AAPM	American Association of Physicists in Medicine
CBCT	Cone Beam Computed Tomography
CPU	Central Processing Unit
CPE	Charged Particle Equilibrium
CSDA	Continuous Slowing Down Approximation
CT	Computed Tomography
CTV	Clinical Target Volume
DICOM	Digital Imaging and COmmunications in Medicine
DTA	Distance To Agreement
DVH	Dose-Volume Histogram
EADL	Livermore Evaluated Atomic Data Library
EBRT	External Beam Radiation Therapy
eBT	Electronic Brachytherapy
ECUT	Transport Cut-off Energy for Electrons
EGS	Electron Gamma Shower
EII	Electron Impact Ionization
EPOM	Effective Point of Measurement
EQD2	EQuivalent Dose in 2 Gy fractions
FAC	Free-Air Ionization Chamber
FWHM	Full Width at Half Maximum
Gy	Gray
HDR	High Dose Rate
HU	Hounsfield Unit
HVL	Half Value Layer

IAEA	International Atomic Energy Agency
ICRU	International Commission on Radiation Units and Measurements
IGRT	Image Guided Radiation Therapy
IMRT	Intensity Modulated Radiation Therapy
IORT	Intraoperative Radiotherapy
kV	Kilovoltage
kVp	Kilovoltage peak
LDR	Low Dose Rate
linac	Linear Accelerator
MC	Monte Carlo
MRI	Magnetic Resonance Imaging
MV	Megavoltage
NIST	National Institute of Standards and Technology
NTCP	Normal Tissue Complication Probability
OAR	Organ at Risk
PCUT	Transport Cut-off Energy for Photons
PDD	Percentage Depth Dose
PET	Positron Emission Tomography
PTV	Planning Target Volume
QA	Quality Assurance
RBE	Relative Biological Effectiveness
RSV	Radiation-Sensitive Volume
RT	Radiation Therapy
SSD	Source to Surface Distance
TCP	Tumor Control Probability
TG	Task Group
TPS	Treatment Planning System
VMAT	Volumetric Modulated Arc Therapy
XCSE	Photon Cross-Section Enhancement

Preface

This thesis presents research conducted at McGill University, focusing on improving the dosimetry of the INTRABEAM system for intraoperative radiotherapy (IORT) in brain cancer treatment. The work encompasses three original research manuscripts, each addressing critical aspects of IORT dosimetry in the context of glioblastoma treatment.

Contribution to original knowledge

This thesis makes several significant contributions to the field of INTRABEAM dosimetry for IORT. The first major contribution is the comprehensive TG-43 characterization of the INTRABEAM system with spherical applicators. This work extends previous bare probe characterization to include all available spherical applicator sizes, providing a complete set of dosimetry parameters necessary for accurate 3D dose calculations within existing brachytherapy treatment planning frameworks. These parameters enable more precise dose calculations while maintaining computational efficiency, addressing a significant gap in clinical practice.

The second key contribution is the novel comparison of dosimetry formalisms for IORT in GBM treatment. Through detailed analysis of different calculation methods, including the current clinical standard (TARGIT method), V4.0 calibration method, C_Q method, and Monte Carlo simulations, this research reveals significant discrepancies in organ-at-risk dose estimates. The findings demonstrate that current clinical practices may underestimate delivered doses, with important implications for treatment planning and patient safety. This work provides the first comprehensive evaluation of these dosimetry methods in the context of the INTRAGO trial, offering valuable insights for improving dose calculation accuracy in clinical settings.

The third major contribution is the comprehensive evaluation of the TG-43 formalism for INTRABEAM IORT in GBM treatment. This study provides a detailed comparison of TG-43

calculations with Monte Carlo simulations in both homogeneous and heterogeneous media, offering new insights into the accuracy and limitations of different dose calculation approaches in complex anatomical scenarios. The research demonstrates that while TG-43 offers improved accuracy over current clinical standards, tissue heterogeneity effects may necessitate more sophisticated calculations in certain cases. This work establishes a practical framework for implementing more accurate dosimetry methods in clinical practice while balancing computational efficiency with accuracy requirements.

These contributions collectively advance the field of IORT dosimetry, providing tools and methodologies for improved treatment planning and dose delivery verification. The research establishes a foundation for enhanced OAR dose estimation accuracy compared to current practice and offers a pathway for improved combined EBRT-IORT treatment planning.

Contribution of authors

The specific contributions of the authors to each manuscript are as follows:

1. *David Santiago Ayala Alvarez, Peter G. F. Watson, Marija Popovic, Veng Jean Heng, Michael D. C. Evans, and Jan Seuntjens, "Monte Carlo calculation of the TG-43 dosimetry parameters for the INTRABEAM source with spherical applicators", Physics in Medicine & Biology, vol. 66, no. 21, 215017, 2021.* (Chapter 4)

   I conceived the study with Peter G. F. Watson, Marija Popovic, and Jan Seuntjens, performed the Monte Carlo simulations and experimental measurements, analyzed the data, and wrote the manuscript. Peter G. F. Watson provided the original Monte Carlo models for the INTRABEAM simulations and assisted in obtaining applicator specifications from the manufacturer. Marija Popovic and Michael D. C. Evans provided assistance in performing the measurements and offered insights from their clinical expertise. Veng Jean Heng created an application in the in-house TPS `Brems` and contributed to the data analysis. Jan Seuntjens supervised the project, provided guidance in study design and data interpretation, and critically reviewed the manuscript. All authors reviewed and approved the final manuscript.

2. *David Santiago Ayala Alvarez, Peter G. F. Watson, Marija Popovic, Veng Jean Heng, Michael D. C. Evans, Valerie Panet-Raymond, and Jan Seuntjens, "Evaluation of dosime-*

try formalisms in intraoperative radiation therapy of glioblastoma", International Journal of Radiation Oncology Biology* Physics, vol. 117, No. 3, pp. 763-773, 2023.* (Chapter 5)

I performed the Monte Carlo simulations and dosimetric analyses and wrote the manuscript. Peter G. F. Watson provided guidance on Monte Carlo simulations and dosimetry calculations. Marija Popovic and Valerie Panet-Raymond facilitated access to randomized patient data and provided clinical insights. Veng Jean Heng contributed to the data analysis and provided support with `Brems` dose calculations. Michael D. C. Evans offered valuable clinical perspectives and assisted in interpreting the results. Jan Seuntjens supervised the project, provided guidance in study design and data interpretation, and critically reviewed the manuscript. All authors contributed to the manuscript revision and approved the final version.

3. *David Santiago Ayala Alvarez, Peter G. F. Watson, Marija Popovic, Veng Jean Heng, Michael D. C. Evans, Valerie Panet-Raymond, and Jan Seuntjens, "Evaluation of the TG-43 formalism for INTRABEAM intraoperative radiotherapy dosimetry in glioblastoma treatment", in preparation for submission to Medical Physics, 2024.* (Chapter 6)

   I performed the Monte Carlo simulations and dosimetric analyses and wrote the manuscript. Peter G. F. Watson provided guidance on Monte Carlo simulations. Marija Popovic and Valerie Panet-Raymond assisted in accessing patient data and ensured compliance with ethical requirements. Veng Jean Heng contributed to the data analysis and provided support with `Brems` dose calculations. Michael D. C. Evans provided clinical insights. Jan Seuntjens supervised the project, guided the research direction, and critically reviewed the manuscript. All authors reviewed the manuscript.

Chapter 1

Introduction

1.1 Cancer and radiotherapy

Cancer is a complex group of diseases characterized by the uncontrolled growth and spread of abnormal cells. It arises from genetic mutations that disrupt normal cell function, leading to the formation of malignant tumors that can invade nearby tissues and metastasize to distant parts of the body [1]. The impact of cancer on global health is profound, with recent estimates indicating its significant burden on individuals, healthcare systems, and societies worldwide.

According to the International Agency for Research on Cancer (IARC), there were an estimated 20 million new cancer cases and 9.7 million cancer deaths globally in 2022 [2]. In Canada, cancer remains a leading cause of morbidity and mortality. The Canadian Cancer Society projected that in 2024, approximately 247,100 new cancer cases would be diagnosed, and 88,100 Canadians would die from cancer [3]. These statistics highlight the critical need for effective cancer prevention, early detection, and treatment strategies.

The approach to cancer treatment is multifaceted, often involving a combination of modalities tailored to the specific type and stage of cancer. The primary treatment options include surgery for the physical removal of tumors and affected tissues, chemotherapy using drugs to kill cancer cells or inhibit their growth, radiotherapy applying ionizing radiation to destroy cancer cells, immunotherapy enhancing the body's immune system to fight cancer, and hormone therapy manipulating hormone levels to slow or stop the growth of certain cancers. These modalities can be used alone or in combination, with one treatment often serving as an adjuvant to enhance the effectiveness of another.

Among these, radiotherapy plays a crucial role in cancer management. Also known as radiation therapy, it involves the use of ionizing radiation, which can range from kilovoltage (kV) photons (30-400 keV) to megavoltage (MV) photons or charged particles (1-25 MeV) to damage or kill cancer cells by targeting their DNA [4]. Radiotherapy is a versatile treatment modality used in both curative and palliative settings. It can be employed as a standalone treatment or as an adjuvant therapy in combination with other modalities to enhance therapeutic outcomes.

The significance of radiotherapy in cancer care is evident from its widespread use. Approximately 50% of all cancer patients receive radiotherapy during their course of illness, and it contributes to 40% of curative treatment for cancer [5]. In Canada, about 50% of cancer patients undergo radiation therapy at some point during their treatment [3].

A fundamental concept in radiotherapy is the therapeutic window, which refers to the range of radiation doses that effectively treat the tumor while remaining below the threshold for unacceptable damage to surrounding healthy tissues. This concept is quantitatively expressed through the therapeutic ratio, which characterizes the relationship between tumor control probability (TCP) and normal tissue complication probability (NTCP) [6], as illustrated in Figure 1.1. The goal of treatment planning is to maximize this ratio by achieving the highest possible tumor control while maintaining acceptable levels of normal tissue complications. Achieving this balance requires precise treatment planning and delivery techniques, which have evolved significantly with technological advancements in the field of radiation oncology.

The ongoing research and development in radiotherapy aim to expand the therapeutic window, allowing for more effective and less toxic treatments. This includes the exploration of novel treatment modalities, improved targeting techniques, and a better understanding of tumor radiobiology. These advancements continue to shape the landscape of cancer treatment, offering hope for improved outcomes and quality of life for cancer patients.

1.2 Radiotherapy modalities

Radiotherapy has evolved significantly since its inception, with various modalities developed to optimize treatment delivery and improve patient outcomes. The choice of modality depends on factors such as cancer type, location, stage, and patient-specific considerations. This section provides an overview of the main radiotherapy modalities currently in clinical use.

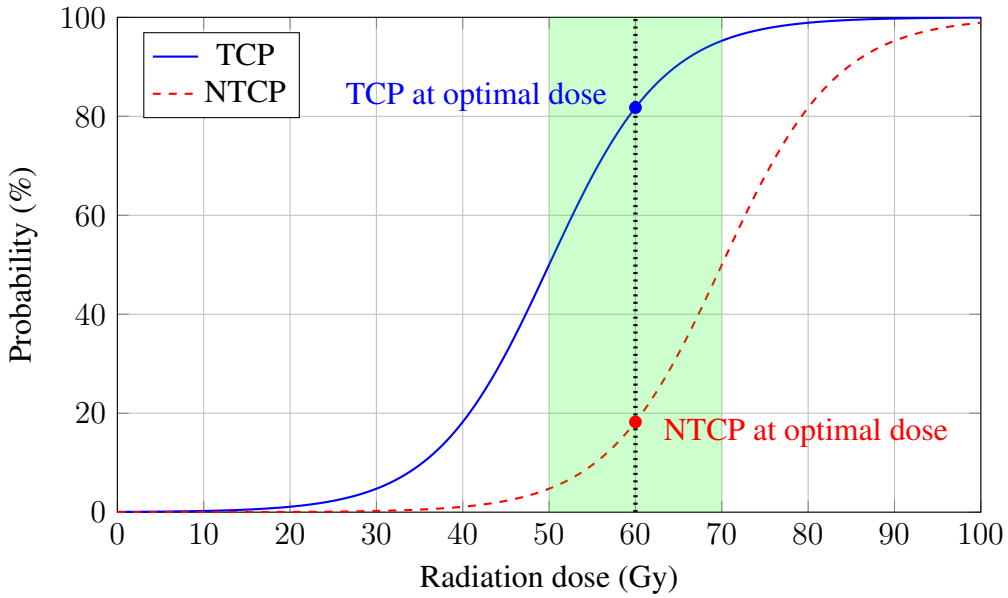

Figure 1.1 Illustration of the therapeutic window and therapeutic ratio concepts in radiotherapy. The curves show the relationship between radiation dose and both tumor control probability (TCP, solid line) and normal tissue complication probability (NTCP, dashed line). The therapeutic window (shaded region) represents the dose range where tumor control can be achieved while maintaining acceptable normal tissue complications. The therapeutic ratio is maximized at the dose where the separation between TCP and NTCP is greatest, indicated by the vertical dotted line.

1.2.1 External beam radiotherapy

External beam radiotherapy (EBRT) is the most widely used form of radiation therapy. In EBRT, radiation is delivered to the tumor from an external source, typically a linear accelerator (linac). Modern linacs can produce both high-energy photon (X-ray) and electron beams, with energies ranging from 4 to 25 MeV [7]. These high-energy beams allow the treatment of deep-seated tumors while sparing the skin and superficial tissues.

The evolution of EBRT has been marked by significant technological advancements, particularly in treatment planning and delivery techniques. Contemporary EBRT employs imaging and computational methods to optimize dose distributions. This process typically begins with acquiring a computed tomography (CT) scan of the patient, which provides three-dimensional anatomical information and allows for accurate delineation of the tumor and surrounding organs at risk (OARs).

Treatment planning systems (TPS) use these CT images to calculate dose distributions within the patient, taking into account tissue heterogeneities and the physical interactions of radiation with matter. This approach enables the creation of conformal dose distributions that maximize tumor coverage while minimizing dose to healthy tissues. Modern techniques such as intensity-modulated radiation therapy (IMRT) and volumetric-modulated arc therapy (VMAT) utilize optimization algorithms to achieve these goals, often employing hundreds of small radiation beams or continuous arc rotations with dynamically varying beam intensities [8].

A key strength of modern EBRT is the ability to generate and evaluate three-dimensional dose distributions. Treatment plans can be assessed using dose-volume histograms (DVH), which provide quantitative information about the radiation dose received by various structures. This capability allows for detailed evaluation of plan quality and facilitates comparison between different treatment options. Image-guided radiation therapy (IGRT) further enhances the precision of EBRT by incorporating imaging during the treatment course. This approach enables adjustment for daily variations in patient positioning and potential changes in tumor size or location, ensuring accurate dose delivery throughout the treatment regimen [9].

While EBRT offers many advantages, it typically involves fractionated treatment schedules delivered over several weeks. This approach leverages radiobiological principles to maximize the therapeutic ratio but can be logistically challenging for some patients and may not be optimal for all tumor types or clinical scenarios.

1.2.2 Brachytherapy

Brachytherapy, derived from the Greek word “brachys” meaning short, involves placing radiation sources directly into or near the tumor. This approach allows for a high dose of radiation to be delivered to the tumor while rapidly falling off with distance, thereby sparing surrounding healthy tissues. The steep dose gradient characteristic of brachytherapy makes it an attractive option for treating tumors that are anatomically well-defined and confined to a specific site without evidence of distant spread [7].

Brachytherapy can be classified based on the dose rate and the placement of radiation sources. Low-dose-rate (LDR) brachytherapy involves the continuous delivery of radiation over a prolonged period, typically several days, using sources such as iodine-125 or palladium-103. High-dose-rate (HDR) brachytherapy delivers high doses of radiation in short fractions, lasting only a few minutes per session, often using sources like iridium-192. Medium-dose-rate (MDR)

brachytherapy falls between LDR and HDR, with treatment durations of several hours (ICRU 1997). The radionuclides used in brachytherapy are chosen based on their half-life, energy spectrum, and physical characteristics [10].

Regarding the placement of radiation sources, brachytherapy can be categorized into interstitial, intracavitary, and surface modalities. Interstitial brachytherapy involves the direct insertion of radiation sources using needles into the tumor tissue and is commonly used for prostate and breast cancers. Intracavitary brachytherapy places the sources within body cavities, such as the cervix or uterus, to treat gynecological cancers. Surface brachytherapy involves placing radiation sources on the skin surface to treat skin cancers [11].

While brachytherapy offers excellent dose conformity, it is invasive and requires careful planning to ensure accurate source positioning and dose calculation. These considerations have motivated the development of alternative approaches that aim to combine the dosimetric advantages of brachytherapy with improved logistics and reduced invasiveness.

1.2.3 Intraoperative radiotherapy

Intraoperative radiotherapy (IORT) is a technique where a high single dose of radiation is delivered directly to the tumor bed during surgery immediately after tumor resection. This approach allows for direct visualization of the tumor and surrounding tissues during surgery, enabling precise radiation delivery while minimizing exposure to surrounding healthy tissues [12].

IORT can be performed using various radiation modalities, including electron beams from specialized mobile linear accelerators, low-energy X-rays from miniature X-ray sources, and high dose rate brachytherapy sources [13]. The ability to deliver high doses in a single session during surgery can reduce the need for postoperative radiation and shorten the overall treatment duration. Moreover, IORT provides the advantage of targeting residual microscopic disease that may be left behind after tumor resection, potentially improving local control rates [14], and allowing potential dose escalation due to reduced normal tissue exposure.

The development of mobile IORT devices has significantly expanded the application of this technique. These devices allow for the delivery of radiation in the operating room, eliminating the need to transport the patient to a shielded radiation therapy vault. This approach has found applications in various cancer types, including breast, pancreatic, and rectal cancers, as well as in the treatment of brain tumors [15].

The integration of IORT into cancer treatment protocols has led to the exploration of new

treatment paradigms, such as accelerated partial breast irradiation and boost dose delivery in combination with external beam radiotherapy. These approaches aim to improve local control while potentially reducing treatment-related toxicity and treatment duration.

1.2.4 Electronic brachytherapy

Electronic brachytherapy (eBT) is a relatively new modality that uses miniature X-ray sources to deliver radiation, typically in the low-energy range (40-50 kVp). Unlike traditional brachytherapy, which uses radioactive isotopes, eBT employs electrically generated X-rays, offering advantages in terms of radiation protection and flexibility of use [16].

Key features of eBT include its switchable radiation source, which eliminates the need for radioactive material handling and storage, and the potential for optimized dose distributions through modulation of beam energy and dwell times. The use of low-energy photons also results in reduced shielding requirements, improving radiation safety for healthcare workers and patients.

Two prominent examples of eBT systems are the Xoft Axxent (iCAD Inc., San Jose, CA) and the INTRABEAM (Carl Zeiss Meditec AG, Oberkochen, Germany) systems. Both operate in the 50 kVp range but differ in their design and specific applications. The Xoft Axxent system uses a miniature X-ray source at the tip of a flexible coolant-filled catheter. It has found applications in accelerated partial breast irradiation, gynecological brachytherapy, and non-melanoma skin cancer treatment. The system's flexibility allows for adaptation to various anatomical sites [17].

The TARGIT-A trial (TARGeted Intraoperative radioTherapy Alone) compared single-fraction targeted intraoperative radiotherapy using the INTRABEAM system to conventional fractionated external beam radiotherapy in early breast cancer. The trial demonstrated non-inferiority of INTRABEAM treatment in terms of local recurrence, with potential benefits in reduced treatment time and improved cosmetic outcomes. The TARGIT-A trial results have significantly contributed to the growing acceptance of IORT as a treatment option in selected breast cancer patients [12].

1.3 INTRABEAM system

The INTRABEAM system is a miniature X-ray source designed for intraoperative radiotherapy and electronic brachytherapy applications. At its core is a compact X-ray source housed within a

probe, which is mounted on an articulated arm for precise positioning during treatment, as shown in Figure 1.2.

The X-ray source generates low-energy photons through a process similar to that used in diagnostic X-ray tubes but on a much smaller scale. As illustrated in Figure 1.2, electrons are produced by the cathode gun and accelerated through the accelerator section. The beam deflector then directs these electrons towards a gold target at the tip of the probe. The interaction of these electrons with the gold target produces x-rays through bremsstrahlung and characteristic radiation processes [18].

The system operates at a maximum potential of 50 kV, resulting in an x-ray spectrum with a maximum energy of 50 keV and an average energy of approximately 20-30 keV, depending on the depth in tissue. This low-energy spectrum results in a steep dose fall-off with distance, allowing for highly localized dose delivery while minimizing exposure to surrounding tissues.

A range of specialized applicators must be used with the system to enable effective clinical treatments. These applicators serve several critical functions that make IORT delivery possible. First, they physically expand the treatment surface to match the size of the surgical cavity, ensuring uniform dose delivery to the target tissue. Without applicators, the bare probe would create an extremely steep and non-uniform dose distribution unsuitable for most clinical applications. Second, the applicator material attenuates and hardens the X-ray beam by filtering out lower energy photons, which improves tissue penetration characteristics. Third, the applicators provide a standardized geometry that allows for reproducible dose delivery and simplifies treatment planning.

The most commonly used are spherical applicators, ranging in diameter from 1.5 to 5.0 cm in 0.5 cm increments. Figure 1.3 shows an example of a 4 cm diameter spherical applicator, which is typically used for breast and brain tumor treatments [12, 20]. During a procedure, the surgeon selects an applicator size that best matches the surgical cavity dimensions after tumor removal. The applicator is then attached to the probe and positioned within the cavity so that its surface makes contact with the tissue requiring treatment. This ensures that the prescribed dose is delivered uniformly to the target tissue while the steep dose fall-off beyond the applicator helps protect surrounding healthy structures.

The effect of spherical applicators on dose distribution is illustrated in Figure 1.4. When compared to conventional EBRT, which delivers a relatively uniform dose distribution using high-energy beams, IORT with the INTRABEAM system creates a distinctly different dose pattern. The applicator transforms the bare probe's output into an approximately spherical high-

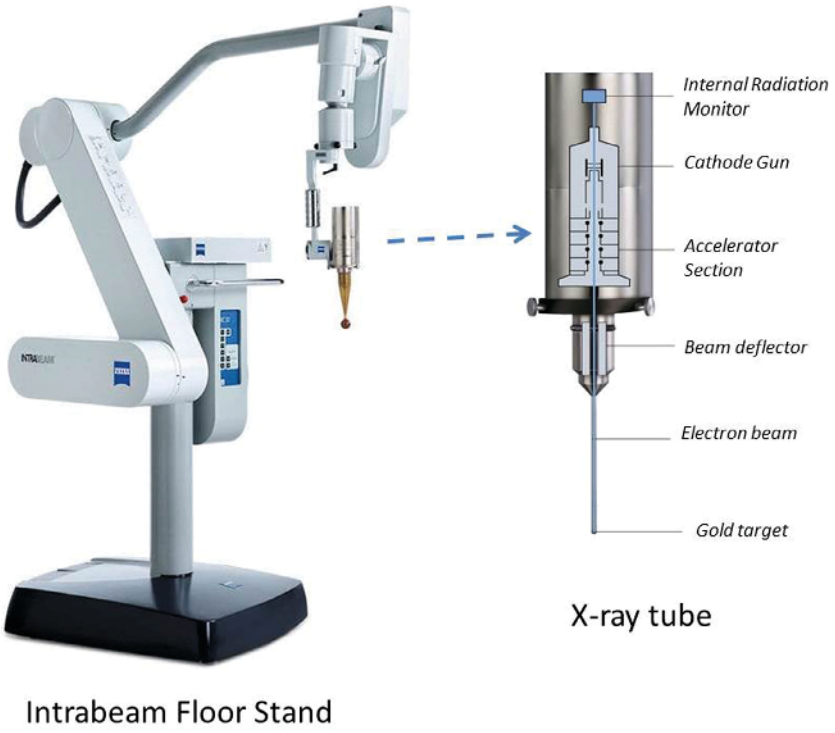

Figure 1.2 The INTRABEAM system. Left: INTRABEAM source with a spherical applicator mounted on the articulated arm and floor stand. The floor stand (dimensions 74 cm $\times$ 194 cm $\times$ 150 cm, W $\times$ H $\times$ L) provides flexibility of movement with millimeter precision in six dimensions. Right: Schematic cross-section of the x-ray source (dimensions 7 cm $\times$ 1 1cm $\times$ 17 cm) showing internal components involved in electron beam generation and transport. The source probe has an outer diameter of 3.2 mm and length of 100 mm, with a 0.5 μm thick gold target at its tip. Key components are labeled, including the internal radiation monitor, cathode gun, accelerator section, beam deflector, electron beam path, and gold target. Figure reproduced from [19] under the Creative Commons Attribution License (CC BY).

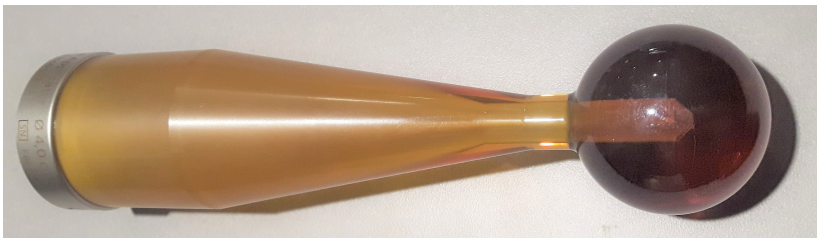

Figure 1.3 A 4 cm diameter spherical applicator used with the INTRABEAM system for intraoperative radiotherapy in breast and brain tumors.

dose region that closely conforms to the surgical cavity. This transformation is achieved through

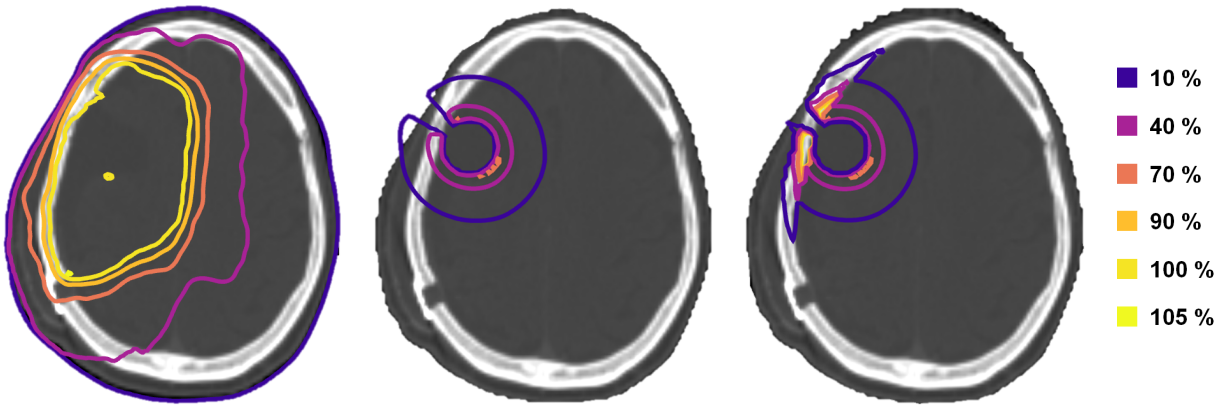

(a) (b) (c)

Figure 1.4 Comparison of dose distributions in an axial CT slice for different treatment delivery techniques: (a) EBRT plan showing a relatively uniform dose distribution typical of high-energy (6 MV) external beam delivery, (b) IORT calculated in water medium demonstrating the characteristic steep dose gradient and an approximately spherically symmetric distribution shaped by the applicator, and (c) IORT calculated with tissue heterogeneity corrections showing subtle variations in dose distribution due to tissue interfaces. The steep dose gradient in IORT (b,c) illustrates how spherical applicators modify the bare probe's output, creating an approximately spherical high-dose region that conforms to the surgical cavity while rapidly falling off to spare surrounding tissues. Isodose lines represent percentage of prescription dose (60 Gy for EBRT, 20 Gy at applicator surface for IORT) as indicated in the color map. Note that while tissue heterogeneity effects are minimal for EBRT at 6 MV, they become more pronounced for IORT due to the increased photoelectric effect at lower energies (50 kVp).

both geometric expansion and beam hardening, with the applicator material preferentially filtering lower-energy photons. The resulting dose distribution shows a characteristic steep gradient, rapidly falling off beyond the target volume. While tissue heterogeneity effects are minimal for high-energy EBRT, they become more pronounced in IORT due to the increased photoelectric effect at the lower energies used (50 kVp vs 6 MV). However, in brain IORT, these tissue heterogeneity effects remain relatively modest as the target region primarily consists of soft tissue, with minimal involvement of high-density structures like the skull.

Other applicator types include flat and surface applicators for skin or superficial lesions, needle applicators for spine metastases treatments, and cylindrical applicators for intracavitary treatments. Each applicator type modifies the isodose distribution to suit different clinical scenarios, enhancing the system's versatility [21].

The INTRABEAM system is controlled via a console that houses the power supply and con-

trol systems. This console allows operators to set and monitor treatment parameters, ensuring accurate dose delivery. The system incorporates several safety features, including an internal radiation monitor that continuously measures the output during treatment. Studies of INTRABEAM output stability have shown excellent consistency, with output variations typically less than 1% from baseline values over extended periods of clinical use [22].

The INTRABEAM system's unique characteristics, particularly its low-energy x-ray spectrum and steep dose gradients, make it a promising tool for localized radiation delivery in various clinical scenarios. One such application that has garnered significant interest is the treatment of glioblastoma multiforme, a particularly aggressive form of brain cancer. The potential of the INTRABEAM system in this context is being explored through clinical trials, which aim to evaluate its efficacy when used in combination with standard treatment protocols.

1.4 Glioblastoma and the INTRAGO trial

Glioblastoma multiforme (GBM) is the most common and aggressive primary malignant brain tumor in adults. It is characterized by rapid growth, extensive infiltration into surrounding brain tissue, and poor prognosis. Despite advances in treatment modalities, the prognosis remains poor, with a median overall survival of 14 to 16 months and a five-year survival rate below 10% [23].

The current standard of care for newly diagnosed GBM, established by Stupp et al. (2005) [24], involves maximal safe surgical resection followed by adjuvant radiotherapy with concomitant and adjuvant temozolomide chemotherapy. However, the limited improvement in patient outcomes over the past decades indicates an urgent need for novel therapeutic approaches.

A significant challenge in GBM treatment is the high rate of local recurrence, with approximately 85% of tumors recurring within 2-3 cm of the original resection margin [25]. This pattern suggests that intensifying local treatment could potentially improve outcomes. IORT has emerged as a promising approach to address this challenge by delivering a targeted boost dose to the tumor bed immediately after resection.

The INTRAGO (INTraoperative RAdiotherapy in Glioblastoma multiforme) trial was initiated to evaluate the safety and efficacy of adding IORT using the INTRABEAM system to the standard treatment regimen for newly diagnosed GBM. The initial phase of this study, INTRAGO I, began in 2014 as a multicenter, open-label, dose-escalation phase I/II trial aimed at determining the maximum tolerated dose of IORT that could be safely delivered in combination with standard

chemoradiotherapy [20]. The trial enrolled 15 patients who were treated with escalating IORT doses (20-40 Gy). The results, published in 2019, demonstrated that IORT was well-tolerated with manageable toxicity and showed promising efficacy in terms of local progression-free survival [26].

Building on these encouraging results, the trial has progressed to its second phase, INTRAGO II (ClinicalTrials.gov Identifier: NCT02685605). This multicentric, prospective, randomized, 2-arm, open-label phase III trial commenced in December 2016 and is being conducted at 19 locations across eight countries. The trial has enrolled 314 patients and aims to test whether the addition of IORT to standard radiochemotherapy can improve the median progression-free survival (PFS) of patients with newly diagnosed GBM. With a primary completion date estimated for June 2024 and study completion in June 2026, INTRAGO II represents one of the most comprehensive evaluations of IORT in GBM treatment to date [26].

In the INTRAGO II protocol, patients undergoing surgical resection for newly diagnosed GBM are randomized to receive either standard treatment alone or standard treatment plus IORT. The IORT is delivered using the INTRABEAM system with an appropriately sized spherical applicator chosen to fit the resection cavity. Currently, the INTRAGO protocol relies on the TARGIT method for dose estimation. This approach uses pre-measured depth-dose curves to estimate the dose based on distances from the applicator surface to organs at risk, which are manually determined using neuronavigation software. This operator-dependent method introduces uncertainties of several millimeters in distance measurements, which can significantly impact dose estimates given the steep dose gradients of the INTRABEAM system.

One key advantage of IORT in GBM treatment is the ability to deliver a high, localized dose of radiation to the tumor bed when it is most vulnerable—immediately after surgery, when tumor cell burden is at its lowest, and before repopulation can occur. Additionally, the steep dose gradient of the low-energy X-rays produced by the INTRABEAM system allows for sparing adjacent normal brain tissue [27]. The potential impact of successfully integrating IORT in GBM treatment extends beyond immediate patient outcomes. While the current INTRAGO trial evaluates IORT as an addition to standard EBRT, future applications might explore IORT as an alternative treatment approach that could reduce the volume of brain tissue exposed to high radiation doses. Moreover, if proven effective, this approach could lead to shortened overall treatment times, potentially improving patients' quality of life during the course of their illness.

1.5 Challenges in INTRABEAM dosimetry

The implementation of the INTRABEAM system for IORT presents unique dosimetric challenges stemming from the physical characteristics of its radiation and the complex treatment scenarios in which it is used.

A primary challenge arises from the low-energy X-rays generated by the INTRABEAM system. With a maximum energy of 50 keV and an average energy of 20-30 keV, these X-rays exhibit steep dose gradients, which, while beneficial for sparing normal tissue, complicate accurate dose calculation and measurement [18]. These steep gradients make precise dose estimation particularly sensitive to uncertainties in distance measurements from the applicator surface to organs at risk. In IORT for glioblastoma multiforme (GBM), the irregular shape of the resection cavity and the positioning of the applicator within it add another layer of complexity to dosimetric calculations [19].

While brain parenchyma is relatively homogeneous in terms of tissue composition, some anatomical considerations remain relevant for dosimetry. The presence of air cavities (such as nasal sinuses) and bony structures near certain organs at risk, as well as reduced backscatter near the skin surface, can affect dose distributions [28]. However, during IORT, the removal of overlying skull for surgical access eliminates some of the major tissue heterogeneities in the immediate vicinity of the applicator.

Various approaches have been explored to address the dosimetric challenges of INTRABEAM IORT. One notable method is the AAPM Task Group No. 43 (TG-43) protocol [29] and its update [30], widely used in brachytherapy dosimetry. This protocol provides a standardized formalism for calculating three-dimensional dose distributions around radiation sources in water-equivalent media. While TG-43 cannot account for tissue heterogeneities, it offers potential advantages over the current one-dimensional TARGIT approach by providing comprehensive dose distributions that could enable more accurate treatment planning and evaluation.

Current dosimetry methods for the INTRABEAM system, including those based on TG-43, rely heavily on water-based calculations. While these provide a good starting point, they may not accurately represent dose distributions in patient-specific scenarios, especially in heterogeneous tissues. The discrepancies between water-based calculations and actual dose distributions in complex anatomical structures can be significant, potentially leading to inaccuracies in treatment planning and dose delivery.

Integration of IORT into existing treatment workflows also presents logistical challenges.

Unlike conventional radiotherapy, where treatment planning can be done over several days, IORT requires rapid decision-making and dose calculation in the operating room. This necessitates the development of fast, accurate dosimetry methods that can be implemented in real-time during surgery [12].

Addressing these dosimetric challenges is crucial for ensuring accurate dose delivery to the target volume while minimizing exposure to surrounding healthy tissues, particularly in sensitive areas like the brain. Improved dosimetry is also necessary for meaningful comparison of treatment outcomes across different patients and clinical trials, enabling the establishment of clear dose-response relationships and optimization of treatment protocols [31].

As IORT with the INTRABEAM system continues to be explored in new clinical applications, such as GBM treatment in the INTRAGO trial, the need for robust dosimetry becomes even more critical. The success of these trials and the potential widespread adoption of this treatment modality depend on our ability to accurately characterize and control the dose delivered to patients. The development and validation of advanced dosimetry methods for the INTRABEAM system, particularly for its application in GBM treatment, form a central focus of ongoing research in this field, including the work presented in this thesis.

1.6 Thesis objectives

This thesis hypothesizes that by developing and validating more accurate dosimetry methods for the INTRABEAM system, particularly through the adaptation and evaluation of the TG-43 protocol, we can improve dose calculation accuracy and provide a more robust foundation for treatment planning in brain IORT.

The specific objectives of this thesis are:

1. To characterize the INTRABEAM source with spherical applicators using the AAPM TG-43 protocol, extending the dosimetry from the bare probe to include all available spherical applicator sizes.

2. To evaluate the impact of different dosimetry approaches on the estimated dose to OARs in INTRAGO patients. This involved comparing the current TARGIT method with more accurate calculation approaches.

3. To assess the feasibility and accuracy of implementing the TG-43 methodology for dose

calculations in clinical practice, comparing it with the current TARGIT method and more complex MC simulations in water and heterogeneous media.

1.7 Thesis outline

This thesis is structured as follows. Chapter 1 has provided an introduction to cancer and radiotherapy, with a focus on intraoperative radiotherapy and the INTRABEAM system. It also introduced glioblastoma and the INTRAGO trial and outlined the challenges in INTRABEAM dosimetry that this research aims to address. Chapter 2 presents the theoretical background necessary for understanding the work presented in this thesis. It covers fundamental concepts in radiation dosimetry, the TG-43 protocol, and Monte Carlo techniques in radiation dosimetry. Chapter 3 details the initial characterization of the INTRABEAM source probe using the AAPM TG-43 protocol, which formed the foundation for the subsequent research. Three original manuscripts are presented in Chapters 4–6. Chapter 4 extends the dosimetry to the INTRABEAM system with spherical applicators, presenting the TG-43 parameters for all available applicator sizes. This chapter extends the work initially presented in [32], which characterized the bare INTRABEAM probe. The extended analysis, including all available spherical applicator sizes, was published as a paper in the journal *Physics in Medicine & Biology* [33]. Chapter 5 evaluates the impact of different dosimetry formalisms on the estimated dose to OAR in INTRAGO protocol patients. This chapter was published as a paper in *International Journal of Radiation Oncology* Biology* Physics* [34]. Chapter 6 assesses the TG-43 methodology in INTRAGO protocol patients, comparing it with the TARGIT method and MC simulations. This chapter is in preparation for submission as a paper to *Medical Physics*. Finally, Chapter 7 summarizes the key findings of this research, discusses their implications for clinical practice, acknowledges the limitations of the study, and suggests directions for future research.

References

[1] D. Hanahan and R. A. Weinberg, “Hallmarks of Cancer: The Next Generation,” *Cell*, vol. 144, no. 5, pp. 646–674, 2011.

[2] F. Bray *et al.*, "Global cancer statistics 2022: GLOBOCAN estimates of incidence and mortality worldwide for 36 cancers in 185 countries," *CA: A Cancer Journal for Clinicians*, vol. 74, no. 3, pp. 229–263, 2024.

[3] D. R. Brenner *et al.*, "Projected estimates of cancer in Canada in 2024," *CMAJ*, vol. 196, no. 18, E615–E623, 2024.

[4] R. Baskar, K. A. Lee, R. Yeo, and K.-W. Yeoh, "Cancer and Radiation Therapy: Current Advances and Future Directions," *International Journal of Medical Sciences*, vol. 9, no. 3, pp. 193–199, 2012.

[5] R. Atun *et al.*, "Expanding global access to radiotherapy," *The Lancet Oncology*, vol. 16, no. 10, pp. 1153–1186, 2015.

[6] M. C. Joiner and van der Kogel, Albert J., Eds., *Basic Clinical Radiobiology*, 5th ed. Boca Raton: CRC Press, 2018.

[7] Podgorsak, E.B., *Radiation oncology physics: A handbook for teachers and students*. Vienna: International Atomic Energy Agency (IAEA), 2005.

[8] S. Webb, "The physical basis of IMRT and inverse planning," *British Journal of Radiology*, vol. 76, no. 910, pp. 678–689, 2003.

[9] D. A. Jaffray, "Image-guided radiotherapy: From current concept to future perspectives," *Nature Reviews Clinical Oncology*, vol. 9, no. 12, pp. 688–699, 2012.

[10] F. M. Khan and J. P. Gibbons, *Khan's the physics of radiation therapy*. Wolters Kluwer Health, 2014.

[11] International Commission on Radiation Units and Measurements, *ICRU Report 58, Dose and volume specification for reporting interstitial therapy*. Bethesda, MD: ICRU Publications, 1997, vol. os-30 Issue 1.

[12] J. S. Vaidya *et al.*, "Risk-adapted targeted intraoperative radiotherapy versus whole-breast radiotherapy for breast cancer: 5-year results for local control and overall survival from the TARGIT-A randomised trial," *The Lancet*, vol. 383, no. 9917, pp. 603–613, 2014.

[13] F. A. Calvo, R. M. Meirino, and R. Orecchia, "Intraoperative radiation therapy: First part: Rationale and techniques," *Critical Reviews in Oncology/Hematology*, vol. 59, no. 2, pp. 106–115, 2006.

[14] U. Veronesi *et al.*, "Intraoperative radiotherapy during breast conserving surgery: A study on 1,822 cases treated with electrons," *Breast Cancer Research and Treatment*, vol. 124, no. 1, pp. 141–151, 2010.

[15] M. Krengli *et al.*, "Clinical and technical characteristics of intraoperative radiotherapy," *Strahlentherapie und Onkologie*, vol. 189, no. 9, pp. 729–737, 2013.

[16] D. J. Eaton, "Electronic brachytherapy—current status and future directions," *British Journal of Radiology*, vol. 88, no. 1049, p. 20 150 002, 2015.

[17] A. Dickler, O. Ivanov, and D. Francescatti, "Intraoperative radiation therapy in the treatment of early-stage breast cancer utilizing xoft axxent electronic brachytherapy," *World Journal of Surgical Oncology*, vol. 7, no. 1, p. 24, 2009.

[18] D. Eaton and S. Duck, "Dosimetry measurements with an intra-operative x-ray device," *Physics in Medicine & Biology*, vol. 55, no. 12, N359, 2010.

[19] A. Sethi, B. Emami, W. Small Jr, and T. O. Thomas, "Intraoperative radiotherapy with INTRABEAM: Technical and dosimetric considerations," *Frontiers in oncology*, vol. 8, p. 74, 2018.

[20] F. A. Giordano *et al.*, "INTRAGO: Intraoperative radiotherapy in glioblastoma multiforme – a Phase I/II dose escalation study," *BMC Cancer*, vol. 14, no. 1, p. 992, 2014.

[21] F. Schneider, S. Clausen, J. Thölking, F. Wenz, and Y. Abo-Madyan, "A novel approach for superficial intraoperative radiotherapy (IORT) using a 50 kV X-ray source: A technical and case report," *Journal of Applied Clinical Medical Physics*, vol. 15, no. 1, pp. 167–176, 2014.

[22] K. S. Armoogum, J. M. Parry, S. K. Souliman, D. G. Sutton, and C. D. Mackay, "Functional intercomparison of intraoperative radiotherapy equipment–Photon radiosurgery system," *Radiation Oncology*, vol. 2, no. 1, p. 11, 2007.

[23] R. Stupp *et al.*, "Maintenance therapy with tumor-treating fields plus temozolomide vs temozolomide alone for glioblastoma: A randomized clinical trial," *JAMA*, vol. 314, no. 23, pp. 2535–2543, 2015.

[24] R. Stupp *et al.*, "Radiotherapy plus concomitant and adjuvant temozolomide for glioblastoma," *New England journal of medicine*, vol. 352, no. 10, pp. 987–996, 2005.

[25] K. Petrecca, M.-C. Guiot, V. Panet-Raymond, and L. Souhami, "Failure pattern following complete resection plus radiotherapy and temozolomide is at the resection margin in patients with glioblastoma," *Journal of Neuro-Oncology*, vol. 111, no. 1, pp. 19–23, 2013.

[26] F. A. Giordano *et al.*, "Intraoperative radiotherapy in newly diagnosed glioblastoma (INTRAGO): An open-label, dose-escalation phase I/II trial," *Neurosurgery*, vol. 84, no. 1, pp. 41–49, 2019.

[27] R. J. Weil *et al.*, "Intraoperative radiotherapy to treat newly diagnosed solitary brain metastasis: Initial experience and long-term outcomes," 2015.

[28] S. Chiavassa *et al.*, "Monte Carlo evaluation of the effect of inhomogeneities on dose calculation for low energy photons intra-operative radiation therapy in pelvic area," *Physica Medica*, vol. 31, no. 8, pp. 956–962, 2015.

[29] R. Nath, L. L. Anderson, G. Luxton, K. A. Weaver, J. F. Williamson, and A. S. Meigooni, "Dosimetry of interstitial brachytherapy sources: Recommendations of the AAPM radiation therapy committee task group no. 43," *Medical Physics*, vol. 22, no. 2, pp. 209–234, 1995.

[30] M. J. Rivard *et al.*, "Update of AAPM Task Group No. 43 Report: A revised AAPM protocol for brachytherapy dose calculations," *Medical Physics*, vol. 31, no. 3, pp. 633–674, 2004.

[31] F. W. Hensley, "Present state and issues in IORT physics," *Radiation Oncology*, vol. 12, no. 1, 2017.

[32] D. S. Ayala Alvarez, P. G. F. Watson, M. Popovic, V. J. Heng, M. D. C. Evans, and J. Seuntjens, "Monte Carlo calculation of the relative TG-43 dosimetry parameters for the INTRABEAM electronic brachytherapy source," *Physics in Medicine and Biology*, vol. 65, no. 24, p. 245 041, 2020.

[33] D. S. Ayala Alvarez, P. G. F. Watson, M. Popovic, V. J. Heng, M. D. C. Evans, and J. Seuntjens, "Monte Carlo calculation of the TG-43 dosimetry parameters for the INTRABEAM source with spherical applicators," *Physics in Medicine & Biology*, vol. 66, no. 21, p. 215 017, 2021.

[34] D. S. Ayala Alvarez *et al.*, "Evaluation of dosimetry formalisms in intraoperative radiation therapy of glioblastoma," *International Journal of Radiation Oncology, Biology, Physics*, vol. 117, no. 3, pp. 763–773, 2023.

Chapter 2

Radiation physics and dosimetry

2.1 Preface

This chapter explores the fundamental concepts of radiation physics and dosimetry that support the research presented in this thesis. Understanding these principles is essential for addressing the complexities involved in the dosimetry of ionizing radiation sources, particularly in the context of the INTRABEAM system applications.

The chapter begins by exploring the physical interactions of photons and electrons with matter, which form the basis for energy deposition in tissue during radiotherapy with photons or electron beams. This is followed by an examination of key dosimetric quantities and concepts, providing the framework for quantifying and measuring radiation absorbed dose. The chapter then progresses to discuss experimental dosimetry techniques, with a focus on those relevant to low-energy X-ray sources. Special attention is given to the TG-43 dosimetry protocol, which plays a crucial role in characterizing brachytherapy sources and has been adapted for use with electronic brachytherapy devices. Finally, we explore the principles of Monte Carlo techniques in radiation dosimetry, which has been essential in this research for modeling complex radiation transport scenarios.

2.2 Radiation physics

2.2.1 Photon interactions in matter

Understanding the interactions of photons with matter is fundamental to radiation dosimetry. As photons traverse matter, they undergo various interactions that lead to the transfer of energy to the medium, ultimately resulting in the absorbed dose that is central to radiotherapy effects.

Photon beam attenuation

When a narrow beam of monoenergetic photons passes through a medium, its intensity decreases exponentially due to absorption and scattering interactions with the material. This attenuation is described by the *Beer-Lambert law*:

$$I(x) = I_0 e^{-\mu x} \tag{2.1}$$

where $I(x)$ is the intensity at depth x, I_0 is the initial intensity, and μ is the linear attenuation coefficient (expressed in units of cm^{-1}). The linear attenuation coefficient represents the probability of photon interaction per unit path length and is dependent on both the photon energy and the properties of the absorbing medium [1]. The mass attenuation coefficient, μ/ρ, where ρ is the density of the medium, is often more convenient as it allows for comparisons between different materials independent of their physical state. It is usually expressed in units of $\text{cm}^2\ \text{g}^{-1}$.

A critical parameter in characterizing beam attenuation is the half-value layer (HVL), defined as the thickness of material required to reduce the beam intensity to half its initial value:

$$\text{HVL} = \frac{\ln(2)}{\mu} \tag{2.2}$$

The HVL, usually expressed as the thickness (in mm or cm) of the target material, provides a practical measure of beam penetration. In low to medium-energy beams, the HVL is often used to specify beam quality, with higher HVL values indicating more penetrating (harder) beams.

Another important concept is the mean free path, which represents the average distance a photon travels between interactions. It is equal to the reciprocal of the linear attenuation coefficient ($1/\mu$). This concept is particularly useful in understanding the spatial distribution of photon interactions, which is important for dosimetry in small volumes or near material interfaces.

Types of photon interactions

In the energy range relevant to the INTRABEAM system (below 50 keV), three main types of photon interactions are significant [2, 3]:

1. Rayleigh (coherent) scattering: In this process, the photon interacts with tightly bound electrons of an atom, causing the atom to vibrate and re-emit a photon of the same energy but in a slightly different direction. No energy is transferred to the medium, but the change in photon direction can affect dose distribution. Rayleigh scattering is most significant for low-energy photons and high-Z materials.

2. Photoelectric effect: This is the dominant interaction for low-energy photons, especially in high-Z materials. The incident photon is completely absorbed by an atom, ejecting an orbital electron (photoelectron) with kinetic energy equal to the difference between the photon energy and the electron binding energy. The mass attenuation coefficient for the photoelectric effect is approximately proportional to $Z^3/(h\nu)^3$, where Z is the atomic number of the absorber, and $h\nu$ is the photon energy. In biological tissue, which contains elements ranging from hydrogen (Z=1) to calcium (Z=20), this Z-dependence makes the photoelectric effect particularly sensitive to local variations in tissue composition.

3. Compton (incoherent) scattering: In this interaction, the incident photon collides with a loosely bound electron, transferring part of its energy and changing direction. The probability of Compton scattering per atom is proportional to Z and decreases with increasing photon energy. Compton scattering is the predominant interaction for photons in the range of approximately 100 keV to 10 MeV in soft tissue, playing a crucial role in the dose deposition for most external beam radiotherapy treatments.

Figure 2.1 illustrates the relative importance of these interactions as a function of photon energy and absorber atomic number. At the low energies used in INTRABEAM IORT (below 50 keV), the photoelectric effect dominates, especially in higher-Z materials. This dominance of the photoelectric effect, combined with its strong Z-dependence, has important implications for dosimetry and modeling considerations in IORT applications.

While pair production is a significant interaction for high-energy photons, it is not relevant for the INTRABEAM system as this interaction requires incident photon energies greater than 1.022 MeV.

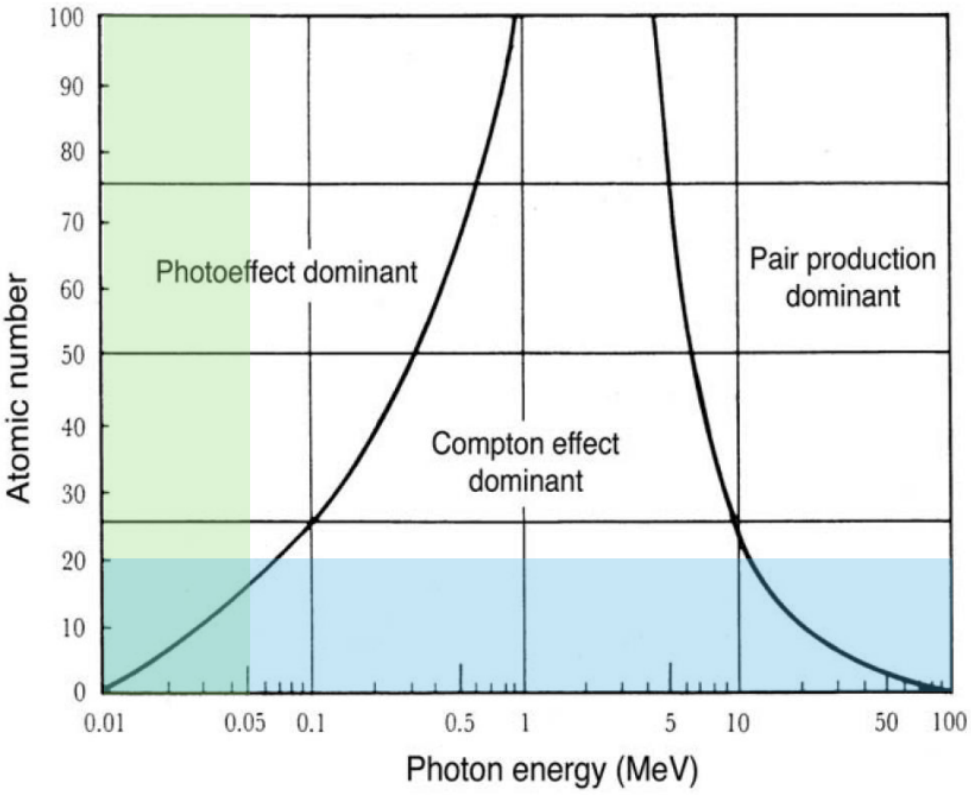

Figure 2.1 Relative predominance of photon interactions as a function of photon energy and absorber atomic number. The lines represent regions where the two neighboring effects are equally probable. Note the dominance of the photoelectric effect at low energies, especially for higher-Z materials, while Compton scattering predominates in the intermediate energy range for most materials of clinical interest. The horizontal band indicates the range of atomic numbers (Z=1-20) present in brain and surrounding tissues, including elements from hydrogen to calcium. The vertical band shows the energy range relevant to INTRABEAM IORT (1-50 keV), from the photon transport cutoff energy to the maximum tube potential. The overlap of these bands, primarily in the photoelectric effect region, illustrates why tissue composition significantly influences dose distributions in INTRABEAM IORT. Figure adapted from [3].

Atomic relaxation processes

When photon interactions, particularly photoelectric absorption, create vacancies in the inner shells of atoms, the atom is left in an excited state. The subsequent relaxation process can lead to two competing phenomena: the emission of characteristic (fluorescence) X-rays or Auger electrons [1].

Characteristic X-rays are produced when an electron from a higher energy level transitions to

fill the vacancy in a lower energy shell. The energy difference between these levels is released as a photon with a discrete energy characteristic of the atom's electronic structure. These X-rays have energies specific to the element and the particular electron transition involved, hence the term "characteristic". Alternatively, the energy released by the electron transition can be transferred to another orbital electron, ejecting it from the atom. This ejected electron is known as an Auger electron. The kinetic energy of the Auger electron is equal to the difference between the initial atomic transition energy and the binding energy of the shell from which it is ejected.

The probability of characteristic X-ray emission versus Auger electron emission depends on the atomic number of the absorbing material and the energy of the initial vacancy. In general, characteristic X-ray emission becomes more probable for higher atomic numbers and for vacancies in inner shells (K-shell vacancies, for example). These atomic relaxation processes contribute to the overall energy deposition pattern in tissue during radiotherapy treatments.

Energy transfer and absorption

The energy transferred from photons to charged particles in the medium is characterized by the mass-energy transfer coefficient, μ_{tr}/ρ (with SI units cm^2 g^{-1}):

$$\frac{\mu_{\text{tr}}}{\rho} = \frac{\mu}{\rho}\frac{\bar{E}_{\text{tr}}}{h\nu} \tag{2.3}$$

where $\bar{E}_{\text{tr}}$ is the average energy transferred to charged particles per interaction, and $h\nu$ is the incident photon energy [1].

Not all of this transferred energy is absorbed locally due to radiative losses. The mass-energy absorption coefficient, μ_{en}/ρ (with SI units cm^2 g^{-1}), accounts for this:

$$\frac{\mu_{\text{en}}}{\rho} = \frac{\mu_{\text{tr}}}{\rho}(1-\bar{g}) \tag{2.4}$$

where $\bar{g}$ is the average fraction of the energy transferred to secondary charged particles that is lost through radiative processes (e.g., bremsstrahlung)[1]. For low photon energies (below about 1 MeV) and low-Z materials, $\bar{g}$ is typically very small, and thus μ_{en}/ρ is nearly equal to μ_{tr}/ρ. This implies that most of the energy transferred to charged particles is absorbed locally, which is advantageous for precise dose delivery in intraoperative radiotherapy applications. However,

[1] We use $\bar{g}$ to express the fact that it accounts for all radiative interactions resulting from the slowing down of the charged particle

as photon energy increases, particularly above 10 MeV, or for high-Z materials, the difference between μ_{tr}/ρ and μ_{en}/ρ becomes more significant due to increased radiative losses, necessitating more complex dosimetry considerations.

2.2.2 Electron interactions in matter

Types of electron interactions

Charged particle interactions occur much more frequently and in a higher concentration than uncharged particles and thus play an important role in the transfer of energy to the medium. Electrons, as charged particles, interact with matter primarily through Coulomb forces. This is particularly relevant in the context of low-energy X-ray sources, where secondary electrons are responsible for the majority of energy deposition.

Electron interactions with matter can be broadly categorized into two types: interactions with orbital electrons and interactions with atomic nuclei. Electron-orbital electron interactions are collisions between the incident electron and orbital electrons of the absorbing medium. They can result in ionization or excitation of atoms in the medium. In ionizing events, the orbital electron receives sufficient energy to be ejected from the atom, potentially causing further ionization. When an incident electron ejects an inner-shell electron from an atom, the subsequent atomic relaxation can result in the emission of characteristic X-rays or Auger electrons. This is the primary mechanism for characteristic X-ray production in the INTRABEAM system, where 50 keV electrons interact with a thin gold target to produce both characteristic X-rays and bremsstrahlung radiation [4, 5].

On the other hand, electron-nucleus interactions occur when an electron passes near an atomic nucleus, experiencing attraction due to the opposing charge. This causes the electron to decelerate and change direction, resulting in the emission of bremsstrahlung radiation [2]. The probability of bremsstrahlung production increases with electron energy and atomic number of the absorber material.

The probability of these interactions depends on the electron energy and the absorber's atomic number. In the low-energy range (below 50 keV), electron-orbital electron interactions dominate, with bremsstrahlung production becoming increasingly significant at higher energies and in higher-Z materials. This interplay between different interaction mechanisms shapes the radiation spectrum produced by electronic brachytherapy devices like the INTRABEAM system.

Stopping power

The rate at which electrons lose energy as they traverse matter is quantified by the stopping power, S, defined as the energy loss per unit path length:

$$S = -\frac{\mathrm{d}E}{\mathrm{d}x} \tag{2.5}$$

where $\mathrm{d}E$ is the energy lost by the electron in traversing a distance $\mathrm{d}x$ [1].

The total stopping power is typically divided into two components: electronic (or collision) stopping power, S_{el}, which accounts for energy losses due to ionization and excitation of atoms in the medium, and radiative stopping power, S_{rad}, which represents energy losses due to bremsstrahlung production. The total stopping power is thus given by:

$$S_{\text{tot}} = S_{\text{el}} + S_{\text{rad}} \tag{2.6}$$

Often, it is more convenient to use the mass stopping power obtained by dividing the stopping power by the density of the medium, ρ:

$$\frac{S}{\rho} = \frac{1}{\rho}\left(-\frac{\mathrm{d}E}{\mathrm{d}x}\right) \tag{2.7}$$

The mass stopping power is typically expressed in MeV cm^2 g^{-1}.

In the low-energy range, the electronic stopping power dominates, with the radiative component becoming more significant at higher energies, particularly for high-Z materials. The ratio of radiative to electronic stopping power is approximately given by:

$$\frac{S_{\text{rad}}}{S_{\text{el}}} \approx \frac{EZ}{700 \pm 100\ \text{MeV}} \tag{2.8}$$

where E is the electron kinetic energy in MeV and Z is the atomic number of the absorber [2].

Electron range

The range of an electron is the distance it travels before coming to rest. Due to the large number of interactions and the possibility of large energy transfers in single collisions, electron paths are tortuous, and their ranges exhibit significant straggling. Consequently, several definitions of electron range exist, each serving different purposes in radiation dosimetry [2].

One commonly used concept is the continuous slowing down approximation (CSDA) range, R_{CSDA}, which represents the path length an electron would travel if it lost energy continuously at a rate equal to the stopping power:

$$R_{\text{CSDA}} = \rho \int_0^{E_0} \frac{\mathrm{d}E}{S_{\text{tot}}(E)} \tag{2.9}$$

where E_0 is the initial electron kinetic energy and $S_{\text{tot}}(E)$ is the total linear stopping power. R_{CSDA} is given in g cm^{-2}) but is commonly expressed per unit density of the absorber material in mm or cm. For low-energy electrons, such as those produced by x-ray sources below 50 keV, the CSDA range in soft tissue is typically less than 0.1 mm. This short range has important implications for dosimetry, particularly in understanding the spatial distribution of energy deposition at microscopic scales.

The CSDA formulation assumes that as a charged particle traverses a medium, it produces secondary particles through the various interactions explained above. Electrons generated from these interactions, known as secondary electrons, can have sufficient kinetic energy to undergo their own Coulomb interactions. These energetic secondary electrons, also termed knock-on electrons or delta rays, can transfer their energy along paths distinct from the primary charged particle. This phenomenon contributes to the complex spatial distribution of energy deposition, extending beyond the track of the primary particle. It is important to note that due to scattering events, the actual depth of maximum penetration into a material is often less than the CSDA range.

2.3 Dosimetric quantities and concepts

Building upon the foundation of radiation physics discussed in the previous section, we now turn our attention to the key dosimetric quantities and concepts that are fundamental to radiation dosimetry. These quantities provide the framework for quantifying and measuring radiation dose, which is essential for the safe and effective use of ionizing radiation in medical applications.

2.3.1 Fluence

At the core of dosimetry is the concept of particle fluence, which describes the number of particles incident on a given area. The particle fluence, Φ, is defined as the quotient of $\mathrm{d}N$ by $\mathrm{d}A$, where

$\mathrm{d}N$ is the number of particles incident on a sphere of cross-sectional area $\mathrm{d}A$ [3, 6]:

$$\Phi = \frac{\mathrm{d}N}{\mathrm{d}A} \tag{2.10}$$

Fluence is typically expressed in units of m^{-2}. A related quantity, energy fluence Ψ, represents the radiant energy incident on a sphere of cross-sectional area $\mathrm{d}A$:

$$\Psi = \frac{\mathrm{d}E}{\mathrm{d}A} = \frac{\mathrm{d}N}{\mathrm{d}A}E = \Phi E \tag{2.11}$$

where $\mathrm{d}E$ is the radiant energy. For particles of energy E, the energy fluence and fluence are related as shown in Eq. 2.11. Energy fluence is typically expressed in units of J m^{-2}.

2.3.2 Kerma

Kerma (kinetic energy released per unit mass) is a dosimetric concept applicable to indirectly ionizing radiation such as photons. It is defined as the quotient of $\mathrm{d}E_{\mathrm{tr}}$ by $\mathrm{d}m$, where $\mathrm{d}E_{\mathrm{tr}}$ is the mean sum of the initial kinetic energies of all charged particles liberated by uncharged particles in a mass $\mathrm{d}m$ of material [2, 6]:

$$K = \frac{\mathrm{d}E_{\mathrm{tr}}}{\mathrm{d}m} \tag{2.12}$$

Kerma is expressed in units of J kg^{-1}, which is given the special name gray (Gy). It is important to note that kerma accounts for the energy transferred to charged particles, regardless of where that energy is ultimately deposited.

Kerma can be further divided into two components: electronic (or collision) kerma and radiative kerma. Electronic kerma, K_{el}, refers to the portion of kerma that results in local energy deposition through excitation and ionization. Radiative kerma, K_{rad}, accounts for energy lost through radiative processes such as bremsstrahlung. Kerma is the sum of these components:

$$K = K_{\mathrm{el}} + K_{\mathrm{rad}} \tag{2.13}$$

The relationship between electronic kerma and kerma can be expressed using the radiation yield, $\bar{g}$, which represents the average fraction of the initial kinetic energy of charged particles that is converted to bremsstrahlung in the course of slowing down:

$$K_{\text{el}} = K(1 - \bar{g}) \tag{2.14}$$

For a monoenergetic photon beam, kerma can be related to energy fluence through the mass-energy transfer coefficient for the material of interest:

$$K = \Psi \frac{\mu_{\text{tr}}}{\rho} \tag{2.15}$$

Similarly, electronic kerma can be expressed in terms of the mass-energy absorption coefficient:

$$K_{\text{el}} = \Psi \frac{\mu_{\text{en}}}{\rho} \tag{2.16}$$

In practice, most radiation fields used in medical applications are polyenergetic. For a polyenergetic photon spectrum, kerma and electronic kerma are calculated by integrating over the energy fluence spectrum:

$$K = \int_0^{E_{\text{max}}} \Psi_E \frac{\mu_{\text{tr}}}{\rho}(E)\mathrm{d}E \tag{2.17}$$

$$K_{\text{el}} = \int_0^{E_{\text{max}}} \Psi_E \frac{\mu_{\text{en}}}{\rho}(E)\mathrm{d}E \tag{2.18}$$

where Ψ_E is the energy fluence spectrum and E_{max} is the maximum photon energy in the spectrum. These relationships are particularly important in the dosimetry of low-energy X-ray sources like the INTRABEAM, where the energy spectrum can significantly influence the dose distribution.

2.3.3 Absorbed dose

Absorbed dose is the most fundamental quantity in radiation dosimetry and is assumed directly related to the biological effects of radiation. It is defined as the mean energy imparted to matter per unit mass:

$$D = \frac{\mathrm{d}\bar{\epsilon}}{\mathrm{d}m} \tag{2.19}$$

where $\mathrm{d}\bar{\epsilon}$ is the mean energy imparted to a mass $\mathrm{d}m$. Like kerma, absorbed dose is expressed

in units of J kg^{-1} or gray (Gy). The mean energy imparted, $d\bar{\epsilon}$, includes the mean radiant energy of all charged and uncharged particles entering a volume of interest, subtracting the mean radiant energy of all particles leaving the volume, plus the mean sum of all the changes in the rest energy of nuclei and particles inside the volume [2].

2.3.4 Charged particle equilibrium

Charged particle equilibrium (CPE) is a condition where the energy carried into a volume by charged particles equals the energy carried out. When CPE exists, absorbed dose and electronic kerma are equal:

$$D \overset{\text{CPE}}{=} K_{\text{el}} \tag{2.20}$$

In the case of low-energy photons, most of the secondary charged particles generated will not travel far and will deposit their energy locally. In this energy range, radiative losses are usually negligible, and kerma can be approximated by electronic kerma, and the absorbed dose will be very well approximated by kerma.

2.4 Experimental dosimetry

The practical application of dosimetric principles relies heavily on the ability to measure radiation quantities accurately. Experimental dosimetry forms the backbone of quality assurance in radiotherapy, validation of computational models, and the development of new treatment techniques. This section explores the fundamental concepts of radiation measurement, with a focus on the detectors and methods relevant to the dosimetry of low-energy X-ray sources such as the INTRABEAM system.

2.4.1 Absolute, reference, and relative dosimetry

In radiation dosimetry, measurements are categorized into three main types: absolute, reference, and relative dosimetry. Each type serves a specific purpose in the chain of traceability and practical application of dose measurements [2].

1. *Absolute dosimetry* refers to the determination of absorbed dose or other dosimetric quantities using a dosimeter that does not require calibration in a known radiation field. These

measurements are typically performed at primary standards laboratories using instruments such as calorimeters or free-air ionization chambers. Absolute dosimetry can be performed in various media, including water and air. For instance, absolute dosimetry of kilovoltage X-ray beams is usually performed using a free-air ionization chamber to determine the air kerma in air from the energy transferred to the mass of air in the chamber's radiation-sensitive volume. The goal of absolute dosimetry is to establish the absorbed dose in terms of fundamental quantities, providing the highest level of accuracy and traceability in the dosimetry chain.

2. *Reference dosimetry*, also known as calibration dosimetry, involves the use of a dosimeter that has been calibrated against a primary standard in a well-characterized reference radiation field. This type of dosimetry is commonly performed in clinical settings to determine the absorbed dose under specific reference conditions. The dosimeter used in reference dosimetry, often an ionization chamber, carries a calibration coefficient traceable to a primary standards laboratory. Reference dosimetry is crucial for establishing the baseline output of radiation therapy machines and ensuring consistency in dose delivery across different treatment centers.

3. *Relative dosimetry* involves measurements of dose distributions relative to a reference point or condition. These measurements are used to characterize beam properties such as percentage depth doses, beam profiles, and output factors. Relative dosimetry does not require an absolute calibration of the dosimeter as long as its response is stable and well-characterized over the range of measurement conditions. This type of dosimetry is essential for treatment planning and quality assurance procedures in radiotherapy.

The interplay between these three types of dosimetry is fundamental to ensuring accurate and consistent dose delivery in radiotherapy. Absolute dosimetry provides the foundation for the entire dosimetry chain, while reference dosimetry links clinical measurements to primary standards. Relative dosimetry, building upon the established reference conditions, allows for the characterization of complex dose distributions encountered in modern radiotherapy techniques.

In the context of low-energy X-ray sources like the INTRABEAM, the distinction between these dosimetry types becomes particularly important. The steep dose gradients and unique beam characteristics of such sources present challenges for conventional dosimetry protocols. As a result, a combination of reference dosimetry (using calibrated detectors) and relative dosimetry

(to map dose distributions) is often employed, with careful consideration of the limitations and uncertainties associated with each approach [7].

The choice of dosimeter for these various types of dosimetry depends on the specific application, the type and energy of radiation, the dose range of interest, and the required measurement accuracy. In this thesis, we focus on two types of dosimeters used for validating Monte Carlo models of the INTRABEAM source: ionization chambers and synthetic diamond detectors. These detectors offer complementary characteristics that make them well-suited for the dosimetry of low-energy X-ray sources.

2.4.2 Ionization chambers

Ionization chambers (sometimes termed ion chambers) are among the most widely used dosimeters in radiotherapy due to their excellent stability, high precision, and well-understood response characteristics. They operate on the principle of collecting the charge produced when radiation ionizes a gas volume [2].

A typical ionization chamber consists of a gas-filled cavity with two electrodes. When radiation passes through the gas, it creates ion pairs. An electric field applied between the electrodes causes these ions to drift, producing a measurable current proportional to the ionization rate and, consequently, to the dose rate in the chamber volume. In radiation therapy applications, the ionization chambers are usually air-filled with their cavity communicating to the ambient temperature and pressure conditions.

Parallel-plate ionization chambers are particularly suitable for low-energy X-ray dosimetry. These chambers feature a flat ionization volume bounded by two parallel electrodes. The entrance window, which serves as one electrode, is typically made of a thin, low-Z material to minimize attenuation and energy dependence. The collecting electrode is surrounded by a guard ring to ensure a uniform electric field in the sensitive volume and reduce leakage currents.

The small separation between electrodes in parallel-plate chambers (typically less than 2 mm) makes them well-suited for measuring steep dose gradients, such as those encountered near the surface in low-energy X-ray beams. However, this design can also make them more susceptible to polarity and recombination effects, which must be carefully accounted for in measurement.

An important concept in ionization chamber dosimetry is the effective point of measurement (EPOM). The EPOM is the point in space to which the measured dose should be assigned. For parallel-plate chambers in high-energy electron and photon beams, the EPOM is typically taken to

be on the inner surface of the entrance window [8], whereas it is taken in the middle of the cavity for low and medium-energy X-rays [9]. However, small shifts may be necessary depending on the beam quality and chamber design. The precise determination of the EPOM is crucial for accurate dose measurements, particularly in regions of high dose gradients where small positioning errors can lead to significant dosimetric uncertainties.

When using ionization air-filled chambers for absolute or reference dosimetry, several correction factors must be applied to account for various influence quantities. These include:

1. Temperature and pressure corrections (k_{TP}): To account for changes in the mass of air in the sensitive volume due to variations in ambient conditions.

2. Ion recombination correction (k_{ion}): To correct for the loss of charge due to recombination of ion pairs before collection.

3. Polarity effect correction (k_{pol}): To account for differences in response when the polarity of the applied voltage is reversed.

4. Electrometer calibration factor (k_{elec}): To convert the electrometer reading to charge or current, when this factor is not already included in the chamber calibration coefficient. Some calibration laboratories provide a combined chamber-electrometer calibration coefficient, in which case a separate electrometer factor is not needed.

2.4.3 Solid-state detectors

Solid-state detectors offer several advantages over gas-filled chambers, including higher sensitivity per unit volume and better spatial resolution. These detectors operate on the principle of radiation-induced conductivity in a solid medium, typically a semiconductor material. When ionizing radiation interacts with the detector material, it creates electron-hole pairs, which can be collected under an applied electric field to produce a measurable signal proportional to the absorbed dose [2, 10].

Among solid-state detectors, synthetic diamond detectors have gained prominence in radiotherapy dosimetry due to their tissue equivalence, high sensitivity, and small size. The PTW microDiamond TN60019, used in this thesis for dosimetric validation of the INTRABEAM system, is an example of such a detector.

Synthetic diamond detectors

Synthetic diamond detectors are fabricated using chemical vapor deposition (CVD) techniques, which allow for the production of high-purity diamond crystals with controlled properties. These detectors operate similarly to semiconductors. When ionizing radiation interacts with the diamond crystal, it generates electron-hole pairs. Under an applied electric field, these charge carriers drift, producing a measurable current proportional to the dose rate [11].

One of the key advantages of synthetic diamond detectors is their small sensitive volume, typically on the order of a few cubic millimeters or less. For instance, the PTW microDiamond TN60019 has a sensitive volume of approximately 0.004 mm^3 [12]. This small size minimizes volume averaging effects in regions of high dose gradients, making them particularly useful for validating Monte Carlo models of sources like INTRABEAM, where steep dose fall-off is observed close to the source. Volume averaging effects occur when the detector's sensitive volume is large relative to the scale of dose variations in the radiation field. The small sensitive volume of diamond detectors allows for more accurate measurements in these high-gradient regions compared to larger detectors like ionization chambers [2].

Synthetic diamond detectors exhibit near tissue equivalence over a wide range of photon energies, including the low-energy range relevant to INTRABEAM dosimetry. The relatively low atomic number ($Z = 6$) of carbon, which is the constituent element of diamond, provides these detectors with radiological properties close to those of both water and soft tissue, making them ideal for accurate dose measurements in clinical settings. This characteristic reduces the need for energy-dependent corrections and simplifies the interpretation of measurements in water phantoms [11]. Another notable advantage of diamond detectors is their radiation hardness, allowing them to withstand high doses without significant degradation in performance. This property ensures long-term stability and reliability in clinical applications [13].

When compared to ionization chambers, diamond detectors are less affected by environmental conditions and do not require extensive corrections for influence quantities such as temperature, pressure, and humidity. These properties make diamond detectors a valuable complement to ionization chambers, particularly in applications requiring high precision and accuracy [10].

However, diamond detectors are not without challenges. They can exhibit dose rate dependence, especially at low dose rates, and their response may vary slightly with accumulated dose. Additionally, their high sensitivity to temperature fluctuations necessitates careful control of measurement conditions [2].

The combination of ionization chambers and synthetic diamond detectors provides a robust approach to validating Monte Carlo models of low-energy X-ray sources. The well-established characteristics and traceability of ionization chambers offer a solid foundation for reference dosimetry, while the high spatial resolution and tissue equivalence of diamond detectors allow for detailed verification of dose distributions in high-gradient regions. This complementary use of detectors enhances the overall confidence in the experimental validation of computational models, a critical step in the development and clinical implementation of advanced radiotherapy techniques such as INTRABEAM [11].

2.5 Brachytherapy dosimetry

2.5.1 TG-43 dosimetry protocol

The AAPM Task Group No. 43 Report (TG-43, 1995) and its update (TG-43U1, 2004) [14, 15] provide a standardized formalism for calculating dose distributions around photon-emitting brachytherapy sources. While subsequent updates (TG-43U1S1 and TG-43U2) [16, 17] have provided additional guidance for conventional brachytherapy sources, the fundamental formalism established in TG-43U1 remains the standard for dosimetry calculations and is particularly suitable for adaptation to electronic brachytherapy sources. This protocol has become the gold standard in brachytherapy dosimetry, offering a consistent framework for dose calculations in various clinical scenarios.

The TG-43 protocol introduces a set of parameters that characterize the dose distribution around a brachytherapy source. For the general 2D formalism, the dose rate at a point $P(r, \theta)$ can be expressed as:

$$\dot{D}(r,\theta) = S_K \Lambda \frac{G_L(r,\theta)}{G_L(r_0,\theta_0)} g_L(r) F(r,\theta) \tag{2.21}$$

where $\dot{D}(r,\theta)$ is the dose rate at the point of interest, S_K is the air-kerma strength, Λ is the dose rate constant, $G_L(r,\theta)$ is the geometry function, $g_L(r)$ is the radial dose function, and $F(r,\theta)$ is the 2D anisotropy function. The subscript L denotes the line-source approximation. The reference position coordinates, typically r_0 = 1 cm and θ_0 = 90°, are used for normalization. Figure 2.2 illustrates the coordinate system used in the TG-43 formalism. This system provides a standardized approach for defining the spatial relationships between the source and points of

interest in the surrounding medium.

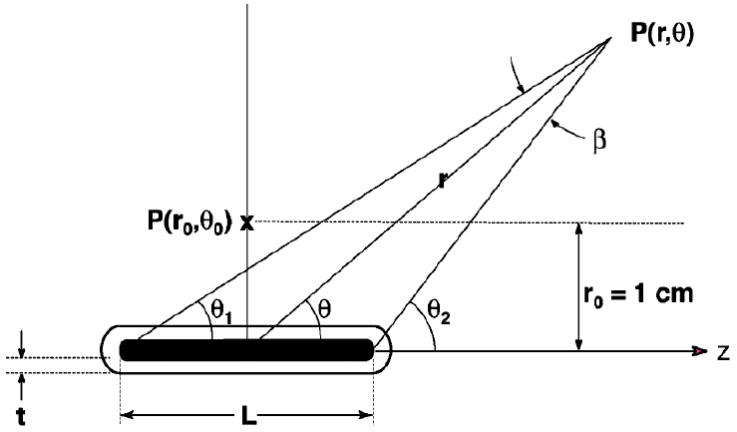

Figure 2.2 Coordinate system used for brachytherapy dosimetry calculations as defined in the TG-43 formalism. The origin is at the center of the active source, with the z-axis aligned along the long axis of the source. Figure reproduced from [15].

For point-source approximations, which are often applicable to small effective sources, the equation simplifies by replacing the geometry function with the inverse square law:

$$\dot{D}(r,\theta) = S_K \Lambda \frac{G_P(r,\theta)}{G_P(r_0,\theta_0)} g_P(r) F(r,\theta) \tag{2.22}$$

where the subscript P denotes the point-source approximation.

Each of these parameters plays a crucial role in characterizing the dose distribution and requires careful determination through measurements or Monte Carlo simulations. Each of these parameters is described in more detail below.

Air-kerma strength

The air-kerma strength, S_K, is a measure of the brachytherapy source output defined as the product of the air-kerma rate at a calibration distance and the square of this distance. The measurement is performed in free space (in air, far from any scattering surfaces) to eliminate the contribution of scattered radiation that would occur near phantom surfaces or walls:

$$S_K = \dot{K}_\delta(d) d^2 \tag{2.23}$$

where $\dot{K}_\delta(d)$ is the air-kerma rate in vacuo due to photons of energy greater than δ (typically

5 keV for low-energy sources), measured at distance d. The "in vacuo" specification indicates that the measurement is corrected for air attenuation and scatter between the source and the point of measurement, providing a quantity that characterizes the intrinsic output of the source. The air-kerma strength is specified in units of U, where 1 U = 1 cGy cm^2 h^{-1} = 1 μGy m^2 h^{-1}.

Dose rate constant

The dose rate constant, Λ, relates the dose rate at the reference position to the air-kerma strength of the source. It is defined as:

$$\Lambda = \frac{\dot{D}(r_0, \theta_0)}{S_K} \tag{2.24}$$

where $\dot{D}(r_0, \theta_0)$ is the dose rate in water at the reference position. The dose rate constant accounts for the effects of source geometry, spatial distribution of radioactivity within the source, encapsulation, and self-filtration within the source structure.

Geometry function

The geometry function, $G(r, \theta)$, accounts for the spatial distribution of radioactivity within the source, neglecting photon absorption and scattering. For a line source approximation, it is given by:

$$G_L(r, \theta) = \begin{cases} \frac{\beta}{Lr \sin\theta} & \text{if } \theta \neq 0^\circ \\ \frac{1}{r^2 - L^2/4} & \text{if } \theta = 0^\circ \end{cases} \tag{2.25}$$

where β is the angle subtended by the active source length L from the point of calculation. For a point-source approximation, the geometry function simplifies to:

$$G_P(r, \theta) = \frac{1}{r^2} \tag{2.26}$$

Radial dose function

The radial dose function, $g(r)$, accounts for the effects of absorption and scatter in the medium along the transverse axis of the source. It is defined as:

$$g_X(r) = \frac{\dot{D}(r,\theta_0)}{\dot{D}(r_0,\theta_0)} \frac{G_X(r_0,\theta_0)}{G_X(r,\theta_0)} \tag{2.27}$$

where X is either L or P, depending on whether the line-source or point-source geometry function is used. The radial dose function accounts for the reduction in dose rate on the transverse plane due to photon scattering and attenuation, excluding the inverse square-law falloff.

Anisotropy function

The 2D anisotropy function, $F(r,\theta)$, describes the angular variation of dose around the source at a given radial distance. It is defined as:

$$F(r,\theta) = \frac{\dot{D}(r,\theta)}{\dot{D}(r,\theta_0)} \frac{G_L(r,\theta_0)}{G_L(r,\theta)} \tag{2.28}$$

The anisotropy function accounts for the angular variation of photon absorption and scatter in the medium and non-uniform self-filtration through the source and encapsulation.

2.5.2 Application to electronic brachytherapy

The adaptation of the TG-43 formalism to electronic brachytherapy (eBT) sources has presented unique dosimetry challenges. While the fundamental principles of the TG-43 protocol remain applicable, the distinct characteristics of eBT sources necessitate modifications to the standard approach [18]. Electronic brachytherapy sources, such as the INTRABEAM system, differ from traditional radioactive sources in several key aspects. These include the ability to switch the radiation on and off, the potential for beam modulation, and the generation of a low-energy X-ray spectrum. While these features offer advantages in terms of radiation safety and treatment flexibility, they also introduce complexities in dosimetric characterization [19].

One of the primary challenges in applying the TG-43 formalism to eBT sources lies in the determination of the air-kerma strength, S_K. For traditional brachytherapy sources, S_K is measured in vacuo and requires corrections for scatter and attenuation in air. However, for eBT sources, these corrections can be substantial, potentially exceeding 25% [20]. This large correction factor is primarily due to the low-energy nature of eBT photons (typically 20-50 keV), which are much more susceptible to photoelectric absorption and scatter in air compared to the higher-energy photons from conventional brachytherapy sources like ^{192}Ir (average energy $\sim$380 keV).

To address this issue, DeWerd et al. (2015) [20] proposed a modified dose calculation formalism for eBT sources. This approach replaces the air-kerma strength with the air-kerma rate measured in air at a specified distance, typically 50 cm from the source. This relatively large distance is chosen to ensure that measurements are made in the far-field region where the inverse square law is valid and to minimize the impact of any geometric uncertainties in source positioning. At 50 cm, small uncertainties in positioning ($\sim$1 mm) result in negligible dose uncertainties ($\sim$0.4%), whereas the same positioning uncertainty at closer distances would have a much larger impact on measurement accuracy. This approach eliminates the need for in-vacuo measurements and the associated large correction factors, thereby improving the accuracy and reproducibility of dose calculations. The modified equation for dose rate calculation, accounting for the specific applicator used, is given by:

$$\dot{D}_i(r,\theta) = \dot{K}_{\text{50cm}}\chi_i(r_0,\theta_0)G_P(r,\theta)g_i(r)F_i(r,\theta) \tag{2.29}$$

where $\dot{K}_{\text{50cm}}$ is the air-kerma rate measured in air at 50 cm from the source, $\chi_i(r_0,\theta_0)$ is the dose-rate conversion coefficient at the reference position for applicator i, and the subscript i denotes the specific applicator used with the eBT source.

The dose-rate conversion coefficient, $\chi_i(r_0,\theta_0)$, is defined as:

$$\chi_i(r_0,\theta_0) = \frac{\dot{D}_i(r_0,\theta_0)}{\dot{K}_{\text{50cm}}} \tag{2.30}$$

This applicator-specific approach acknowledges that different applicators can significantly alter the beam characteristics and dose distribution of eBT sources. For systems like INTRABEAM, which offer a range of applicator sizes and shapes, it would be necessary to determine the appropriate dosimetry parameters for each applicator configuration individually [19]. These functions can vary substantially between different applicator types due to differences in material composition, shape, and size, which affect beam attenuation and scatter characteristics [21].

The geometry function, $G_P(r,\theta)$, for eBT sources is typically approximated using the point-source model due to the small size of the focal spot. This simplification is often justified for miniature X-ray sources like the INTRABEAM, where the effective source size is on the order of 1 mm or less [22]. The radial dose function, $g(r)$, and the anisotropy function, $F(r,\theta)$, for eBT sources exhibit characteristics distinct from those of traditional brachytherapy sources. The low-energy photon spectrum of eBT sources results in a steeper dose gradient and more pronounced anisotropy, particularly in the vicinity of the source [23]. These functions must be carefully

determined through a combination of measurements and Monte Carlo simulations, taking into account the specific design features of each eBT source and its associated applicators.

The low-energy photon spectrum of eBT sources makes them more susceptible to spectral changes as the beam penetrates tissue. This can lead to variations in the effective beam quality with depth, potentially affecting the accuracy of dose calculations based on water-equivalent assumptions. While not explicitly addressed in the TG-43 formalism, these effects should be considered when applying the protocol to eBT sources, particularly in treatment sites with significant tissue heterogeneities [24].

2.5.3 Effects of tissue heterogeneities: TG-186 formalism

While the TG-43 formalism has been widely adopted for brachytherapy dosimetry, its assumption of a homogeneous water medium can lead to significant dose calculation errors in clinical scenarios where tissue heterogeneities are present. The AAPM Task Group 186 (TG-186) addressed this limitation by providing recommendations for model-based dose calculation methods in brachytherapy that account for tissue heterogeneities and applicator attenuation [25].

The impact of tissue heterogeneities on dose distributions is particularly pronounced in low-energy brachytherapy, including electronic brachytherapy sources. This is due to the dominance of the photoelectric effect at low photon energies, which is highly dependent on the atomic number of the absorbing medium in addition to its physical density. Figure 2.3 illustrates the variation in mass-energy absorption coefficients relative to water for different tissues across a range of photon energies. As seen in Figure 2.3, at energies relevant to the INTRABEAM system (around 20 keV), the mass-energy absorption coefficients of cortical bone can be approximately seven times that of water.

The TG-186 report recommends considering dose reporting to different media, shifting focus from the traditionally used dose to water in medium ($D_{w,m}$) to dose to medium in medium ($D_{m,m}$). This approach is particularly relevant for brachytherapy in heterogeneous tissues, as it directly accounts for the varied absorption properties of different media. For the INTRABEAM system, which operates at a maximum potential of 50 kV, the secondary electrons have energies below 50 keV. According to data from the ESTAR database [26], the continuous slowing down approximation (CSDA) range for electrons in water at these energies is very short. For instance, 10 keV electrons have a CSDA range of approximately 2.5 µm, while 30 keV electrons have a range of about 18 µm [25]. These ranges are significantly smaller than typical tissue

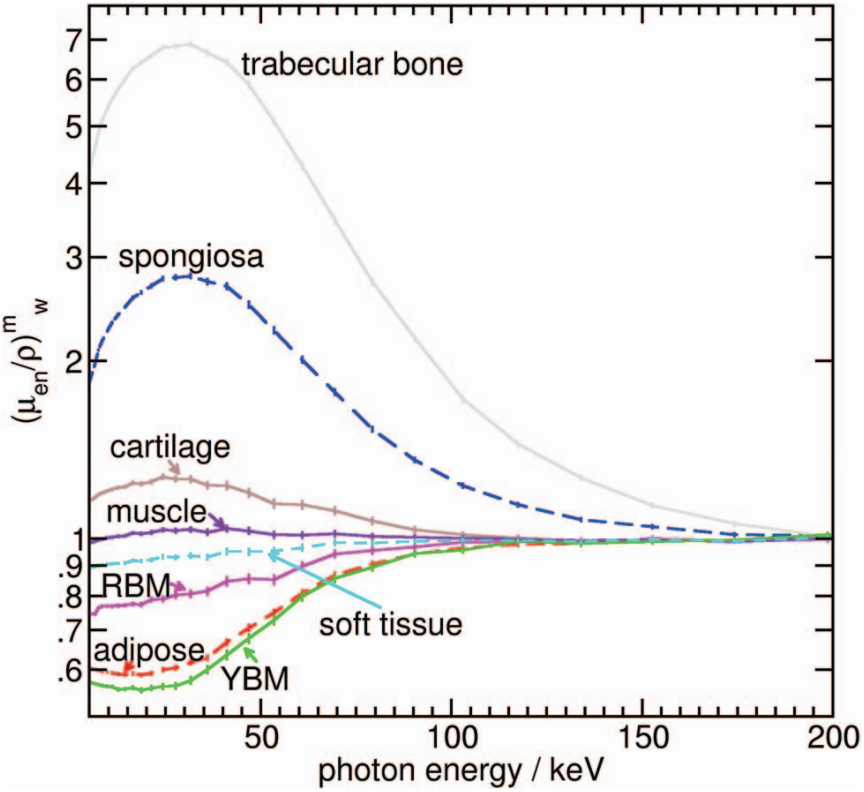

Figure 2.3 Mass-energy absorption coefficients for various materials relative to those for water for energies from 5 to 200 keV. Figure reproduced from [25].

heterogeneities encountered in clinical scenarios, which are often on a scale of millimeters or larger. Moreover, these electron ranges are considerably smaller than the voxel sizes typically used in Monte Carlo simulations for INTRABEAM dosimetry, which are typically on the order of 0.5 mm. These differences in scale justify the assumption of local energy deposition and allow for the simplification of dose calculations in heterogeneous media for low-energy sources. Consequently, for these low-energy photon sources, the absorbed dose can be approximated by the electronic kerma, leading to the following relationship between dose to water in medium ($D_{w,m}$) and dose to medium in medium ($D_{m,m}$):

$$D_{\mathrm{w,m}} = D_{\mathrm{m,m}} \frac{(\bar{\mu}_{\mathrm{en}}/\rho)_{\mathrm{w}}}{(\bar{\mu}_{\mathrm{en}}/\rho)_{\mathrm{m}}} \tag{2.31}$$

where $(\bar{\mu}_{\mathrm{en}}/\rho)_{\mathrm{w}}$ and $(\bar{\mu}_{\mathrm{en}}/\rho)_{\mathrm{m}}$ are the mass-energy absorption coefficients for water and the medium, respectively, averaged over the local photon energy spectrum.

The implementation of model-based dose calculation algorithms, as recommended by TG-

186, can lead to significant differences in calculated dose distributions compared to the TG-43 formalism. While tissue heterogeneity effects are generally less pronounced in brain IORT for glioblastoma, where the treatment volume is primarily in relatively homogeneous brain tissue, and the overlying skull bone segment is surgically removed during the procedure, some considerations remain relevant. For instance, deeper-lying OARs, such as the optic nerves and chiasm, are often near bony structures of the skull base, and air cavities in the nasal region can affect dose calculations for nearby structures. Moreover, at the low energies used by the INTRABEAM system (average energy $\sim$20-30 keV), even modest differences in tissue composition can affect dose deposition due to the dominance of the photoelectric effect, which is highly dependent on the atomic composition of the absorbing medium.

Chiavassa et al. (2015) conducted a comprehensive analysis of heterogeneities effects in INTRABEAM treatments, demonstrating that neglecting tissue heterogeneities could lead to dose errors exceeding 5% in soft tissues and up to 30% in bone structures [24]. However, due to the steep dose gradients characteristic of the INTRABEAM system, the impact of tissue composition on dose to distant OARs is often secondary to the geometric effects of source-to-OAR distance. Their study showed that dose differences between water-based calculations and heterogeneous media calculations were most significant in regions close to the applicator surface, with effects diminishing at greater distances where doses are already substantially reduced by geometric falloff.

However, it is important to interpret these dosimetric differences in the context of biological effects and clinical endpoints. While the physical dose to bone may be significantly higher than to soft tissue, the biological impact may not be proportional to this difference. This is because radiation effects in tissues are largely mediated through aqueous interactions, free radical production, and indirect effects. The cellular dose, which is more directly related to biological effect, remains closely related to the dose to water. This consideration is particularly relevant in brain IORT, where most of the high-dose region is within relatively homogeneous brain tissue, and the most significant heterogeneity effects occur in regions receiving lower doses due to geometric fall-off.

The TG-186 report emphasizes the importance of accurate tissue composition data for dose calculations. While the report recommends using CT imaging to determine tissue densities and, where possible, to infer tissue composition, this approach can be computationally intensive and may not always be feasible in all clinical settings. As a practical alternative, standardized tissue compositions from sources such as ICRU Report 44 [27] and ICRP Publication 89 [28] can

provide a reasonable approximation for many applications.

Despite the benefits of model-based dose calculations in providing a more accurate representation of energy deposition, their implementation presents challenges. These include the need for accurate tissue composition data, increased computational resources, and the development of new protocols for treatment planning and dose reporting. The balance between highly detailed, patient-specific calculations and more generalized, efficient methods remains an active area of research in brachytherapy dosimetry [29]. For time-sensitive procedures like IORT, this balance is particularly crucial, as treatment decisions often need to be made while the patient is still in surgery.

2.6 INTRABEAM dosimetry

The INTRABEAM system, as introduced in Section 1.3, presents unique dosimetric challenges due to its low-energy x-ray spectrum and steep dose gradients. These characteristics necessitate specialized dosimetry approaches to ensure accurate dose delivery in clinical applications. While the TARGIT protocol remains the clinical standard for INTRABEAM dosimetry, alternative methods have been developed to improve dose calculation accuracy. This section explores the evolution of INTRABEAM dosimetry methods, beginning with the TARGIT protocol and progressing to more recent developments, including the manufacturer's V4.0 calibration method and the Monte Carlo-based C_Q method.

2.6.1 TARGIT dosimetry method

The TARGIT (TARGeted Intraoperative radioTherapy) dosimetry method was established at the onset of the TARGIT-A clinical trial for breast cancer and has since been widely adopted for INTRABEAM dosimetry in various applications [30]. This method forms the basis of the manufacturer's calibration process and provides tabulated depth dose data for clinical use.

The INTRABEAM system is calibrated by the manufacturer (Carl Zeiss Meditec AG, Jena, Germany) using a water phantom and a PTW 23342 soft x-ray ionization chamber [31]. The calibration procedure employs an exposure-based approach using a calibration coefficient, N_X, against a free-air chamber primary standard. The rate of absorbed dose at different depths in water is determined from current measurements according to:

$$\dot{D}_{\mathrm{w}}^{\mathrm{TARGIT}}(z)\left[\frac{Gy}{min}\right] = I_{T,P}(z)[A]\, N_X \left[\frac{R}{C}\right]\, k_Q\, f \left[\frac{Gy}{R}\right]\, 60 \left[\frac{s}{min}\right] \tag{2.32}$$

where $I_{T,P}(z)$ is the measured current corrected for temperature and pressure, k_Q corrects for beam quality differences from calibration conditions, and f is the exposure to absorbed dose to water (roentgen-to-gray) conversion factor. This method uses a reference energy value of 20 keV, which is derived from half-value layer (HVL) measurements of the INTRABEAM X-ray source at a water depth of 10 mm [31]. For the nominal accelerating voltage of 50 kV used in the INTRABEAM system, the measured HVL of 0.64 mm Al corresponds to an effective energy of approximately 20.4 keV. This reference energy serves as the basis for determining the values of k_Q and f. Importantly, both k_Q and f are treated as depth-independent in this formalism. At the reference energy of 20 keV, the roentgen-to-gray conversion factor f has a value of 8.81 mGy/R, as extracted from ICRU Report 17 [32]. The beam quality correction factor k_Q is given as 1.000 for the beam qualities T30 and T50 (where "T" denotes a tungsten target X-ray beam and the number represents the generating potential in kV), which better represent the INTRABEAM beam quality [31]. This designation follows the standard nomenclature for low-energy X-ray beam qualities used in dosimetry protocols, where T30 and T50 correspond to beam qualities with half-value layers similar to those generated by the INTRABEAM's 50 kV beam after penetration through tissue.

The resulting depth dose rate curves, referred to as TARGIT doses, are provided to end-users in tabulated form for clinical use. These tables form the basis for treatment planning and dose estimation in IORT procedures using the INTRABEAM system. It is important to note that this calibration method was established before the TARGIT-A trial (pre-2000) and has been maintained to ensure consistency in delivered prescription doses, despite the development of improved kilovoltage dosimetry protocols such as AAPM TG-61 [9] or IAEA TRS 398 [33] and its revision IAEA TRS 398 Rev.1 [34].

2.6.2 Zeiss V4.0 method

To verify the calibration tables provided by the manufacturer, Zeiss developed the V4.0 method, which allows for independent measurements in the clinic. This method utilizes the Zeiss Water Phantom, shown in Figure 2.4, which includes two plastic holders to accommodate a PTW 34013 soft x-ray ionization chamber.

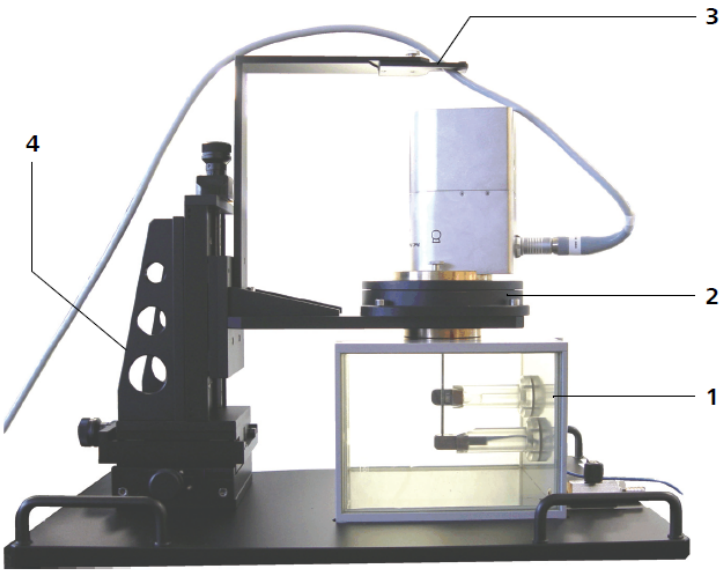

Figure 2.4 Zeiss Water Phantom components: (1) water tank, (2) rotary stage, (3) cable holder, and (4) positioning unit. The phantom design allows for precise depth dose and isotropy measurements using a non-waterproof ionization chamber. Figure reproduced from [35]

In the Zeiss V4.0 method, the absorbed dose to water is calculated using the following equation:

$$\dot{D}_{\mathrm{w}}^{\mathrm{V4.0}}(z) = M(z)\, N_K\, k_Q\, k_{K_{\mathrm{a}} \to D_{\mathrm{w}}} \tag{2.33}$$

where $M(z)$ represents the average current measurements at different depths z, corrected for temperature and pressure, N_K is the air kerma calibration coefficient of the chamber, k_Q is the correction factor for beam quality, and $k_{K_{\mathrm{a}} \to D_{\mathrm{w}}}$ is an air kerma to dose to water conversion factor provided by Zeiss. The relationship between the TARGIT dose and the Zeiss V4.0 dose is expressed as:

$$\dot{D}_{\mathrm{w}}^{\mathrm{V4.0}}(z) = \frac{\dot{D}_{\mathrm{w}}^{\mathrm{TARGIT}}(z)}{f'(z)} \tag{2.34}$$

where $f'(z)$ is a depth-dependent conversion factor. According to the manufacturer, the discrepancies arise due to differences in ionization chamber models and calibration schemes. The PTW 23342, used in TARGIT, and the PTW 34013, used in the Zeiss phantom, have distinct effective points of measurement due to variations in chamber volume and entrance window dimensions. The PTW 23342 is calibrated in terms of exposure using $f = 0.881$ cGy/R, while the

PTW 34013 is calibrated in air kerma, and kerma is converted to absorbed dose to water using $k_{K_a \to D_w}$. Additionally, the design of the waterproof holders can influence dose measurements. Another contributing factor is the beam quality variations due to beam hardening, as the INTRABEAM spectrum changes with depth in water, affecting the measured dose in both methods to different extents. The necessity for this conversion factor has been criticized, as the absorbed dose to water should, by definition, be independent of the experimental measurement setup [36].

2.6.3 C_Q method

Recent studies have shown that the TARGIT method may underestimate the absorbed dose, particularly for smaller applicators [4]. To address this issue, Watson et al. developed the C_Q method, which aims to provide a more accurate dosimetry approach for the INTRABEAM system [4, 37]. The C_Q method introduces a depth-dependent factor, $C_Q(z)$, which is calculated using Monte Carlo simulations that include full modeling of all chamber details and spectral changes in the phantom. This factor converts measurements made in water with an air-kerma calibrated ionization chamber into absorbed dose rate to water. The dose rate according to the C_Q method is given by:

$$\dot{D}_w^{C_Q}(z) = M(z)\, C_Q(z)\, N_K \tag{2.35}$$

where $M(z)$ is the measured current (corrected for influence quantities), N_K is the air-kerma calibration coefficient, and C_Q is the Monte Carlo calculated chamber conversion factor from air-kerma in a reference beam to absorbed dose to water for the measurement beam. This approach accounts for the beam quality variations with depth and provides a more accurate conversion from air-kerma to absorbed dose to water.

The C_Q method represents a significant advancement in INTRABEAM dosimetry, addressing the limitations of both the TARGIT and Zeiss V4.0 methods. By accounting for beam quality variations with depth and providing a more accurate conversion from air-kerma to absorbed dose to water, it offers a more reliable basis for dose calculations in IORT. This is particularly crucial when considering doses to organs at risk (OARs), where the TARGIT method has been shown to potentially underestimate the delivered dose significantly [37–41]. However, while the C_Q method offers substantial improvements, specific challenges remain in GBM IORT dosimetry. All three methods discussed (TARGIT, V4.0, and C_Q) share a fundamental limitation: they rely on measurements performed in water phantoms under full scatter conditions. In clinical IORT

scenarios, the surgical cavity creates tissue-air interfaces that significantly alter these scatter conditions, particularly affecting the dose near cavity surfaces. This effect is especially pronounced at the low energies used by INTRABEAM, where backscatter contributions form a substantial component of the delivered dose. Although the treatment volume itself is primarily in relatively homogeneous brain tissue, and the overlying skull bone segment is surgically removed during the procedure, accurate dose calculation to OARs remains complex. This complexity arises from the steep dose gradients characteristic of low-energy X-rays, combined with the need to evaluate dose to structures near the skull base and air cavities, such as the optic nerves and chiasm, where both tissue heterogeneities and varying backscatter conditions affect the dose distribution. These considerations, along with the necessity to accurately combine IORT with EBRT dose distributions for treatment planning, lead us to consider Monte Carlo methods as our most accurate approach for comprehensive dose evaluation. The following section will delve into these Monte Carlo techniques, exploring their principles and applications relevant to INTRABEAM dosimetry.

2.7 Monte Carlo methods

Monte Carlo (MC) simulations have become an indispensable tool in medical physics, particularly in the field of radiation dosimetry. These computational methods offer a powerful approach to modeling complex radiation transport phenomena, providing insights that are often challenging or impossible to obtain through experimental measurements alone. In the context of this thesis, MC techniques play a crucial role in characterizing the dose distributions of the INTRABEAM system and validating experimental measurements.

2.7.1 Basics of Monte Carlo simulations

At its core, Monte Carlo simulation in radiation transport is a statistical sampling method that simulates the trajectories of individual particles (e.g., photons, electrons) as they interact with matter. The method derives its name from the use of random numbers to make decisions about particle interactions, analogous to the randomness of games in a casino [42].

The fundamental principle of MC simulations in radiation transport involves tracking particles from their origin through a series of interactions until they either escape the region of interest or their energy falls below a predetermined threshold. Each interaction is governed by probability distributions derived from physical cross-sections, which describe the likelihood of various inter-

action types (e.g., photoelectric absorption, Compton scattering) occurring at different energies and in different materials.

The process of an MC simulation in radiation transport involves a series of interconnected steps that model the journey of individual particles through matter. It begins with the generation of a particle, assigning to it initial parameters such as position, direction, and energy based on the characteristics of the radiation source being simulated. As this particle traverses the medium, the distance to its next interaction site is sampled from an exponential distribution, which is determined by the total interaction cross-section of the medium. Upon reaching this interaction site, the type of interaction (e.g., photoelectric absorption, Compton scattering) is randomly selected based on the relative probabilities of different interaction mechanisms at the particle's current energy. The outcome of this interaction, including energy deposition, potential secondary particle production, and any change in the particle's direction, is then sampled from the appropriate differential cross-sections. This process of transport and interaction continues, with each step being governed by random sampling from physically-based probability distributions until the particle either escapes the defined geometry or its energy falls below a predetermined cutoff value. To achieve statistically significant results, this entire sequence is repeated for millions of primary particles, with the collective behavior of these simulated particles providing a robust representation of the radiation transport process.

The power of MC methods lies in their ability to accurately model complex geometries and account for detailed physics processes. This is particularly important in dosimetry applications where the interplay between radiation and matter can be highly complex, especially in heterogeneous media or near material interfaces [43]. In the context of the INTRABEAM system, MC simulations allow for detailed modeling of the x-ray source, including the electron beam characteristics, target interactions, and beam-modifying components such as applicators, the patient, or in the case of calibration and quality assurance measurements, the phantom and detector geometry details.

The statistical nature of MC simulations means that the accuracy of the results improves with the number of simulated particles, typically following a $1/\sqrt{N}$ relationship, where N is the number of particle histories. However, this also means that achieving high precision can be computationally intensive, especially in regions of low dose. This computational cost has historically been a limiting factor in the widespread adoption of MC methods in clinical practice, but advancements in computing power and efficiency-enhancing techniques have made MC simulations increasingly feasible for routine use [44].

2.7.2 Variance reduction techniques

Variance reduction techniques (VRTs) are methods employed in Monte Carlo simulations to improve the efficiency of calculations without compromising the accuracy of the results. These techniques aim to reduce the statistical uncertainty of the quantities of interest for a given number of particle histories or, conversely, to achieve a desired level of uncertainty with fewer histories [2, 44]. In the context of this thesis, several VRTs were employed to optimize the simulation of the INTRABEAM system. The key techniques used include:

- **Photon splitting**: This technique involves splitting a single photon into multiple photons with reduced statistical weights. Each split photon is then transported independently, effectively increasing the number of photons contributing to the scored quantities without increasing the number of primary particles. This is particularly useful for improving statistics in regions of interest that are far from the source or in low-probability interaction events.

- **Uniform bremsstrahlung splitting**: Applied specifically to bremsstrahlung events, this technique splits each bremsstrahlung photon into a predetermined number of photons with reduced weights. This enhances the sampling of the bremsstrahlung spectrum, which is crucial for accurately modeling the x-ray production in the INTRABEAM target [45].

- **Russian roulette**: This general technique is used to terminate particles selectively based on a survival probability, typically applied to maintain particle population balance when other VRTs increase particle numbers. Surviving particles have their statistical weights increased inversely proportional to the survival probability. In our simulations, range-based Russian roulette was employed as a specific application of this technique. It was used to terminate electrons that did not have sufficient energy to reach the scoring volume, thus reducing computation time. This approach assumes a low probability of bremsstrahlung production for these low-energy electrons. Russian roulette was also applied to secondary charged particles produced through photon splitting or cross-section enhancement to manage their statistical weights effectively.

- **Photon cross-section enhancement**: This method artificially increases the photon interaction cross-sections in specified regions, typically near detectors or in areas of interest. The statistical weights of the resulting particles are adjusted to maintain an unbiased result. To

ensure the effectiveness of this technique, the enhancement is applied not only in the region of interest but also in neighboring regions within the range of secondary electrons. This approach prevents the introduction of high-weight electrons from non-enhanced regions, which could otherwise compromise the statistical gains. Additionally, Russian roulette is applied to electrons created in the enhanced regions to increase their statistical weight, maintaining overall balance in the simulation.

- **Bremsstrahlung cross-section enhancement**: Similar to photon cross-section enhancement, this technique artificially increases the probability of bremsstrahlung production. It was particularly useful in our simulations for improving the efficiency of modeling X-ray production in the INTRABEAM target.

In addition to these VRTs, we also employed other efficiency-enhancing techniques that, while not strictly classified as variance reduction methods, significantly improved our simulation efficiency:

- **Intermediate phase-space storage**: This method involves storing particle information (position, direction, energy, and statistical weight) at a predefined surface, typically at the boundary between two regions of the simulation geometry. In our case, we used this technique to store particle data at the applicator surface of the INTRABEAM system. The resulting phase-space file can then be used as a source for subsequent simulations, avoiding the need to repeatedly simulate particle transport through the source and applicator for different geometries or scoring configurations. This approach is particularly beneficial when multiple simulations with varying downstream geometries are required, as it significantly reduces overall computation time.

- **Track-length estimator**: This fluence-based scoring technique calculates energy deposition based on the track length of particles through a volume rather than only at discrete interaction points. For photons, this allows every particle passing through a volume to contribute to the kerma estimate, regardless of whether an interaction occurs. The track-length estimator is particularly beneficial for improving statistics in small scoring volumes or in regions of low interaction probability [46].

It's important to note that while VRTs can greatly enhance simulation efficiency, their implementation requires careful consideration to ensure that the underlying physics is not compromised or that their implementation suffers from other unwanted effects. The selection and tuning

of VRTs must be validated against non-VRT simulations and, where possible, experimental measurements to confirm the accuracy of the results [42].

2.7.3 EGSnrc code system

The EGSnrc (Electron-Gamma Shower National Research Council) code system is a comprehensive, open-source software package for the Monte Carlo simulation of radiation transport through matter. Developed and maintained by the National Research Council of Canada, EGSnrc has gained vast applicability in medical physics for its accuracy, flexibility, and extensive validation in radiotherapy applications [47]. The code system is particularly well-suited for simulating radiation transport in the energy range relevant to medical physics, from a few keV to several hundred MeV. EGSnrc employs state-of-the-art physics models and cross-section data to simulate the wide range of particle interactions discussed in Sections 2.2.1 and 2.2.2. The code system allows for detailed customization of simulation parameters, enabling users to balance computational efficiency with the desired level of physical accuracy.

In EGSnrc, photon transport is performed through an analog simulation process. The code models several key photon interaction mechanisms, including photoelectric absorption, Compton scattering, and Rayleigh scattering, as described in Section 2.2.1. For photoelectric absorption, the total cross-section can be taken from preset libraries or user-supplied. The interacting element and electronic shell are explicitly sampled for compounds and mixtures, with the photoelectron direction sampled from the Sauter distribution [48]. Compton scattering is modeled using the Klein-Nishina formula with the inclusion of electron binding effects and Doppler broadening using the relativistic impulse approximation. Rayleigh scattering, while off by default, should be activated for simulations involving photons below 1 MeV, with atomic form factors based on the work of Hubbell and Øverbø (1979) [49].

A critical aspect of photon transport in EGSnrc is the choice of photon cross-section data. The default is to use the NIST XCOM database [50], which contains up-to-date photon cross-sections for all elements from 1 keV to 100 GeV. However, the MCDF-XCOM database may be preferable for low-energy applications. This database incorporates renormalized photoelectric cross-sections based on the work of Sabbatucci and Salvat (2016) [51], which have shown better agreement with recent experimental data for low-energy photons.

For electron transport, EGSnrc employs a condensed history approach categorized as “Class II” in the Berger classification [52]. This method groups collisions with small energy losses

into a single large raytracing step, while catastrophic collisions with energy losses above given threshold energies are treated separately and simulated explicitly. Bremsstrahlung production is modeled explicitly for photon energies above a threshold (typically 1 keV for low-energy applications), with sub-threshold events accounted for in the restricted radiative stopping power. Inelastic collisions are treated explicitly when the scattered electron's kinetic energy exceeds a specified threshold, with the Møller cross-section used for electron-electron scattering by default. Options are available to account for K- and L-shell binding energies through electron impact ionization (EII).

Elastic scattering in EGSnrc uses an exact multiple elastic scattering theory based on Goudsmit-Saunderson distributions away from material boundaries. Near boundaries, the step transport algorithm switches to single elastic scattering to avoid interface artifacts, with the transition occurring at a default of 3 elastic mean free paths perpendicular distance from the electron to the closest boundary.

`egs++`, `egs_chamber`, and `egs_brachy`

The EGSnrc system includes a C++-based geometry and source library called `egs++`, which provides a flexible framework for defining complex simulation geometries and particle sources [53]. This library is utilized by various user codes within the EGSnrc system, including `egs_chamber` and `egs_brachy`, which are particularly relevant for low-energy dosimetry applications.

The `egs_chamber` user code, developed by Wulff et al. (2008) [54], is specialized for the simulation of ionization chamber response. It incorporates advanced variance reduction techniques optimized for calculations involving ionization chambers, such as photon cross-section enhancement in the chamber cavity and correlated sampling for perturbation factor calculations. This code allows for detailed modeling of chamber geometry, including features like the chamber wall, central electrode, and guard rings, which are crucial for accurate simulation of detector response.

The `egs_brachy` user code, created by Chamberland et al. (2016) [55], is designed specifically for brachytherapy dosimetry calculations. It features a robust geometry package for modeling complex source and applicator geometries and includes advanced variance reduction techniques optimized for brachytherapy applications. `egs_brachy` implements a track-length estimator for photon energy deposition (kerma approximation), which significantly improves the ef-

ficiency of dose calculations in low-energy photon regimes. The code's ability to handle complex geometries allows for accurate representation of various brachytherapy sources and applicators.

Both `egs_chamber` and `egs_brachy` benefit from the advanced physics models and cross-section data of the EGSnrc system. This includes the use of XCOM or MCDF-XCOM photon cross-sections, which are particularly important for accurate low-energy photon transport, and the implementation of detailed atomic relaxation cascades. The combination of these user codes, built upon the `egs++` library and the core EGSnrc physics, provides a comprehensive framework for simulating a wide range of scenarios in medical physics, from detector response to complex dose distributions in brachytherapy applications.

Both codes can also utilize patient CT data for dose calculations in heterogeneous media. While CT numbers (Hounsfield Units) are commonly used to determine material densities and compositions for Monte Carlo simulations, alternative approaches include using standardized tissue compositions from sources such as ICRU Report 44 [27] and ICRP Publication 89 [28] based on pre-defined anatomical structures. In either approach, the CT dataset provides the geometric framework for radiation transport and dose scoring in the Monte Carlo simulation.

References

[1] E. B. Podgorsak, *Radiation physics for medical physicists, second edition*. Springer, 2010.

[2] P. Andreo, D. T. Burns, A. E. Nahum, J. Seuntjens, and F. H. Attix, *Fundamentals of ionizing radiation dosimetry*. Wiley-Vch, 2017.

[3] Podgorsak, E.B., *Radiation oncology physics: A handbook for teachers and students*. Vienna: International Atomic Energy Agency (IAEA), 2005.

[4] P. G. F. Watson, M. Popovic, and J. Seuntjens, "Determination of absorbed dose to water from a miniature kilovoltage x-ray source using a parallel-plate ionization chamber," *Physics in Medicine and Biology*, vol. 63, no. 1, p. 015 016, 2017.

[5] J. C. Yanch and K. J. Harte, "Monte Carlo simulation of a miniature, radiosurgery x-ray tube using the ITS 3.0 coupled electron-photon transport code," *Medical Physics*, vol. 23, no. 9, pp. 1551–1558, 1996.

[6] D. J. Thomas, "ICRU Report 85, Fundamental quantities and units for ionizing radiation," *Radiation Protection Dosimetry*, vol. 150, no. 4, pp. 550–552, 2012.

[7] D. Eaton, "Quality assurance and independent dosimetry for an intraoperative x-ray device," *Medical physics*, vol. 39, no. 11, pp. 6908–6920, 2012.

[8] P. R. Almond *et al.*, "AAPM's TG-51 protocol for clinical reference dosimetry of high-energy photon and electron beams," *Medical physics*, vol. 26, no. 9, pp. 1847–1870, 1999.

[9] C.-M. Ma *et al.*, "AAPM protocol for 40-300 kV x-ray beam dosimetry in radiotherapy and radiobiology," *Medical Physics*, vol. 28, no. 6, pp. 868–893, 2001.

[10] W. U. Laub and R. Crilly, "Clinical radiation therapy measurements with a new commercial synthetic single crystal diamond detector," *Journal of Applied Clinical Medical Physics*, vol. 15, no. 6, pp. 92–102, 2014.

[11] I. Ciancaglioni *et al.*, "Dosimetric characterization of a synthetic single crystal diamond detector in clinical radiation therapy small photon beams," *Medical Physics*, vol. 39, no. 7Part1, pp. 4493–4501, 2012.

[12] M. Marinelli, G. Prestopino, C. Verona, and G. Verona-Rinati, "Experimental determination of the PTW 60019 microDiamond dosimeter active area and volume," *Medical physics*, vol. 43, no. 9, pp. 5205–5212, 2016.

[13] T. Shimaoka, S. Koizumi, and Kaneko, "Recent progress in diamond radiation detectors," *Functional Diamond*, vol. 1, no. 1, pp. 205–220, 2022.

[14] R. Nath, L. L. Anderson, G. Luxton, K. A. Weaver, J. F. Williamson, and A. S. Meigooni, "Dosimetry of interstitial brachytherapy sources: Recommendations of the AAPM radiation therapy committee task group no. 43," *Medical Physics*, vol. 22, no. 2, pp. 209–234, 1995.

[15] M. J. Rivard *et al.*, "Update of AAPM Task Group No. 43 Report: A revised AAPM protocol for brachytherapy dose calculations," *Medical Physics*, vol. 31, no. 3, pp. 633–674, 2004.

[16] M. J. Rivard *et al.*, "Supplement to the 2004 update of the AAPM Task Group No. 43 Report," *Medical Physics*, vol. 34, no. 6Part1, pp. 2187–2205, 2007.

[17] M. J. Rivard *et al.*, "Supplement 2 for the 2004 update of the AAPM Task Group No. 43 Report: Joint recommendations by the AAPM and GEC-ESTRO," *Medical Physics*, vol. 44, no. 9, e297–e338, 2017.

[18] M. J. Rivard, S. D. Davis, L. A. DeWerd, T. W. Rusch, and S. Axelrod, "Calculated and measured brachytherapy dosimetry parameters in water for the Xoft Axxent X-Ray Source: An electronic brachytherapy sourcea)," *Medical Physics*, vol. 33, no. 11, pp. 4020–4032, 2006.

[19] D. J. Eaton, "Electronic brachytherapy—current status and future directions," *British Journal of Radiology*, vol. 88, no. 1049, p. 20 150 002, 2015.

[20] L. A. DeWerd, W. S. Culberson, J. A. Micka, and S. J. Simiele, "A modified dose calculation formalism for electronic brachytherapy sources," *Brachytherapy*, vol. 14, no. 3, pp. 405–408, 2015.

[21] D. S. Ayala Alvarez, P. G. F. Watson, M. Popovic, V. J. Heng, M. D. C. Evans, and J. Seuntjens, "Monte Carlo calculation of the TG-43 dosimetry parameters for the INTRABEAM source with spherical applicators," *Physics in Medicine & Biology*, vol. 66, no. 21, p. 215 017, 2021.

[22] D. Eaton and S. Duck, "Dosimetry measurements with an intra-operative x-ray device," *Physics in Medicine & Biology*, vol. 55, no. 12, N359, 2010.

[23] D. S. Ayala Alvarez, P. G. F. Watson, M. Popovic, V. J. Heng, M. D. C. Evans, and J. Seuntjens, "Monte Carlo calculation of the relative TG-43 dosimetry parameters for the INTRABEAM electronic brachytherapy source," *Physics in Medicine and Biology*, vol. 65, no. 24, p. 245 041, 2020.

[24] S. Chiavassa *et al.*, "Monte Carlo evaluation of the effect of inhomogeneities on dose calculation for low energy photons intra-operative radiation therapy in pelvic area," *Physica Medica*, vol. 31, no. 8, pp. 956–962, 2015.

[25] L. Beaulieu *et al.*, "Report of the Task Group 186 on model-based dose calculation methods in brachytherapy beyond the TG-43 formalism: Current status and recommendations for clinical implementation," *Medical physics*, vol. 39, no. 10, pp. 6208–6236, 2012.

[26] M. Berger, J. Coursey, and M. Zucker, *ESTAR, PSTAR, and ASTAR: Computer programs for calculating stopping-power and range tables for electrons, protons, and helium ions (version 1.21). [Online] available: Http://physics.nist.gov/Star (accessed july 2024)*, 1999.

[27] International Commission on Radiation Units and Measurements, *ICRU Report 44, Tissue substitutes in radiation dosimetry and measurement*. ICRU Publications, Bethesda, MD, 1989.

[28] J. Valentin, "Basic anatomical and physiological data for use in radiological protection: Reference values: ICRP Publication 89," *Annals of the ICRP*, vol. 32, no. 3-4, pp. 1–277, 2002.

[29] V. Peppa *et al.*, "A MC-based anthropomorphic test case for commissioning model-based dose calculation in interstitial breast 192-Ir HDR brachytherapy," *Medical Physics*, vol. 50, no. 7, pp. 4675–4687, 2023.

[30] J. S. Vaidya *et al.*, "Risk-adapted targeted intraoperative radiotherapy versus whole-breast radiotherapy for breast cancer: 5-year results for local control and overall survival from the TARGIT-A randomised trial," *The Lancet*, vol. 383, no. 9917, pp. 603–613, 2014.

[31] Carl Zeiss Meditec AG, "INTRABEAM dosimetry, brochure EN_30_010_155ii," manual, 2011.

[32] International Commission on Radiation Units and Measurements, *ICRU Report 17, Radiation dosimetry: X rays generated at potentials of 5 to 150 KV*. ICRU Publications, Washington, DC, 1970.

[33] P. Andreo *et al.*, "IAEA TRS-398–Absorbed dose determination in external beam radiotherapy: An international code of practice for dosimetry based on standards of absorbed dose to water," *International Atomic Energy Agency*, 2000.

[34] *Absorbed dose determination in external beam radiotherapy* (Technical Reports Series No. 398 (Rev. 1)). Vienna: International Atomic Energy Agency (IAEA), 2024.

[35] Carl Zeiss Meditec AG, "INTRABEAM water phantom – instructions for use, G-30-1767-en version 5.0," manual, 2015.

[36] F. W. Hensley, "Present state and issues in IORT physics," *Radiation Oncology*, vol. 12, no. 1, 2017.

[37] P. G. F. Watson, H. Bekerat, P. Papaconstadopoulos, S. Davis, and J. Seuntjens, "An investigation into the INTRABEAM miniature x-ray source dosimetry using ionization chamber and radiochromic film measurements," *Medical Physics*, vol. 45, no. 9, pp. 4274–4286, 2018.

[38] P. G. F. Watson, M. Popovic, L. Liang, N. Tomic, S. Devic, and J. Seuntjens, "Clinical Implication of Dosimetry Formalisms for Electronic Low-Energy Photon Intraoperative Radiation Therapy," *Practical Radiation Oncology*, vol. 11, no. 1, e114–e121, 2021.

[39] W. S. Culberson *et al.*, "Dose-rate considerations for the INTRABEAM electronic brachytherapy system: Report from the American association of physicists in medicine task group no. 292," *Medical Physics*, vol. 47, no. 8, e913–e919, 2020.

[40] M. Y. Shaikh, J. Burmeister, R. Scott, L. K. Kumaraswamy, A. Nalichowski, and M. C. Joiner, "Dosimetric evaluation of incorporating the revised V4.0 calibration protocol for breast intraoperative radiotherapy with the INTRABEAM system," *Journal of Applied Clinical Medical Physics*, vol. 21, no. 2, pp. 50–59, 2020.

[41] A. Abudra'a, B. Chauvenet, J. Gouriou, J. Plagnard, R. Itti, and I. Aubineau-Lanièce, "Dosimetry formalism and calibration procedure for electronic brachytherapy sources in terms of absorbed dose to water," *Physics in Medicine and Biology*, vol. 65, no. 14, p. 145 006, 2020.

[42] D. W. O. Rogers and A. F. Bielajew, "Monte Carlo techniques of electron and photon transport for radiation dosimetry," *The Dosimetry of Ionizing Radiation*, 1990.

[43] D. W. O. Rogers, "Fifty years of Monte Carlo simulations for medical physics," *Physics in Medicine & Biology*, vol. 51, no. 13, R287, 2006.

[44] J. Seco and F. Verhaegen, *Monte Carlo techniques in radiation therapy*. CRC press, 2013.

[45] I. Kawrakow, D. W. O. Rogers, and B. R. B. Walters, "Large efficiency improvements in BEAMnrc using directional bremsstrahlung splitting," *Medical Physics*, vol. 31, no. 10, pp. 2883–2898, 2004.

[46] J. Williamson, "Monte Carlo evaluation of kerma at a point for photon transport problems," *Medical Physics*, vol. 14, no. 4, pp. 567–576, 1987.

[47] I. Kawrakow and D. W. O. Rogers, "The EGSnrc code system: Monte Carlo simulation of electron and photon transport," National Research Council Canada, Ottawa, Canada, Tech. Rep. PIRS-701, 2019.

[48] F. Sauter, "Über den atomaren Photoeffekt in der K-Schale nach der relativistischen Wellenmechanik Diracs," *Annalen der Physik*, vol. 403, no. 4, pp. 454–488, 1931.

[49] J. H. Hubbell and I. O/verbo/, "Relativistic atomic form factors and photon coherent scattering cross sections," *Journal of Physical and Chemical Reference Data*, vol. 8, no. 1, pp. 69–106, 1979.

[50] M. J. Berger *et al.*, "XCOM: Photon cross sections database (version 1.5). [Online] available: Http://physics.nist.gov/xcom (accessed september 2020)," *National Institute of Standards and Technology, Gaithersburg, MD*, 2010.

[51] L. Sabbatucci and F. Salvat, "Theory and calculation of the atomic photoeffect," *Radiation Physics and Chemistry*, vol. 121, pp. 122–140, 2016.

[52] Martin J. Berger, "Monte Carlo calculation of the penetration and diffusion of fast charged particles," in *Methods in Computational Physics*, B. Alder, S. Fernbach, and M. Rotenberg, Eds., vol. 1, Academic Press, New York, pp. 135–215.

[53] I. Kawrakow, E. Mainegra-Hing, F. Tessier, and B. R. B. Walters, "The egsnrc C++ class library, NRC report PIRS-898 (rev a)," National Research Council Canada, Ottawa, Canada, Tech. Rep., 2009.

[54] J. Wulff, K. Zink, and I. Kawrakow, "Efficiency improvements for ion chamber calculations in high energy photon beams," *Medical Physics*, vol. 35, no. 4, pp. 1328–1336, 2008.

[55] M. J. P. Chamberland, R. E. P. Taylor, D. W. O. Rogers, and R. M. Thomson, "Egs_brachy: A versatile and fast Monte Carlo code for brachytherapy," *Physics in Medicine & Biology*, vol. 61, no. 23, pp. 8214–8231, 2016.

Chapter 3

INTRABEAM source modeling and initial TG-43 parameter calculations

3.1 Preface

This chapter explores the fundamental steps in characterizing the INTRABEAM source using Monte Carlo (MC) simulations, focusing on the initial modeling of the bare probe and the calculation of its TG-43 dosimetry parameters. It is important to note that the work presented here stems directly from research conducted during my previous Master of Science (MSc) program. The findings and methodologies discussed in this chapter were initially compiled in my MSc thesis [1] and subsequently published in a peer-reviewed paper in Physics in Medicine & Biology (Ayala Alvarez et al., 2020) [2]. This work established the foundation for the more advanced investigations into spherical applicators and clinical applications in glioblastoma treatment, which are explored in subsequent chapters of this PhD thesis.

The chapter begins by detailing the MC modeling process for the INTRABEAM source, including comprehensive descriptions of the geometry, materials, and beam characteristics. These elements are needed for accurate simulation of the low-energy x-ray spectrum and steep dose gradients characteristic of the INTRABEAM system. The methods employed for calculating TG-43 parameters, such as the radial dose function and 2D anisotropy function, are then explained. Additionally, the chapter describes the experimental measurements used to validate the MC model, involving both ionization chamber and diamond detector setups.

Portions of this chapter, including several figures and data tables, are adapted from work previously published as: Ayala Alvarez DS, Watson PGF, Popovic M, Heng VJ, Evans MDC, Seuntjens J. Monte Carlo calculation of the

relative TG-43 dosimetry parameters for the INTRABEAM electronic brachytherapy source. *Physics in Medicine & Biology*. 2020;**65**:245041. Reproduced with permission from Institute of Physics Publishing.

3.2 INTRABEAM source modeling

3.2.1 Geometry and materials

It is important to model the INTRABEAM source accurately for precise dosimetric calculations. Building upon the general description provided in Section 1.3, this section details the geometry and material composition of the source used in our Monte Carlo (MC) simulations.

The INTRABEAM source consists of a miniature X-ray tube housed within a needle-like probe. The probe has an outer diameter of 3.2 mm and a length of 100 mm. At its distal end, a 0.5 μm thick gold target is deposited on the inner surface of a hemispherical tip [3, 4]. This target is where bremsstrahlung and characteristic x-rays are produced. The distal 16 mm of the probe serves as an x-ray window and is composed of beryllium, chosen for its low atomic number to minimize photon attenuation [4]. The remainder of the probe body is made of nickel. Biocompatible layers encase the entire length of the probe. Three thin coating layers encase the entire length of the probe: nickel oxide (NiO), nickel (Ni), and chromium nitride (CrN), each 2.5 μm thick. These layers protect the probe materials from corrosion and wear and enhance mechanical strength and durability while providing a biocompatible surface as a redundant safety measure. Table 3.1 presents the detailed material specifications of the INTRABEAM source, including the thicknesses of various components. Figure 3.1 illustrates the geometry of the INTRABEAM source as modeled in our MC simulations. The figure includes a detailed cross-sectional view of the source tip, highlighting the beryllium window, gold target, and biocompatible layers.

Table 3.1 Material specifications of the INTRABEAM source probe.

Component	Material	Thickness (μm)
Target	Au	1.0
Body	Be	500
Biocompatible layers	NiO	2.5
	Ni	2.5
	CrN	2.5

Data adapted from Nwankwo et al. (2013) [5].

It is important to note that the foundation for this geometric model was provided by Dr. Peter Watson, who developed an MC model of the source during his PhD research [6]. Watson's work provided a starting point for our simulations, which we then modified and expanded upon for our specific research objectives [2].

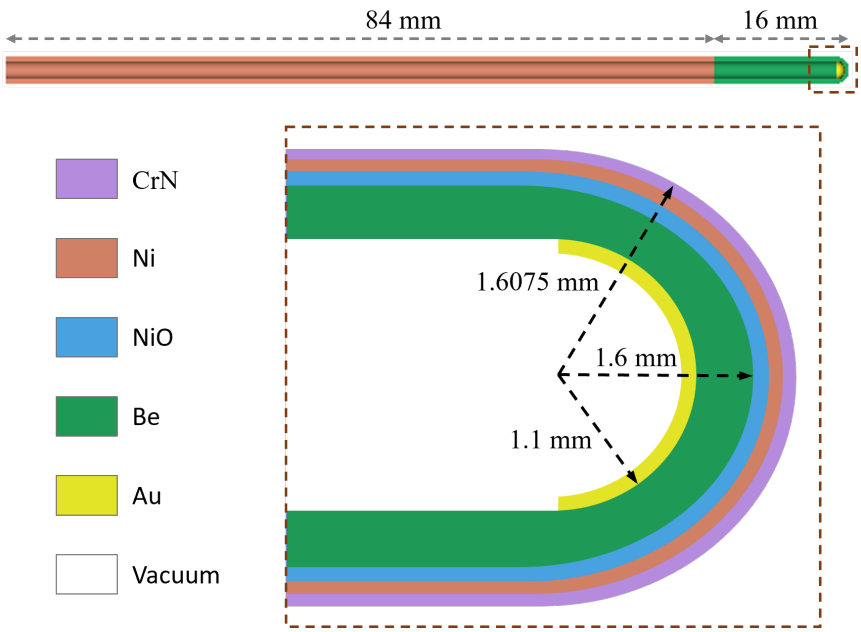

Figure 3.1 Schematic representation of the INTRABEAM source geometry used in MC simulations. The image on top shows the overall probe structure. The inset provides a magnified cross-sectional view of the source tip, detailing the beryllium window, gold target, and biocompatible layers. Note that the inset is not to scale. Figure adapted from [2]

3.2.2 Beam characteristics

The INTRABEAM system generates X-rays through the interaction of an electron beam with the gold target at the probe tip. Understanding the characteristics of this electron beam is important for accurate MC modeling of the subsequent x-ray production and distribution. In our model, the electron beam is simulated with a Gaussian energy distribution centered at 50 keV with a full width at half maximum (FWHM) of 5 keV [7]. This energy distribution reflects the acceleration potential applied in the INTRABEAM system and accounts for the inherent energy spread in the electron beam. A notable feature of the INTRABEAM source is its internal beam deflection system. This system uses a magnetic deflector to oscillate the electron beam about the probe's central axis, resulting in a more uniform dose distribution around the source [7–9]. To model this effect, we implemented a beam geometry where electrons strike the gold target in a pattern of two concentric rings. Based on the findings of Clausen et al. (2012) [7], these rings were defined with radii of 0.6 to 0.7 mm and 0.7 to 0.8 mm, with weighting factors of 1.05 and 1.55, respectively. Figure 3.2 illustrates this ring-shaped electron beam model as implemented in our MC simulations. This beam model, incorporating both the energy distribution and spatial characteristics of the electron beam, allows for a more accurate representation of the x-ray production process in the INTRABEAM source. It accounts for the effects of the internal beam deflection system, which is intended to achieve a more isotropic dose distribution that facilitates its clinical application.

In addition to the ring-shaped model, we also investigated an alternative particle source configuration, referred

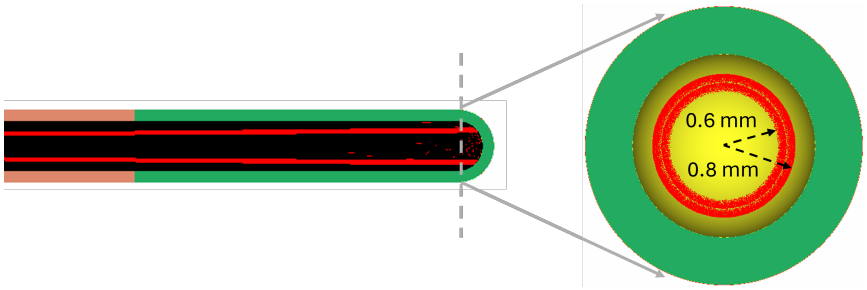

Figure 3.2 Visualization of the modeled electron beam structure in the INTRABEAM source. The image shows the two concentric rings representing the electron impact pattern on the gold target, with radii ranging from 0.6 to 0.8 mm. This model accounts for the internal beam deflection system used to achieve a more isotropic dose distribution.

to as the 'spotted-shaped source'. This model, based on the work of Abudra'a et al. (2020) [10], consists of sixteen homogeneous and parallel electron source spots equally spaced at the base of the gold target. This approach aims to more accurately represent the pulsed nature of the beam oscillation, which has been observed to generate a segmented distribution of x-ray emission spots on the gold target [11, 12]. Both the ring-shaped and spotted-shaped source models employed a Gaussian energy distribution with a mean energy of 50 keV and FWHM of 5 keV.

The resulting x-ray spectrum from this electron beam interaction with the gold target consists of both bremsstrahlung and characteristic x-rays. As shown in Figure 3.3, the spectrum includes significant contributions from the L-shell characteristic x-rays of gold (in the range of 9-14 keV) and the K-shell x-rays of nickel (7.5 and 8.3 keV) from the biocompatible layers [4, 5, 9, 13]. The mean photon energy at the source tip is approximately 19 keV, which is significantly lower than that of conventional radiotherapy beams. This low-energy spectrum results in steep dose gradients and increased sensitivity to material composition, emphasizing the need for accurate modeling in dosimetric calculations.

3.2.3 Monte Carlo simulation parameters

The Monte Carlo (MC) simulations in this study were performed using the EGSnrc code system, specifically the `egs_brachy` (v2017.09.15) user code [14]. This code is optimized for brachytherapy dosimetry calculations and allows for rapid dose calculations by approximating dose to electronic kerma obtained via a track-length estimator. All relevant EGSnrc physics processes for low-energy photons were included. These encompassed Rayleigh scattering, bound Compton scattering, photoelectric absorption, and atomic relaxations for K, L, M, and N shells. Electron impact ionization was modeled using the PENELOPE libraries [15]. The bremsstrahlung cross-sections were based on the NRC database [16]. For this first part of the study, the photon cross-sections were based on the XCOM [17] database. The transport cut-off energy for photons (PCUT) was set at 1 keV, while for electrons inside the source (ECUT), it was set at 512 keV (1 keV kinetic energy). Outside the source, electrons were not transported (ECUT = 1 MeV) as the dose was approximated as electronic kerma. This approximation is valid for the low-energy range of the INTRABEAM system, where the range of secondary electrons is typically less than the voxel size used in dose scoring.

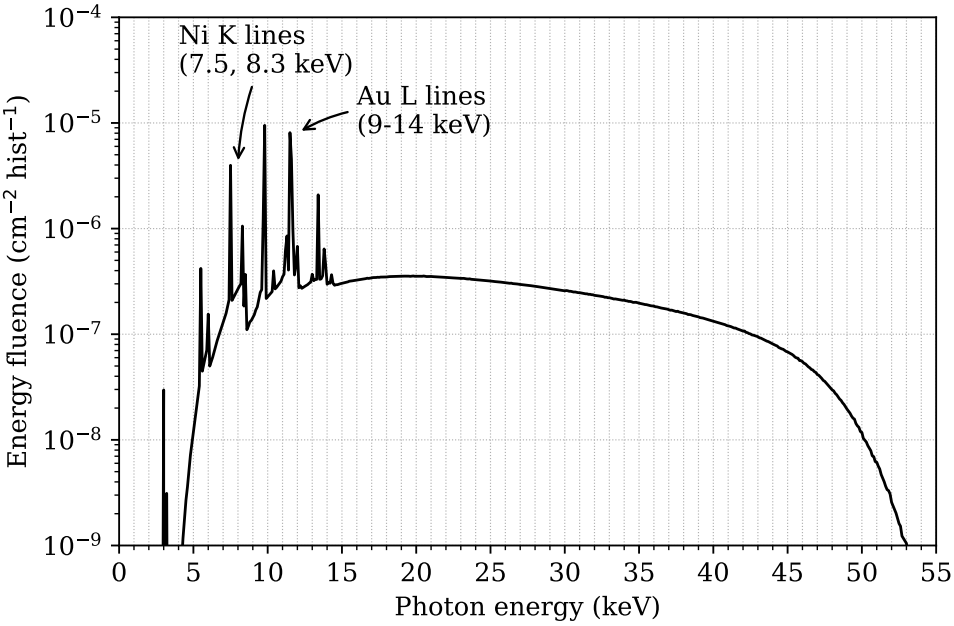

Figure 3.3 Energy fluence spectrum of the INTRABEAM bare probe measured in air at the probe surface. The spectrum shows prominent characteristic x-ray peaks from the gold target (Au L lines) and the nickel layer (Ni K lines), superimposed on a bremsstrahlung continuum that extends up to the maximum electron energy of 50 keV.

Several variance reduction techniques were employed to enhance simulation efficiency. These included bremsstrahlung cross-section enhancement in the gold target by a factor of 50 and uniform bremsstrahlung splitting with a factor of 100. Range-based Russian roulette was also used. The simulations were run from the interactions of the electron beam striking the gold target. Cross-section data for the materials in the source geometry were generated using the EGSnrc application g [18], covering the energy range from 1 keV to 100 keV. This range adequately encompasses the entire energy spectrum of the INTRABEAM system (Figure 3.3), ensuring accurate transport modeling of the simulated low-energy photons and electrons. Simulations were performed for both the ring-shaped and spotted-shaped source models to assess the impact of these different beam configurations on the resulting dose distributions.

In addition to `egs_brachy`, the `egs_chamber` user code was employed for MC model validation, particularly for simulations involving ionization chambers and diamond detectors. The transport parameters used in `egs_chamber` were consistent with those used in `egs_brachy` simulations. However, `egs_chamber` utilized additional variance reduction techniques (VRTs) as described in Section 2.7.2. These included photon cross-section enhancement in the chamber cavity. Furthermore, intermediate phase-space storage was used to improve simulation efficiency by obtaining data from particles entering a pre-defined volume enclosing all the chamber positions and then using it as a source for subsequent simulations.

3.2.4 TG-43 parameter calculation methods and setup

The calculation of TG-43 parameters for the INTRABEAM source was performed considering its small effective source size. Following the approach of Rivard et al. (2006) [19] for the Xoft electronic brachytherapy source, we adopted the 2D formalism with a point-source approximation to describe the geometry function, $G_{\mathrm{p}}(r,\theta) = 1/r^2$, and radial dose function, $g_{\mathrm{p}}(r)$. However, we retained the 2D formalism to account for polar anisotropy, $F(r,\theta)$, in all regions around the source probe. Figure 3.4 illustrates the coordinate system used for our TG-43 calculations. The origin was placed at the source tip, with $\theta = 0^\circ$ pointing away from the source, along the source long axis.

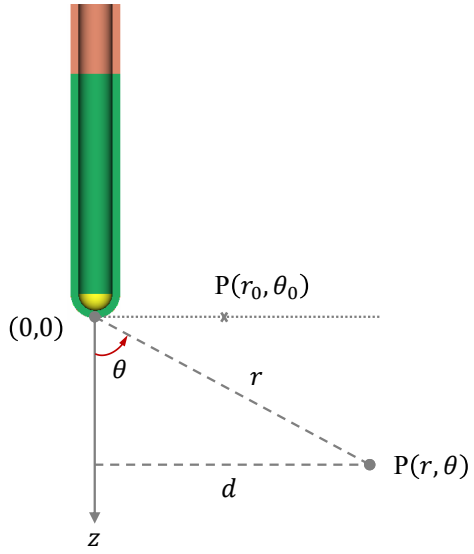

Figure 3.4 Coordinate system employed for TG-43 parameter calculations of the INTRABEAM source. The origin is located at the source tip, with $\theta = 0^\circ$ oriented along the source long axis, pointing away from the source. Figure reproduced from [2].

Dose rates were scored in a set of annular bins centered on the source longitudinal axis. These bins covered a region from -5 cm to 5 cm in the z-direction and 0 to 5 cm radially, with 0.04 cm intervals in both directions. While treatment planning systems typically require data over more extended volumes, this region was chosen as representative, capturing the area where most of the dose is delivered and where the MC model could be accurately validated. The scoring volume consisted of liquid water with a mass density of 1.0 g/cm^3 and an atomic composition of 2:1 for H:O. This volume was immersed in a larger spherical phantom of 20 cm radius with the same water composition to ensure full scattering conditions [19, 20]. Both the water phantom and scoring volume were centered at the source tip.

To achieve sufficient statistical precision, 3×10^9 particle histories were simulated. This resulted in type A uncertainties (k = 1) ranging from 0.1% to 0.5% over the source longitudinal axis at distances of 1 to 5 cm from the source tip. Partial volume effects were corrected in phantom voxels overlapping with the source geometry. These effects occur because the energy is stored only in the phantom portion of the voxel, but it is divided by the total voxel volume to calculate the absorbed dose. In these cases, the scored energy, E, in the phantom portion of the voxel was

divided by the partial volume, p, of the voxel outside the source:

$$D = \frac{E}{pV\rho} \tag{3.1}$$

where V is the total voxel volume and ρ is the media density. The partial volume factor, p, was precalculated by subdividing each voxel into 8000 subvoxels and determining the fraction outside the source.

Note that for air-kerma calculations, as presented in Chapter 4, a similar annular scoring approach was used at 50 cm from the source, which differs from primary standard measurement conditions where free-air chambers employ specific collimation to limit scattered radiation contributions. While this simplified scoring approach was sufficient for our initial characterization of the source, it's worth noting that more comprehensive simulation geometries incorporating explicit collimation might be needed for precise air-kerma calculations matching primary standard conditions.

3.3 Monte Carlo model validation

Validation of the Monte Carlo model is a critical step in ensuring the accuracy and reliability of the simulations. This section describes the experimental measurements and comparison procedures used to validate our MC model of the INTRABEAM source.

3.3.1 Experimental setup and measurements

Two types of detectors were used for the experimental validation: a parallel-plate ionization chamber (PTW 34013) and a synthetic diamond detector (PTW microDiamond TN60019). These detectors were chosen for their complementary characteristics, which make them particularly suitable for measurements in the low-energy X-ray beams produced by the INTRABEAM system. The PTW 34013 ionization chamber is an air-kerma-calibrated parallel-plate chamber designed for soft X-ray measurements. A schematic diagram of this chamber is shown in Figure 3.5. This detector features a small sensitive volume of 0.005 cm^3, enclosed between two electrodes forming a cylindrical volume of 1.45 mm radius and 0.9 mm thickness. The chamber's entrance window, made of 0.03 mm thick polyethylene, has a total area density of 2.76 mg cm^{-2} [21]. The PTW microDiamond TN60019, illustrated in Figures 3.6 and 3.7, is a synthetic diamond detector with a nominal sensitive volume of 0.004 mm^3. The detector's small size and near-tissue equivalence make it particularly suitable for measurements in high-dose gradient regions [22].

The experimental setups for measurements with both detectors are shown in Figure 3.8. A Zeiss water phantom was used for the ionization chamber measurements, with the chamber placed in the plastic holder below the source needle. Since the Zeiss water phantom is designed exclusively for use with the PTW 34013 ionization chamber, the microDiamond detector measurements were performed using a separate Wellhöfer water phantom with an automated 3D scanning system (WP700, version V 3.51.00, Wellhöfer Dosimetrie (IBA), Germany).

Measurements with the ionization chamber followed the methodology described by Watson et al. (2017) [13], based on the Zeiss water phantom manual [23]. Charge data was acquired from 60-second readings at various depths along the central axis of the source, ranging from 2 to 50 mm from the source tip. The effective point of

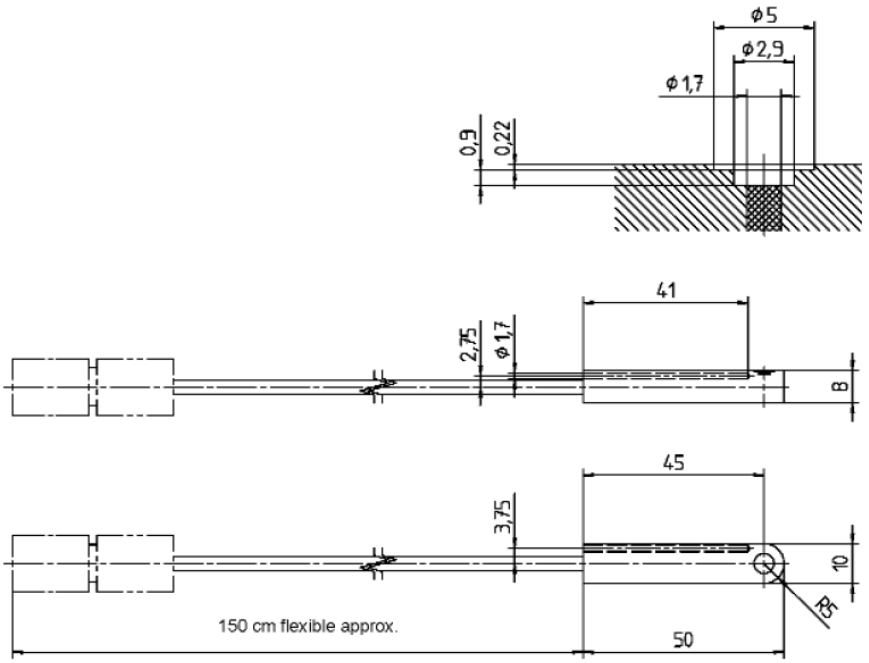

Figure 3.5 Schematic diagram of the PTW 34013 parallel-plate ionization chamber. The inset provides details of the measuring volume. This chamber design is optimized for soft X-ray measurements, with a small sensitive volume to minimize perturbation effects. Figure reproduced from [21].

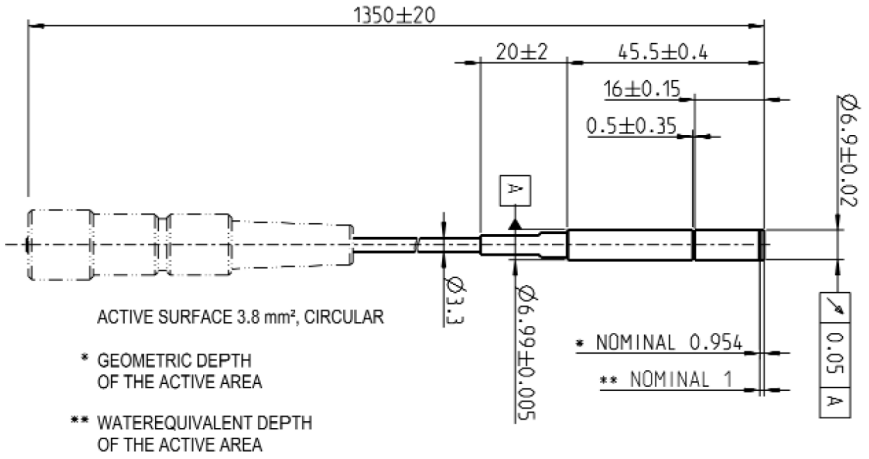

Figure 3.6 Schematic representation of the PTW microDiamond TN60019 detector. The compact design allows for high spatial resolution measurements that are useful for characterizing the steep dose gradients of the INTRABEAM source. Figure reproduced from [21].

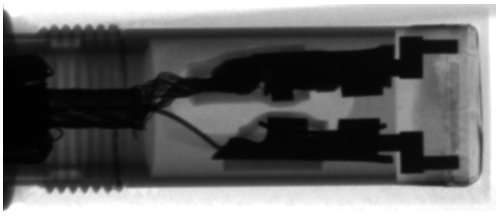

Figure 3.7 Micro-CT projection image of the PTW microDiamond TN60019 detector, revealing its internal components. The image was acquired using a MEDISO NanoScan SdC at the McGill University Health Centre, with an x-ray tube setup of 35 kVp and 1 mAs. This image was used to confirm the dimensions for the modeled geometry.

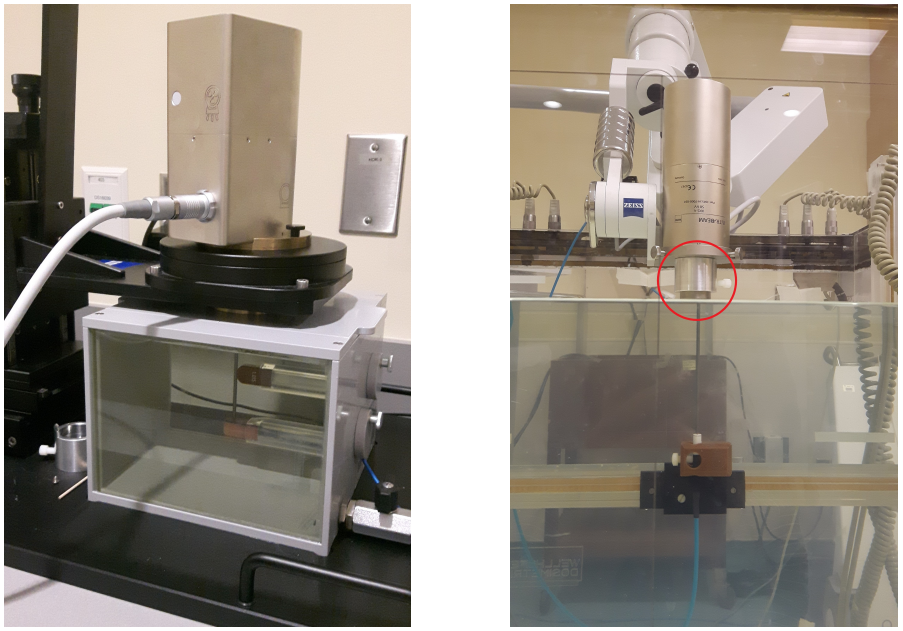

(a) (b)

Figure 3.8 Experimental setups for INTRABEAM dosimetry. (a) Measurements with the PTW 34013 ionization chamber in a Zeiss water phantom. The chamber is positioned in a plastic holder below the source. (b) Measurements with the PTW TN60019 microDiamond detector in a Wellhöfer water phantom using an automated 3D scanning system. The red circle indicates an in-house accessory used to bypass the INTRABEAM interlock system for bare probe measurements. Figure reproduced from [2].

measurement (EPOM) of the chamber was carefully considered in positioning. For the microDiamond detector, measurements were performed along the source longitudinal axis at depths ranging from 0.2 to 50 mm in water, with higher resolution (0.1 mm steps) in the high gradient region near the source. An in-house built accessory was used to bypass the INTRABEAM interlock system, allowing measurements with the bare probe. Both detectors were connected to appropriate electrometers: a PTW UNIDOS E for the ionization chamber and a Wellhöfer CU500E or

Keithley 6517A for the microDiamond detector. The use of different electrometers for the microDiamond allowed for cross-validation of the measurement system.

3.3.2 Comparison with Monte Carlo simulations

To validate the computational model, the MC simulations of depth-dose curves along the source axis were compared with experimental measurements. Statistical analysis of the differences between measured and simulated doses was performed, considering the uncertainties associated with both the measurements and the MC simulations.

For the ionization chamber, the MC-calculated dose to the chamber's sensitive volume was compared directly with the measured charge, which was converted to dose using appropriate calibration and correction factors. For the microDiamond detector, a more complex approach was necessary due to the energy dependence of the detector response in the low-energy range. MC simulations were performed to calculate both the dose to a small volume of water and the dose to the diamond in the detector's sensitive volume. A correction factor, $C^{\mathrm{w}}_{\mathrm{dia}}$, was derived as the ratio of these doses:

$$C^{\mathrm{w}}_{\mathrm{dia}}(z) = \frac{D_{\mathrm{w}}(z)}{D_{\mathrm{dia}}(z)} \tag{3.2}$$

where $D_{\mathrm{w}}(z)$ and $D_{\mathrm{dia}}(z)$ are the doses to water and diamond, respectively, at depth z. This factor was then applied to the microDiamond measurements to obtain water-equivalent dose values for comparison with MC simulations.

Uncertainty analysis

The validation analysis considered combined standard uncertainties (k = 1) that include both type A (statistical) and type B (systematic) components. For measurements with the PTW 34013 ionization chamber, type A uncertainties correspond to the standard deviation of the mean of three consecutive readings at each detector position (0.02% and 0.09% at 10 and 40 mm, respectively). Type B uncertainties are dominated by positioning uncertainty ($\pm$0.1 mm in the Zeiss water phantom), which affects the dose reading differently depending on the gradient at each depth. The resulting positioning uncertainties were 2.2% and 0.7% at 10 and 40 mm, respectively.

For the microDiamond detector measurements, type A uncertainties from repeated readings averaged 0.2% and 0.3% at 10 and 40 mm, respectively. Type B uncertainties were higher for this setup due to the manual positioning in the Wellhöfer water phantom ($\pm$0.5 mm precision), resulting in positioning uncertainties of 14% and 4.8% at 10 and 40 mm, respectively, averaged for both detectors.

For MC calculations with the ionization chamber, type A uncertainties from statistical fluctuations were 2.4% and 3.6% at 10 and 40 mm, with additional type B uncertainties (2.0% and 0.9% at the same depths) arising from chamber plate separation tolerances. The total combined uncertainties (k = 1) for the ionization chamber calculations were thus 3.1% and 3.7% at these evaluation points. For the microDiamond detector calculations, statistical uncertainties were lower (0.7% and 1.0% at 10 and 40 mm), with negligible geometric uncertainties due to the detector's well-defined and validated construction.

3.4 Results and validation

This section presents the results of our Monte Carlo (MC) simulations and their validation against experimental measurements. We will examine the depth-dose characteristics, radial dose function, and 2D anisotropy function of the INTRABEAM source.

3.4.1 Monte Carlo model validation

The validation of our MC model involved comparing simulated depth-dose curves with measurements obtained using both the PTW 34013 ionization chamber and the PTW TN60019 microDiamond detector.

Ionization chamber measurements

Figure 3.9 presents the comparison between MC-calculated depth doses and measurements using the PTW 34013 ionization chamber in the Zeiss water phantom. Two INTRABEAM sources (denoted as *Source 1* and *Source 2*) were used in this test. Depth dose curves were normalized to unity at a reference +depth of 10 mm.

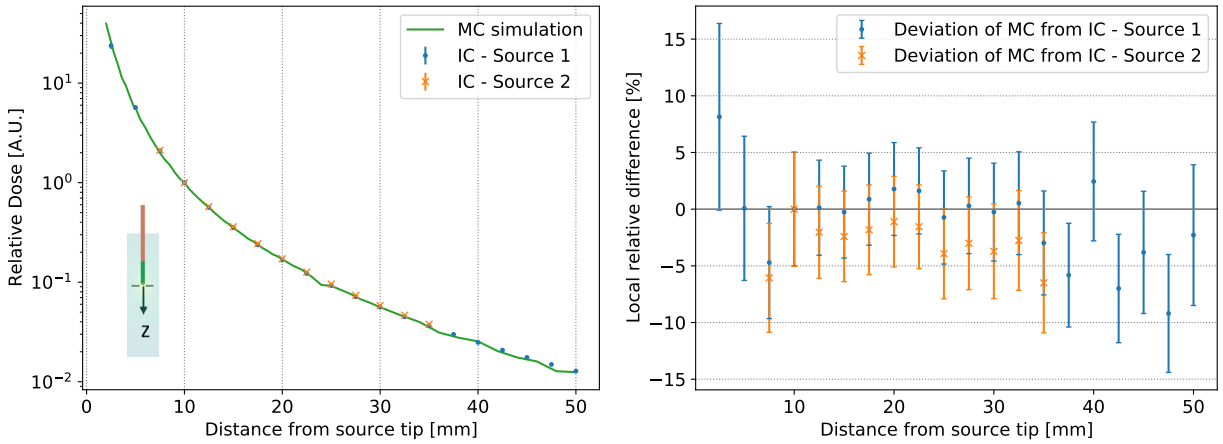

(a) (b)

Figure 3.9 Comparison of MC-calculated and measured depth doses using the PTW 34013 ionization chamber. (a) Depth-dose curves for the INTRABEAM source normalized at 10 mm depth. MC calculations are compared with measurements from two different INTRABEAM sources (*Source 1* and *Source 2*). The inset shows the measurement geometry, where z indicates the distance from the source tip along the probe's longitudinal axis. (b) Local relative differences between MC simulations and measurements for both sources. Figure reproduced from [2].

The results show good agreement between MC calculations and measurements, particularly at depths beyond 10 mm from the source tip. For *Source 1*, MC calculations exhibit local relative differences from measurements of up to 9% at depths beyond 10 mm. In this region, absolute differences varied from -0.2% to 0.3% of the value at the reference point. For *Source 2*, local relative differences between our MC calculations and the measurements reached

up to 6% in the water depth range of 7.5 to 35 mm. Beyond 10 mm distances from the source, absolute differences varied within the range 0.1% to 1.2%. Larger discrepancies were observed closer to the source tip. Measurements exhibited a relative difference of up to 8% at 2.5 mm depth from *Source 1* and 6% for *Source 2* at 7.5 mm. These differences can be attributed to the steep dose gradient in this region, which amplifies the impact of small positioning uncertainties and volume-averaging effects.

The comparison between measurements from two different INTRABEAM sources (*Source 1* and *Source 2*) revealed some variations in output, consistent with previous reports in the literature [9, 24]. These differences likely result from minor variations in source manufacturing, particularly in components critical to x-ray beam generation, such as the gold target thickness and shape and the electron beam characteristics.

Diamond detector measurements

Figure 3.10 shows the comparison between MC calculations and measurements using the PTW TN60019 microDiamond detector in the Wellhöfer water phantom. These measurements were performed using *Source 1*, the same source used for one set of the ionization chamber measurements, with two different microDiamond detectors (denoted as *microD1* and *microD2*) to ensure measurement reproducibility.

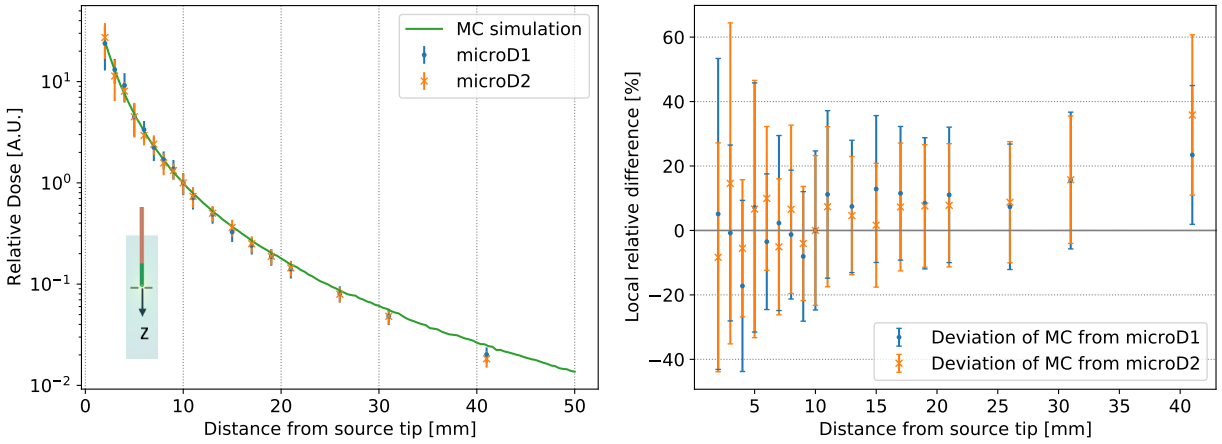

(a) (b)

Figure 3.10 Comparison of MC-calculated and measured depth doses using the PTW TN60019 microDiamond detector with INTRABEAM *Source 1*. (a) Depth-dose curves for the INTRABEAM source normalized at 10 mm depth. Results from two microDiamond detectors are shown. The inset shows the measurement geometry, where z indicates the distance from the source tip along the probe's longitudinal axis, identical to the ionization chamber measurements. (b) Local relative differences between MC simulations and measurements for both detectors. Figure reproduced from [2].

The microDiamond measurements showed agreement with MC simulations within the estimated uncertainties across the entire range of measured depths. The relative deviations of the calculations from the measurements at points located less than 10 mm from the source tip, along the source axis, exhibit average values of 6% for the

microDiamond detector. This improved agreement compared to the ionization chamber results can be attributed to the smaller sensitive volume of the microDiamond detector, which reduces volume averaging effects in regions of steep dose gradients.

3.4.2 Radial dose function

The MC-calculated radial dose function, $g_p(r)$, for the INTRABEAM source is presented in Figure 3.11, along with comparative data for other commonly used brachytherapy sources.

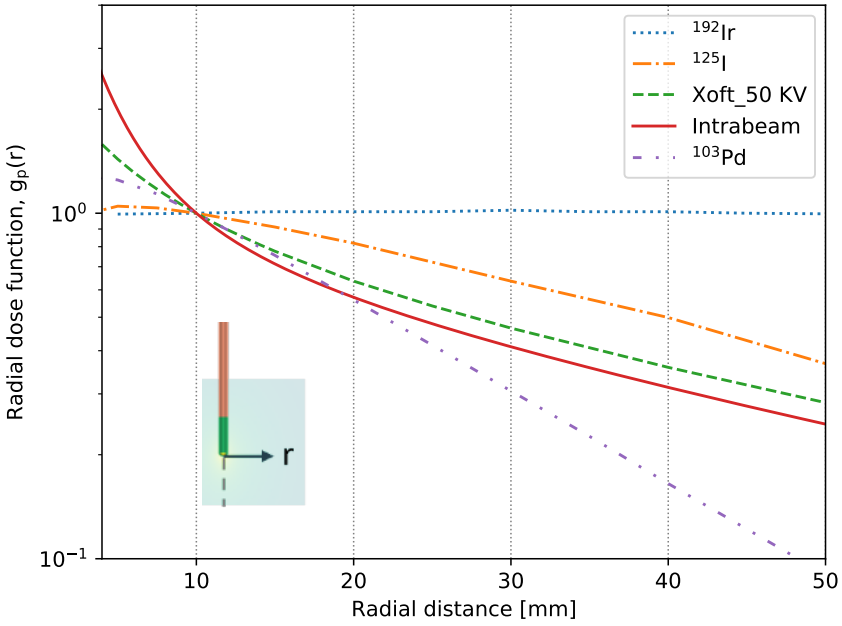

Figure 3.11 Radial dose function of the INTRABEAM source compared to the Xoft source operated at 50 kV (data from Hiatt et al. (2015) [20]) and common brachytherapy sources ^{192}Ir, ^{125}I, and ^{103}Pd (data from Rivard et al. (2004) [25]). The inset shows the geometry for the radial dose function calculation, where r indicates the radial distance from the source tip, measured perpendicular to the probe's longitudinal axis ($\theta = 90°$). The INTRABEAM exhibits a steeper gradient near the source compared to conventional radionuclide sources. Figure reproduced from [2].

The INTRABEAM source exhibits a notably steeper dose fall-off close to the source surface compared to conventional brachytherapy radionuclides. The gradient is particularly pronounced within the first 10 mm from the source, with $g_p(r)$ values of 2.510, 1.645, and 1.232 at 4, 6, and 8 mm, respectively. Beyond approximately 20 mm, the fall-off becomes more gradual, resembling that of the Xoft Axxent electronic brachytherapy source and ^{125}I. The Type A uncertainties (k = 1) of the MC simulations varied from 0.013% to 0.018% at radial distances of 0.2 cm to 5 cm. The complete set of radial dose function data is provided in Table 3.2 in Appendix 3.5.

3.4.3 2D anisotropy function

The 2D anisotropy function, $F(r, \theta)$, MC-calculated for the INTRABEAM source is shown in Figure 3.12. This function characterizes the angular variation of dose around the source at different radial distances.

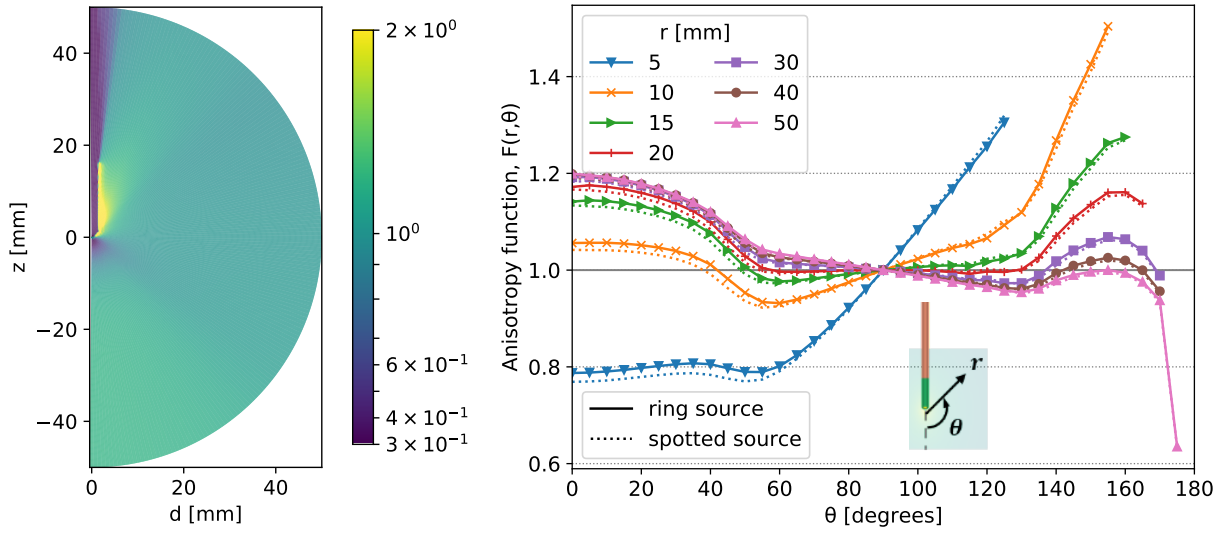

(a) (b)

Figure 3.12 2D anisotropy function for the INTRABEAM source. (a) Color map representation of the anisotropy function using the ring-shaped source model. (b) Anisotropy function curves at various distances from the source tip for the ring-shaped source model (solid lines) and the spotted-shaped source model (dotted lines). The inset shows the geometry for the anisotropy calculations, where r indicates the radial distance from the source tip and θ represents the polar angle measured from the probe's longitudinal axis. Figure reproduced from [2].

Figure 3.12(a) presents a color map of the anisotropy function, revealing significant variations in dose distribution around the source. The anisotropy is particularly pronounced in regions close to the probe walls. Deviations from isotropy of up to 55% were observed at 10 mm from the source tip and 155°. This substantial anisotropy near the source surface gradually diminishes with increasing distance, reflecting the complex interplay between the source geometry and the low-energy photon interactions. The anisotropy function exhibits several notable features. Two main regions of higher intensity are observed towards the distal and proximal directions of the source, separated by a region of lower intensity in the range $\theta \approx [55°, 130°]$. This pattern likely results from the primary beam transmission at the gold target and the back-scattered component, respectively. The distribution is influenced by the radii of incidence of the electron beam onto the hemispherical target after internal deflection. It's worth noting that the reference line for the 2D anisotropy function ($\theta = 90°$) was set on the plane traversing the source tip, not on the plane traversing the effective photon source position. The effective source is located inside the gold target hemisphere, a few millimeters above the source tip. This choice of reference affects the observed anisotropy, particularly in the proximity of the source end towards the distal direction.

Figure 3.12(b) presents a comparison of the 2D anisotropy functions obtained from the ring-shaped and spotted-shaped source models. The results demonstrate a remarkably similar behavior between the two models, with relative differences not exceeding 0.3% towards the central axis of the source probe. This close agreement suggests that the macroscopic dose distribution is not significantly affected by the specific details of the electron beam model as long as the overall spatial distribution of electron impact on the target is accurately represented. The consistency between these two distinct approaches to modeling the electron beam provides additional confidence in the robustness of our MC simulations. It also suggests that the simplified ring-shaped model may be sufficient for most clinical dosimetry applications of the INTRABEAM source.

The full dataset for the 2D anisotropy function, based on the ring-shaped source model, is provided in Table 3.3 in Appendix 3.5.

3.5 Discussion of initial findings

The results presented in this chapter provide a comprehensive characterization of the INTRABEAM bare probe using Monte Carlo simulations and experimental validation. While these findings offer valuable insights into the dosimetric properties of the INTRABEAM source, they also highlight areas requiring further investigation, many of which are addressed in the following chapters.

The validation of our Monte Carlo model against experimental measurements demonstrated good agreement, particularly at distances beyond 10 mm from the source tip. The observed discrepancies in the high-gradient region close to the source underscore the challenges in accurately measuring and simulating dose distributions for low-energy X-ray sources. The improved agreement observed with the microDiamond detector compared to the ionization chamber emphasizes the need for high-resolution dosimetry techniques and careful consideration of detector characteristics in experimental measurements in steep dose gradient regions.

The PTW 34013 ionization chamber measurements, while valuable for validation, were subject to geometric uncertainties that warrant careful consideration. The chamber's plate separation tolerance, which cannot be precisely known for individual chambers, introduces uncertainties in Monte Carlo calculations. These geometric uncertainties contributed to the type B uncertainties in our simulations (2.0% at 10 mm depth). Our approach of combining measurements from both ionization chamber and microDiamond detectors helped mitigate the impact of these geometric uncertainties on model validation. The microDiamond detector's well-defined geometry and smaller sensitive volume provided complementary validation data less affected by geometric uncertainties, particularly in high-gradient regions.

The radial dose function of the INTRABEAM source exhibits a notably steeper gradient compared to conventional brachytherapy radionuclides, especially within the first 10 mm from the source. This characteristic, primarily due to the low-energy photon spectrum, has important clinical implications for dose localization and sparing of surrounding tissues. However, it also necessitates careful treatment planning and precise source positioning. These considerations become even more critical when applicators are used, as explored in Chapter 4 of this thesis.

The 2D anisotropy function reveals significant variations in dose distribution around the source, with deviations from isotropy of up to 55% at 10 mm and 155°. This pronounced anisotropy, more significant than that typically observed in conventional brachytherapy sources, emphasizes the need for accurate 3D dose calculations in treatment

planning. The comparison between ring-shaped and spotted-shaped source models suggests that a simplified ring-shaped model may be sufficient for most clinical scenarios. However, this finding warrants further investigation in the context of different applicator geometries, as addressed in subsequent chapters.

While the TG-43 parameters derived in this study provide a comprehensive dataset for characterizing the INTRABEAM bare probe, it is important to recognize the limitations of the TG-43 formalism when applied to low-energy electronic brachytherapy sources. The assumption of a homogeneous water medium in TG-43 may lead to inaccuracies in dose calculations, particularly in heterogeneous tissues or near material interfaces [26]. Chapter 5 of this thesis directly addresses this limitation by evaluating the effect of different dosimetry formalisms, including Monte Carlo simulations in heterogeneous media, on organ-at-risk doses in intraoperative radiotherapy for glioblastoma.

The findings of this initial study have several implications for clinical practice in intraoperative radiotherapy applications. While the INTRABEAM system is not used without any applicator in clinical settings, there are specialized applications that employ minimal applicators, such as needle applicators for spinal treatments [27]. However, for the majority of clinical applications, including those in brain and breast cancer treatments, the INTRABEAM system is used with more substantial applicators. In our research, we focused specifically on spherical applicators, which are required for adapting the treatment to specific clinical scenarios. These applicators significantly modify the dose distribution from that of the bare probe. Therefore, while the characterization of the bare probe provides essential foundational knowledge, the dosimetric parameters calculated for the INTRABEAM system with spherical applicators, as presented in subsequent chapters, offer more clinically relevant data for treatment planning and dose calculations in IORT.

The current clinical standard for INTRABEAM dosimetry in many applications, including the INTRAGO trial for glioblastoma treatment, relies on the TARGIT method. However, this method has limitations in accounting for the full 3D dose distribution and tissue heterogeneities. Chapter 6 of this thesis addresses these limitations by evaluating the TG-43 formalism as a potential alternative to the TARGIT standard in IORT of glioblastoma, building upon the foundational work presented in this chapter.

In conclusion, this initial characterization of the INTRABEAM source using Monte Carlo simulations and experimental validation provides valuable insights into its dosimetric properties and sets the stage for the more advanced investigations presented in subsequent chapters. The derived TG-43 parameters for the bare probe offer a foundation for improved dose calculations while also highlighting areas requiring further investigation. The following chapters build upon this work, addressing the limitations identified here and extending the analysis to more clinically relevant scenarios, ultimately contributing to improved accuracy in dose delivery for intraoperative radiotherapy applications.

Appendix

Table 3.2 Radial dose function data, $g_p(r)$, for the INTRABEAM source calculated using the TG-43 point-source model. Type A uncertainties are included.

r (mm)	$g_{\mathrm{p}}(r)$	uncertainty (%)
2	4.782	0.013
4	2.510	0.012
6	1.645	0.011
8	1.232	0.010
10	1.000	0.009
12	0.854	0.009
14	0.753	0.010
16	0.678	0.010
18	0.619	0.010
20	0.571	0.010
22	0.530	0.011
24	0.495	0.011
26	0.464	0.012
28	0.436	0.012
30	0.411	0.012
32	0.388	0.013
34	0.367	0.013
36	0.348	0.014
38	0.330	0.014
40	0.313	0.015
42	0.298	0.015
44	0.283	0.016
46	0.270	0.016
48	0.257	0.017
50	0.245	0.018

Table 3.3 2D anisotropy function data, $F(r,\theta)$, for the INTRABEAM source using the ring-shaped source model. 'NA' indicates points inside the source where $F(r,\theta)$ is not determined.

	Radial distance from the source tip, r [mm]								
Polar angle, θ ($^\circ$)	2	4	6	8	10	20	30	40	50
0	0.394	0.686	0.868	0.982	1.056	1.172	1.192	1.199	1.199
5	0.395	0.686	0.869	0.983	1.056	1.175	1.192	1.195	1.196
10	0.399	0.689	0.870	0.984	1.057	1.172	1.189	1.192	1.192
15	0.404	0.693	0.873	0.984	1.055	1.167	1.183	1.186	1.187
20	0.410	0.699	0.875	0.983	1.052	1.160	1.175	1.178	1.179
25	0.417	0.706	0.876	0.981	1.047	1.150	1.165	1.168	1.169
30	0.428	0.712	0.877	0.977	1.040	1.138	1.152	1.155	1.156
35	0.441	0.718	0.876	0.970	1.029	1.122	1.136	1.139	1.140
40	0.453	0.721	0.869	0.957	1.012	1.099	1.114	1.118	1.120
45	0.467	0.721	0.854	0.933	0.982	1.064	1.080	1.087	1.091
50	0.485	0.721	0.840	0.910	0.953	1.029	1.048	1.057	1.064
55	0.509	0.728	0.834	0.895	0.934	1.004	1.024	1.035	1.043
60	0.541	0.746	0.842	0.897	0.932	0.997	1.016	1.026	1.034
65	0.584	0.775	0.860	0.909	0.939	0.996	1.013	1.022	1.028
70	0.640	0.811	0.884	0.925	0.950	0.997	1.010	1.018	1.022
75	0.707	0.852	0.911	0.942	0.962	0.999	1.008	1.014	1.017
80	0.786	0.898	0.939	0.961	0.975	1.000	1.006	1.009	1.012
85	0.883	0.947	0.969	0.981	0.988	1.000	1.003	1.005	1.006
90	1.000	1.000	1.000	1.000	1.000	1.000	1.000	1.000	1.000
95	NA	NA	1.031	1.019	1.012	1.000	0.997	0.995	0.994
100	NA	NA	1.063	1.037	1.023	1.000	0.993	0.990	0.988
105	NA	NA	1.094	1.057	1.035	0.998	0.989	0.985	0.982
110	NA	NA	1.127	1.076	1.046	0.996	0.984	0.979	0.976
115	NA	NA	1.159	1.093	1.054	0.992	0.980	0.974	0.969
120	NA	NA	1.187	1.107	1.066	0.997	0.979	0.970	0.965
125	NA	NA	1.235	1.148	1.093	0.996	0.973	0.963	0.957
130	NA	NA	1.318	1.191	1.119	1.001	0.973	0.961	0.954
135	NA	NA	1.440	1.270	1.178	1.026	0.988	0.971	0.962
140	NA	NA	NA	1.389	1.268	1.070	1.018	0.994	0.979
145	NA	NA	NA	1.503	1.351	1.107	1.041	1.009	0.990
150	NA	NA	NA	NA	1.425	1.135	1.056	1.019	0.997
155	NA	NA	NA	NA	1.504	1.160	1.068	1.026	1.000
160	NA	NA	NA	NA	NA	1.161	1.064	1.020	0.994
165	NA	NA	NA	NA	NA	1.138	1.040	1.000	0.976
170	NA	NA	NA	NA	NA	NA	0.989	0.956	0.938
175	NA	NA	NA	NA	NA	NA	NA	NA	0.635

References

[1] D. S. Ayala Alvarez, "Dosimetric studies on the INTRABEAM electronic brachytherapy source," M.S. thesis, McGill University Libraries, 2020.

[2] D. S. Ayala Alvarez, P. G. F. Watson, M. Popovic, V. J. Heng, M. D. C. Evans, and J. Seuntjens, "Monte Carlo calculation of the relative TG-43 dosimetry parameters for the INTRABEAM electronic brachytherapy source," *Physics in Medicine and Biology*, vol. 65, no. 24, p. 245 041, 2020.

[3] M. Dinsmore *et al.*, "A new miniature x-ray source for interstitial radiosurgery: Device description," *Medical Physics*, vol. 23, no. 1, pp. 45–52, 1996.

[4] J. C. Yanch and K. J. Harte, "Monte Carlo simulation of a miniature, radiosurgery x-ray tube using the ITS 3.0 coupled electron-photon transport code," *Medical Physics*, vol. 23, no. 9, pp. 1551–1558, 1996.

[5] O. Nwankwo, S. Clausen, F. Schneider, and F. Wenz, "A virtual source model of a kilovoltage radiotherapy device," *Physics in Medicine & Biology*, vol. 58, no. 7, pp. 2363–2375, 2013.

[6] P. Watson, "Dosimetry of a miniature x-ray source used in intraoperative radiation therapy," Ph.D. thesis, McGill University Libraries, 2019.

[7] S. Clausen *et al.*, "A Monte Carlo based source model for dose calculation of endovaginal TARGIT brachytherapy with INTRABEAM and a cylindrical applicator," *Zeitschrift Fur Medizinische Physik*, vol. 22, no. 3, pp. 197–204, 2012.

[8] D. S. Biggs and E. S. Thomson, "Radiation properties of a miniature X-ray device for radiosurgery," *The British Journal of Radiology*, vol. 69, no. 822, pp. 544–547, 1996.

[9] F. Moradi *et al.*, "Monte Carlo skin dose simulation in intraoperative radiotherapy of breast cancer using spherical applicators," *Physics in Medicine and Biology*, vol. 62, no. 16, pp. 6550–6566, 2017.

[10] A. Abudra'a, B. Chauvenet, J. Gouriou, J. Plagnard, R. Itti, and I. Aubineau-Lanièce, "Dosimetry formalism and calibration procedure for electronic brachytherapy sources in terms of absorbed dose to water," *Physics in Medicine and Biology*, vol. 65, no. 14, p. 145 006, 2020.

[11] P. Sievers, T. Schneider, T. Michel, and G. Anton, "X-ray spectroscopy with photon counting imaging detectors such as Timepix," in *2011 IEEE nuclear science symposium conference record*, IEEE, 2011, pp. 1826–1828.

[12] T. Schneider, "Towards reference dosimetry of electronic brachytherapy sources," 2017.

[13] P. G. F. Watson, M. Popovic, and J. Seuntjens, "Determination of absorbed dose to water from a miniature kilovoltage x-ray source using a parallel-plate ionization chamber," *Physics in Medicine and Biology*, vol. 63, no. 1, p. 015 016, 2017.

[14] M. J. P. Chamberland, R. E. P. Taylor, D. W. O. Rogers, and R. M. Thomson, "Egs_brachy: A versatile and fast Monte Carlo code for brachytherapy," *Physics in Medicine & Biology*, vol. 61, no. 23, pp. 8214–8231, 2016.

[15] D. Bote and F. Salvat, "Calculations of inner-shell ionization by electron impact with the distorted-wave and plane-wave Born approximations," *Physical Review A*, vol. 77, no. 4, p. 042 701, 2008.

[16] I. Kawrakow and D. W. O. Rogers, "The EGSnrc code system: Monte Carlo simulation of electron and photon transport," National Research Council Canada, Ottawa, Canada, Tech. Rep. PIRS-701, 2019.

[17] M. J. Berger *et al.*, "XCOM: Photon cross sections database (version 1.5). [Online] available: Http://physics.nist.gov/xcom (accessed september 2020)," *National Institute of Standards and Technology, Gaithersburg, MD*, 2010.

[18] E. Mainegra-Hing, D. Rogers, R. Townson, B. Walters, F. Tessier, and I. Kawrakow, "The EGSnrc g application," National Research Council Canada, Ottawa, Canada, Tech. Rep. PIRS-3100, 2020.

[19] M. J. Rivard, S. D. Davis, L. A. DeWerd, T. W. Rusch, and S. Axelrod, "Calculated and measured brachytherapy dosimetry parameters in water for the Xoft Axxent X-Ray Source: An electronic brachytherapy sourcea)," *Medical Physics*, vol. 33, no. 11, pp. 4020–4032, 2006.

[20] J. R. Hiatt, S. D. Davis, and M. J. Rivard, "A revised dosimetric characterization of the model S700 electronic brachytherapy source containing an anode-centering plastic insert and other components not included in the 2006 model," *Medical Physics*, vol. 42, no. 6Part1, pp. 2764–2776, 2015.

[21] PTW-Freiburg, "Ionizing radiation detectors – including codes of practice, D165.229.00/11. Available at: Http://biowel.com/pdf/PTW/Detectors.pdf (accessed july 2019)," manual, 2018.

[22] M. Marinelli, G. Prestopino, C. Verona, and G. Verona-Rinati, "Experimental determination of the PTW 60019 microDiamond dosimeter active area and volume," *Medical physics*, vol. 43, no. 9, pp. 5205–5212, 2016.

[23] Carl Zeiss Meditec AG, "INTRABEAM water phantom – instructions for use, G-30-1767-en version 5.0," manual, 2015.

[24] K. S. Armoogum, J. M. Parry, S. K. Souliman, D. G. Sutton, and C. D. Mackay, "Functional intercomparison of intraoperative radiotherapy equipment–Photon radiosurgery system," *Radiation Oncology*, vol. 2, no. 1, p. 11, 2007.

[25] M. J. Rivard *et al.*, "Update of AAPM Task Group No. 43 Report: A revised AAPM protocol for brachytherapy dose calculations," *Medical Physics*, vol. 31, no. 3, pp. 633–674, 2004.

[26] L. Beaulieu *et al.*, "Report of the Task Group 186 on model-based dose calculation methods in brachytherapy beyond the TG-43 formalism: Current status and recommendations for clinical implementation," *Medical physics*, vol. 39, no. 10, pp. 6208–6236, 2012.

[27] P. Krauss *et al.*, "Intraoperative radiotherapy combined with spinal stabilization surgery—a novel treatment strategy for spinal metastases based on a first single-center experiences," *Journal of Neuro-Oncology*, vol. 168, no. 3, pp. 445–455, 2024.

Chapter 4

Monte Carlo calculation of the TG-43 dosimetry parameters for the INTRABEAM source with spherical applicators

David Santiago Ayala Alvarez, Peter G. F. Watson, Marija Popovic, Veng Jean Heng, Michael D. C. Evans and Jan Seuntjens

Article published in: *Physics in Medicine & Biology*, **66**(21):215017, 2021

4.1 Preface

The spherical applicators are crucial components of the INTRABEAM system, designed to modify and optimize the dose distribution for intraoperative radiotherapy (IORT) treatments. These hollow spherical shells, when placed over the source probe, serve multiple purposes in beam modification and dose delivery. They physically expand the treatment surface to match the geometry of the surgical cavity while providing a more uniform dose distribution around the applicator surface. The applicator material attenuates and hardens the beam by preferentially removing low-energy photons, which helps reduce the steep dose gradient characteristic of the bare probe. In smaller applicators (15-30 mm diameter), an additional aluminium filter further hardens the beam, improving the penetration characteristics for treating deeper tissues. This combination of geometric expansion and beam modification enables

the delivery of a more homogeneous dose to the target tissue while maintaining the rapid dose fall-off beyond the treatment volume that is desirable for OAR sparing.

This chapter builds on the foundational work presented in Chapter 3, shifting the focus from the bare probe to the clinically relevant configuration of the INTRABEAM system with spherical applicators. While the previous chapter established the methodology for characterizing the bare probe using the TG-43 protocol, this work extends that approach to include all available spherical applicator sizes, addressing a critical need in clinical practice. The comprehensive set of TG-43 parameters presented here enables accurate three-dimensional dose calculations within existing brachytherapy treatment planning frameworks, setting the stage for the clinical evaluations described in subsequent chapters.

During review of the thesis, it was noted that our methodology for air-kerma rate calculations differs from primary standard measurement conditions. Specifically, while the NIST standard for electronic brachytherapy sources employs collimation to reduce scattered radiation contributions, our Monte Carlo simulations used an annular scoring region at 50 cm around the source tip without explicit collimation. This methodological difference could affect the calculated dose-rate conversion coefficients by an amount that remains to be quantified. This limitation is further discussed in Chapter 7.

The uncertainty analysis presented in Table 4.2 could be expanded to include additional Monte Carlo uncertainty components as outlined in the AAPM TG-138 report [1]. These might include uncertainties associated with source emissions modeling, radiation transport code implementation, cross-section data, and scoring algorithms. While our analysis focused on the dominant uncertainties for our specific setup (statistical uncertainty and applicator geometry tolerances), a more comprehensive uncertainty budget considering these additional components could provide further insight into the overall accuracy of the calculations.

It should be noted that while our Monte Carlo calculations were validated against measurements of depth dose curves along the source axis, we did not perform experimental validation of calculated dose rates at the TG-43 reference position (1 cm from the applicator surface at 90 degrees). This reference position, lying in the transverse plane at the level of the source tip, was not directly accessible in our measurement setup. Future work could benefit from additional experimental validation at this reference position, though such measurements would require careful consideration of positioning accuracy given the steep dose gradients characteristic of the INTRABEAM system.

4.2 Abstract

The relative TG-43 dosimetry parameters of the INTRABEAM (Carl Zeiss Meditec AG, Jena, Germany) bare probe were recently reported by Ayala Alvarez et al. [2]. The current study focuses on the dosimetry characterization of the INTRABEAM source with the eight available spherical applicators according to the TG-43 formalism using Monte Carlo (MC) simulations. This report includes the calculated dose-rate conversion coefficients that determine the absolute dose rate to water at a reference point of 10 mm from the applicator surface, based on calibration air-kerma rate measurements at 50 cm from the source on its transverse plane. Since the air-kerma rate measurements are not yet provided from a standards laboratory for the INTRABEAM, the values in the present study were calculated with MC. This approach is aligned with other works in the search for standardization of the dosimetry of electronic brachytherapy sources. As a validation of the MC model, depth dose calculations along the source axis

were compared with calibration data from the source manufacturer. The calculated dose-rate conversion coefficients were 434.0 for the bare probe, and 683.5, 548.3, 449.9, 376.5, 251.0, 225.6, 202.8, and 182.6 for the source with applicators of increasing diameter from 15 to 50 mm, respectively. The radial dose and the 2D anisotropy functions of the TG-43 formalism were also obtained and tabulated in this document. This work presents the data required by a treatment planning system for the characterization of the INTRABEAM system in the context of intraoperative radiotherapy applications.

4.3 Introduction

During the last two decades, the INTRABEAM system (Carl Zeiss Meditec AG, Jena, Germany) and the Xoft Axxent® (iCAD, Inc. Nashua, NH) have been the most utilized electronic brachytherapy (eBT) sources [3]. The INTRABEAM has been extensively used for breast intraoperative radiotherapy (IORT), with TARGIT trials as some of the best known published clinical trials [4]. Clinical trials are still underway to show impact of INTRABEAM IORT in the setting of brain irradiation of glioblastoma multiforme surgical cavity [5, 6].

The INTRABEAM system features a miniature electron accelerator where low-energy x-ray photons are produced after the electrons strike a gold target. The INTRABEAM source is used with clinical applicators that vary in shape and size, depending on clinical application. Spherical INTRABEAM applicators are most widely used in IORT settings. They are available in different sizes ranging in diameter from 15 to 50 mm in steps of 5 mm (described by Eaton 2012 [7]).

In current clinical practice, the dosimetry of the INTRABEAM relies on calibration depth dose data provided by the manufacturer. The calibration curves for the bare source probe are measured in water along the probe axis. In addition, depth-specific transfer functions are provided, and they convert bare probe data to depth dose curves for each applicator. Independent dosimetry methods for the INTRABEAM that are feasible in the clinical workflow have been proposed but a consensus dosimetry protocol, with traceability to a primary standards dosimetry laboratory (PSDL), is yet to be developed. In this context, the National Institute of Standards and Technology (NIST) initiated a new primary standard to be applied to eBT sources [8]. The NIST standard has been used to calibrate the Xoft Axxent source [9] based on a modification of the American Association of Physicists in Medicine (AAPM) Task Group No. 43 Report (TG-43) [10] and its updated version (TG-43U1) [11]. With this variation, the absorbed dose at a reference point in water is obtained from the air-kerma rate measured at 50 cm from the source axis in a PSDL using a dose-rate conversion coefficient [12]. Well chambers have been accepted and calibrated as transfer instruments that permit the transfer of air-kerma rate measurements to secondary calibration facilities, making the standards viable for clinical use [8, 12]. Currently, there is no accepted air-kerma-based primary standard for the INTRABEAM system. In parallel to the NIST research, an approach in terms of absorbed dose to water has been developed at the National Metrology Institute of Germany (PTB) [13]. With this method, the dose to water at a reference depth of 10 mm, along the source axis, is obtained from calibration air-kerma measurements at reference conditions. Abudra'A et al. [14] reported the results of the PTB standard evaluated in the INTRABEAM system with a spherical applicator of 40 mm diameter. A different approach has been developed by Watson et al. [15–17] in which a depth-dependent Monte Carlo (MC) calculated factor, C_Q, converts air-kerma rates obtained with an air-kerma calibrated ionization chamber (PTW 34013) to absorbed dose to water.

During the IORT workflow with INTRABEAM, treatment times and dose to critical structures are determined based on the tabulated calibration data, the prescription dose, and the distance from applicator surface [18, 19]. This approach provides a 1D dose distribution and assumes isotropic dose falloff. However, accurate 3D dose distributions accounting for the source polar anisotropy are required in order to assess the relative dose contributions of IORT and complementary techniques. In this context, Shamsabadi et al. [20] have modeled the INTRABEAM source with spherical applicators using GEANT4 and evaluated the polar anisotropy in dose distribution at 10 mm from the applicators' surface. They have also assessed the impact of such applicators on the spectral and dosimetric characteristics of the x-ray beam. A convenient alternative for 3D dose calculations with eBT sources would be to explore their similarity to radionuclide brachytherapy sources and characterize the eBT source according to the AAPM TG-43 protocol. TG-43-based treatment planning systems (TPS) are fast and available in most clinics offering brachytherapy with radionuclides. The TG-43 formalism was previously used to characterize the Xoft Axxent source [21, 22]. For the INTRABEAM, relative TG-43 parameters were recently reported for the bare probe [2].

The aim of this work is to characterize the INTRABEAM source with spherical applicators according to the TG-43 formalism using MC simulations. A complete set of TG-43 data of the INTRABEAM will permit 3D dose distribution calculations within the treatment planning framework that exists for brachytherapy with radionuclides. Moreover, it will provide a means of assessing cumulative dose distributions of IORT and external beam radiotherapy on patient's 3D images.

4.4 Materials and Methods

4.4.1 INTRABEAM source and spherical applicators

The INTRABEAM system contains a miniature x-ray source where electrons are accelerated towards a 0.5 μm thick gold target situated on the inner surface of an evacuated 100 mm long, 3.2 mm outer diameter needle [23, 24]. The electron source spectrum exhibits a Gaussian distribution of energy centered at 50 keV and full width at half maximum (FWHM) of 5 keV [25]. Following the interaction of electrons with the target, x-rays are produced by fluorescence and bremsstrahlung. Clinical use of the system is usually carried out with a nominal 50 kV tube voltage and a current of 40 μA. A MC model of the INTRABEAM source probe was previously developed and validated by Watson et al. 2017, 2018, 2019, and the relative TG-43 parameters for the system's bare probe were obtained [2]. In this work, the specifications for source geometry and materials were reproduced using the `egs++` library [26] of EGSnrc. The electron beam was modeled as two concentric rings of radii 0.6 to 0.7 mm and 0.7 to 0.8 mm, with weighting factors of 1.05 and 1.55, respectively [25].

MC simulations of the dose distributions in water using the INTRABEAM system with spherical applicators were performed. These applicators were placed on the INTRABEAM source with the source tip at the sphere center. The bulk material of the applicators is a biocompatible polyetherimide called ULTEM [27] with a nominal mass density of 1.27 g/cm^3. The smallest applicators with diameters of 15 to 30 mm include an aluminium (Al) filter to provide a degree of beam hardening by preferentially absorbing low-energy photons. Simulated applicator geometries with their materials are shown in figure 4.1(b) for a 40 mm diameter applicator, and in (c) for the smallest 15 mm diameter applicator. Detailed dimensions and material compositions were provided by Zeiss and are propri-

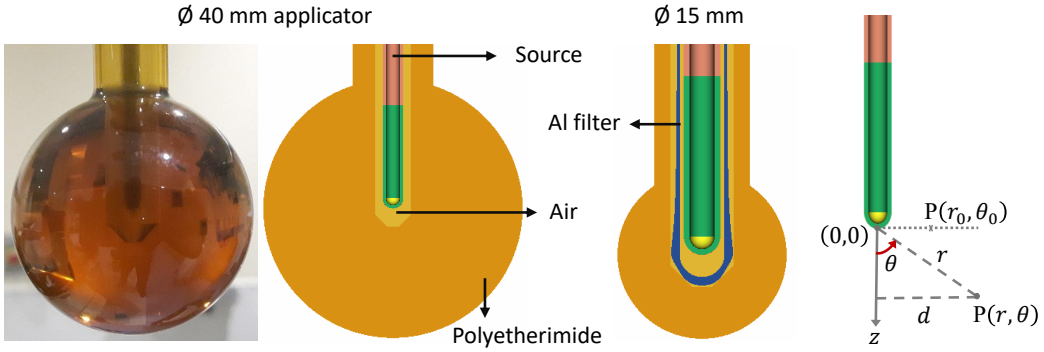

(a) (b) (c) (d)

Figure 4.1 Rendering of the spherical applicators models for the MC simulations. In (a), a picture of the 40 mm diameter applicator is compared with its simulation geometry shown in (b). In (c), the 15 mm applicator rendering is presented as an example of the smallest applicators, with sphere diameters from 15 to 30 mm, which include an aluminium filter. (d) shows the reference coordinate system used for determining the TG-43 parameters for the INTRABEAM source.

etary. The water phantom and annular scoring volumes were the same as presented by Ayala Alvarez et al. (2020) [2] for simulations of the bare probe. The dose distribution was obtained outside the applicator volume and partial volume effects in voxels at the applicator surface were corrected following the procedure described by Clausen et al. (2012) [25].

4.4.2 Radiation transport parameters

Monte Carlo simulations were performed using `egs_brachy` (v2017.09.15) [28] from the EGSnrc code system. The range of the secondary electrons produced by low-energy photons is generally small compared to macroscopic millimeter-sized voxels. For instance, the range of the secondary electrons produced by the INTRABEAM photon spectrum in water would be of around 1.8×10^{-3} cm [29], which is near two orders of magnitude smaller than the minimum linear dimension of the scoring voxels used in this study (1 mm). Therefore, dose to water was approximated as water electronic kerma obtained via a tracklength estimator, resulting in reduced computation times. The computation of kerma with `egs_brachy` makes use of precalculated mass energy-absorption coefficients for water (ρ = 1.0 g cm^{-3}) provided as a separate file in the EGSnrc code system. Simulations were run in two stages for each spherical applicator. In the first stage, 1×10^8 starting electrons were transported from the ring-shaped electron beam inside the probe, and a phase space was scored at the applicator surface with data of the particles energy, position, velocity, charge and statistical weight. In the second stage, particles were run from the phase space generated for each applicator, and doses were scored in 0.4 mm thick annular water voxels centered at the source axis. On average, 7.8×10^8 histories were run in the second stage, depending on the number of particles stored in the phase space file for each applicator. A list of the physics processes and transport parameters is presented in table 4.1,

following the recommendations of the AAPM TG-268 [30] for the reporting of MC studies. As variance reduction techniques, bremsstrahlung cross-sections were enhanced in the gold target by a factor of 50, and bremsstrahlung events were split by a factor of 100 during the first stage of the simulations.

4.4.3 TG-43 parameters

Relative TG-43 parameters have been previously reported for the Xoft Axxent source [22] and the INTRABEAM bare probe [2]. For both sources the effective focal spot is small and the point-source approximation was used to model the geometry function, $G_{\mathrm{P}}(r,\theta)$. With this assumption, the geometry function obeys the inverse square law of the distance from the source. With the TG-43 formalism, the measured air-kerma strength, S_{K}, required a conversion of the air-kerma rate to *in-vacuo* conditions by applying corrections for scatter and attenuation in air and in the surrounding media. However, this procedure was not appropriate for eBT sources, since the scatter and attenuation corrections were significant. For example, the attenuation correction for the Xoft source was higher than 25% [12]. For this reason, a modified formalism using the air-kerma rate measured in air, instead of air-kerma strength, was developed at the National Institute of Standards and Technology (NIST) [8]. Based on the air-kerma rate standard, DeWerd et al. (2015) [12] proposed a modified formalism to calculate the dose rate in water according to

$$\dot{D}_i(r,\theta) = \dot{K}_{50\mathrm{cm}}\,\chi_i(10\,\mathrm{mm},\,\pi/2)\,G_{\mathrm{P}}(r,\theta)\,g_i(r)\,F_i(r,\theta), \tag{4.1}$$

where the subscript i makes reference to the dose rate calculation using an applicator i, $\dot{K}_{50\mathrm{cm}}$ is the air-kerma rate measured in air at 50 cm from the source axis on the transverse plane at the source tip level, with traceability to a PSDL, χ_i is called the dose-rate conversion coefficient at the reference point in water ($r_0 = 10$ mm from applicator surface and θ_0 = 90°), $G_{\mathrm{p}}(r,\theta) = 1/r^2$ is the geometry function with point-source approximation, and $g_i(r)$ and $F_i(r,\theta)$ are the radial dose function and the 2D anisotropy function for the applicator i, respectively. The dose-rate conversion coefficient, χ_i, was calculated as

$$\chi_i(10\,\mathrm{mm},\,\pi/2) = \left(\frac{\dot{K}_{50\mathrm{cm}}}{\dot{D}_i(10\,\mathrm{mm},\,\pi/2)}\right), \tag{4.2}$$

where $\dot{D}_i(10\,\mathrm{mm},\,\pi/2)$ is the dose rate measured at the reference point in water [12].

The origin of coordinates for calculations corresponds to the intersection of the source longitudinal axis with the external surface of the source needle (source tip). According to the manufacturer, this point coincides with the center of the spherical applicators. r distances were measured from the source tip and θ = 0° pointed towards the distal part of the probe as shown in figure 4.1(d).

Air-kerma rate and dose-rate conversion coefficients.

NIST (or another PSDL) do not currently maintain a standard for the INTRABEAM system, and as such $\dot{K}_{50\mathrm{cm}}$ cannot be measured with traceability to a PSDL. For this study, $\dot{K}_{50\mathrm{cm}}$ was obtained from the air-kerma, K_{air},

Table 4.1 Summary of the characteristics of the MC method used to obtain the TG-43 parameters.

Item	Description	References
Code	EGSnrc 2019	Kawrakow & Rogers [31]
	`egs++` library, EGSnrc 2019 master branch	Kawrakow et al. [26]
	`egs_brachy` (v2017.09.15)	Chamberland et al. [28]
Validation	The MC model was validated by comparison of computed depth dose profiles along the source axis with the calibration data provided by the manufacturer (Carl Zeiss AG)	
Timing	Time required to obtain each applicator phase space: $\sim$10 h with a cluster of 124 cores split in five nodes of Intel(R) Xeon(R) CPU models: two E5-2697 v3 @ 2.60 GHz, two E5-2687W @ 3.10 GHz and one Gold 6140 @ 2.30 GHz. The time required to obtain the dose distribution in water from the phase space for each applicator was $\sim$100 h	
Source description	Two stages: **1.** Divergent electron beam hitting the target in the shape of two concentric rings with a Gaussian distribution of energy centered at 50 keV with a FWHM of 5 keV. **2.** Phase-space data stored at each applicator surface	Clausen et al. [25]
Cross-sections	Photoelectric and Rayleigh scattering: XCOM	Berger et al. [32]
	Compton: relativistic impulse approximation	Kawrakow & Rogers [31]
	Bremsstrahlung: NRC	Kawrakow & Rogers [31]
	Electron impact ionization: PENELOPE	Bote & Salvat [33]
	Atomic relaxations with explicit M and N-shell transitions: EADL	Watson & Seuntjens [34]
Transport parameters	Boundary crossing algorithm: Exact	Kawrakow & Rogers [31]
	PCUT = 1 keV. ECUT inside the source = 512 keV. Electrons were not transported outside the source (ECUT = 1 MeV)	
Variance reduction techniques	Bremsstrahlung and photon cross-section enhancement, uniform bremsstrahlung splitting	Chamberland et al. [28]
Scored quantities	Absorbed dose to water (collision kerma approximation)	
# histories /statistical uncertainty	For $\dot{D}_i(10\,\mathrm{mm},\,\pi/2)$: 1×10^8 original particles/ 0.03% uncertainty, in average for all applicators	
Statistical methods	History-by-history	Chamberland et al. [28]
Postprocessing	Data normalized at 10 mm from the applicator surface	

calculated from the MC simulated fluence spectra in air at 50 cm from the source as

$$K_{\mathrm{air}} = \sum_i \Phi_i \, E_i \left(\frac{\mu_{\mathrm{tr}}}{\rho} \right)_{i,\mathrm{air}}, \tag{4.3}$$

where Φ_i is the photon fluence for energy bin i, E_i is the photon bin energy, and $(\mu_{\mathrm{tr}}/\rho)_{i,\mathrm{air}}$ is the mass energy transfer coefficient of air. Mass energy transfer coefficients can be obtained with the EGSnrc application g [35]. The fluence spectra, Φ_i, was obtained with MC using the spectrum scoring option *energy fluence in region* in `egs_brachy`. The simulations were run from the ring-shaped electron beam inside the source probe with 3×10^8 starting histories for each applicator and the bare probe. For the geometry, the source with applicator was immersed in a 700 mm radius sphere of air with relative humidity of 40% as recommended by TG-43U1. Exploiting the azimuthal symmetry of the system, the scoring volume consisted of an annular air region of 1 mm radial thickness (inner radius 499.5 mm, outer radius 500.5 mm) and 10 mm axial thickness (in the z range -5.0 to 5.0 mm).

The MC simulations gave photon fluence per history in units of 1/(cm^2 hist), and K_{air} data were calculated with (4.3) in units of MeV/(g hist). $\dot{K}_{50\mathrm{cm}}$ values are then calculated as

$$\dot{K}_{50\mathrm{cm}} = \left(\frac{K_{\mathrm{air}}}{\mathrm{hist}} \right) I, \tag{4.4}$$

where I is the beam current. Since the INTRABEAM is operated at a current of 40 μA = (4/1.6 $\times$ 10^{-14}) hist/s, $\dot{K}_{50\mathrm{cm}}$ values were calculated in units of Gy/s by applying a factor of 4×10^4 to the K_{air}/hist results. Subsequently, χ_i values were obtained for each applicator using the $\dot{D}_i(10\,\mathrm{mm},\, \pi/2)$ values from the simulations in water.

4.4.4 Source calibration

The INTRABEAM system is calibrated by Zeiss using a PTW 23342 soft x-ray ionization chamber in water with a dedicated waterproof holder [19, 36]. The PTW 23342 is a large-body parallel-plate ionization chamber with a collecting air volume of 0.02 cm^3. The chamber is calibrated in terms of exposure and the measurements are converted to absorbed dose rates to water by means of the so-called f-factor, which is obtained from ICRU Report 17 for 20 keV monoenergetic photons [37]. As discussed by Watson et al. 2017, 2018, 2019, the f-factor does not account for spectral variations in energy for INTRABEAM photons at different depths in water. This dosimetry procedure is called the TARGIT dose-rate method, as it was used to determine dose-rate data for the TARGIT-A clinical trial for breast cancer [4].

The source manufacturer provides a dedicated phantom called INTRABEAM Water Phantom [18] that can be used in the clinic to verify the depth dose profiles from calibration. Measurements with this phantom are performed with a different ionization chamber, the PTW 34013, which is calibrated in terms of air-kerma. In order to compare the measurements in the clinic with the PTW 34013 chamber to the TARGIT-based calibration data, a depth-dependent correction factor must be applied. While this correction factor is an aggregate of several effects, its dominant contribution is the volume averaging of a detector, especially close to the source [19]. Since 2016, depth dose calibration data with the PTW 34013 chamber are measured by the manufacturer using the so-called

V4.0 calibration method [36]. V4.0 and TARGIT calibration data are provided with each INTRABEAM source in the form of dose-rate tables measured at different distances from the source tip in the range 3 to 45 mm in 0.5 mm steps. Depth-dependent applicator transfer functions are calculated as the ratio of doses measured with and without the applicator. Applicator transfer functions are also provided by the manufacturer in a separate file.

4.4.5 Validation of the MC model

The MC model of the source was validated by comparing depth dose calculations in water for each spherical applicator against depth dose calibration data provided by Zeiss using the V4.0 calibration method. Data used to validate the MC model correspond to the calculations of the dose rates along the source longitudinal axis at distances measured from the source tip. Calibration dose rates of each applicator were obtained by multiplying the V4.0 dose rates of the bare probe by the corresponding transfer function. Depth dose curves were normalized at 10 mm from the applicator surface.

In contrast to the TG-43 formalism, Zeiss defines anisotropy as the relative percent difference of the dose at a certain point to the value at the same distance along θ = 0°, and not θ = 90° [18]. The applicator anisotropy, A_{iso}, is defined by Zeiss as the difference of the source with applicator anisotropy, $(X+A)_{\mathrm{iso}}$, and the bare probe anisotropy, X_{iso}:

$$A_{\mathrm{iso}} = (X + A)_{\mathrm{iso}} - X_{\mathrm{iso}}. \tag{4.5}$$

The applicator calibration file provided by the manufacturer includes measured applicator anisotropies at 10 mm from the applicator surface. These values were calculated with our MC model and the results were compared to the calibration data.

4.5 Results and Discussion

4.5.1 Uncertainty analyses

Uncertainties on $\dot{D}_i(10\,\mathrm{mm},\,\pi/2)$ calculations were obtained following the recommendations of the International Organization for Standardization Guide to the Expression of Uncertainty in Measurement (ISO GUM) [38] adapted for photon-emitting brachytherapy sources in the TG-138 report [1]. Type A uncertainties of the simulations correspond to the statistical fluctuations per scoring volume reported in a '.3ddose' file. The k = 1 statistical uncertainties in the $\dot{D}_i(10\,\mathrm{mm},\,\pi/2)$ simulations were $\sim$0.03%, averaged for all applicators. As a type B uncertainty, the effect of the tolerance in the fabrication of the Al filter for the smallest applicators was evaluated, comparing the dose output of the thinner and thicker versions of it to that of the nominal dimensions. The axial position of the filter relative to the probe location was also varied according to the given construction tolerances. The estimated geometry uncertainties for $\dot{D}_i(10\,\mathrm{mm},\,\pi/2)$ were up to 0.4%. This leads to combined standard uncertainties (k = 1) for the MC calculations of up to 0.4% for smaller applicators and 0.04% for larger applicators at the reference position. Uncertainties in the small applicators were therefore dominated by geometry tolerances of the Al filter. The uncertainty budget is presented in table 4.2. A confidence level of 95% in the calculations is obtained by providing expanded uncertainties to a coverage factor of two (k = 2).

Table 4.2 Uncertainty budget for the MC calculation of the dose rate at the reference point, $\dot{D}_i(10\,\mathrm{mm},\,\pi/2)$, for all spherical applicators. Since the Al filter is not present in the applicators with diameters 35 to 50 mm, the corresponding uncertainty cells were marked as 'NA'.

	Applicator diameter [mm]							
Uncertainty component	15	20	25	30	35	40	45	50
MC calculation								
Statistical uncertainty [%]	0.03	0.03	0.03	0.03	0.03	0.03	0.03	0.04
Al filter geometry [%]	0.4	0.3	0.3	0.4	NA	NA	NA	NA
Standard uncertainty (k = 1) [%]	0.4	0.3	0.3	0.4	0.03	0.03	0.03	0.04
Expanded uncertainty (k = 2) [%]	**0.8**	**0.6**	**0.6**	**0.8**	**0.06**	**0.06**	**0.06**	**0.06**

Table 4.3 Uncertainty on the calibration dose rate data at 10 mm from the spherical applicators' surface, along the source probe axis, due to positioning tolerances.

	Applicator diameter [mm]							
Uncertainty component	15	20	25	30	35	40	45	50
Calibration data								
Position (plus radius) [mm]	0.5	0.5	0.4	0.6	0.7	0.7	0.6	0.7
Position (minus radius) [mm]	0.4	0.5	0.5	0.3	0.0	0.0	0.0	0.0
Positional uncertainty [%]	**6.3**	**6.1**	**4.2**	**4.6**	**4.2**	**3.9**	**2.8**	**3.1**

The statistical uncertainties on the depth dose to water simulations along the source axis were below 0.9% for all applicators. The maximum uncertainty was reported for the furthest position from the surface of the 50 mm diameter applicator, and it is due to reduced fluence in the most distant voxel. The uncertainties along the source axis due to the Al filter tolerances were larger as getting close to the Al filter, thus the maximum was found at the surface of the 15 mm diameter applicator with a value of 2.0%. The total MC combined uncertainties along the source axis were below 2.0% and were dominated by the geometry contribution of the Al filter tolerances in the smallest applicators. The total uncertainties on the normalized MC depth dose curves were calculated through uncertainty propagation and were all below 2.4% with a maximum at the surface of the 15 mm diameter applicator.

Calibration data are provided by the manufacturer with applicator positional tolerances in the radial direction (plus and minus) as shown in table 4.3 for all applicators. The influence of the positioning tolerances on the dosimetric uncertainty was determined as the difference in dose rate at each depth in water when applying a positional offset to the fitted depth dose curve. The dose rate positional uncertainties are dependent on the slope of the dose fall-off, which will depend on the distance from the source tip and the beam hardening through the applicator materials. For instance, the largest dose rate positional uncertainty is 12.5% and it is observed at the surface of the 15 mm diameter applicator, which is the closest point to the source tip. The corresponding uncertainties at 10 mm from the applicators' surface, along $\theta = 0°$, varied from 2.8% to 6.3% for all applicators.

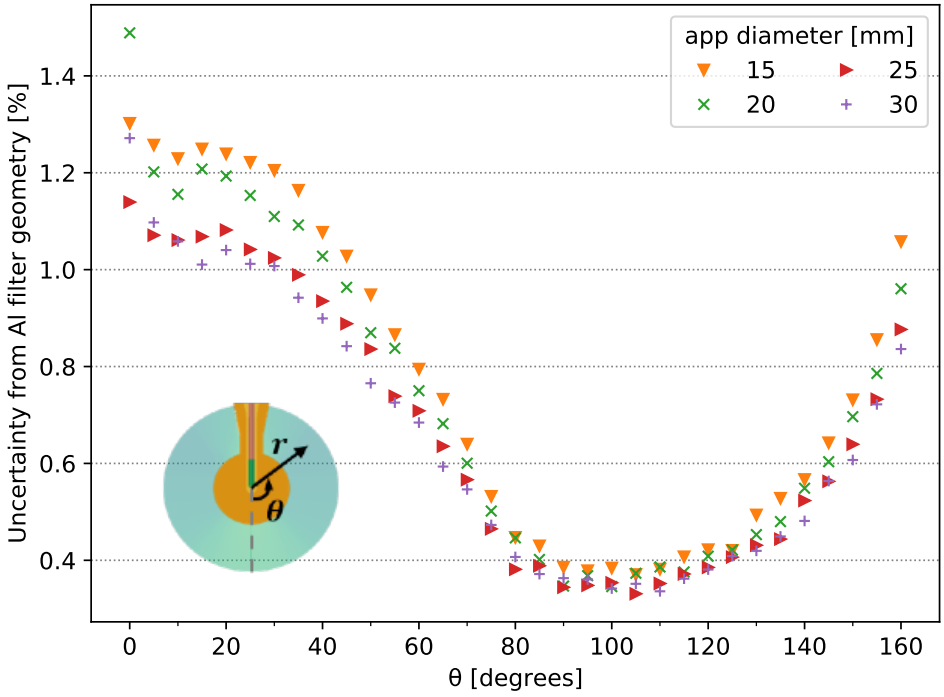

Figure 4.2 Dose calculation uncertainties due to geometry variations of the Al filter construction within tolerance values. The curves shown were calculated at 10 mm from the applicator surface for the smallest applicators of diameters 15 to 30 mm.

The geometry uncertainties on the MC calculated dose rates, due to the tolerance on the thickness of the Al filter, are dependent on the polar angular position around the applicator. This behaviour is presented in figure 4.2 for the smallest applicators as calculated at 10 mm from the applicator surface in the polar angular range $\theta = 0°$ to $160°$. It is to be noticed from the figure, however, that the geometry uncertainties at the reference point were close to their minimum, compared to the larger values at the positions proximal to the source axis, with a maximum exhibited towards the forwarded beam direction, reaching a value of $\sim$1.5% at $\theta = 0°$ for the 20 mm diameter applicator.

4.5.2 Validation of the MC model

The in-water depth dose curves calculated along the source axis with MC for the eight applicators are shown in figure 4.3 together with the calibration measurements provided in the Zeiss calibration data tables. For the latter, the V4.0 method was used, whereby the depth-dependent transfer function parameters specific to each applicator were multiplied by the dose at the same depth for the bare probe. All curves are normalized to unity at a depth of 10 mm from the applicator surface. All distances are measured from the source tip and only data outside the applicators' volume is presented in figure 4.3. The plots are shown on a log-linear scale to better appreciate the local relative differences at deeper positions in water.

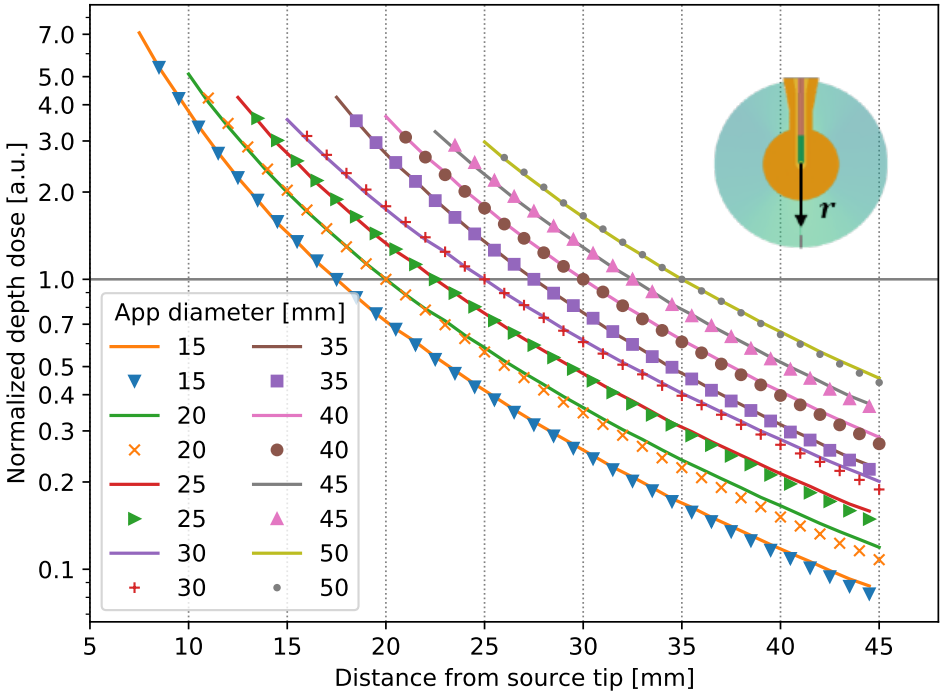

Figure 4.3 Depth-dose curves along the source longitudinal axis for the INTRABEAM system with spherical applicators ranging in diameter from 15 mm to 50 mm in steps of 5 mm. The curves are normalized at 10 mm from the applicator surface. The distances shown are measured from the source tip. The MC calculated data (marks only) are compared to the data provided by the manufacturer (Carl Zeiss) in the calibration file (solid lines).

Figure 4.4 presents the local relative differences of the MC simulated dose profiles and the calibration data for all applicators along the source central axis. The error bars in the figure represent the combined standard uncertainties of the difference, with coverage factor 1 (k = 1). In general, these combined uncertainties were strongly dominated by calibration positional uncertainties, especially close to the source, due to the steep gradients in dose distribution. At distances of up to 30 mm from the source tip, the observed local relative differences were within the total uncertainties. At depths beyond 30 mm, MC calculations exhibit local relative differences from calibration data of up to 8% for the 20 mm diameter applicator and were larger for the smallest applicators. The larger discrepancies exhibited in the smallest applicators can be correlated to the uncertainties of their Al filter construction shown in table 4.2. However, the differences were still within k = 2 standard uncertainties, validating the MC model.

The calculated applicator anisotropy, as described by Zeiss according to (4.1), is shown in figure 4.5 as obtained at 10 mm from all the applicators' surface, in the polar angle range $\theta = 0°$ to $130°$. The error bars included in the plots correspond to the combined standard uncertainties accounting for the tolerances in the Al filter manufacturing for the smallest applicators and statistical fluctuations in the simulations.

The calibration data include measured polar anisotropies for each spherical applicator which ranged between

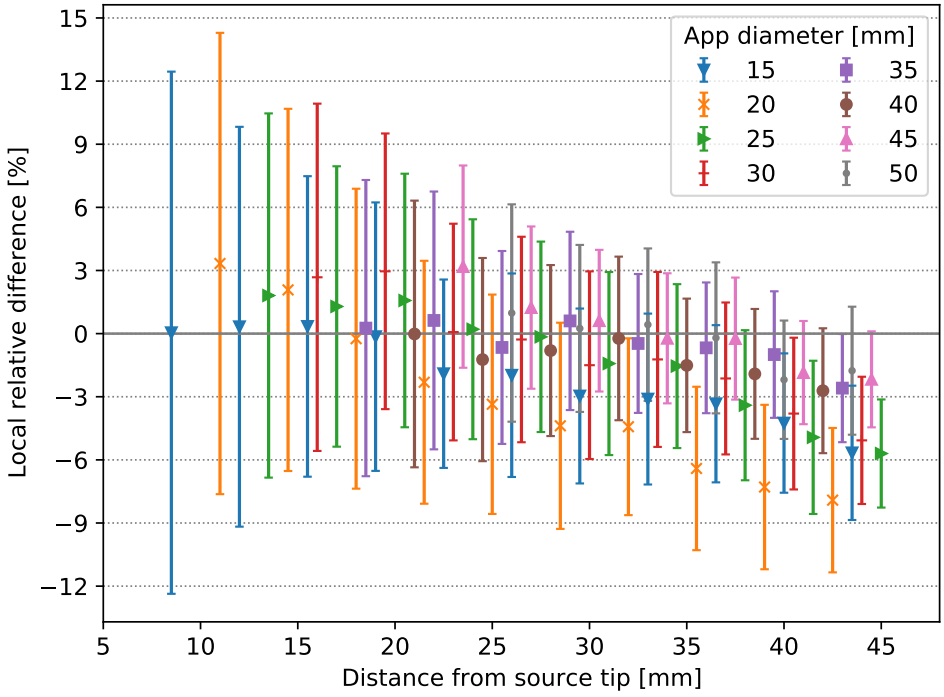

Figure 4.4 Deviations from MC simulations to calibration data provided by the source manufacturer (Carl Zeiss), expressed as local relative differences, for the INTRABEAM source with each of the eight spherical applicators.

-8.1% and 5.9%. All the MC calculated anisotropies in this study were found within the provided exemplary calibration data. This result is consistent with that provided byShamsabadi et al. (2020) [20], who reported anisotropies in the same range at 10 mm distance from the applicators' surface.

4.5.3 Photon fluence spectra, air-kerma rates and dose-rate conversion coefficients.

The MC simulated photon fluence spectra scored in air at 50 cm from the source tip are presented in figure 4.6. Figure 4.6(a) shows the spectrum of the bare probe and the spectra of the source with spherical applicators of various diameters are presented in figure 4.6(b). The spectral change caused by the presence of the applicators, relative to the bare probe spectrum, is noticeable in figure 4.6 as a decrease in the intensity of the fluorescence peaks and a large relative contribution of bremsstrahlung x-rays. For the low-energy range of the spectrum, the Coulombic interactions of the incoming electrons with the orbital electrons of the K and L shells of the gold target and nickel wall atoms play a significant role in the x-ray production inside the INTRABEAM needle. Atomic relaxation leads to fluorescence photons with a photon spectrum dominated by the fluorescence L-lines of gold (in the range 9 to

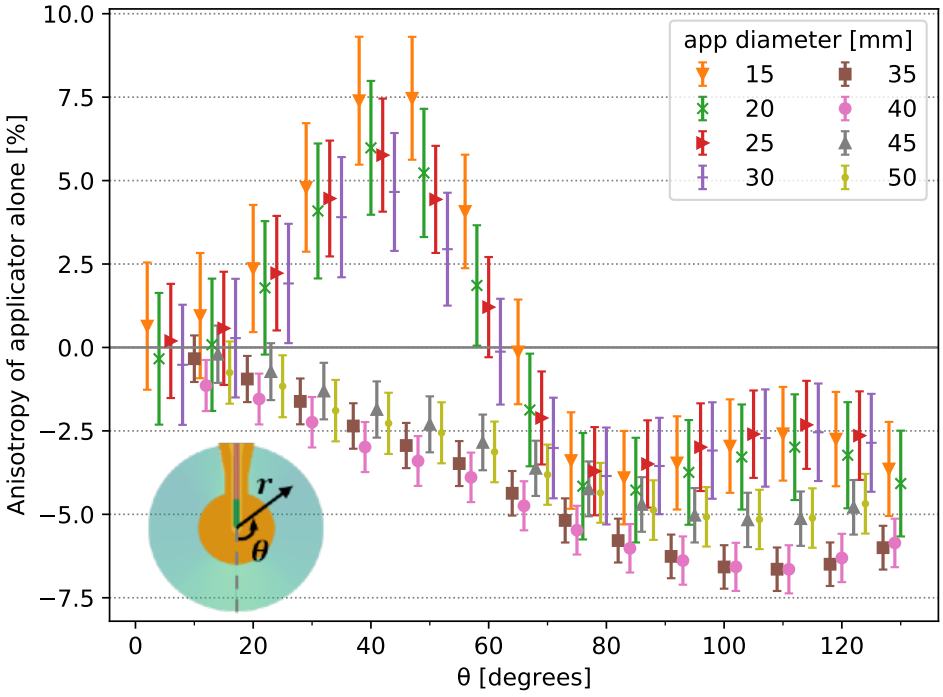

Figure 4.5 MC calculated anisotropy of the spherical applicators alone (after subtracting the bare probe anisotropy), at 10 mm from the applicators' surface, along the angular range θ = 0° to 130°. The applicator anisotropy was calculated according to the manufacturer specifications (Carl Zeiss) relative to θ = 0° and subtracting the bare probe anisotropy.

14 keV) and K-lines of nickel (7.5 and 8.3 keV) [15, 24, 39, 40]. The presence of the Al filter in the smallest applicators hardens the photon beam, resulting in a marked effect on the spectral distribution exhibited as a greater attenuation of characteristic x-ray peaks. As seen in figure 4.6(b), the bremsstrahlung peak is displaced towards higher energies for applicators with Al filter and in proportion with the diameter of the polyetherimide sphere. The fluence averaged energy, $\bar{E}_\Phi$, the total photon fluence, Φ, and the fluence averaged transfer coefficients, $\overline{(\mu_{\rm tr}/\rho)}_{{\rm air},\Phi}$, were calculated at the scoring voxel for the bare probe and for the source with applicators of increasing diameter from 15 to 50 mm, and are reported in table 4.4.

The air-kerma data for each applicator, obtained from the spectra in air using (4.3), and the corresponding air-kerma rates calculated with (4.4) for a current of 40 μA are presented in table 4.4. As an approximate calculation test using the fluence averaged energies and transfer coefficients from table 4.4 would give average $K_{\rm air}$ values of 3.203×10^{-9} and 4.021×10^{-10} MeV/(g hist) for the bare probe and the 40 mm diameter applicator, for example, which from (4.4) and a current of 40 μA would give $\dot{K}_{\rm 50cm}$ values of 12.81×10^{-2} and 1.413×10^{-2} mGy/s, which coincide with the calculated values reported in table 4.4.

$\dot{D}(10\,{\rm mm},\,\pi/2)$ values were obtained from the MC calculations performed for the relative TG-43 parameters in water and are also reported in table 4.4, followed by the corresponding dose-rate conversion coefficients, χ,

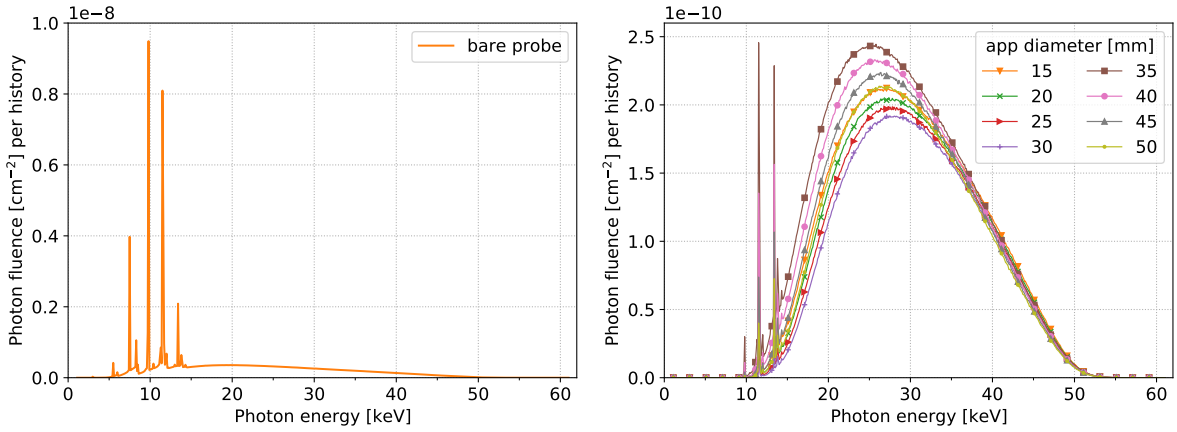

(a) (b)

Figure 4.6 Photon fluence spectra scored in air at 50 cm from the source axis in an annular volume for (a) the INTRABEAM bare probe and (b) the INTRABEAM source with spherical applicators.

calculated for the bare probe and the source with applicators.

4.5.4 Radial dose function

The calculated radial dose functions for the INTRABEAM source with the spherical applicators are shown in figure 4.7. The function has been calculated from the applicator surface to 50 mm from the source tip. Figure 4.7 is presented in terms of the distance from applicator surface. As recommended in the TG-43 formalism, the radial dose functions were obtained along $\theta = 90°$ taking as reference position the point located at 10 mm from the applicator surface. A point-source approximation was used, thus the inverse square law behaviour accounted for in the geometry function of (4.1) was removed in the calculated radial dose function. The function data for all applicators are presented also in table 4.5 for distances from the source tip in the range 2 to 50 mm. For completeness, the radial dose function of the INTRABEAM bare probe previously reported by Ayala Alvarez et al. (2020) [2] is also presented in this table. The k = 1 type A uncertainties of the MC simulations with applicators, not shown in the table, varied from 0.03% to 0.05%, with the maximum obtained at 50 mm for the case of the 50 mm diameter applicator.

As can be observed in figure 4.7, the radial dose function behaviour is split in two groups of applicator diameters. The applicators with larger diameters of 35 to 50 mm exhibit a steeper radial dose function than that of the smaller applicators. The flattened behaviour observed in the smallest applicators is due to the beam hardening occurring at the Al filter (Al filter is not present in larger applicators). Spectral variations of the incoming beams, as they pass through different media, are more prominent at smaller distances from the source as inferred from the curves separation near the applicators' surface and the smoother and converging behaviour of the curves as moving away from the source tip. Because the Al filter pre-hardens the beam, as seen in the average photon energy for each applicator (table 4.4), there is less beam hardening occurring through the water, hence the less steep radial dose function of the smallest applicators.

Table 4.4 Total photon fluence, Φ, fluence averaged energy, $\bar{E}_\Phi$, fluence averaged transfer coefficient, $\overline{(\mu_{\rm tr}/\rho)}_{{\rm air},\Phi}$, and air-kerma rate, $\dot{K}_{50cm}$, calculated from the photon fluence spectra at 50 cm from the source tip (at θ = 90°), absorbed-dose rate to water at the reference point of 10 mm from the applicator surface, $\dot{D}(10\,{\rm mm},\,\pi/2)$, and dose-rate conversion coefficient, χ, for the INTRABEAM bare probe and all spherical applicators. The data shown were calculated for the system operated at a current of 40 μA.

		Applicator diameter [mm]							
Parameter	Bare probe	15	20	25	30	35	40	45	50
Φ [$\times 10^{-8}$ cm^{-2} hist^{-1}]	12.98	4.81	4.57	4.35	4.15	5.54	5.17	4.86	4.57
$\bar{E}_\Phi$ [keV]	20.4	29.8	30.1	30.3	30.5	28.5	28.9	29.3	29.6
$\overline{(\mu_{\rm tr}/\rho)}_{{\rm air},\Phi}$ [cm^2/g]	1.211	0.212	0.202	0.194	0.188	0.255	0.236	0.222	0.211
$\dot{K}_{50cm}$ [$\times 10^{-2}$ mGy/s]	12.81	1.216	1.111	1.026	0.952	1.608	1.413	1.263	1.142
$\dot{D}(10\,{\rm mm},\,\pi/2)$ [mGy/s]	55.60	8.310	6.093	4.613	3.582	4.036	3.187	2.561	2.085
χ	434.0	683.5	548.3	449.9	376.5	251.0	225.6	202.8	182.6

4.5.5 2D anisotropy function

The TG-43 2D anisotropy functions were calculated with the validated MC model of the source with all the spherical applicators. Based on the source construction specifications, azimuthal symmetry was assumed. As example, the polar anisotropy of the 40 mm diameter applicator is presented in figure 4.8 at different distances from the applicator surface as a function of polar angle (θ). Since the 2D anisotropy is calculated only outside the applicator, the data is presented between θ = 0° and up to $\theta \approx$ 160°. Some dosimetry aspects can be inferred from figure 4.8. For instance, a larger anisotropy is observed near the source axis, towards θ = 0° and θ = 180°, indicating a strong contribution from primary and back-scattered components of the beam compared to the transverse dose delivered with the system. The forward directed anisotropy is larger, reaching values of up to 27%, which can be related to the selection of the system's origin at the outer surface of the source tip instead of the effective source position. These effects were also exhibited in the published bare probe anisotropy data [2]. Calculated 2D anisotropy data for all the applicators are presented in tables 4.6 to 4.8 for polar angles 0° to 170° in steps of 5° and different radial distances from the source tip. The radial and angular binning used to generate the provided 2D anisotropy tables permit linear-linear interpolation resulting in differences no larger than $\pm$2% from the MC calculations, as recommended in the TG-43U1 protocol.

The polar anisotropy at 10 mm from the applicator surface is presented in figure 4.9 for all the applicators as a function of polar angle. For the smallest applicators, the effect of the Al filter is exhibited as a decrease in anisotropy close to the source axis, towards θ = 0° and θ = 180°, where the back-scattered beam is shielded along a larger relative path through aluminium. When comparing the 2D anisotropy at 10 mm from the applicators' surface to that previously reported for the bare probe by Ayala Alvarez et al. (2020) [2], a less homogeneous dose distribution is exhibited at θ angles 0° to 90° with the presence of the applicators, whereas the reverse effect was observed at angles 90° to 180°. This phenomenon can be attributed to the larger added attenuation material of the applicators towards the transverse reference line compared to that added in the forward direction of the beam from the source effective

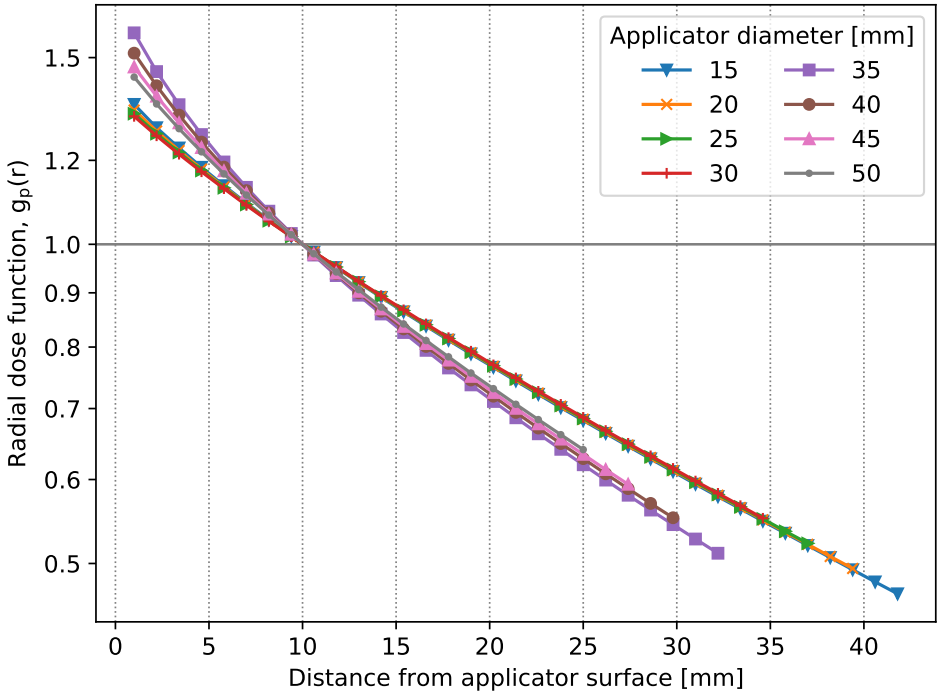

Figure 4.7 Radial dose functions for the INTRABEAM system with the available spherical applicators. The subscript "p" indicates that a point-source approximation was used in the calculations. The enhanced penetration of the smallest applicators is attributed to the beam pre-hardening throughout the added aluminium filter.

position. The increased relative x-ray filtration towards the reference line makes the 2D anisotropy values larger at small angles. The added forward anisotropy with the presence of the applicators was also reported by Shamsabadi et al. (2020) [20] and Eaton et al. (2013) [41].

4.6 Conclusion

The dosimetric parameters recommended by the TG-43 formalism and adapted for eBT sources were calculated with MC for the INTRABEAM source with the eight spherical applicators. Specifically, the air-kerma rate at 50 cm, the dose-rate conversion coefficients, the radial dose function and the 2D-anisotropy function for the INTRABEAM system were obtained and tabulated. The MC model was validated with calibration data provided by the manufacturer, with local relative differences found within the estimated uncertainties. The present work strengthens the conjoint effort towards the dosimetry standardization of eBT by showing the feasibility of its application to the INTRABEAM system with the spherical applicators of common clinical use in IORT. A dose to water method was employed in which the dose-rate to water at a reference point is obtained from calibration air-kerma rates in measurement condi-

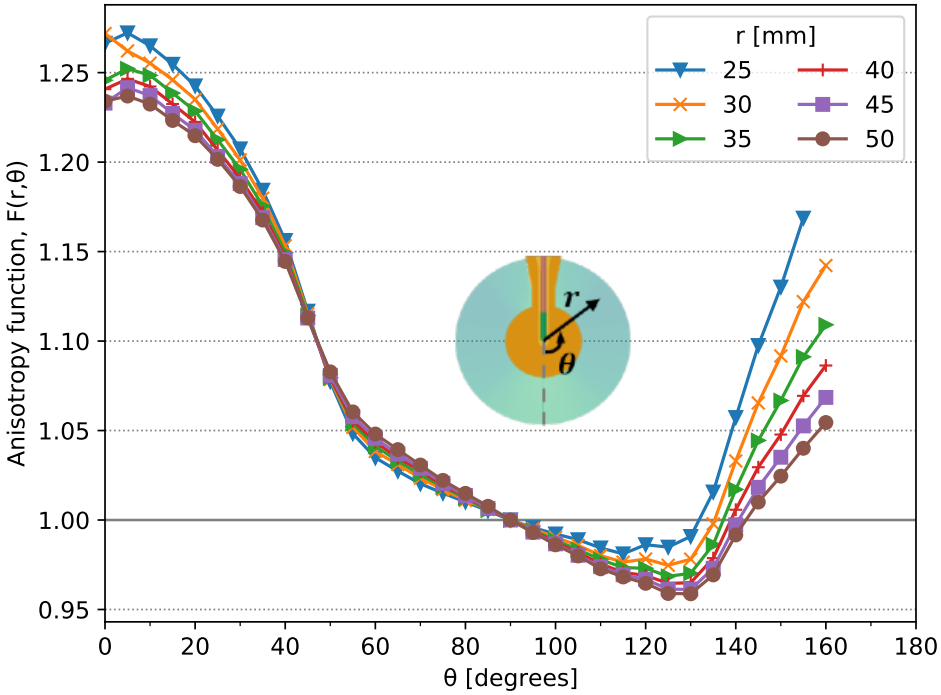

Figure 4.8 2D anisotropy function of the INTRABEAM source with the 40 mm diameter applicator calculated at several distances from the source tip in the polar angle range $\theta = 0°$ to 160°.

tions using a MC calculated dose-rate conversion coefficient. It is to be noted, however, that the calculated dose-rate conversion coefficients can differ from the calibration ones once a consensus on the measurement of air-kerma rate at a primary standards dosimetry laboratory has been reached. This is akin to the multiplicity of dose-rate constants available for a given brachytherapy source, as stated in the TG-43U1 [11], depending on the calibration standard to which the reference dose rate was normalized.

Although the results were obtained herein for a dedicated source and applicator, the methodology can be extended to other applicators and eBT sources. The data reported in this manuscript can be used to feed a TPS to obtain dose distributions in IORT applications where the surrounding tissues are considered water-equivalent for low-energy photons. Further research is needed to assess the implementation of the data obtained with the TG-43 formalism and correct for tissue heterogeneities in more general patient-specific calculations.

Acknowledgements

The authors wish to thank Mathias Benker of Carl Zeiss for details on the INTRABEAM spherical applicators. D.S.A.A. acknowledges the financial support from the Fonds de recherche du Québec – Santé (FRQS, grant number: 292924). This work was presented at the COMP Annual Scientific Meeting 2021, virtual meeting, June 22–25, 2021.

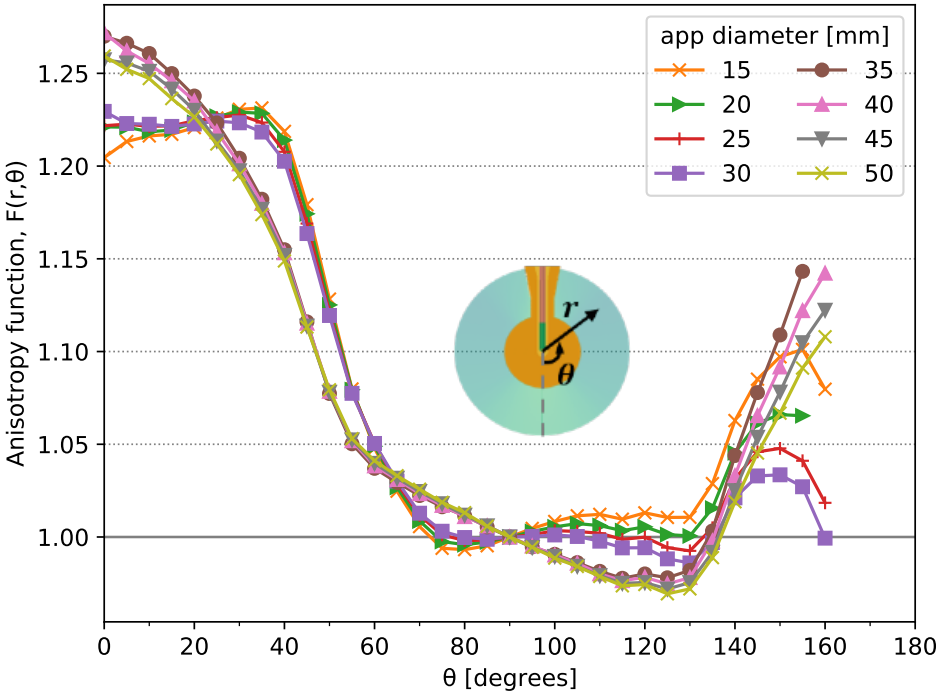

Figure 4.9 2D anisotropy function curves calculated at 10 mm from the surface of the INTRABEAM spherical applicators in the polar angle range $\theta = 0°$ to 160°.

Appendix

The following tables in this section summarize the relative TG-43 parameters, $g_{\mathrm{p}}(r)$ and $F(r,\theta)$, calculated with MC for the INTRABEAM source with the eight available spherical applicators.

Table 4.5 MC calculated radial dose function data, $g_{\mathrm{p}}(r)$, for the INTRABEAM bare probe and with spherical applicators. The TG-43 point-source model has been used. Points located inside the applicator, for which $g_{\mathrm{p}}(r)$ is not determined, are indicated by 'NA'.

		Applicator diameter [mm]							
r [mm]	bare probe	15	20	25	30	35	40	45	50
2	4.782	NA	NA	NA	NA	NA	NA	NA	NA
4	2.510	NA	NA	NA	NA	NA	NA	NA	NA
6	1.645	NA	NA	NA	NA	NA	NA	NA	NA
8	1.232	1.381	NA	NA	NA	NA	NA	NA	NA
10	1.000	1.274	1.362	NA	NA	NA	NA	NA	NA
12	0.854	1.186	1.288	1.249	NA	NA	NA	NA	NA
14	0.753	1.111	1.201	1.303	NA	NA	NA	NA	NA
16	0.678	1.045	1.126	1.217	1.320	NA	NA	NA	NA
18	0.619	0.986	1.059	1.141	1.232	1.639	0.105	NA	NA
20	0.571	0.933	1.000	1.074	1.156	1.428	1.593	NA	NA
22	0.530	0.884	0.946	1.014	1.088	1.276	1.427	1.444	NA
24	0.495	0.839	0.897	0.960	1.028	1.157	1.285	1.430	NA
26	0.464	0.798	0.852	0.910	0.973	1.061	1.172	1.296	1.438
28	0.436	0.760	0.810	0.864	0.923	0.981	1.079	1.187	1.308
30	0.411	0.724	0.771	0.821	0.876	0.911	1.000	1.096	1.203
32	0.388	0.690	0.734	0.782	0.833	0.851	0.932	1.018	1.113
34	0.367	0.659	0.700	0.745	0.793	0.797	0.870	0.949	1.036
36	0.348	0.629	0.668	0.710	0.755	0.748	0.816	0.888	0.967
38	0.330	0.601	0.638	0.677	0.720	0.704	0.767	0.834	0.906
40	0.313	0.574	0.609	0.646	0.687	0.665	0.723	0.785	0.851
42	0.298	0.549	0.582	0.617	0.655	0.628	0.682	0.740	0.802
44	0.283	0.526	0.557	0.590	0.626	0.595	0.645	0.698	0.756
46	0.270	0.503	0.533	0.564	0.598	0.563	0.611	0.660	0.715
48	0.257	0.482	0.510	0.540	0.572	0.534	0.579	0.625	0.676
50	0.245	0.461	0.488	0.517	0.547	0.507	0.549	0.592	0.640

Table 4.6 MC calculated 2D anisotropy function data, $F(r,\theta)$, for the INTRABEAM source with the 15 and 20 mm diameter spherical applicators. Points located inside the applicators, for which $F(r,\theta)$ is not determined, are indicated by 'NA'.

	Radial distance from the source tip, r [mm]												
	Applicator 15 mm							Applicator 20 mm					
θ [°]	8	10	15	20	30	40	50	12	15	20	30	40	50
0	1.118	1.155	1.197	1.207	1.228	1.239	1.238	1.177	1.199	1.221	1.235	1.211	1.193
5	1.119	1.158	1.204	1.221	1.228	1.230	1.227	1.183	1.204	1.221	1.228	1.228	1.229
10	1.127	1.163	1.207	1.221	1.229	1.227	1.227	1.186	1.204	1.219	1.226	1.227	1.226
15	1.134	1.167	1.209	1.221	1.227	1.225	1.225	1.188	1.206	1.219	1.225	1.224	1.221
20	1.145	1.177	1.214	1.224	1.225	1.221	1.218	1.199	1.214	1.224	1.224	1.221	1.216
25	1.165	1.194	1.221	1.227	1.224	1.218	1.213	1.211	1.222	1.227	1.222	1.217	1.211
30	1.191	1.212	1.230	1.229	1.220	1.211	1.205	1.226	1.230	1.229	1.220	1.211	1.203
35	1.217	1.230	1.234	1.227	1.213	1.201	1.194	1.238	1.235	1.228	1.212	1.200	1.192
40	1.231	1.233	1.224	1.213	1.195	1.184	1.176	1.234	1.226	1.214	1.195	1.184	1.175
45	1.211	1.202	1.185	1.173	1.158	1.150	1.145	1.200	1.187	1.174	1.158	1.149	1.143
50	1.165	1.150	1.133	1.124	1.116	1.112	1.110	1.146	1.135	1.125	1.116	1.111	1.109
55	1.108	1.093	1.082	1.078	1.078	1.078	1.081	1.091	1.083	1.079	1.077	1.078	1.079
60	1.058	1.049	1.047	1.049	1.054	1.057	1.061	1.049	1.048	1.049	1.053	1.057	1.059
65	1.018	1.016	1.021	1.027	1.035	1.041	1.045	1.019	1.021	1.027	1.034	1.040	1.043
70	0.988	0.990	1.001	1.009	1.020	1.026	1.031	0.995	1.001	1.009	1.019	1.025	1.029
75	0.970	0.974	0.989	0.998	1.009	1.016	1.020	0.980	0.989	0.998	1.008	1.015	1.018
80	0.969	0.975	0.989	0.996	1.004	1.009	1.012	0.982	0.988	0.996	1.004	1.008	1.011
85	0.982	0.986	0.993	0.997	1.001	1.004	1.006	0.990	0.993	0.997	1.001	1.004	1.004
90	1.000	1.000	1.000	1.000	1.000	1.000	1.000	1.000	1.000	1.000	1.000	1.000	1.000
95	1.020	1.014	1.007	1.002	0.999	0.997	0.996	1.012	1.007	1.003	0.999	0.997	0.995
100	1.041	1.028	1.012	1.005	0.997	0.993	0.991	1.022	1.013	1.005	0.997	0.993	0.990
105	1.060	1.041	1.018	1.006	0.995	0.989	0.986	1.031	1.018	1.007	0.995	0.989	0.985
110	1.074	1.050	1.021	1.005	0.992	0.984	0.979	1.038	1.021	1.006	0.991	0.985	0.979
115	1.085	1.055	1.019	1.002	0.987	0.979	0.974	1.040	1.020	1.003	0.987	0.979	0.973
120	1.092	1.061	1.024	1.005	0.985	0.975	0.969	1.045	1.026	1.005	0.985	0.975	0.969
125	1.110	1.072	1.024	1.000	0.977	0.966	0.961	1.052	1.026	1.001	0.978	0.967	0.960
130	1.127	1.081	1.026	0.999	0.975	0.963	0.957	1.057	1.028	1.001	0.975	0.963	0.956
135	1.168	1.114	1.047	1.015	0.984	0.969	0.960	1.084	1.048	1.016	0.984	0.969	0.960
140	1.232	1.168	1.086	1.045	1.005	0.985	0.973	1.127	1.086	1.045	1.005	0.985	0.972
145	1.274	1.205	1.112	1.065	1.018	0.994	0.980	1.155	1.108	1.061	1.015	0.993	0.978
150	NA	1.232	1.127	1.075	1.022	0.996	0.981	1.162	1.114	1.066	1.017	0.994	0.978
155	NA	NA	1.134	1.075	1.019	0.993	0.978	1.168	1.118	1.065	1.013	0.989	0.975
160	NA	NA	NA	1.053	1.000	0.977	0.964	NA	1.102	1.047	0.997	0.975	0.962
165	NA	NA	NA	1.007	0.961	0.947	0.941	NA	NA	1.003	0.959	0.947	0.940
170	NA	NA	NA	NA	0.898	NA	NA	NA	NA	NA	0.897	NA	NA

Table 4.7 MC calculated 2D anisotropy function data, $F(r,\theta)$, for the INTRABEAM source with the 25, 30 and 35 mm diameter spherical applicators. Points located inside the applicators, for which $F(r,\theta)$ is not determined, are indicated by 'NA'.

	Radial distance from the source tip, r [mm]													
	Applicator 25 mm					Applicator 30 mm					Applicator 35 mm			
θ [°]	15	20	30	40	50	17	20	30	40	50	20	30	40	50
0	1.198	1.215	1.237	1.230	1.239	1.196	1.214	1.226	1.230	1.232	1.289	1.278	1.249	1.263
5	1.200	1.217	1.227	1.226	1.223	1.208	1.217	1.225	1.224	1.223	1.281	1.263	1.249	1.240
10	1.201	1.218	1.225	1.224	1.222	1.209	1.215	1.223	1.223	1.222	1.275	1.257	1.244	1.234
15	1.205	1.218	1.224	1.222	1.219	1.211	1.218	1.222	1.221	1.218	1.262	1.247	1.234	1.227
20	1.212	1.223	1.224	1.219	1.215	1.216	1.221	1.221	1.218	1.213	1.249	1.236	1.223	1.215
25	1.220	1.226	1.222	1.215	1.209	1.225	1.226	1.221	1.214	1.209	1.231	1.221	1.209	1.202
30	1.231	1.229	1.219	1.210	1.203	1.230	1.228	1.217	1.208	1.201	1.211	1.202	1.193	1.186
35	1.236	1.227	1.211	1.200	1.191	1.233	1.227	1.210	1.198	1.190	1.187	1.181	1.173	1.169
40	1.226	1.213	1.194	1.182	1.173	1.222	1.214	1.193	1.180	1.172	1.157	1.155	1.149	1.146
45	1.189	1.174	1.158	1.148	1.142	1.182	1.174	1.157	1.146	1.141	1.115	1.116	1.115	1.114
50	1.136	1.125	1.115	1.111	1.108	1.132	1.125	1.115	1.109	1.108	1.075	1.080	1.081	1.084
55	1.084	1.079	1.077	1.078	1.077	1.082	1.079	1.076	1.076	1.078	1.045	1.052	1.057	1.060
60	1.048	1.049	1.054	1.056	1.059	1.048	1.049	1.052	1.056	1.059	1.030	1.040	1.045	1.049
65	1.020	1.026	1.035	1.040	1.043	1.023	1.026	1.034	1.039	1.043	1.021	1.032	1.036	1.040
70	1.000	1.008	1.019	1.025	1.029	1.002	1.007	1.017	1.024	1.028	1.016	1.025	1.028	1.031
75	0.987	0.997	1.009	1.014	1.018	0.991	0.996	1.007	1.014	1.018	1.011	1.018	1.021	1.024
80	0.987	0.995	1.004	1.008	1.011	0.990	0.994	1.003	1.008	1.011	1.007	1.013	1.014	1.015
85	0.993	0.997	1.002	1.004	1.005	0.994	0.996	1.000	1.003	1.005	1.003	1.006	1.007	1.007
90	1.000	1.000	1.000	1.000	1.000	1.000	1.000	1.000	1.000	1.000	1.000	1.000	1.000	1.000
95	1.007	1.003	0.999	0.997	0.996	1.005	1.002	0.998	0.996	0.995	0.997	0.995	0.994	0.993
100	1.013	1.006	0.998	0.994	0.991	1.010	1.005	0.997	0.993	0.991	0.995	0.991	0.988	0.987
105	1.019	1.007	0.995	0.989	0.985	1.014	1.007	0.995	0.989	0.986	0.994	0.986	0.982	0.980
110	1.022	1.007	0.992	0.984	0.979	1.014	1.007	0.991	0.985	0.980	0.991	0.981	0.976	0.973
115	1.021	1.004	0.988	0.979	0.974	1.014	1.004	0.987	0.979	0.974	0.989	0.976	0.972	0.968
120	1.027	1.007	0.986	0.976	0.968	1.018	1.006	0.986	0.975	0.969	0.998	0.977	0.969	0.965
125	1.027	1.002	0.979	0.967	0.960	1.016	1.002	0.978	0.967	0.961	1.003	0.975	0.965	0.959
130	1.029	1.001	0.976	0.964	0.956	1.018	1.002	0.975	0.964	0.956	1.013	0.978	0.965	0.959
135	1.050	1.016	0.985	0.970	0.960	1.035	1.016	0.984	0.969	0.960	1.045	0.997	0.979	0.969
140	1.086	1.045	1.005	0.985	0.972	1.067	1.046	1.004	0.985	0.972	1.100	1.034	1.008	0.992
145	1.107	1.061	1.016	0.993	0.977	1.086	1.061	1.015	0.992	0.977	1.149	1.065	1.030	1.010
150	1.112	1.064	1.016	0.992	0.977	1.088	1.062	1.014	0.991	0.977	1.196	1.093	1.050	1.026
155	1.105	1.058	1.010	0.987	0.972	1.080	1.055	1.008	0.986	0.973	1.247	1.124	1.072	1.043
160	1.082	1.033	0.992	0.972	0.961	1.046	1.022	0.984	0.969	0.959	NA	1.153	1.093	1.060
165	NA	0.995	0.955	0.944	0.938	NA	NA	0.948	0.941	0.937	NA	NA	1.129	1.086
170	NA	NA	0.898	NA	NA	NA	NA	NA	NA	NA	NA	NA	NA	NA

Table 4.8 MC calculated 2D anisotropy function data, $F(r, \theta)$, for the INTRABEAM source with the 40, 45 and 50 mm diameter spherical applicators. Points located inside the applicators, for which $F(r, \theta)$ is not determined, are indicated by 'NA'.

	Radial distance from the source tip, r [mm]											
	Applicator 40 mm				Applicator 45 mm				Applicator 50 mm			
θ [°]	25	30	40	50	25	30	40	50	28	30	40	50
0	1.266	1.272	1.241	1.234	1.280	1.276	1.232	1.226	1.279	1.275	1.243	1.253
5	1.272	1.262	1.247	1.237	1.271	1.260	1.246	1.238	1.263	1.259	1.244	1.237
10	1.265	1.255	1.242	1.232	1.266	1.256	1.241	1.233	1.259	1.254	1.239	1.228
15	1.254	1.246	1.232	1.223	1.254	1.245	1.233	1.226	1.248	1.245	1.230	1.222
20	1.242	1.235	1.222	1.215	1.242	1.233	1.222	1.215	1.237	1.233	1.220	1.212
25	1.226	1.219	1.207	1.202	1.225	1.217	1.207	1.201	1.222	1.218	1.206	1.199
30	1.207	1.201	1.191	1.186	1.206	1.201	1.191	1.186	1.204	1.200	1.190	1.183
35	1.184	1.180	1.172	1.168	1.183	1.179	1.172	1.168	1.181	1.178	1.169	1.165
40	1.156	1.153	1.147	1.144	1.156	1.154	1.148	1.145	1.154	1.152	1.147	1.143
45	1.116	1.115	1.113	1.113	1.114	1.113	1.113	1.114	1.115	1.114	1.112	1.111
50	1.077	1.079	1.080	1.083	1.076	1.078	1.080	1.084	1.079	1.078	1.080	1.082
55	1.048	1.052	1.055	1.060	1.049	1.051	1.055	1.061	1.051	1.051	1.054	1.059
60	1.035	1.038	1.044	1.048	1.034	1.038	1.044	1.049	1.037	1.038	1.043	1.047
65	1.027	1.031	1.035	1.039	1.026	1.030	1.036	1.040	1.029	1.030	1.035	1.038
70	1.020	1.023	1.028	1.031	1.019	1.023	1.027	1.032	1.022	1.024	1.027	1.030
75	1.015	1.017	1.019	1.022	1.015	1.017	1.020	1.024	1.016	1.017	1.020	1.022
80	1.010	1.011	1.013	1.015	1.009	1.011	1.013	1.016	1.011	1.012	1.013	1.014
85	1.005	1.006	1.006	1.008	1.005	1.006	1.007	1.009	1.006	1.005	1.006	1.007
90	1.000	1.000	1.000	1.000	1.000	1.000	1.000	1.000	1.000	1.000	1.000	1.000
95	0.996	0.995	0.994	0.993	0.996	0.995	0.994	0.994	0.995	0.995	0.993	0.992
100	0.992	0.990	0.988	0.986	0.992	0.990	0.988	0.988	0.991	0.990	0.988	0.987
105	0.989	0.986	0.982	0.980	0.989	0.985	0.982	0.981	0.988	0.986	0.982	0.980
110	0.984	0.980	0.976	0.973	0.985	0.981	0.977	0.975	0.983	0.981	0.976	0.974
115	0.981	0.976	0.971	0.968	0.982	0.977	0.972	0.970	0.980	0.977	0.972	0.969
120	0.986	0.978	0.969	0.965	0.986	0.979	0.970	0.966	0.982	0.979	0.970	0.965
125	0.985	0.975	0.965	0.959	0.987	0.976	0.965	0.961	0.981	0.976	0.964	0.959
130	0.991	0.978	0.965	0.959	0.993	0.980	0.966	0.961	0.986	0.981	0.967	0.959
135	1.016	0.998	0.979	0.969	1.018	0.999	0.980	0.971	1.008	1.001	0.980	0.970
140	1.057	1.033	1.006	0.992	1.060	1.034	1.007	0.993	1.046	1.036	1.007	0.991
145	1.097	1.065	1.030	1.010	1.099	1.065	1.030	1.010	1.080	1.067	1.029	1.008
150	1.130	1.092	1.048	1.025	1.133	1.093	1.049	1.026	1.109	1.093	1.048	1.023
155	1.169	1.122	1.069	1.040	1.170	1.122	1.071	1.042	1.141	1.122	1.069	1.040
160	1.193	1.142	1.086	1.054	1.191	1.139	1.085	1.055	1.158	1.140	1.084	1.052
165	1.267	1.191	1.117	1.078	1.229	1.169	1.106	1.073	1.169	1.147	1.097	1.067
170	NA	NA	NA	NA	NA	NA	NA	NA	NA	NA	NA	NA

References

[1] L. A. DeWerd *et al.*, "A dosimetric uncertainty analysis for photon-emitting brachytherapy sources: Report of AAPM Task Group No. 138 and GEC-ESTRO," *Medical physics*, vol. 38, no. 2, pp. 782–801, 2011.

[2] D. S. Ayala Alvarez, P. G. F. Watson, M. Popovic, V. J. Heng, M. D. C. Evans, and J. Seuntjens, "Monte Carlo calculation of the relative TG-43 dosimetry parameters for the INTRABEAM electronic brachytherapy source," *Physics in Medicine and Biology*, vol. 65, no. 24, p. 245 041, 2020.

[3] R. Nath *et al.*, "Guidelines by the AAPM and GEC-ESTRO on the use of innovative brachytherapy devices and applications: Report of task group 167," *Medical physics*, vol. 43, no. 6Part1, pp. 3178–3205, 2016.

[4] J. S. Vaidya *et al.*, "Risk-adapted targeted intraoperative radiotherapy versus whole-breast radiotherapy for breast cancer: 5-year results for local control and overall survival from the TARGIT-A randomised trial," *The Lancet*, vol. 383, no. 9917, pp. 603–613, 2014.

[5] F. A. Giordano *et al.*, "INTRAGO: Intraoperative radiotherapy in glioblastoma multiforme – a Phase I/II dose escalation study," *BMC Cancer*, vol. 14, no. 1, p. 992, 2014.

[6] F. A. Giordano *et al.*, "Intraoperative radiotherapy in newly diagnosed glioblastoma (INTRAGO): An open-label, dose-escalation phase I/II trial," *Neurosurgery*, vol. 84, no. 1, pp. 41–49, 2019.

[7] D. Eaton, "Quality assurance and independent dosimetry for an intraoperative x-ray device," *Medical physics*, vol. 39, no. 11, pp. 6908–6920, 2012.

[8] S. M. Seltzer, M. O'Brien, and M. G. Mitch, "New national air-kerma standard for low-energy electronic brachytherapy sources," *Journal of research of the National Institute of Standards and Technology*, vol. 119, pp. 554–574, 2014.

[9] J. R. Hiatt, M. J. Rivard, and H. G. Hughes, "Simulation evaluation of NIST air-kerma rate calibration standard for electronic brachytherapy," *Medical Physics*, vol. 43, no. 3, pp. 1119–1129, 2016.

[10] R. Nath, L. L. Anderson, G. Luxton, K. A. Weaver, J. F. Williamson, and A. S. Meigooni, "Dosimetry of interstitial brachytherapy sources: Recommendations of the AAPM radiation therapy committee task group no. 43," *Medical Physics*, vol. 22, no. 2, pp. 209–234, 1995.

[11] M. J. Rivard *et al.*, "Update of AAPM Task Group No. 43 Report: A revised AAPM protocol for brachytherapy dose calculations," *Medical Physics*, vol. 31, no. 3, pp. 633–674, 2004.

[12] L. A. DeWerd, W. S. Culberson, J. A. Micka, and S. J. Simiele, "A modified dose calculation formalism for electronic brachytherapy sources," *Brachytherapy*, vol. 14, no. 3, pp. 405–408, 2015.

[13] T. Schneider, D. Radeck, and J. Šolc, "Development of a new primary standard for the realization of the absorbed dose to water for electronic brachytherapy x-ray sources," *Brachytherapy*, vol. 15, S27–S28, 2016.

[14] A. Abudra'a, B. Chauvenet, J. Gouriou, J. Plagnard, R. Itti, and I. Aubineau-Lanièce, "Dosimetry formalism and calibration procedure for electronic brachytherapy sources in terms of absorbed dose to water," *Physics in Medicine and Biology*, vol. 65, no. 14, p. 145 006, 2020.

[15] P. G. F. Watson, M. Popovic, and J. Seuntjens, "Determination of absorbed dose to water from a miniature kilovoltage x-ray source using a parallel-plate ionization chamber," *Physics in Medicine and Biology*, vol. 63, no. 1, p. 015 016, 2017.

[16] P. G. F. Watson, H. Bekerat, P. Papaconstadopoulos, S. Davis, and J. Seuntjens, "An investigation into the INTRABEAM miniature x-ray source dosimetry using ionization chamber and radiochromic film measurements," *Medical Physics*, vol. 45, no. 9, pp. 4274–4286, 2018.

[17] P. Watson, "Dosimetry of a miniature x-ray source used in intraoperative radiation therapy," Ph.D. thesis, McGill University Libraries, 2019.

[18] Carl Zeiss Meditec AG, "INTRABEAM dosimetry, brochure EN_30_010_155ii," manual, 2011.

[19] W. S. Culberson *et al.*, "Dose-rate considerations for the INTRABEAM electronic brachytherapy system: Report from the American association of physicists in medicine task group no. 292," *Medical Physics*, vol. 47, no. 8, e913–e919, 2020.

[20] R. Shamsabadi, H. R. Baghani, B. Azadegan, and A. A. Mowlavi, "Monte Carlo based analysis and evaluation of energy spectrum for low-kV IORT spherical applicators," *Zeitschrift für Medizinische Physik*, vol. 30, no. 1, pp. 60–69, 2020.

[21] M. J. Rivard, S. D. Davis, L. A. DeWerd, T. W. Rusch, and S. Axelrod, "Calculated and measured brachytherapy dosimetry parameters in water for the Xoft Axxent X-Ray Source: An electronic brachytherapy sourcea)," *Medical Physics*, vol. 33, no. 11, pp. 4020–4032, 2006.

[22] J. R. Hiatt, S. D. Davis, and M. J. Rivard, "A revised dosimetric characterization of the model S700 electronic brachytherapy source containing an anode-centering plastic insert and other components not included in the 2006 model," *Medical Physics*, vol. 42, no. 6Part1, pp. 2764–2776, 2015.

[23] M. Dinsmore *et al.*, "A new miniature x-ray source for interstitial radiosurgery: Device description," *Medical Physics*, vol. 23, no. 1, pp. 45–52, 1996.

[24] J. C. Yanch and K. J. Harte, "Monte Carlo simulation of a miniature, radiosurgery x-ray tube using the ITS 3.0 coupled electron-photon transport code," *Medical Physics*, vol. 23, no. 9, pp. 1551–1558, 1996.

[25] S. Clausen *et al.*, "A Monte Carlo based source model for dose calculation of endovaginal TARGIT brachytherapy with INTRABEAM and a cylindrical applicator," *Zeitschrift Fur Medizinische Physik*, vol. 22, no. 3, pp. 197–204, 2012.

[26] I. Kawrakow, E. Mainegra-Hing, F. Tessier, and B. R. B. Walters, "The egsnrc C++ class library, NRC report PIRS-898 (rev a)," National Research Council Canada, Ottawa, Canada, Tech. Rep., 2009.

[27] Carl Zeiss Meditec AG, "INTRABEAM system from ZEISS – technical specifications, EN_30_010_0158iv," manual, 2017.

[28] M. J. P. Chamberland, R. E. P. Taylor, D. W. O. Rogers, and R. M. Thomson, "Egs_brachy: A versatile and fast Monte Carlo code for brachytherapy," *Physics in Medicine & Biology*, vol. 61, no. 23, pp. 8214–8231, 2016.

[29] L. Beaulieu *et al.*, "Report of the Task Group 186 on model-based dose calculation methods in brachytherapy beyond the TG-43 formalism: Current status and recommendations for clinical implementation," *Medical physics*, vol. 39, no. 10, pp. 6208–6236, 2012.

[30] I. Sechopoulos *et al.*, "RECORDS: Improved reporting of montE CarlO RaDiation transport studies: Report of the AAPM research committee task group 268," *Medical physics*, vol. 45, no. 1, e1–e5, 2018.

[31] I. Kawrakow and D. W. O. Rogers, "The EGSnrc code system: Monte Carlo simulation of electron and photon transport," National Research Council Canada, Ottawa, Canada, Tech. Rep. PIRS-701, 2019.

[32] M. J. Berger *et al.*, "XCOM: Photon cross sections database (version 1.5). [Online] available: Http://physics.nist.gov/xcom (accessed september 2020)," *National Institute of Standards and Technology, Gaithersburg, MD*, 2010.

[33] D. Bote and F. Salvat, "Calculations of inner-shell ionization by electron impact with the distorted-wave and plane-wave Born approximations," *Physical Review A*, vol. 77, no. 4, p. 042 701, 2008.

[34] P. G. Watson and J. Seuntjens, "Effect of explicit M and N-shell atomic transitions on a low-energy x-ray source," *Medical physics*, vol. 43, no. 4, pp. 1760–1763, 2016.

[35] E. Mainegra-Hing, D. Rogers, R. Townson, B. Walters, F. Tessier, and I. Kawrakow, "The EGSnrc g application," National Research Council Canada, Ottawa, Canada, Tech. Rep. PIRS-3100, 2020.

[36] M. Y. Shaikh, J. Burmeister, R. Scott, L. K. Kumaraswamy, A. Nalichowski, and M. C. Joiner, "Dosimetric evaluation of incorporating the revised V4.0 calibration protocol for breast intraoperative radiotherapy with the INTRABEAM system," *Journal of Applied Clinical Medical Physics*, vol. 21, no. 2, pp. 50–59, 2020.

[37] International Commission on Radiation Units and Measurements, *ICRU Report 17, Radiation dosimetry: X rays generated at potentials of 5 to 150 KV*. ICRU Publications, Washington, DC, 1970.

[38] JCGM, "Evaluation of measurement data—Guide to the expression of uncertainty in measurement. GUM 1995 with minor corrections. JCGM 100:2008," 2008.

[39] O. Nwankwo, S. Clausen, F. Schneider, and F. Wenz, "A virtual source model of a kilovoltage radiotherapy device," *Physics in Medicine & Biology*, vol. 58, no. 7, pp. 2363–2375, 2013.

[40] F. Moradi *et al.*, "Monte Carlo skin dose simulation in intraoperative radiotherapy of breast cancer using spherical applicators," *Physics in Medicine and Biology*, vol. 62, no. 16, pp. 6550–6566, 2017.

[41] D. Eaton, B. Earner, P. Faulkner, and N. Dancer, "A national dosimetry audit of intraoperative radiotherapy," *The British Journal of Radiology*, vol. 86, no. 1032, p. 20 130 447, 2013.

Chapter 5

Evaluation of dosimetry formalisms in intraoperative radiation therapy of glioblastoma

David Santiago Ayala Alvarez, Peter G. F. Watson, Marija Popovic, Veng Jean Heng, Michael D. C. Evans, Valerie Panet-Raymond and Jan Seuntjens

Article published in: *International Journal of Radiation Oncology* Biology* Physics*, **117**(3):763–773, 2023

5.1 Preface

This chapter builds on the dosimetric characterizations presented in Chapters 3 and 4, shifting the focus to the clinical application of the INTRABEAM system in the treatment of glioblastoma multiforme (GBM). It addresses a critical gap between the theoretical dosimetry of the INTRABEAM system and its practical implementation in the INTRAGO clinical trial. By evaluating different dosimetry formalisms, including the current clinical standard (TARGIT method) and more advanced approaches, this chapter provides insights into the accuracy of dose calculations in real-world clinical scenarios.

The comparison of dosimetry methods presented in this article is crucial for understanding the potential limitations of current clinical practices and the implications of using more sophisticated calculation approaches. This work sets the stage for the comprehensive evaluation of the TG-43 formalism in Chapter 6 and directly informs the discussion on future directions for improving IORT dosimetry in GBM treatment.

5.2 Abstract

Purpose: The INTRAGO clinical trial assesses survival in glioblastoma patients treated with intraoperative radiotherapy (IORT) using the INTRABEAM. Treatment planning for INTRABEAM relies on vendor-provided in-water depth dose curves obtained according to the TARGIT dosimetry protocol. However, recent studies have shown discrepancies between the estimated TARGIT dose from the delivered dose. This work evaluates the effect of the choice of dosimetry formalism on organs at risk (OAR) doses.

Methods and Materials: A treatment planning framework for INTRABEAM was developed to retrospectively calculate the IORT dose in eight INTRAGO patients. These patients received an IORT prescription dose of 20 to 30 Gy, in addition to EBRT. The IORT dose was obtained using (a) the TARGIT method; (b) the manufacturer's V4.0 method; (c) the C_Q method, which uses an ionization chamber Monte Carlo (MC) calculated factor; (d) MC dose-to-water; and (e) MC dose-to-tissue. The IORT dose was converted to EQD2.

Results: According to the TARGIT method, the OAR dose constraints were respected in all cases. However, the other formalisms estimated a higher mean dose to OARs and revealed one case where the constraint for brainstem was exceeded. The addition of the EBRT and TARGIT IORT doses resulted in 10 cases of OARs exceeding the dose constraints. The more accurate MC calculation of dose-to-tissue led to the highest dosimetric differences, with 3, 3, 2, 2, 2, and 2 cases (out of 8) exceeding the dose constraint to the brainstem, optic chiasm, optic nerves, and lenses, respectively. Moreover, the mean cumulative dose to brainstem exceeded its constraint of 66 Gy with the MC dose-to-tissue method, which was not evident with the current INTRAGO clinical practice.

Conclusions: The current clinical approach of calculating the IORT dose with the TARGIT method may considerably underestimate doses to nearby OARs. In practice, OAR dose constraints may have been exceeded, as revealed by more accurate methods.

5.3 Introduction

Glioblastoma (GBM) is the most common and aggressive primary tumour of the brain, with a median overall survival of little more than one year [1, 2]. The current standard of care consists of surgery followed by concomitant external beam radiotherapy (EBRT) and chemotherapy. Intraoperative radiotherapy (IORT) aims to improve locoregional tumour control by delivering a single high dose of radiation directly on the margins of the excised tumour immediately after surgery. INTRAGO is an ongoing phase III clinical trial designed to assess the progression-free survival improvement with IORT (ClinicalTrials.gov identifier: NCT02685605) in the treatment of GBM [3, 4]. Patients are randomized into two groups: 1. Patients who receive the current standard-of-care EBRT dose regimen, and 2. Patients who receive the current standard-of-care EBRT dose regimen in addition to IORT. The IORT of INTRAGO is performed using the INTRABEAM system (Carl Zeiss Meditec AG, Jena, Germany), which produces low-energy x-rays (50 kVp) with a miniature electron accelerator and spherical applicators of diameters ranging from 1.5 to 5 cm, in steps of 0.5 cm, to match the resection cavity size.

The current widely accepted clinical practice in INTRAGO procedures is as follows: The vendor provides in-water depth dose rate curves tabulated in a calibration file for each source to estimate INTRABEAM dose. These curves are measured by the INTRABEAM manufacturer (Zeiss) along the source axis according to the TARGIT

dosimetry protocol, which was established in 1998 at the onset of the TARGIT-A clinical trial [5]. Next, according to the INTRAGO protocol, the user reads the dose from the table at a distance roughly indicative of the nearest separation to each organ at risk (OAR), converts it to 2 Gy fractions equivalent dose (EQD2), and adds it to the EBRT dose to get the total, most conservative dose to the OAR. However, studies have shown that this TARGIT approach may be problematic, with an estimated dose that deviates from the delivered dose by up to 80% [6–10]. In addition, the current IORT treatment planning method greatly oversimplifies the clinical situation because it does not take into account polar anisotropy of source and applicators [11, 12], tissue heterogeneity, or backscatter conditions.

The aim of this work was to investigate the impact of the dosimetry formalism on the dose to OARs of INTRAGO patients. In this study, we compare the OAR dose estimated with the TARGIT method with four alternative dosimetry formalisms that are arguably more accurate than the current clinical practice as they more adequately reflect an absorbed dose standard. The first approach is the V4.0 calibration method, the second is the C_Q method, and the remaining two are MC-based, with and without consideration of tissue heterogeneity. To accurately model the 3D dose distribution, we developed a new IORT dose calculation interface using an in-house treatment planning system (TPS) that accounts for source anisotropy, tissue heterogeneity, and backscatter conditions. Additionally, the software enables volumetric summation of the doses from IORT and EBRT, allowing for the generation of cumulative dose-volume histograms (DVH) that can inform the process of iterative dose optimization of the EBRT treatment plan.

5.4 Methods and Materials

5.4.1 Study Design

In this study, the IORT dose was retrospectively calculated on patients enrolled in the INTRAGO trial. The analysis involved dosimetric data of the first eight patients of the trial that were treated at McGill University Health Centre at the time of writing this manuscript. Per INTRAGO protocol (ClinicalTrials.gov identifier: NCT02685605), a prescription dose of 30 Gy to the applicator surface is recommended, but a dose reduction to no less than 20 Gy is allowed to prevent unacceptable risk to any nearby OAR. In the studied cohort, the IORT prescribed doses, at the surface of the applicator, were 20, 25, and 30 Gy in two, four, and two cases, respectively. All patients received preoperative and early postoperative magnetic resonance imaging (MRI) scans to guide and assess the surgery. A postoperative CT was acquired several days in advance of EBRT for the purpose of treatment planning. The planning CT was co-registered with the postoperative MRI scan, and the EBRT planning target volume (PTV) was contoured on the planning CT as defined using the peritumoral edema displayed in the MRI plus a 2 cm margin. The EBRT dose prescription was 60 Gy delivered in 30 fractions to 95% of the PTV, per the aforementioned protocol. All EBRT plans were created with intensity modulated radiotherapy (IMRT), with Varian Eclipse: External Beam Planning TPS (version 15.6) using the anisotropic analytical algorithm (AAA) (version 11.0.31 or 15.5.06) dose calculation algorithm (Varian Medical Systems, Inc., Palo Alto, CA), and were planned to be delivered using a Varian TrueBeam linear accelerator.

5.4.2 INTRABEAM Dosimetry

TARGIT, V4.0 and C_Q Dosimetry Formalisms

The INTRABEAM manufacturer provides a calibration file with depth dose rates which are measured according to the TARGIT formalism. This ensures consistency in the delivered dose across centers participating in the TARGIT-A trial, among others [9]. However, recent dosimetry formalisms for low energy photons have been proven more accurate [6, 8]. In 2016, Zeiss updated its calibration method to V4.0, developed for the PTW 34013 air-kerma calibrated ionization chamber which Zeiss supplies to users as part of the quality control package for the INTRABEAM system. The V4.0 formalism allows verification in the clinic of the calibration consistency, and it involves measuring the depth dose rate along the source axis in a water phantom provided by Zeiss. The TARGIT dose rate to water, $\dot{D}_{\mathrm{w}}^{TARGIT}$, and the V4.0 dose rate to water, $\dot{D}_{\mathrm{w}}^{V4.0}$, are correlated by

$$\dot{D}_{\mathrm{w}}^{V4.0}(z) = \frac{\dot{D}_{\mathrm{w}}^{TARGIT}(z)}{f'(z)}, \tag{5.1}$$

where the depth-dependent conversion factor, $f'(z)$, is provided in the calibration file. The $f'(z)$ factor is explained in the Water Phantom Instruction Manual (version 5.0) as an aggregate of different causes, including the different ionization chambers, holders, and dose rate formulas used in both methods [13].

An alternative dosimetry formalism was developed by Watson et al. [6], in which an MC calculated factor, $C_Q(z)$, converts air-kerma rates in calibration beam quality, for an air-kerma calibrated ionization chamber, to absorbed dose rate to water in INTRABEAM beam quality. The C_Q dose rate can be obtained from the V4.0 dose rate according to

$$\dot{D}_{\mathrm{w}}^{C_Q}(z) = \frac{\dot{D}_{\mathrm{w}}^{V4.0}(z)\, C_Q(z)}{k_Q\, k_{K_{\mathrm{a}}\rightarrow D_{\mathrm{w}}}}, \tag{5.2}$$

where k_Q is the beam quality correction factor that accounts for differences in the reference beam and INTRABEAM beam, and $k_{K_{\mathrm{a}}\rightarrow D_{\mathrm{w}}}$ is an air-kerma to dose-to-water conversion factor. Both quantities are provided on the PTW calibration certificate of the ionization chamber for several beam qualities. The Water Phantom Manual indicates that the INTRABEAM is best represented by the TW30 beam quality [13], and the corresponding values were used in this work. $C_Q(z)$ was obtained as a fitted function to C_Q data along the source axis provided by Watson et al. [6].

The different dosimetry formalisms discussed have different correction factors that impact the estimated dose. For example, for this study, the $f'(z)$ factor provided by the manufacturer in the source calibration file takes values ranging from 0.5104 at 3 mm from the source tip to 0.8919 at 45 mm from the source tip. At the surface of the spherical applicators, the f'(z) factor takes the values 0.7004, 0.7495, 0.7832, 0.8076, 0.826, 0.8403, 0.8516, and 0.8606 for the applicators with diameters 1.5 to 5 cm, respectively. In addition, the k_Q and $k_{K_{\mathrm{a}}\rightarrow D_{\mathrm{w}}}$ factors for the PTW 34013 ionization chamber are provided in the calibration file as 1.00 and 1.048, respectively. The $C_Q(z)$ factor ranges from 1.1651 at 7.5 mm to 1.1235 at 35 mm. At the applicators' surface, for instance, the $C_Q(z)$ factor takes the values 1.1651, 1.1581, 1.1536, 1.1499, 1.1465, 1.1431, 1.1398, and 1.1365 for all the applicators. Using equations 5.1 and 5.2, we can expect that with respect to the V4.0 formalism, the TARGIT dose may be underestimating the physical dose by up to nearly 50% at 3 mm from the source tip, which is a significant deviation. With respect to the C_Q method, the TARGIT method may be underestimating the delivered dose by a factor of

0.6300, 0.6782, 0.7115, 0.7360, 0.7550, 0.7704, 0.7830, and 0.7936, at the applicators' surface for the applicator diameters 1.5 to 5 cm, respectively. For example, the estimated dose with the TARGIT method at the surface of the 1.5 cm applicator is expected to be only around 63% of the dose estimated with the C_Q formalism.

The TARGIT, V4.0, and C_Q depth dose rates for the INTRABEAM probe are converted to depth dose rates for the INTRABEAM with applicators using transfer functions. The transfer functions are supplied by Zeiss in a calibration file that accompanies each spherical applicator, and they depend on the distance (depth) from the applicator surface to point of interest in water. These functions are, in fact, ratios of doses measured with and without the applicator. They reflect the material composition of the applicator, are unidimensional, and assume source isotropy.

MC Dose Calculations

IORT dose distributions were also obtained with MC simulations performed with the `egs_brachy` application [14] of the *EGSnrc* particle transport code. The code optimizes the computation time by using a track-length estimator approach that exploits the short range of secondary electrons produced with the INTRABEAM photon energy relative to the voxel size of the dose grid. Geometry and materials of the INTRABEAM source probe are available in literature [11, 15, 16]. The spherical applicators' specifications are proprietary to Zeiss and were provided by the manufacturer. Phase space files were scored at the surface of each applicator and were generated and validated in a previous study [12]. The phase space files were then used as the particle source for the patient-specific dose calculations. The MC transport parameters are consistent with those reported by Ayala Alvarez et al. [12] and are summarized in Table 5.1 for this study. The dose was scored in voxelized phantoms bounded by the patient's external body contour and with voxel size $2 \times 2 \times 2$ mm^3.

To assess the impact of tissue heterogeneity on dose to OARs, the IORT dose was calculated both in water (MC_w) and in heterogeneous medium (MC_{het}). For the first, a liquid water composition of 2:1 for H:O and uniform mass density of 0.998 g cm^{-3} was specified in all voxels inside the body contour. For the latter, material densities and elemental compositions of tissues were obtained from the International Commission on Radiation Units and Measurements (ICRU) Reports 44 and 46 and the International Commission on Radiological Protection (ICRP) Report 89 [22–24], as presented in Table 5.2. Using these published values, voxels in brain, cranium, pituitary, and eye lens were assigned their respective material densities and elemental compositions. Voxels outside of the body contour were assigned a constant material density and composition of air.

5.4.3 IORT Treatment Planning Platform and Cumulative Dose Assessment

The INTRAGO trial relies on the TARGIT dosimetry, which is used to determine the IORT irradiation time by dividing the TARGIT dose rate at the applicator surface, by the prescription dose. For this study, the treatment time obtained with the TARGIT method is used as a reference to calculate depth dose curves with the five dosimetry formalisms evaluated, namely, TARGIT, V4.0, C_Q, MC_w and MC_{het}.

A new treatment planning module for IORT volumetric dose calculations was developed in an in-house TPS

Table 5.1 Summary of the relevant MC characteristics and input parameters used in this study.

Item	Description	References
Code	EGSnrc 2019	Kawrakow and Rogers [17]
	`egs++` library, EGSnrc 2019 master branch	Kawrakow et al. [18]
	`egs_brachy` (v2017.09.15)	Chamberland et al. [14]
Validation	Previously validated	Ayala Alvarez et al. [11], Ayala Alvarez et al. [12]
Timing	Time required to obtain each applicator phase space: $\sim$10 h with a cluster of 124 cores split in five nodes of Intel(R) Xeon(R) CPU models: two E5-2697 v3 @ 2.60 GHz, two E5-2687W @ 3.10 GHz and one Gold 6140 @ 2.30 GHz. The average time per node required to obtain patient-specific dose distributions from the phase space was 8–19 minutes	
Source description	Phase-space data stored at each applicator surface	Ayala Alvarez et al. [12]
Cross-sections	Photoelectric and Rayleigh scattering: XCOM	Berger et al. [19]
	Compton: relativistic impulse approximation	Kawrakow and Rogers [17]
	Bremsstrahlung: NRC	Kawrakow and Rogers [17]
	Electron impact ionization: PENELOPE	Bote and Salvat [20]
	Atomic relaxations with explicit M and N-shell transitions: EADL	Watson and Seuntjens [21]
Transport parameters	Boundary crossing algorithm: Exact	Kawrakow and Rogers [17]
	PCUT = 1 keV. Electrons were not transported outside the source (ECUT = 1 MeV)	
Variance reduction techniques	Bremsstrahlung and photon cross-section enhancement, uniform bremsstrahlung splitting	Chamberland et al. [14]
Scored quantities	Absorbed dose (collision kerma approximation)	
# histories /statistical uncertainty	1×10^8 histories from the phase space /average type A uncertainty of the scored dose at 1 cm from the applicator surface was 0.2%	
Statistical methods	History-by-history	Chamberland et al. [14]
Postprocessing	DVH data was obtained for each evaluated OAR	

Abbreviations: DVH = dose-volume histograms; OAR = organ at risk.

called `Brems`. The patient's planning CT data sets were imported into `Brems`, together with the pre-calculated EBRT dose distributions and contours of the PTV and OARs. IORT volumetric dose distributions were generated on the EBRT planning CT for each dosimetry formalism. To obtain the 3D dose distributions, a python script was written to interpolate TARGIT depth-dose data and assign a dose value to each voxel of the dose phantom as a function of its distance to the applicator surface. The interpolation (and extrapolation) of the data was done by determining the best fitting parameters to analytical functions provided by the manufacturer [25]. The TARGIT

Table 5.2 Mass density and elemental composition of tissues evaluated in this study.

Tissue	Mass density ($g\ cm^{-3}$)	Weight fraction (%)											
		H	C	N	O	Na	Mg	P	S	Cl	K	Ar	Ca
Brain[a,b,c]	1.04	10.7	14.5	2.2	71.2	0.2	—	0.4	0.2	0.3	0.3	—	—
Eye lens[a,b,c]	1.07	9.6	19.5	5.7	64.6	0.1	—	0.1	0.3	0.1	—	—	—
Pituitary gland[c]	—	10.5	25.6	2.7	60.2	0.1	—	0.2	0.3	0.2	0.2	—	—
Cranium[b]	1.61	5.0	21.2	4.0	43.5	0.1	0.2	8.1	0.3	—	—	—	17.6
Water[a,b,c]	1.00	11.2	—	—	88.8	—	—	—	—	—	—	—	—
Air (dry)[a]	0.0012	—	—	75.5	23.2	—	—	—	—	—	—	1.3	—

[a] Data from ICRU Report 44 [22]; [b] Data from ICRU Report 46 [23]; [c] Data from ICRP Report 89 [24]

dose distribution was stored in a DICOM format. By using a separate Python script, V4.0 and C_Q dose distribution DICOM files were then obtained applying equations 5.1 and 5.2 to the generated TARGIT dose file. By design, this procedure assumes an isotropic dose distribution, in contrast to the MC dose calculations. Analytical function fitting was also used for the applicator transfer functions. The resulting TARGIT, V4.0, and C_Q DICOM dose files were imported into the `Brems` treatment planning framework for visualization, dose summation, and DVH analyses. The MC_w and MC_{het} dose rate distributions were obtained through `Brems` using `egs_brachy` as the simulation engine.

Multiple plan doses can be added in `Brems` to calculate cumulative DVH parameters. Since the low energy photons of the INTRABEAM exhibit a higher relative biological effectiveness (RBE) than reference EBRT beams, and IORT is delivered in a single fraction, the IORT doses were converted to EQD2 before summing both plans [26, 27]. Following the INTRAGO protocol, an RBE of 1.5 and an α/β of 2 for the OARs were used [3]. The EBRT and IORT plans were added in `Brems`, and cumulative DVH was obtained. The dose to OARs in the cumulative plan was assessed with reference to pre-defined dose constraints provided in the INTRAGO protocol for the brainstem, optic chiasm, optic nerves, lenses, and retinae. As requested in the protocol, the evaluation was performed based on the maximal point dose ($D_{0.03cc}$: maximal dose received by a volume greater than 0.03 cm^3) to planning risk volumes (PRV), which corresponds to the OAR plus a 3 mm safety margin.

Differences between the IORT $D_{0.03cc}$ metric calculated with the TARGIT method and with the four alternative methods were evaluated for statistical significance using a paired sample Wilcoxon signed rank test with a criterion of $p \leq 0.05$. Due to the increased interest in the V4.0 method after its introduction by the manufacturer, the analysis was also performed between the V4.0 method and the C_Q, MC_w, and MC_{het} methods. The same test was used to evaluate the significance of the impact on OAR dose when adding IORT dose distributions to the EBRT-only plan.

Table 5.3 Maximal point dose to planning risk volumes (PRV) calculated with the dose distributions obtained with the reference TARGIT, the Zeiss V4.0, the C_Q, the MC to water (MC_w), and the MC to tissue (MC_{het}) formalisms. The data shown correspond to the mean, in Gy, and the number of cases that exceeded the dose constraint (n_{exc}) in a cohort of eight patients. Data exceeding the constraints are shown in bold.

Tissue	Dose metric	Dose constraint	IORT dosimetry formalism				
			TARGIT (mean [n_{exc}])	V4.0 (mean [n_{exc}])	C_Q (mean [n_{exc}])	MC_w (mean [n_{exc}])	MC_{het} (mean [n_{exc}])
Brainstem	$D_{0.03cc}$ (Gy)	10	3.8 [0]	4.4 **[1]**	4.7 **[1]**	4.4 **[1]**	4.7 **[1]**
Chiasm	$D_{0.03cc}$ (Gy)	10	1.7 [0]	2.0 [0]	2.1 [0]	1.8 [0]	3.4 [0]
Optic Nerve R	$D_{0.03cc}$ (Gy)	10	1.0 [0]	1.2 [0]	1.2 [0]	1.0 [0]	2.8 [0]
Optic Nerve L	$D_{0.03cc}$ (Gy)	10	1.1 [0]	1.3 [0]	1.3 [0]	1.0 [0]	2.6 [0]

Abbreviations: $D_{0.03cc}$ = maximal dose received by a volume greater than 0.03 cm^3; IORT = intraoperative radiotherapy.

5.5 Results

5.5.1 Dosimetric Analysis

The IORT $D_{0.03cc}$ to OARs are presented in Table 5.3 as the cohort's mean values for the TARGIT, V4.0, C_Q, MC_w, and MC_{het} dosimetry formalisms. The dosimetric evaluation was conducted on the brainstem, optic chiasm, and optic nerves, and the dose metric was compared to the dose constraint of 10 Gy recommended in the INTRAGO protocol. According to the TARGIT method, no patients exceeded the IORT OAR dose constraints (Table 5.3). However, for one patient, the four additional investigated methods revealed a brainstem $D_{0.03cc}$ dose in excess of the proposed OAR dose constraint. A Wilcoxon signed rank test revealed that the OAR dose calculated with the V4.0, C_Q, and MC to tissue (MC_{het}) formalisms was significantly higher than that calculated with the reference TARGIT formalism ($p < 0.05$), and that the brainstem $D_{0.03cc}$ calculated with the MC to water (MC_w) formalism also exceeded the TARGIT formalism ($p < 0.05$). Compared to the V4.0 method, the C_Q and MC_{het} methods resulted in significantly higher OAR doses as revealed by a Wilcoxon test. Furthermore, the V4.0 estimated dose to the optic chiasm and optic nerves was statistically significantly higher than that of the MC_w method ($p < 0.05$).

The mean $D_{0.03cc}$ to OARs resulting from the combined EBRT + IORT plans are presented in Table 5.4, together with data for the EBRT-only plan. The brainstem, optic chiasm, optic nerves, lenses, and retinae were defined as OARs, and the dose constraints of the INTRAGO protocol for the combined plan were used as evaluation criteria.

As shown in Table 5.4, in two cases, the OAR dose constraint was exceeded for the lens from the EBRT plan alone. When the EBRT dose was combined with the TARGIT IORT dose, the number of patients exceeding the dose constraints exhibited an increase in some OARs, namely, the brainstem, optic chiasm, optic nerves, and lenses. The use of more accurate methods reveals an increased mean dose to the brainstem and optic chiasm and one additional patient exceeding the brainstem limit. The more accurate MC calculation to tissue led to the highest dosimetric differences with 3, 3, 2, and 2 cases (out of 8) exceeding the dose constraints to brainstem, optic chiasm, optic nerves, and lenses, respectively. Conversely for the right lens, MC_{het} (and MC_w) resulted in one fewer case with the exceeded lens dose constraint, as compared to other methods. The C_Q method shows one additional case exceeding the optic nerve constraint.

Table 5.4 Maximal point dose ($D_{0.03\mathrm{cc}}$) to planning risk volumes (PRV) calculated with the dose distributions obtained with the EBRT-only plan, and with the EBRT combined with the IORT obtained with the reference TARGIT, the Zeiss V4.0, the C_Q, the MC to water (MC_w), and the MC to tissue (MC_{het}) dosimetry formalisms. The data shown correspond to the mean, in Gy, and the number of cases that exceeded the dose constraint (n_{exc}) in a cohort of eight patients. Data exceeding the constraints are shown in bold.

		Dosimetry formalism					
Tissue	Dose constraint	EBRT (mean [n_{exc}])	EBRT + IORT(TARGIT) (mean [n_{exc}])	EBRT + IORT(V4.0) (mean [n_{exc}])	EBRT + IORT(C_Q) (mean [n_{exc}])	EBRT + IORT(MC_w) (mean [n_{exc}])	EBRT + IORT(MC_{het}) (mean [n_{exc}])
Brainstem	66	50.3 [0]	60.8 [**2**]	63.9 [**3**]	66.0 [**3**]	64.7 [**3**]	**67.4** [**3**]
Chiasm	55	40.7 [0]	42.9 [**2**]	43.4 [**2**]	43.7 [**2**]	43.1 [**2**]	45.1 [**3**]
Optic Nerve R	55	34.0 [0]	35.1 [**1**]	35.3 [**1**]	35.4 [**1**]	35.0 [**1**]	37.8 [**2**]
Optic Nerve L	55	33.6 [0]	35.1 [0]	35.4 [0]	35.6 [**1**]	35.0 [0]	39.0 [**2**]
Retina R	50	16.1 [0]	16.5 [0]	16.6 [0]	16.6 [0]	16.3 [0]	16.2 [0]
Retina L	50	11.0 [0]	11.2 [0]	11.2 [0]	11.2 [0]	11.1 [0]	11.0 [0]
Lens R	7	5.1 [**2**]	5.3 [**3**]	5.3 [**3**]	5.3 [**3**]	5.2 [**2**]	5.1 [**2**]
Lens L	7	5.3 [**2**]	5.5 [**2**]	5.5 [**2**]	5.5 [**2**]	5.4 [**2**]	5.4 [**2**]

Abbreviations: EBRT = external beam radiotherapy; IORT = intraoperative radiotherapy.

A notched box-and-whisker plot of the $D_{0.03\mathrm{cc}}$ to OARs' distribution is shown in Figure 5.1. The figure highlights the increased OAR dose exceeding the constraints for the brainstem, optic chiasm, and optic nerves when adding the EBRT and IORT plans compared to the EBRT plan alone. The outliers above the brainstem boxes in the plot resulted from one case where the treatment volume was in close proximity to the OAR, causing the largest impact in the MC_{het} dose distribution for this OAR. In fact, although the mean dose calculated with the MC_{het} method to the brainstem exceeded its dose constraint of 66 Gy (Table 5.4), Figure 5.1 reveals that this mean augmentation with respect to the calculated dose to water is due to the outlier. The notches in the plot represent the 95% confidence interval (95% CI) of the median. For the brainstem, the median EBRT-only $D_{0.03\mathrm{cc}}$ was 51.7 (95% CI: 47.7—55.6), and for the combined plans was 61.8 (95% CI: 56.6—67.0), 63.3 (95% CI: 56.4—70.2), 64.4 (95% CI: 56.3—72.5), 63.9 (95% CI: 56.2—71.7), and 62.7 (95% CI: 56.1—69.4) when using the TARGIT, V4.0, C_Q, MC_w and MC_{het} IORT calculation methods, respectively. With the exception of retinae, a Wilcoxon signed rank test shows that all OAR $D_{0.03\mathrm{cc}}$ calculated with the combined EBRT+IORT methods were statistically significantly higher (with $p < 0.05$) than the $D_{0.03\mathrm{cc}}$ calculated with the EBRT plan alone.

5.5.2 Uncertainty Estimation

The calibration data provided by Zeiss includes uncertainty on the applicator transfer coefficients due to positional tolerances of the spherical applicators. The positional tolerances lead to type B uncertainty in TARGIT dose rate at the reference 1 cm from the applicators' surface ranging from 2.8% to 6.3%, with the maximum exhibited near the smallest 1.5 cm diameter applicator due to the steep dose gradient in the proximity of the source. The maximum standard error in the conversion factor, $f'(z)$, is reported as 5.1% in the Water Phantom Instruction Manual [13]. The calibration certificate of the PTW 34013 ionization chamber reports an uncertainty of 2% for the product

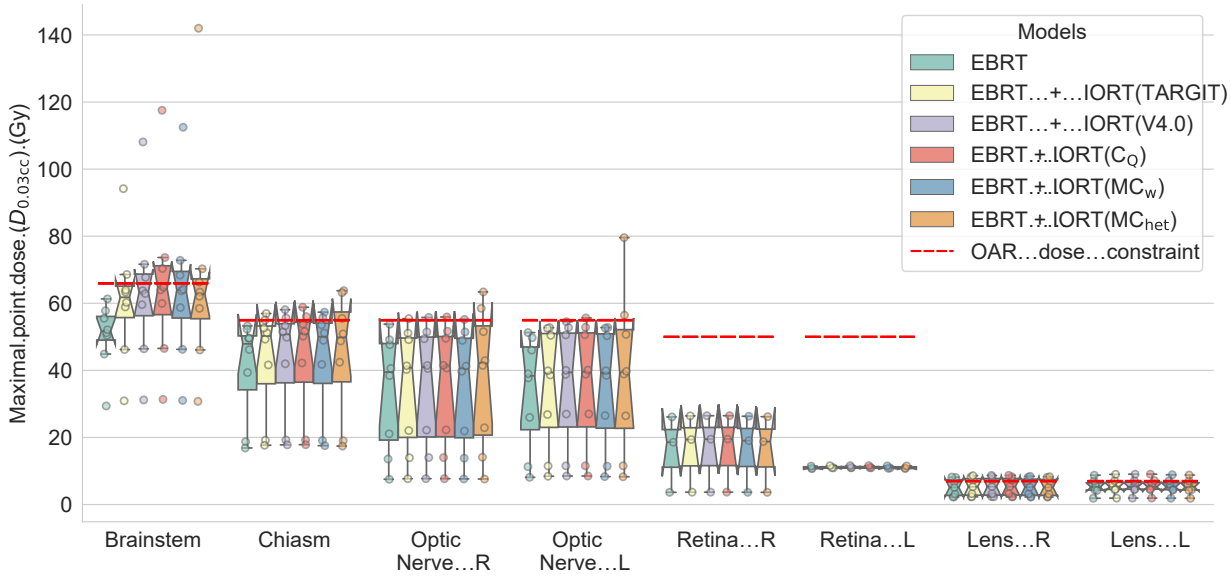

Figure 5.1 Maximal point dose to planning risk volumes (PRV) obtained for the EBRT-only and for the combined EBRT + IORT plans, using the IORT obtained according to the TARGIT, the Zeiss V4.0, the C_Q, the MC to water (MC_w), and the MC to tissue (MC_{het}) dosimetry formalisms. Circles represent individual cases, and the coloured boxes enclose the interquartile range (Q1–Q3) of the median. The dose constraints are shown in dashed red for reference. *Abbreviations:* $D_{0.03cc}$ = maximal dose received by a volume greater than 0.03 cm^3; EBRT = external beam radiotherapy; IORT = intraoperative radiotherapy; OAR = organ at risk.

k_Q $k_{K_a \to D_w}$. It was found that C_Q uncertainties are dependent on the geometry tolerance of the ionization chamber, dominated by the cavity plate separation [6]. This uncertainty was reported in Appendix E1 of Watson et al. [7] to be 1.2 to 1.8% and the C_Q fit uncertainty was reported to be in the range 0.5 to 1.1% at the reference position. These values led to combined uncertainties (k = 1) of 4.4, 6.8, and 7.3%, averaged over all applicator diameters, for the TARGIT, V4.0, and C_Q dose rates, respectively. The uncertainty budget for all the dose calculation formalisms is summarized in Table 5.5.

We performed MC simulations for each of the eight study cases using 1×10^8 histories from the corresponding applicator's phase space file. The resulting type A uncertainty was on average 0.2% at a distance of 1 cm from the applicator surface. Table 5.5 summarizes the MC type A uncertainties for the three applicators used in the study, for both MC_w and MC_{het} formalisms. The uncertainty remained below 0.5% along the source axis for all applicators at distances up to 5 cm from the source tip. However, the type A statistical uncertainty increased with distance from the source due to a reduction in photon fluence in distant voxels. The maximum value of 0.5% was observed in a heterogeneous phantom, in which the presence of bone caused an increased photon attenuation due to its higher mass energy absorption coefficient. The type B uncertainties related to the manufacturing and geometry of the aluminum filter present in the smaller applicators were assessed by performing simulations with different filter thicknesses and axial positions inside the applicator, within the tolerances reported by the manufacturer. The results showed that

dose uncertainties were dependent on the distance from the source and the polar angle around the applicator, and were evaluated to be up to 1.5% at 1 cm from the applicator surface, on its longitudinal axis, leading to combined MC uncertainties of less than 1.3% at this position.

Table 5.5 Uncertainty on the dose rate estimated at 10 mm from the surface of each spherical applicator, along the source axis, for the TARGIT, V4.0, C_Q, MC_w, and MC_{het} formalisms.

	Applicator diameter (mm)							
Uncertainty component	15	20	25	30	35	40	45	50
TARGIT formalism								
Positional uncertainty (%)	6.3	6.1	4.2	4.6	4.2	3.9	2.8	3.1
Standard uncertainty (%, k = 1)	**6.3**	**6.1**	**4.2**	**4.6**	**4.2**	**3.9**	**2.8**	**3.1**
V4.0 formalism								
Positional uncertainty (%)	6.3	6.1	4.2	4.6	4.2	3.9	2.8	3.1
$f'(z)$ conversion factor (%)	5.1	5.1	5.1	5.1	5.1	5.1	5.1	5.1
Standard uncertainty (%, k = 1)	**8.1**	**8.0**	**6.6**	**6.9**	**6.6**	**6.4**	**5.8**	**6.0**
C_Q formalism								
Positional uncertainty (%)	6.3	6.1	4.2	4.6	4.2	3.9	2.8	3.1
$f'(z)$ conversion factor (%)	5.1	5.1	5.1	5.1	5.1	5.1	5.1	5.1
$k_Q\, k_{K_a \to D_w}$ (%)	2.0	2.0	2.0	2.0	2.0	2.0	2.0	2.0
C_Q geom (%)	1.8	1.7	1.6	1.4	1.3	1.2	1.2	1.2
C_Q fit (%)	0.5	0.5	0.5	0.6	0.7	0.8	1.0	1.1
Standard uncertainty (%, k = 1)	**8.6**	**8.4**	**7.1**	**7.3**	**7.1**	**6.9**	**6.3**	**6.5**
MC_w formalism								
Statistical uncertainty (%)	—	—	—	0.2	0.2	0.2	—	—
Al filter geometry (%)	1.3	1.5	1.1	1.3	NA	NA	NA	NA
Standard uncertainty (%, k = 1)	—	—	—	**1.3**	**0.2**	**0.2**	—	—
MC_{het} formalism								
Statistical uncertainty (%)	—	—	—	0.2	0.2	0.2	—	—
Al filter geometry (%)	1.3	1.5	1.1	1.3	NA	NA	NA	NA
Standard uncertainty (%, k = 1)	—	—	—	**1.3**	**0.2**	**0.2**	—	—

5.6 Discussion

The OAR dose results presented in Table 5.3 are an indication that the current standard TARGIT method is underestimating the actual dose received by GBM patients. This is consistent with previous investigations and published studies. Watson et al. [6] reported that the estimated TARGIT dose was lower than the V4.0 and the C_Q dose with differences up to 60% and 80%, respectively, at 5 mm from the applicator surface. Shaikh et al. [9] reported that

the V4.0 predicted dose rates were 16% to 43% greater than the TARGIT dose rates at the applicators' surface. The calibration data provided by the manufacturer for the source used in this study indicates that the TARGIT dose is smaller than the V4.0 dose, with differences varying from 14% to 30% at the applicators' surface, and the maximum difference exhibited at the surface of the 1.5 cm diameter applicator. Although the TARGIT method employed in INTRAGO allows consistency with dose prescription used in the TARGIT trial, there is strong evidence that the patients are receiving significantly higher physical doses to the GBM resection cavity than planned [7].

The underestimation of the IORT dose has implications in the evaluation of the OAR dose when combining IORT and EBRT doses in the course of GBM treatment. Table 5.4 shows higher dose estimations with methods other than TARGIT, leading to OAR doses in excess of the recommended OAR dose constraints. Our analysis showed that the dose constraint to the brainstem was exceeded in one additional case when evaluated with the more accurate methods presented here. In clinical practice, having an accurate IORT dose assessment, in this case, could have potentially resulted in a more conservative dose prescription from IORT or subsequent EBRT. Ultimately, more accurate IORT dose information allows the radiation oncologist to design safer, more efficacious treatment plans, and potentially avoid serious side effects from OAR overdose.

Compared with the MC simulations in water, the C_Q method resulted in one additional patient exceeding the optic nerve dose constraint, and the V4.0 and C_Q methods exhibited one additional case exceeding the lens' dose constraint. The differences in these methods can at least partially be attributed to the effect of the source and applicators' polar anisotropy, only accounted for in the MC methods, which has been reported to reach values of up to 27% [12].

The tissue heterogeneity effect in the dose calculation can be seen from Table 5.4 where the brainstem mean dose has exceeded the dose constraint, in contrast with all in-water calculation methods. The absorbed dose evaluated according to MC_{het} was higher for the brainstem, optic chiasm, and optic nerves, compared to all the other methods, and three additional cases were found to exceed the optic nerves dose constraint, in relation to MC_w. The aforementioned results indicate that an IORT TPS should account for tissue heterogeneity for accurate dose estimations. The report of the AAPM TG-186 examines the impact of tissue composition on the absorbed dose, and their evaluation covers the energy regime relevant to the INTRABEAM source [28]. In general, water-based methods satisfying the TG-43 formalism conditions tend to underestimate the dose to bone and overestimate the dose covering the PTV. This effect is correlated to the tissue-to-water ratio of mass energy absorption coefficients at photon energies below 50 keV, where the photoelectric effect takes predominance, which is larger for bone and lower for air, adipose, and soft tissues. The dose distribution will be also affected by other factors such as attenuation in bony tissue and reduced backscatter from air outside the body contour. For instance, the lower backscatter in air may be correlated to the observed reduction of dose to lens in Table 5.4. It was also noted a marked absorbed dose reduction behind bone in one of the cases that resulted in a lower dose to optic nerves. It should be noted that the OAR dose evaluation was estimated based on the PRVs recommended in the INTRAGO protocol. These volumes were generated around the OARs without differentiating enclosed types of tissue, and they were found to add bone voxels in some OARs. To better estimate the impact of the added bone tissue in OAR dose estimation, new DVHs were generated using PRVs without bone voxels. As the first evident results, the major outliers that took place for the optic chiasm and optic nerves in the MC_{het} distribution, as seen in Figure 5.1, were removed, with a subsequent reduction in the OAR dose median and mean. The MC_{het} brainstem outlier decreased to 123 Gy $D_{0.03cc}$, which was still higher than with all

other methods. In general, the new numbers of cases exceeding the dose constraints with the MC_{het} were identical to the estimated numbers with the MC_w method.

Current INTRAGO practice includes the evaluation of point doses to OARs based on the provided TARGIT dose rate curves, the prescription dose, and the distance of the OAR from the applicator surface. However, this method does not allow for three-dimensional dose distributions required in a TPS to generate DVHs for PTV and OARs, nor does it allow for an accurate evaluation of combined IORT and EBRT dose distributions. Besides, a manual estimation of point doses to each OAR is time consuming and prone to human errors, especially when the 'apparent' closest point of the OAR to the applicator is not really the one receiving the highest dose due to, for example, tissue heterogeneity effects. Table 5.4 shows a significant number of patients exceeding the dose constraints for brainstem, optic chiasm, optic nerves, and an additional patient for the lens when using the TARGIT method, compared to the EBRT-only plan. Furthermore, not accounting for IORT doses properly may lead to significantly different OAR dose estimations as evidenced in the brainstem dose distributions of Figure 5.1 where the median EBRT-only $D_{0.03\mathrm{cc}}$ was statistically significantly lower, at the 95% confidence level (two sigma), than the median $D_{0.03\mathrm{cc}}$ of any of the combined plans. In fact, the Wilcoxon signed rank test showed that all combined EBRT+IORT methods resulted in significantly higher $D_{0.03\mathrm{cc}}$ to all OARs, except retinae, than the EBRT-only plan. This is evidence of the importance of properly accounting for the OAR dose received during IORT, which is not negligible. These deviations were not identified in the current practice in the INTRAGO study, demonstrating the inaccuracies in underlying assumptions related to the current standard INTRAGO procedure that lacks a computational dose calculation. RADIANCE (GMV Innovating Solutions, Madrid, Spain) is a dedicated TPS for IORT that aims to overcome this limitation by allowing the calculation of IORT dose distributions with MC and its combination with EBRT dose on patient CT data sets [29]. This tool has yet to become widely deployed for use in INTRABEAM treatment planning and, to date, it has not been used to determine OAR doses received during GBM treatments within the INTRAGO trial, to our knowledge. We have developed an application on the in-house `Brems` software tailored for IORT dose calculations from INTRABEAM on patients' CT with MC.

The present study is based on the clinical INTRAGO workflow, in which the IORT dose is converted to EQD2 and then added to the EBRT dose, as planned for 2 Gy fractions without further dose manipulation. It should be noted, however, that the 2 Gy per EBRT fraction is only occurring at the prescription isodose, with different dose values actually delivered at other locations in the patient, especially where the OARs of interest may be located. This discrepancy in the dose per fraction can lead to a different biological response in each type of tissue. Some centers have started incorporating TPS that account for EQD2 conversion of EBRT dose distributions. We have conducted a preliminary investigation of the effect of converting the EBRT dose to EQD2. In the eight studied cases, the differences in the OAR dose distributions were not statistically significant, within the 95% confidence interval of the median, for EBRT only, and for each plan combination with all IORT calculation methods. However, more research is needed and planned for an extended patient cohort.

This is a retrospective study with some limitations. One potential limitation is the accuracy of the source/applicator placement in the CT images and the cavity deformation during our dose estimations. We acknowledge that the exact position of the applicator during IORT and the deformation of the cavity with the applicator in place could impact the accuracy of the calculated $D_{0.03\mathrm{cc}}$ to OARs. While we made an effort to determine the applicator's position and orientation with respect to the treatment cavity using the co-registered postoperative MRI

on the planning CT, we acknowledge that this method has some inherent limitations. Intraoperative imaging to determine the exact deformation of the cavity with the applicator in place and the exact position of the applicator during IORT would improve the accuracy of the dose estimation, but obtaining intraoperative images would add time and complexity to the procedure. Another limitation is that the current dose calculations rely on EBRT planning CT obtained after IORT was completed. Therefore, it is of interest to incorporate intraoperative dose calculations that will allow better estimation of IORT irradiation times and prescription dose limitations before delivering the radiation treatment. Different studies have evaluated the feasibility of using intraoperative images for IORT treatment planning. Namely, the dosimetry during breast intraoperative electron radiotherapy (IOERT) has been successfully implemented with the intraoperative C-arm and O-arm systems [30, 31]. The CT on-rails system has also been used for intraoperative dosimetry of breast high dose rate IORT [32–35]. Besides the feasibility of intraoperative imaging, the calculation times with the MC model for this study were short, with an average time per node spanning within the range of 8–19 minutes when using predefined phase space files from the applicators' surface. Therefore, the inclusion of intraoperative MC calculations in the IORT clinical workflow is both practical and accurate.

5.7 Conclusion

A retrospective study has been conducted on patients that received IORT for GBM, in combination with EBRT, within the INTRAGO clinical trial, and is the first in evaluating OAR dose estimated with different IORT dosimetry formalisms. For this purpose, we have used an in-house developed treatment planning framework to calculate patient-specific volumetric dose from IORT and to combine it with adjuvant EBRT dose. The methodology was applied to a cohort of GBM cases in the context of the INTRAGO clinical trial and has revealed inaccuracies in the current standard procedure. Properly accounting for the combined IORT and EBRT doses reveal that patients can exceed the OAR dose constraints. Moreover, the study shows that the TARGIT dosimetry formalism used when planning patients underestimates the dose to OARs. In fact, if accurate IORT dose distributions were provided at the time of planning, some patients could have had the IORT dose reduced, or they could have been removed from the INTRAGO trial. In our cohort of eight INTRAGO patients, the most accurate $\mathrm{MC}_{\mathrm{het}}$ dose calculation revealed that one additional patient exceeded the OAR dose constraint for the brainstem, one for optic chiasm, and three for optic nerves.

Ideally, INTRAGO IORT planning would involve patient-specific MC tissue dose calculation, which would be incorporated into the optimization of the EBRT plan.

Acknowledgements

The authors wish to thank Mathias Benker of Carl Zeiss for details on the INTRABEAM spherical applicators. D.S. Ayala Alvarez acknowledges the financial support from the Fonds de recherche du Québec – Santé (FRQS, grant number: 292924). This work was funded in part by the Canadian Institutes of Health Research (CIHR, Foundation Grant No. FDN-143257), and by the Natural Sciences and Engineering Research Council (NSERC, Grant No. RGPIN-2019-06746). J. Seuntjens has a patent pertaining to surgical cavity sizers for brachytherapy and intraopera-

tive radiation therapy (US Patent US20160287901A1). P. Watson received travel support from Zeiss to present part of this work at the 2022 International Low Energy X-ray IORT User Meeting (ILEXIUM), Bonn, Germany.

References

[1] R. Stupp *et al.*, "Radiotherapy plus concomitant and adjuvant temozolomide for glioblastoma," *New England journal of medicine*, vol. 352, no. 10, pp. 987–996, 2005.

[2] R. Stupp *et al.*, "Effects of radiotherapy with concomitant and adjuvant temozolomide versus radiotherapy alone on survival in glioblastoma in a randomised phase III study: 5-year analysis of the EORTC-NCIC trial," *The Lancet Oncology*, vol. 10, no. 5, pp. 459–466, 2009.

[3] F. A. Giordano *et al.*, "INTRAGO: Intraoperative radiotherapy in glioblastoma multiforme – a Phase I/II dose escalation study," *BMC Cancer*, vol. 14, no. 1, p. 992, 2014.

[4] F. A. Giordano *et al.*, "Intraoperative radiotherapy in newly diagnosed glioblastoma (INTRAGO): An open-label, dose-escalation phase I/II trial," *Neurosurgery*, vol. 84, no. 1, pp. 41–49, 2019.

[5] J. S. Vaidya *et al.*, "Risk-adapted targeted intraoperative radiotherapy versus whole-breast radiotherapy for breast cancer: 5-year results for local control and overall survival from the TARGIT-A randomised trial," *The Lancet*, vol. 383, no. 9917, pp. 603–613, 2014.

[6] P. G. F. Watson, H. Bekerat, P. Papaconstadopoulos, S. Davis, and J. Seuntjens, "An investigation into the INTRABEAM miniature x-ray source dosimetry using ionization chamber and radiochromic film measurements," *Medical Physics*, vol. 45, no. 9, pp. 4274–4286, 2018.

[7] P. G. F. Watson, M. Popovic, L. Liang, N. Tomic, S. Devic, and J. Seuntjens, "Clinical Implication of Dosimetry Formalisms for Electronic Low-Energy Photon Intraoperative Radiation Therapy," *Practical Radiation Oncology*, vol. 11, no. 1, e114–e121, 2021.

[8] W. S. Culberson *et al.*, "Dose-rate considerations for the INTRABEAM electronic brachytherapy system: Report from the American association of physicists in medicine task group no. 292," *Medical Physics*, vol. 47, no. 8, e913–e919, 2020.

[9] M. Y. Shaikh, J. Burmeister, R. Scott, L. K. Kumaraswamy, A. Nalichowski, and M. C. Joiner, "Dosimetric evaluation of incorporating the revised V4.0 calibration protocol for breast intraoperative radiotherapy with the INTRABEAM system," *Journal of Applied Clinical Medical Physics*, vol. 21, no. 2, pp. 50–59, 2020.

[10] A. Abudra'a, B. Chauvenet, J. Gouriou, J. Plagnard, R. Itti, and I. Aubineau-Lanièce, "Dosimetry formalism and calibration procedure for electronic brachytherapy sources in terms of absorbed dose to water," *Physics in Medicine and Biology*, vol. 65, no. 14, p. 145 006, 2020.

[11] D. S. Ayala Alvarez, P. G. F. Watson, M. Popovic, V. J. Heng, M. D. C. Evans, and J. Seuntjens, "Monte Carlo calculation of the relative TG-43 dosimetry parameters for the INTRABEAM electronic brachytherapy source," *Physics in Medicine and Biology*, vol. 65, no. 24, p. 245 041, 2020.

[12] D. S. Ayala Alvarez, P. G. F. Watson, M. Popovic, V. J. Heng, M. D. C. Evans, and J. Seuntjens, "Monte Carlo calculation of the TG-43 dosimetry parameters for the INTRABEAM source with spherical applicators," *Physics in Medicine & Biology*, vol. 66, no. 21, p. 215 017, 2021.

[13] Carl Zeiss Meditec AG, "INTRABEAM water phantom – instructions for use, G-30-1767-en version 5.0," manual, 2015.

[14] M. J. P. Chamberland, R. E. P. Taylor, D. W. O. Rogers, and R. M. Thomson, "Egs_brachy: A versatile and fast Monte Carlo code for brachytherapy," *Physics in Medicine & Biology*, vol. 61, no. 23, pp. 8214–8231, 2016.

[15] O. Nwankwo, S. Clausen, F. Schneider, and F. Wenz, "A virtual source model of a kilovoltage radiotherapy device," *Physics in Medicine & Biology*, vol. 58, no. 7, pp. 2363–2375, 2013.

[16] P. G. F. Watson, M. Popovic, and J. Seuntjens, "Determination of absorbed dose to water from a miniature kilovoltage x-ray source using a parallel-plate ionization chamber," *Physics in Medicine and Biology*, vol. 63, no. 1, p. 015 016, 2017.

[17] I. Kawrakow and D. W. O. Rogers, "The EGSnrc code system: Monte Carlo simulation of electron and photon transport," National Research Council Canada, Ottawa, Canada, Tech. Rep. PIRS-701, 2019.

[18] I. Kawrakow, E. Mainegra-Hing, F. Tessier, and B. R. B. Walters, "The egsnrc C++ class library, NRC report PIRS-898 (rev a)," National Research Council Canada, Ottawa, Canada, Tech. Rep., 2009.

[19] M. J. Berger *et al.*, "XCOM: Photon cross sections database (version 1.5). [Online] available: Http://physics.nist.gov/xcom (accessed september 2020)," *National Institute of Standards and Technology, Gaithersburg, MD*, 2010.

[20] D. Bote and F. Salvat, "Calculations of inner-shell ionization by electron impact with the distorted-wave and plane-wave Born approximations," *Physical Review A*, vol. 77, no. 4, p. 042 701, 2008.

[21] P. G. Watson and J. Seuntjens, "Effect of explicit M and N-shell atomic transitions on a low-energy x-ray source," *Medical physics*, vol. 43, no. 4, pp. 1760–1763, 2016.

[22] International Commission on Radiation Units and Measurements, *ICRU Report 44, Tissue substitutes in radiation dosimetry and measurement*. ICRU Publications, Bethesda, MD, 1989.

[23] International Commission on Radiation Units and Measurements, *ICRU Report 46, Photon, electron, proton and neutron interaction data for body tissues*. ICRU Publications, Bethesda, MD, 1992.

[24] J. Valentin, "Basic anatomical and physiological data for use in radiological protection: Reference values: ICRP Publication 89," *Annals of the ICRP*, vol. 32, no. 3-4, pp. 1–277, 2002.

[25] Carl Zeiss Meditec AG, "INTRABEAM dosimetry, brochure EN_30_010_155ii," manual, 2011.

[26] C. Herskind *et al.*, "Biology of high single doses of IORT: RBE, 5 R's, and other biological aspects," *Radiation Oncology*, vol. 12, no. 1, pp. 1–14, 2017.

[27] Q. Liu, F. Schneider, L. Ma, F. Wenz, and C. Herskind, "Relative Biologic Effectiveness (RBE) of 50 kV X-rays measured in a phantom for intraoperative tumor-bed irradiation," *International Journal of Radiation Oncology* Biology* Physics*, vol. 85, no. 4, pp. 1127–1133, 2013.

[28] L. Beaulieu *et al.*, "Report of the Task Group 186 on model-based dose calculation methods in brachytherapy beyond the TG-43 formalism: Current status and recommendations for clinical implementation," *Medical physics*, vol. 39, no. 10, pp. 6208–6236, 2012.

[29] M. F. Valdivieso-Casique *et al.*, "RADIANCE—A planning software for intra-operative radiation therapy," *Translational Cancer Research*, vol. 4, no. 2, pp. 196–209, 2015.

[30] H. R. Baghani, M. Robatjazi, S. R. Mahdavi, N. Nafissi, and M. E. Akbari, "Breast intraoperative electron radiotherapy: Image-based setup verification and in-vivo dosimetry," *Physica Medica*, vol. 60, pp. 37–43, 2019.

[31] V. García-Vázquez *et al.*, "Assessment of intraoperative 3D imaging alternatives for IOERT dose estimation," *Zeitschrift für Medizinische Physik*, vol. 27, no. 3, pp. 218–231, 2017.

[32] S. W. Dutta *et al.*, "Implementation of an HDR brachytherapy–based breast IORT program: Initial experiences," *Brachytherapy*, vol. 18, no. 3, pp. 285–291, 2019.

[33] D. M. Trifiletti *et al.*, "Intraoperative breast radiation therapy with image guidance: Findings from CT images obtained in a prospective trial of intraoperative high-dose-rate brachytherapy with CT on rails," *Brachytherapy*, vol. 14, no. 6, pp. 919–924, 2015.

[34] R. Jones *et al.*, "Dosimetric comparison of 192Ir high-dose-rate brachytherapy vs. 50 kV x-rays as techniques for breast intraoperative radiation therapy: Conceptual development of image-guided intraoperative brachytherapy using a multilumen balloon applicator and in-room CT imaging," *Brachytherapy*, vol. 13, no. 5, pp. 502–507, 2014.

[35] T. E. Hassinger *et al.*, "Utility of CT imaging in a novel form of high-dose-rate intraoperative breast radiation therapy," *Journal of medical imaging and radiation oncology*, vol. 62, no. 6, pp. 835–840, 2018.

Chapter 6

Evaluation of the TG-43 formalism for INTRABEAM intraoperative radiotherapy dosimetry in glioblastoma treatment

David Santiago Ayala Alvarez, Peter G. F. Watson, Marija Popovic, Veng Jean Heng, Michael D. C. Evans, Valerie Panet-Raymond and Jan Seuntjens

Article in preparation for submission to *Medical Physics*

6.1 Preface

This chapter represents the culmination of the dosimetric investigations presented in this thesis, focusing on the evaluation of the TG-43 formalism for INTRABEAM IORT dosimetry in glioblastoma treatment. Building on the foundational work of Chapters 3 and 4, and informed by the clinical dosimetry comparisons in Chapter 5, this study provides a comprehensive assessment of the TG-43 approach in a clinical context. It addresses the critical question of whether the TG-43 formalism can offer a practical compromise between computational efficiency and dosimetric accuracy for routine clinical use.

This chapter offers valuable insights into the potential for improving IORT dosimetry in clinical practice by comparing TG-43 calculations with both the current clinical standard (TARGIT method) and more complex Monte Carlo simulations. The findings presented here directly inform the discussion on future research directions and the potential for clinical implementation of advanced dosimetry methods in IORT for GBM treatment.

6.2 Abstract

Background: Intraoperative radiation therapy (IORT) using the INTRABEAM system has shown promise in glioblastoma treatment. However, accurate dosimetry remains challenging due to the low-energy photons used and the complex tissue heterogeneities in the brain. Current clinical practice relies on the TARGIT method, but more sophisticated approaches, including the TG-43 formalism and Monte Carlo (MC) simulations, warrant investigation for potential improvements in dose calculation accuracy.
Purpose: To evaluate the TG-43 dosimetry formalism for IORT dose calculations in glioblastoma treatment using the INTRABEAM system, comparing it with the TARGIT method and MC simulations.
Methods: We analyzed the dose distributions in 20 patients from the INTRAGO trial. The TG-43 formalism was validated against MC simulations in water (MC_w) using global/local dose differences and gamma analysis (1%/1mm). Organ at risk (OAR) doses were calculated using TG-43, TARGIT, MC_w, and MC in heterogeneous media (MC_{het}). Combined IORT and external beam radiotherapy (EBRT) doses were evaluated.
Results: TG-43 showed good agreement with MC_w, with a 98.0% gamma pass rate. The mean global dose difference was -0.07% $\pm$ 0.29%. For OARs, TG-43 and MC_w were similar (mean differences $\leq$0.1%), while TARGIT underestimated doses by 0.1-1.7%. MC_{het} showed larger deviations, especially near bony structures (up to 1.9% $\pm$ 1.4% for optic nerves). Combined IORT+EBRT analysis revealed more OAR constraint violations than identified by current clinical practice. Calculation times for TG-43 (0.6 seconds on average) were significantly shorter than for MC simulations (16-18 hours on a computing cluster).
Conclusions: The TG-43 formalism provides a reasonable compromise between accuracy and computational efficiency for IORT dose calculations in glioblastoma treatment. It offers improved accuracy over TARGIT while being more clinically feasible than full MC simulations. Implementation of TG-43 or similar 3D dose calculation methods could enhance IORT treatment planning and OAR dose estimation.

6.3 Introduction

Among primary brain malignancies, glioblastoma stands out as the most aggressive, with patients typically surviving only slightly more than a year, even with the application of current therapeutic approaches [1, 2]. Standard of care management includes surgery, followed by external beam radiation therapy (EBRT) and chemotherapy. Intraoperative radiotherapy (IORT) has emerged as a promising approach to enhance locoregional tumour control by delivering a single post-resection high dose of radiation directly to the tumour bed.

The INTRABEAM system (Carl Zeiss Meditec AG, Jena, Germany) is widely used for IORT in various cancer treatments, including glioblastoma. It features a miniature X-ray source producing low-energy photons (50 kVp) and can be combined with spherical applicators to match the resection cavity size. However, accurate dosimetry for IORT remains challenging, especially in complex anatomical sites like the brain, due to steep dose gradients and tissue heterogeneities.

Currently, the most accepted clinical practice for INTRABEAM IORT dosimetry relies on the TARGeted Intraoperative radioTherapy (TARGIT) method, using vendor-provided in-water depth dose curves [3]. Recent studies have highlighted significant discrepancies between TARGIT-estimated doses and actual delivered doses, raising con-

cerns about the accuracy of this approach [4–8].

Alternative methods have been proposed to address these dosimetry challenges. The TG-43 formalism [9], widely used in brachytherapy, has shown promise in accurately estimating dose distributions for the INTRABEAM system [10, 11]. This approach generates full 3D dose distributions in water while being computationally efficient. However, its application in IORT for glioblastoma treatment requires clinical evaluation. Monte Carlo (MC) simulations represent the gold standard for dose calculations, especially in scenarios involving complex geometries and tissue heterogeneities. While MC methods can account for factors such as tissue composition variations and applicator design, the computational resources required can be prohibitive for routine clinical use in IORT.

The INTRAGO clinical trial is currently assessing the impact of IORT on survival in glioblastoma patients [12]. This trial relies on the TARGIT method for dose calculations, which may lead to inaccuracies in estimating doses to organs at risk (OARs). A more accurate dosimetry method could potentially improve treatment planning and outcome assessment. Recent advancements in IORT dosimetry include the development of dedicated treatment planning systems (TPS), such as RADIANCE (GMV Innovating Solutions, Madrid, Spain), which aims to provide more accurate dose calculations using MC simulations [13]. However, the adoption of such systems in clinical practice for glioblastoma treatments remains limited.

This study aims to evaluate the TG-43 dosimetry formalism for OAR dose calculations and dose distributions in IORT for glioblastoma using the INTRABEAM system. We compare TG-43 doses with the standard TARGIT method and more sophisticated MC simulations, including both dose-to-water (MC_w) and dose-to-tissue (MC_{het}) approaches. By analyzing a cohort of 20 patients from the INTRAGO trial, we explore the potential of the TG-43 formalism to improve the accuracy of dose calculations in clinical practice.

Our investigation includes a comprehensive validation of the TG-43 formalism against MC simulations, followed by an analysis of its performance in estimating OAR doses. We also examine the impact of combining IORT with EBRT on cumulative OAR doses, a critical consideration in the context of the INTRAGO trial. Through this work, we aim to provide insights into the dosimetric accuracy and limitations of various calculation methods, focusing on the potential of the TG-43 formalism to enhance IORT treatment planning for glioblastoma.

6.4 Materials and Methods

6.4.1 Study design and data collection

This study involves a retrospective analysis of 20 patients enrolled in the INTRAGO clinical trial at McGill University Health Centre. The cohort consists of two arms: 10 patients who received IORT plus standard of care with EBRT, and 10 patients in the control arm who received standard EBRT without IORT. IORT patients underwent treatment using the INTRABEAM system following surgical resection, with prescribed doses ranging from 20 to 30 Gy delivered to the applicator surface. Preoperative and postoperative magnetic resonance imaging (MRI) scans guided surgery and treatment planning. Postoperative computed tomography (CT) scans were acquired for treatment planning several days before EBRT. The planning CT was co-registered with the postoperative MRI to define the planning target volume (PTV) and OARs.

For patients in the control arm, hypothetical IORT plans were created using average applicator diameters and

prescription doses from the IORT arm. The spherical applicator's center was positioned at the center of the gross tumour volume (GTV), with the source axis aligned with the PTV's central axis. Dose data were collected for eight OARs: brainstem, optic chiasm, optic nerves, retinae, and lenses.

6.4.2 Dosimetry formalisms

Four different dosimetry formalisms were evaluated for IORT dose calculations:

TARGIT method

The TARGIT method estimates the IORT dose using vendor-provided in-water depth dose curves. These curves, measured along the source axis according to the TARGIT protocol, determine the dose at a distance roughly indicative of the nearest separation to each OAR [7]. A fitting function to the calibration data was used to obtain TARGIT dose distributions in the patients' CT.

TG-43 formalism

The TG-43 formalism uses calculated dosimetry parameters such as dose-rate conversion coefficients, radial dose functions, and 2D anisotropy functions in water. Our implementation followed the updated TG-43 protocol recommendations [9] for its use in TPSs. Radial dose function and 2D anisotropy function data were obtained from our previous work on INTRABEAM with spherical applicators [11].

Dose distributions were calculated in CT voxelized phantoms using interpolation and extrapolation functions for tabulated data, per TG-43 recommendations. Due to the lack of standardized air-kerma data for INTRABEAM, we calculated the dose rate at the TG-43 reference position (1 cm from the applicator surface at 90 degrees in water) using the MC model employed in MC_w simulations. TG-43 calculations assumed water for the entire calculation volume, providing dose distributions similar to MC_w calculations. Dose rates were converted to absolute dose by normalizing with the irradiation time calculated to deliver the prescription dose to the applicator surface using the TARGIT method. These calculations were performed using a custom Python script, with results stored as DICOM files for each patient.

MC simulations

MC simulations were conducted using `egs_brachy` [14] from the EGSnrc code system to model the INTRABEAM source and spherical applicators. Simulations were performed in two phases:

1. An electron source with Gaussian energy distribution centered at 50 keV was modelled inside the INTRABEAM probe vacuum. Electrons collided with the gold target to produce photons through bremsstrahlung and fluorescence. Bremsstrahlung photon splitting and cross-section enhancement improved simulation efficiency and accuracy. A phase space file was scored at the spherical applicator surface for each applicator diameter.

2. Previously scored phase-space files were used as simulation sources. Particles were transported through patients' CT representation. Two MC methods were employed: a) MC_w: Simulates dose distributions in a uniform density water medium, assuming air outside the patient contour. b) MC_{het}: Accounts for tissue heterogeneity by assigning appropriate material densities and elemental compositions to different tissues based on published values from ICRU and ICRP [15–17].

The simulations used low-energy photon transport parameters, with electron transport turned off outside the source. This approximation is valid for the INTRABEAM's low-energy spectrum (maximum 50 keV), where secondary electron ranges in soft tissue are typically between 1 µm and 20 µm [18]. These ranges are considerably shorter than the voxel sizes used in our dose calculations, justifying the use of the electronic kerma approximation. The track-length estimator was used for efficient dose scoring. MCDF-XCOM photon cross-sections were utilized for higher accuracy. Table 6.1 summarizes the relevant MC characteristics and input parameters, following AAPM TG-268 recommendations [19].

The MC simulations provided results in Gy/history, which were then converted to clinical dose rates (Gy/min) for the INTRABEAM system operating at its nominal tube current of 40 µA. This conversion was performed using a factor of approximately 1.50×10^{16}, which accounts for the charge per electron and the operating current of the device. Dose distributions for TARGIT, TG-43, and MC models were stored as DICOM files. These files were used for dose distribution comparisons and OAR dose analyses using custom Python scripts and our in-house TPS, `Brems`. Following the calculation of IORT doses using these various methods, the resultant dose distributions were combined with the EBRT dose distributions for comprehensive analysis. This combination allowed for the evaluation of cumulative doses to OARs, accounting for both the high-dose IORT component and the fractionated EBRT regimen.

6.4.3 EBRT treatment planning

EBRT plans were developed for each patient following standard clinical protocols. Treatment planning was conducted using a postoperative CT acquired several days before EBRT initiation. This CT was co-registered with the postoperative MRI to facilitate accurate target volume delineation. The planning target volume (PTV) was defined on the planning CT as the peritumoral edema visible on the MRI plus a 2 cm margin. The EBRT prescription dose was 60 Gy delivered in 30 fractions, with the goal of covering 95% of the PTV.

EBRT plans were created using the intensity-modulated radiation therapy (IMRT) technique with the Varian Eclipse External Beam Planning TPS (version 15.6, Varian Medical Systems, Inc., Palo Alto, CA). Dose calculations were performed using the anisotropic analytical algorithm (AAA, version 11.0.31 or 15.5.06). The AAA calculates dose in water but accounts for tissue heterogeneities by adjusting for the electron density of each voxel in the patient's CT image [26, 27]. For the high energies used in EBRT (typically $\geq$ 6 MV), differences between dose calculated in water and dose to medium are generally small in soft tissues, though they can be more pronounced in bone or air cavities [28]. This contrasts with the low-energy regime of INTRABEAM IORT ($<$ 50 keV), where tissue composition effects are more significant. Plans were designed for delivery using a Varian TrueBeam linear accelerator.

For the combined EBRT and IORT dose analysis, the EBRT dose distributions from Eclipse were imported into

Table 6.1 Summary of the relevant MC characteristics and input parameters used in this study.

Item	Description	References
Code	EGSnrc 2019	Kawrakow and Rogers [20]
	`egs++` library, EGSnrc 2019 master branch	Kawrakow et al. [21]
	`egs_brachy` (v2017.09.15)	Chamberland et al. [14]
Validation	Previously validated	Ayala Alvarez et al. [10, 11]
Timing	The time required to obtain each applicator phase space was ∼10 h. The average time per node to obtain patient-specific dose distributions from the phase space was 6–26 minutes with a cluster of 160 cores split in six nodes of Intel(R) Xeon(R) CPU models: two E5-2697 v3 @ 2.60 GHz, two E5-2687W @ 3.10 GHz, a Gold 6140 @ 2.30 GHz, and a Gold 5220 @ 2.20 GHz	
Source description	Phase-space data stored at each applicator surface	Ayala Alvarez et al. [11]
Cross-sections	Photons (photoelectric and Rayleigh scattering): MCDF-XCOM	Sabbatucci and Salvat [22], Valdes-Cortez et al. [23]
	Compton: relativistic impulse approximation	Kawrakow and Rogers [20]
	Bremsstrahlung: NRC	Kawrakow and Rogers [20]
	Electron impact ionization: PENELOPE	Bote and Salvat [24]
	Atomic relaxations with explicit M and N-shell transitions: EADL	Watson and Seuntjens [25]
Transport parameters	Boundary crossing algorithm: Exact	Kawrakow and Rogers [20]
	PCUT = 1 keV. Electrons were not transported outside the source (ECUT = 1 MeV)	
Variance reduction techniques	Bremsstrahlung and photon cross-section enhancement, and uniform bremsstrahlung splitting were used when scoring phase spaces	Chamberland et al. [14]
Scored quantities	Absorbed dose (electronic kerma approximation)	
Histories/statistical uncertainty	1×10^8 histories from the phase space /average type A uncertainty of the scored dose at 1 cm from the applicator surface was 0.2%	
Statistical methods	History-by-history	Chamberland et al. [14]
Postprocessing	DVH data was obtained for each evaluated OAR	

Abbreviations: DVH = dose-volume histograms; OAR = organ at risk.

our in-house TPS, `Brems`. This allowed for the superposition of EBRT doses with the IORT doses calculated using various methods (TARGIT, TG-43, MC_w, and MC_{het}), enabling a comprehensive evaluation of cumulative dose to OARs.

6.4.4 Validation of TG-43 dose calculations

To validate TG-43 dose calculations, we performed a voxel-wise comparison against MC_w simulations for a patient case selected to be representative of typical treatment scenarios. This case, treated with a 40 mm applicator and a prescription dose of 30 Gy, was chosen based on several criteria: the tumor location was relatively centered in the brain, relatively close to multiple OARs, allowing visualization of dose distributions in all cardinal planes, and enabling comprehensive evaluation of dose calculation differences in regions of clinical interest. The anatomical location and treatment parameters (applicator size and prescription dose) were also consistent with median values observed across the patient cohort.

The analysis, conducted using DICOM dose files, included global dose differences, local dose differences, and gamma analysis. Global dose difference was calculated as the difference between MC_w and TG-43 doses, normalized to the prescription dose: Global difference $= 100 \times (D_{MC_w} - D_{\text{TG-43}})/D_{\text{prescription}}$, where D_{MC_w} and $D_{\text{TG-43}}$ are the doses calculated by MC_w and TG-43, respectively, and $D_{\text{prescription}}$ is the prescription dose. The local dose difference was calculated as the percentage difference relative to the local TG-43 dose: Local difference $= 100 \times (D_{MC_w} - D_{\text{TG-43}})/D_{\text{TG-43}}$. These definitions align with those provided by Beaulieu et al. (2023) for commissioning model-based dose calculation algorithms [29].

A critical difference between TG-43 and MC_w simulations was the treatment of the external medium. TG-43 assumed water everywhere, while MC_w used air outside the patient's contour, affecting backscatter radiation near the patient's skin. Gamma analysis with 1%/1mm criteria assessed overall agreement between TG-43 and MC_w distributions. Voxels outside the patient contour and inside the applicator were excluded from the analyses. Axial, coronal, and sagittal views of dose differences and gamma index distributions were generated, along with histograms. Isodose lines for both TG-43 and MC_w calculations were overlaid to facilitate visual comparison.

6.4.5 TPS and OAR dose calculations

Following the validation of TG-43 calculations, the impact of different models on OAR dose was evaluated for all 20 patients in the study cohort. A new IORT module was developed in `Brems` to integrate IORT and EBRT doses, enabling cumulative dose-volume histogram (DVH) analyses for each patient. IORT doses were calculated using the TARGIT, TG-43, MC_w, and MC_{het} formalisms. To account for the difference in biological effectiveness between IORT and EBRT, IORT doses were converted to equivalent 2 Gy fractions (EQD2) using relative biological effectiveness of 1.5 for the INTRABEAM photon energy and an α/β ratio of 2 for OARs in the brain. Cumulative dose distributions were obtained by adding IORT and EBRT plans, and DVHs were generated for each OAR based on planning risk volumes, which add a 3-mm margin to each OAR.

As per the INTRAGO protocol, plan evaluation used the near maximum dose metric ($D_{0.03\text{cc}}$), defined as the minimum dose received by the hottest volume of 0.03 cm^3 in the OAR, as recommended by ICRU Report 91 for reporting doses to serial organs [30]. For the MC_{het} model, the dose metric was evaluated excluding enclosed bone voxels to avoid potential overestimation due to high atomic number. Bone structures were identified based on pre-contoured bone structures available in the RTSS files, which included delineations of OARs, GTV, PTV, and other relevant anatomical structures.

6.4.6 Data analysis

Data analysis was conducted using Python 3.9.13 with `numpy`, `pandas`, `matplotlib`, `seaborn`, and `scipy.stats` libraries. The study comprised two stages: first, validating TG-43 against MC_w simulations for a representative case, and second, comparing OAR doses across different dosimetry models for the entire cohort. Comprehensive descriptive statistics for the $D_{0.03cc}$ metric were calculated for each OAR and model, including mean, standard deviation, median, interquartile range (IQR), and 95% confidence interval (CI) of the median. The 95% CI was calculated as $\pm 1.57 \times \text{IQR}/\sqrt{n}$. To assess different calculation models, we computed absolute dose differences between each IORT model and TG-43, calculated as a percentage of the prescription dose:

$$\text{Absolute dose difference (\%)} = 100 \times \frac{\text{Model dose} - \text{TG-43 dose}}{\text{Prescription dose}} \tag{6.1}$$

Given the non-normal distribution of dose differences, we employed Wilcoxon signed-rank paired tests to compare doses calculated by each model (TARGIT, MC_w, MC_{het}) to TG-43 for each OAR. Visualization plots included boxplots showing $D_{0.03cc}$ distributions for each OAR and model for both IORT-only and combined EBRT+IORT scenarios, with individual data points and OAR dose constraints. Additional boxplots displayed absolute dose differences between each model and TG-43 for IORT-only scenarios.

For the validation stage, global dose difference analysis, local dose difference analysis, and gamma analysis (1%/1mm criteria) compared TG-43 and MC_w distributions. Histograms and axial, coronal, and sagittal views of dose differences and gamma index distributions were generated. All statistical tests used a significance level of $\alpha = 0.05$, with p-values of less than 0.001 reported as $p < 0.001$ for clarity.

6.5 Results

6.5.1 Validation of TG-43 dose calculations

The validation of TG-43 dose calculations against MC_w simulations was performed for a representative patient case treated with a 40 mm applicator and a prescription dose of 30 Gy. Figure 6.1 shows the global dose difference distribution between TG-43 and MC_w calculations. The global dose difference analysis yielded a mean difference of -0.07% with a standard deviation of 0.29% relative to the prescription dose. The majority of voxels (95%) had global dose differences within $\pm 0.5\%$ of the prescription dose, with maximum underestimation and overestimation by TG-43 of 16.2% and 67.6% of the prescription dose, respectively.

Figure 6.2 presents the results of the gamma analysis performed with 1%/1mm criteria. The analysis resulted in a pass rate of 98.0%, with a mean gamma index of 0.12 and a median of 0.04. The maximum gamma index observed was 6.85.

The local dose difference distribution between TG-43 and MC_w calculations is illustrated in Figure 6.3. The analysis revealed a mean difference of 1.2% with a standard deviation of 13.7% relative to the local TG-43 dose. The maximum local underestimation by TG-43 was 99.7%, while the maximum overestimation was 280.0%. Examination of the spatial distribution of dose differences showed that larger discrepancies occurred near the patient's

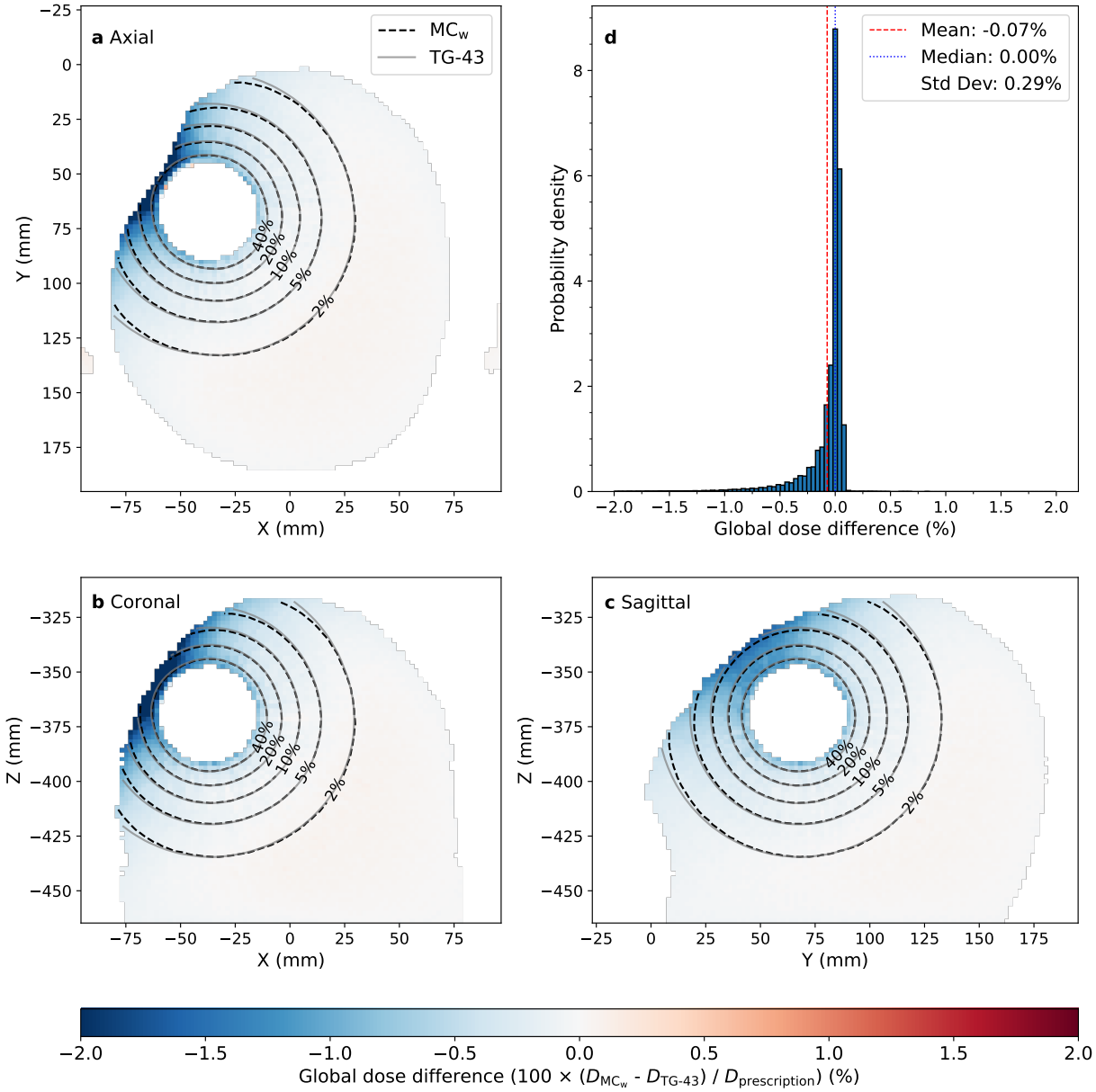

Figure 6.1 Global dose difference distribution between TG-43 and MC$_w$ calculations for a representative patient. (a) Axial, (b) coronal, and (c) sagittal views of the dose difference maps. (d) Histogram of global dose differences. The colorbar represents the percentage difference relative to the prescription dose. Isodose lines for 2%, 5%, 10%, 20%, and 40% of the prescription dose are shown for both TG-43 (solid gray) and MC$_w$ (dashed black) calculations.

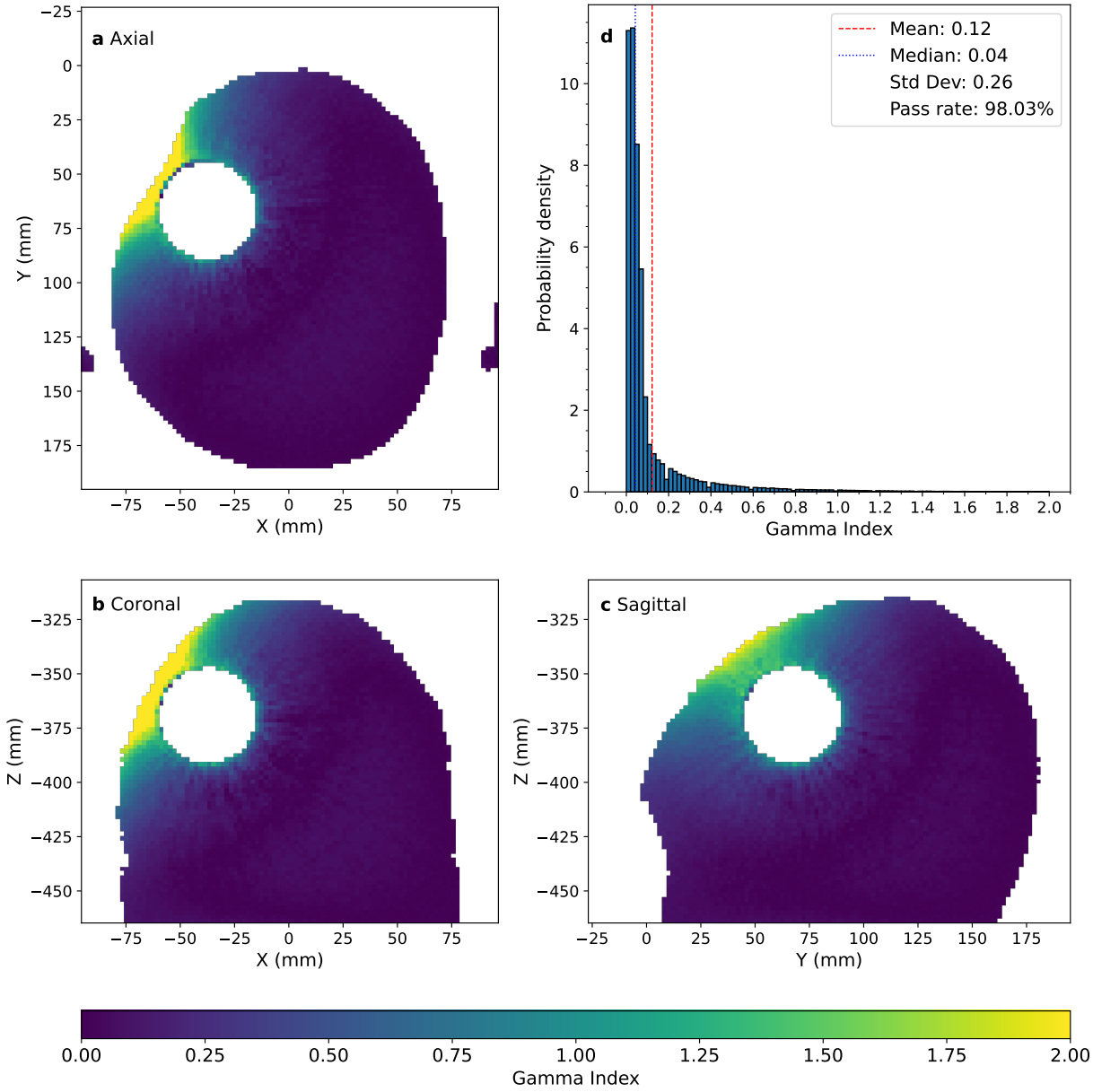

Figure 6.2 Gamma analysis results for TG-43 vs MC_w dose distributions using 1%/1mm criteria for a representative patient. (a) Axial, (b) coronal, and (c) sagittal views of the gamma index distribution. (d) Histogram of gamma index values. The colorbar represents the gamma index, with values below 1 indicating agreement within the specified criteria.

skin and in low-dose regions, particularly beyond the 2% isodose line. Near the patient's skin, MC_w calculations consistently predicted lower doses compared to TG-43.

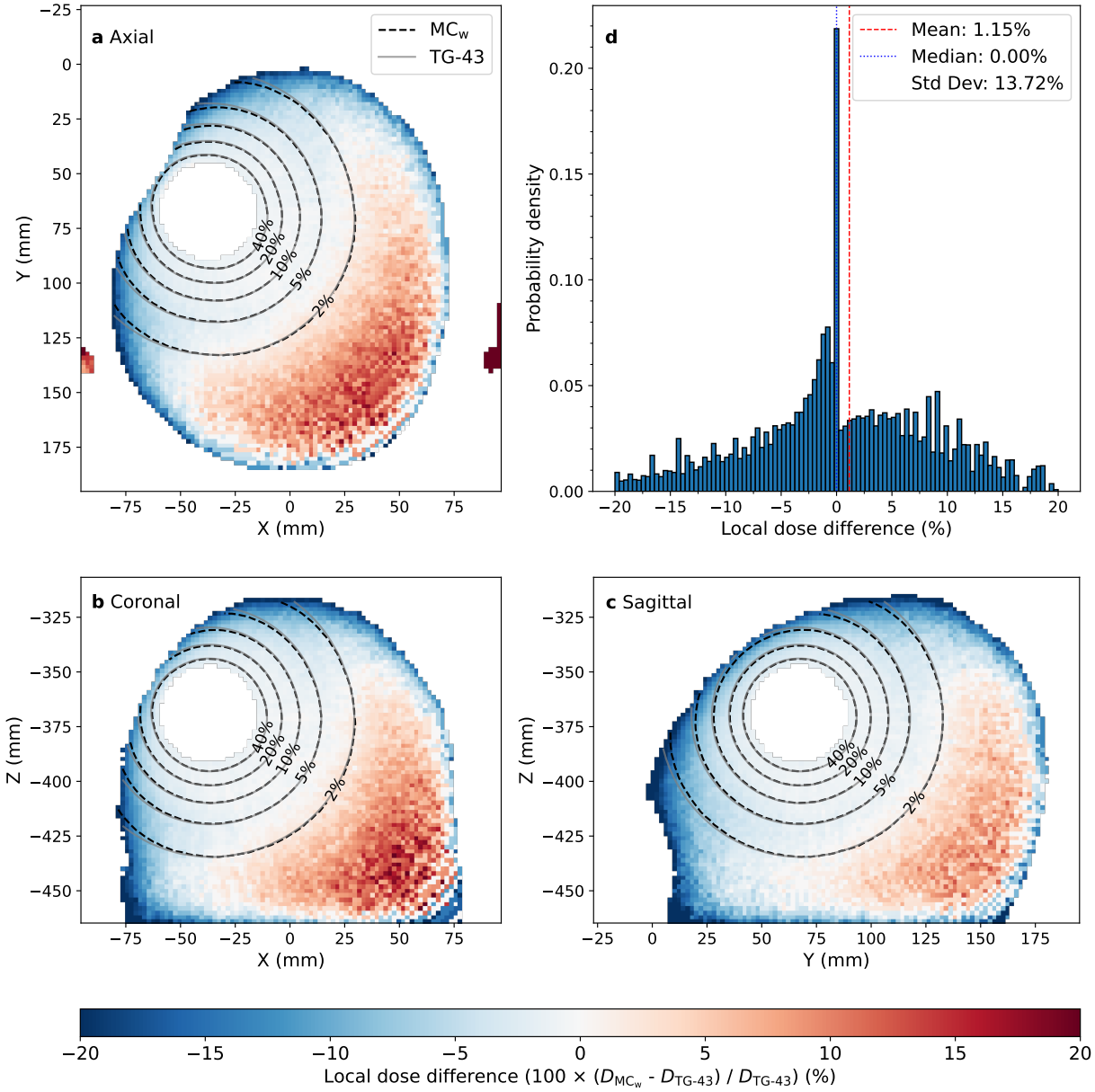

Figure 6.3 Local dose difference distribution between TG-43 and MC_w calculations for a representative patient. (a) Axial, (b) coronal, and (c) sagittal views of the local dose difference maps. (d) Histogram of local dose differences. The colorbar represents the percentage difference relative to the local TG-43 dose. Isodose lines for 2%, 5%, 10%, 20%, and 40% of the prescription dose are shown for both TG-43 (solid gray) and MC_w (dashed black) calculations.

6.5.2 IORT-only OAR dose distributions

Table 6.2 presents the $D_{0.03cc}$ to OARs calculated with the IORT plans across the four calculation models. The brainstem received the highest doses among all OARs, with mean $D_{0.03cc}$ values ranging from 3.0 ± 2.2 Gy (TARGIT) to 3.4 ± 2.5 Gy (TG-43). MC_w showed nearly identical results to TG-43, while MC_{het} predicted slightly lower doses (3.3 ± 2.5 Gy).

For the chiasm, mean doses ranged from 1.2 ± 1.0 Gy (TARGIT) to 1.7 ± 1.3 Gy (MC_{het}), with MC_{het} predicting higher doses compared to other models for this structure. Both optic nerves showed similar patterns across models, with MC_{het} consistently predicting higher doses. The right optic nerve mean doses ranged from 0.5 ± 0.4 Gy (TARGIT) to 1.1 ± 0.7 Gy (MC_{het}), while the left optic nerve showed slightly higher doses, ranging from 0.6 ± 0.9 Gy (TARGIT) to 1.0 ± 1.2 Gy (MC_{het}). Retinae and lenses received the lowest doses across all models, with mean values generally below 0.2 Gy. MC_{het} showed slightly lower doses for these structures compared to other models, particularly for the lenses. Figure 6.4 provides a visual representation of these dose distributions, illustrating the variations between models and the spread of data for each OAR.

Table 6.2 Near maximum dose ($D_{0.03cc}$) to OARs calculated with the IORT plans in a cohort of 20 patients.

Tissue	TG-43 (Gy)	TARGIT (Gy)	MC_w (Gy)	MC_{het} (Gy)
Brainstem	3.4 ± 2.5	3.0 ± 2.2	3.4 ± 2.4	3.3 ± 2.5
Chiasm	1.4 ± 1.1	1.2 ± 1.0	1.4 ± 1.1	1.7 ± 1.3
Optic Nerve R	0.6 ± 0.5	0.5 ± 0.4	0.6 ± 0.5	1.1 ± 0.7
Optic Nerve L	0.7 ± 0.9	0.6 ± 0.9	0.7 ± 0.9	1.0 ± 1.2
Retina R	0.2 ± 0.2	0.1 ± 0.2	0.2 ± 0.2	0.1 ± 0.1
Retina L	0.1 ± 0.2	0.1 ± 0.2	0.1 ± 0.2	0.1 ± 0.1
Lens R	0.1 ± 0.1	0.1 ± 0.1	0.1 ± 0.1	0.0 ± 0.0
Lens L	0.1 ± 0.1	0.0 ± 0.1	0.1 ± 0.1	0.0 ± 0.0

Data presented as mean ± standard deviation.
Abbreviations: IORT = intraoperative radiotherapy.

6.5.3 Absolute dose metric differences

Table 6.3 and Figure 6.5 display the absolute dose differences between TARGIT, MC_w, and MC_{het} models compared to TG-43. TARGIT consistently underestimated doses compared to TG-43, with statistically significant differences ($p \leq 0.05$) across all OARs. Mean differences ranged from -0.1% to -1.7%. The largest difference was observed for the brainstem (-1.7 ± 1.1%), while the smallest differences were for the retinae and lenses (-0.1% to -0.2%).

MC_w showed minimal differences from TG-43, with mean differences of 0.0% for all OARs and standard deviations ≤ 0.1%. Interestingly, MC_w showed small but statistically significant differences for the optic nerves (p = 0.026 for the right, p = 0.049 for the left) despite both models assuming water-equivalent media.

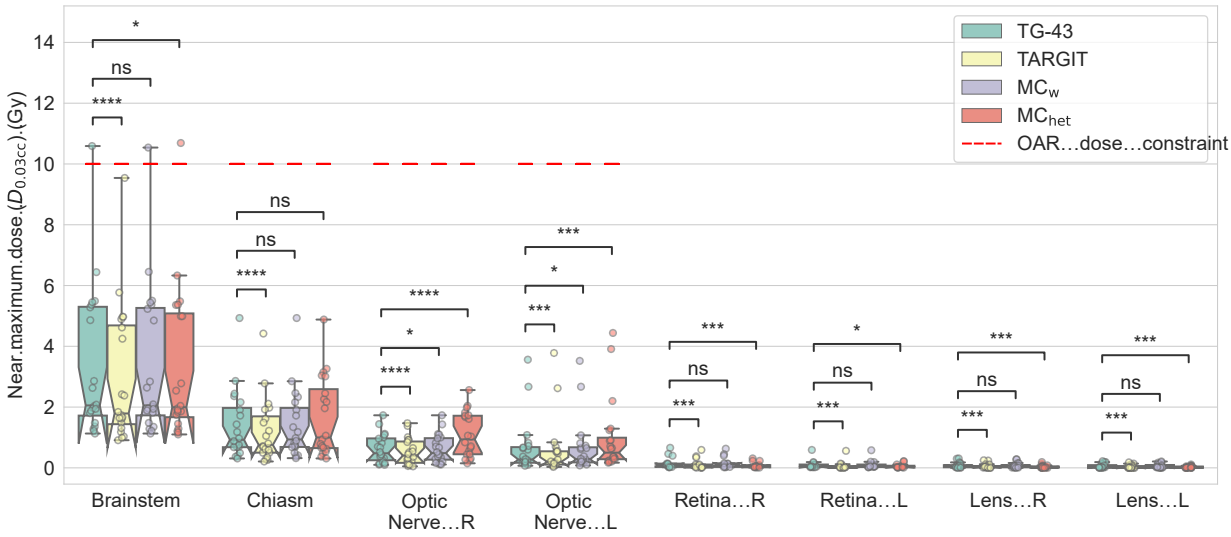

Figure 6.4 Distribution of near maximum doses ($D_{0.03\text{cc}}$) to OARs for IORT plans calculated using four different dosimetry models: TG-43, TARGIT, MC_w, and MC_{het}. The boxplots show the median (horizontal line), interquartile range (box), and range (whiskers) of doses for each OAR and model. Individual data points are overlaid to show the spread of the data. The red dashed line represents the OAR dose constraint where applicable. Statistical significance of differences between models is indicated by asterisks: * $p \leq 0.05$, ** $p \leq 0.01$, *** $p \leq 0.001$, **** $p \leq 0.0001$, ns (not significant).

MC_{het} exhibited the largest and most variable deviations from TG-43, with notably higher dose differences predicted for the optic nerves (1.9 ± 1.4% for the right, 1.3 ± 1.9% for the left) and chiasm (1.1 ± 2.1%). MC_{het} predicted lower doses for the brainstem (-0.2 ± 0.3%), retinae (-0.2% to -0.3%), and lenses (-0.1% to -0.2%) compared to TG-43.

6.5.4 Combined EBRT+IORT dose distributions

Table 6.4 and Figure 6.6 illustrate the combined EBRT+IORT dose distributions. The brainstem showed the highest doses, with mean $D_{0.03\text{cc}}$ values ranging from 55.7 ± 8.3 Gy (EBRT alone) to 64.0 ± 13.8 Gy (EBRT+IORT(TG-43) and EBRT+IORT(MC_{het})). The addition of IORT increased the mean dose by approximately 8 Gy across all models. All combined models showed instances exceeding the brainstem constraint of 66 Gy.

For the chiasm, mean doses ranged from 41.8 ± 14.1 Gy (EBRT alone) to 43.9 ± 15.5 Gy (EBRT+IORT(MC_{het})), remaining below the 55 Gy constraint, though with some outliers exceeding this limit. The impact of IORT was less pronounced for this structure, with increases of about 2 Gy.

The optic nerves showed moderate doses, with the right optic nerve mean doses ranging from 31.0 ± 16.1 Gy (EBRT alone) to 31.7 ± 16.4 Gy (EBRT+IORT(MC_w)). The left optic nerve showed slightly lower doses, ranging from 27.2 ± 17.2 Gy (EBRT alone) to 28.0 ± 18.1 Gy (EBRT+IORT(TG-43)), with several outliers approaching or

Table 6.3 Near maximum dose ($D_{0.03\text{cc}}$) absolute dose differences between the TARGIT, MC_w, and MC_het IORT dose calculation models and the TG-43 reference model in a cohort of 20 patients.

Tissue	TARGIT − TG-43 (%)	MC_w − TG-43 (%)	MC_het − TG-43 (%)
Brainstem	$-1.7 \pm 1.1^{*}$	0.0 ± 0.1	$-0.2 \pm 0.3^{*}$
Chiasm	$-0.8 \pm 0.5^{*}$	0.0 ± 0.1	1.1 ± 2.1
Optic Nerve R	$-0.4 \pm 0.3^{*}$	$0.0 \pm 0.0^{*}$	$1.9 \pm 1.4^{*}$
Optic Nerve L	$-0.3 \pm 0.3^{*}$	$0.0 \pm 0.1^{*}$	$1.3 \pm 1.9^{*}$
Retina R	$-0.2 \pm 0.1^{*}$	0.0 ± 0.0	$-0.3 \pm 0.4^{*}$
Retina L	$-0.1 \pm 0.1^{*}$	0.0 ± 0.0	$-0.2 \pm 0.4^{*}$
Lens R	$-0.1 \pm 0.1^{*}$	0.0 ± 0.0	$-0.2 \pm 0.2^{*}$
Lens L	$-0.1 \pm 0.1^{*}$	0.0 ± 0.0	$-0.1 \pm 0.2^{*}$

The absolute dose difference is calculated as a percentage of the prescription dose and is presented as mean ± standard deviation.
Abbreviations: IORT = intraoperative radiotherapy.
* Significant difference (p-value ≤ 0.05, Wilcoxon signed-rank test).

exceeding the 55 Gy constraint. Adding IORT resulted in minimal increases ($\leq$ 1 Gy) for both optic nerves.

Retinae and lenses showed the lowest doses and least variability between models. For retinae, mean doses ranged from 11.2 ± 6.2 Gy to 14.1 ± 7.9 Gy across all models. Lenses received mean doses between 4.9 ± 2.2 Gy and 5.3 ± 2.7 Gy, with some cases exceeding the 7 Gy constraint across all models.

6.5.5 Calculation times

The calculation times for different dosimetry methods varied significantly. For MC_w simulations, the average calculation time per node ranged from 9.8 to 26.2 minutes, with a mean of 20.1 minutes. The total calculation time across all nodes for each patient ranged from 12.8 to 21.6 hours, with an average of 18.3 hours. MC_het simulations showed similar but slightly lower computation times, with average times per node ranging from 6.3 to 19.6 minutes (mean 15.1 minutes) and total times ranging from 13.9 to 18.6 hours (mean 16.2 hours). These calculations were performed on a high-performance computing cluster, as detailed in Table 6.1. In contrast, TG-43 calculations were substantially faster, with an average computation time of 0.6 seconds per patient, ranging from 0.5 to 1.0 seconds, on a single laptop with an Intel(R) Core(TM) i7-9750H CPU @ 2.60GHz and 16 GB RAM.

6.6 Discussion

This study provides a comprehensive evaluation of the TG-43 formalism for IORT dose calculations in glioblastoma treatment, comparing it with the current clinical standard (TARGIT method) and more complex Monte Carlo sim-

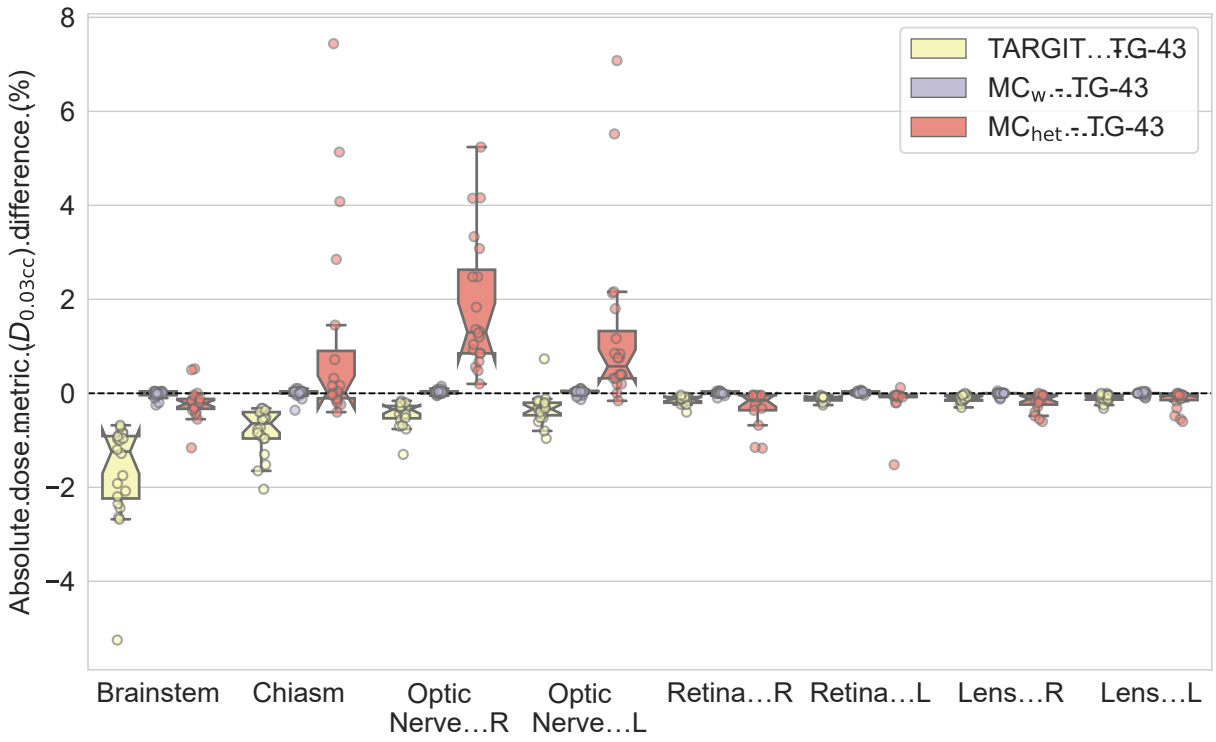

Figure 6.5 Absolute dose differences in near maximum dose ($D_{0.03cc}$) between TARGIT, MC_w, and MC_{het} models compared to the TG-43 reference model for IORT plans. The absolute dose difference is calculated as a percentage of the prescription dose. The boxplots show the median (horizontal line), interquartile range (box), and range (whiskers) of dose differences for each OAR and model comparison. Individual data points are overlaid to show the spread of the data. The dashed line at 0% represents no difference from the TG-43 model.

ulations. While the ongoing INTRAGO trial must maintain its established TARGIT-based protocol, our evaluation of TG-43 performance demonstrates its potential value for future clinical implementations, particularly in enabling real-time decision-making regarding IORT prescription doses based on OAR constraints with patients still on the treatment table. This capability could be especially valuable if IORT for glioblastoma becomes standard practice following the completion of the INTRAGO trial.

Our validation of TG-43 against MC_w simulations demonstrated good overall agreement, with a 98.0% gamma pass rate using 1%/1mm criteria. Global dose difference analysis revealed a mean difference of -0.07% (standard deviation: 0.29%) relative to the prescription dose, suggesting a slight dose overestimation by TG-43. However, discrepancies were observed in low-dose regions and near the patient's skin, highlighting the importance of recognizing TG-43's limitations in areas where tissue heterogeneities and boundary conditions significantly influence dose distribution.

The observed differences between TG-43 and MC_w calculations can be attributed to several factors. Near the patient's skin, MC_w consistently predicted lower doses compared to TG-43, likely due to the reduced backscatter

Table 6.4 Near maximum dose ($D_{0.03cc}$) to OARs calculated with the combined EBRT and IORT plans in a cohort of 20 patients.

Tissue	EBRT (Gy)	EBRT + IORT(TG-43) (Gy)	EBRT + IORT(TARGIT) (Gy)	EBRT + IORT(MC_w) (Gy)	EBRT + IORT(MC_{het}) (Gy)
Brainstem	55.7 ± 8.3	64.0 ± 13.8	62.4 ± 12.3	63.9 ± 13.7	64.0 ± 13.8
Chiasm	41.8 ± 14.1	43.8 ± 15.4	43.4 ± 15.2	43.8 ± 15.4	43.9 ± 15.5
Optic Nerve R	31.0 ± 16.1	31.6 ± 16.4	31.5 ± 16.4	31.7 ± 16.4	31.3 ± 16.4
Optic Nerve L	27.2 ± 17.2	28.0 ± 18.1	27.9 ± 18.1	28.0 ± 18.0	27.8 ± 18.2
Retina R	14.0 ± 7.8	14.1 ± 7.9	14.1 ± 7.9	14.1 ± 7.9	14.0 ± 8.0
Retina L	11.2 ± 6.2	11.3 ± 6.3	11.3 ± 6.3	11.3 ± 6.3	11.3 ± 6.2
Lens R	5.2 ± 2.7	5.3 ± 2.7	5.2 ± 2.7	5.3 ± 2.7	5.2 ± 2.6
Lens L	4.9 ± 2.2	5.0 ± 2.2	5.0 ± 2.2	5.0 ± 2.2	5.0 ± 2.2

Data presented as mean $\pm$ standard deviation.
Abbreviations: EBRT = external beam radiotherapy; IORT = intraoperative radiotherapy.

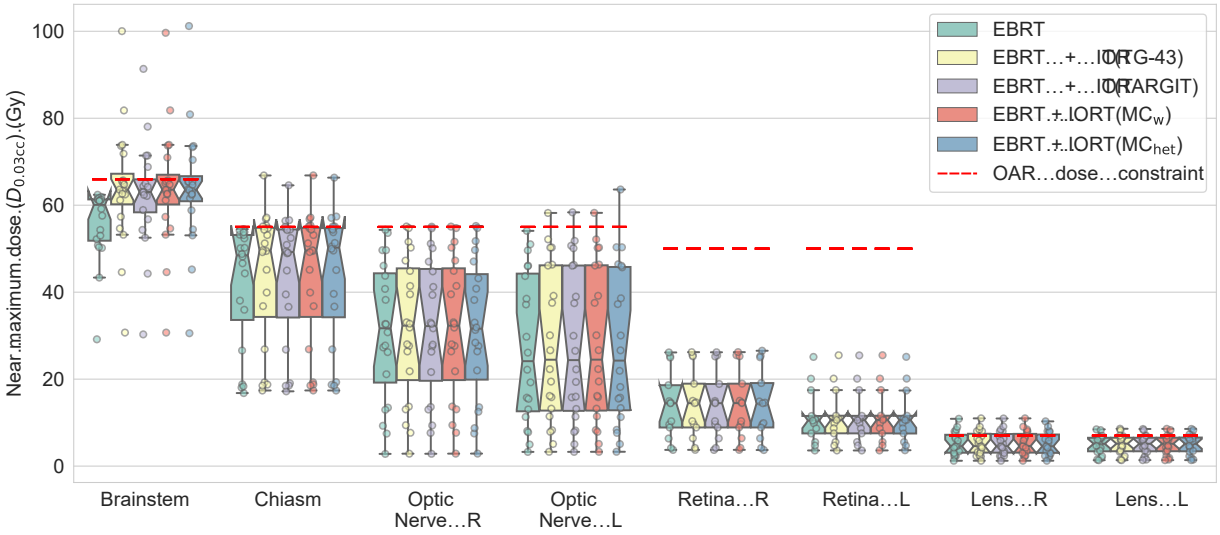

Figure 6.6 Distribution of near maximum doses ($D_{0.03cc}$) to OARs for combined EBRT and IORT plans. The figure compares EBRT alone with combined EBRT+IORT using four different IORT dosimetry models: TG-43, TARGIT, MC_w, and MC_{het}. The boxplots show the median (horizontal line), interquartile range (box), and range (whiskers) of doses for each OAR and treatment scenario. Individual data points are overlaid to show the spread of the data. The red dashed line represents the OAR dose constraint where applicable.

in MC_w simulations, which model air outside the patient contour. This effect is particularly relevant for superficial structures such as the lenses and retinae. In low-dose regions, particularly beyond the 2% isodose line, larger

local dose differences were observed. These differences may be partially attributed to the use of MCDF-XCOM cross-sections in the current MC simulations, compared to the XCOM cross-sections used in previous TG-43 parameter calculations [10, 11]. While these discrepancies in low-dose regions may have limited clinical impact, they emphasize the need for consistent cross-section data across dosimetry models for comprehensive comparisons.

When comparing TG-43 to other dosimetry formalisms across the patient cohort, the TARGIT model consistently underestimated doses compared to TG-43 across all OARs. This underestimation was statistically significant, with mean differences ranging from -0.1% to -1.7% of the prescription dose. The largest discrepancy was observed for the brainstem (-1.7 $\pm$ 1.1%), which also received the highest absolute doses among all OARs. These findings are consistent with previous studies that have reported TARGIT underestimation of delivered doses [4, 6].

In contrast, the MC_w model showed remarkable agreement with TG-43 in OAR dose estimations, with only minor, albeit occasionally statistically significant, differences. The mean differences were 0.0% for all OARs, with standard deviations $\leq 0.1\%$. This concordance suggests that the TG-43 formalism provides a reasonable approximation of dose distribution in water-like tissues for the INTRABEAM system. While the overall agreement was excellent, small but statistically significant differences were observed for the optic nerves. The mean differences in dose for the optic nerves were 0.01 Gy bilaterally, constituting less than 0.05% of the prescription dose. These differences, although statistically significant, are unlikely to be clinically relevant. The sensitivity of the Wilcoxon signed-rank test, particularly in the context of small sample sizes and low dose levels, likely contributed to detecting these significant differences. Several factors could contribute to these small discrepancies. Boundary conditions may play a role, as MC_w simulations model air outside the patient contour, potentially affecting backscatter near tissue boundaries. The optic nerves, being relatively superficial structures, might be more susceptible to these effects. Additionally, the use of MCDF-XCOM cross-sections in the current MC simulations, compared to the XCOM cross-sections used in previous TG-43 parameter calculations, may contribute to discrepancies, particularly in low-dose regions. Despite the large number of particle histories simulated, inherent statistical uncertainties in MC_w results could also contribute to the observed differences. This observation emphasizes the importance of evaluating both statistical significance and clinical relevance in the interpretation of dosimetric comparisons.

The MC_{het} model demonstrated the most substantial deviations from TG-43, particularly for structures near bony anatomy such as the optic nerves and chiasm. For the right optic nerve, MC_{het} predicted a mean dose of 1.1 $\pm$ 0.7 Gy compared to 0.6 $\pm$ 0.5 Gy for TG-43, representing a mean difference of 1.9 $\pm$ 1.4% of the prescription dose. The left optic nerve showed similar trends. However, the clinical significance of these differences requires careful consideration, as the absolute doses remained below OAR constraints in most cases, and the mean differences (0.22 Gy for right, 0.26 Gy for left) were small relative to the prescription doses of 20-30 Gy.

The observed differences between MC_{het} and TG-43 calculations for OARs near bony structures, such as the optic chiasm and optic nerves, can be attributed to the predominance of the photoelectric effect at low photon energies, which is approximately proportional to Z^3, leading to higher energy absorption in high-Z materials like bone. Conversely, the lower doses predicted by MC_{het} for lenses, retinae, and brainstem compared to TG-43 can be explained by two factors. First, as noted by the AAPM TG-186 report [18], soft tissues generally absorb less radiation dose than water at low photon energies. Second, the reduced backscatter from air outside the patient contour in MC_{het} calculations, compared to the water-everywhere assumption in TG-43, may contribute to lower doses in structures near the skin surface, such as lenses and retinae.

When considering combined EBRT+IORT doses, the differences between models became less pronounced relative to the total prescribed dose. However, the addition of IORT dose led to more instances of OAR constraint violations, particularly for the brainstem and optic structures. These results demonstrate the importance of careful treatment planning and potentially individualized OAR constraints when combining IORT with EBRT.

The analysis of combined EBRT+IORT doses reveals that the choice of IORT calculation model has a relatively small impact on the total dose received by OARs. However, the addition of IORT led to more instances of OAR constraint violations, particularly for the brainstem and optic structures. It is important to note that the dose constraints used in this study, particularly for IORT plans, were recommended in the INTRAGO protocol with limited prior experience in these energy ranges for brain IORT. The observation that many OARs exceeded combined dose constraints when IORT was added to EBRT, despite IORT doses alone generally respecting their constraints, raises questions about the appropriateness of the established IORT dose constraints. This finding suggests that current IORT constraints may be too lenient to guarantee safe combinations with EBRT, and further research is needed to refine these constraints based on clinical outcomes and more accurate dosimetry.

It is worth noting that our implementation of the TG-43 formalism used MC-calculated dose rates at the reference position in water rather than published dose-rate conversion coefficients due to the lack of standardized air-kerma data for the INTRABEAM system. Currently, no primary standard exists for the INTRABEAM system providing calibration air-kerma data measured at a standards laboratory for the specific source used. Ideally, such calibration data would allow the use of dose-rate conversion coefficients, like those we previously published for INTRABEAM with spherical applicators [11], to independently determine the absorbed dose rate to water at the TG-43 reference position. Instead, we calculated the reference dose rate directly using our MC_w simulation model. While this approach ensures consistency between our TG-43 and MC simulations, it introduces a correlation between the two models. Consequently, the strong agreement observed between TG-43 and MC results in this study should be interpreted with this limitation in mind.

Once air-kerma standards are established for the INTRABEAM system, MC results should be renormalized to measured air-kerma rates rather than relying on nominal tube current for absolute output calculations. Experience with other electronic brachytherapy sources, such as the Xoft Axxent, has shown that measured outputs can be substantially lower than MC-calculated outputs based on the nominal tube current. These differences could arise from uncertainties in target modeling, inaccuracy of the electron current actually impinging on the target, or other factors affecting source output. The development of standardized calibration data for the INTRABEAM system would enable fully independent validation of dosimetry models in future studies.

The TG-43 method, while assuming a homogeneous water medium, offers a good compromise between accuracy and computational efficiency. Our analysis of calculation times demonstrates this efficiency. While MC simulations required an average of 18.3 and 16.2 hours for MC_w and MC_{het}, respectively, using a high-performance computing cluster, TG-43 calculations were completed in less than a second (average 0.6 seconds) on a standard laptop. This immense reduction in computation time, coupled with the good agreement between TG-43 and MC_w results, supports the use of TG-43 as an efficient and reasonably accurate method for IORT dose calculations in clinical practice. Furthermore, the 3D dose distributions generated by TG-43 can be easily combined with EBRT dose distributions, allowing for more comprehensive plan optimization and OAR dose constraint evaluation. However, the limitations of TG-43 in accounting for tissue heterogeneities should be considered, especially in cases where

high accuracy is critical near tissue interfaces or in highly heterogeneous regions.

While this study focused on IORT dosimetry in the brain, the methodology could be applied to other anatomical regions to explore the implications of different tissue compositions and more complex geometries. The TG-43 formalism, calculated in water, may have limitations in scenarios where OARs significantly deviate from water-equivalent composition or are in close proximity to bone and air interfaces. Future studies should investigate the applicability of TG-43 in more heterogeneous anatomical sites, such as breast (near lung and ribs) or skin, where tissue composition deviations from water may be more pronounced.

The TG-43 formalism offers several advantages over the current TARGIT method used in clinical practice for the INTRAGO protocol. While the TARGIT method relies on manual estimation of point doses to OARs based on preoperative MRI and lookup tables, TG-43 provides full 3D dose distributions that account for source polar anisotropy around the source and applicator. This approach allows a more accurate determination of $D_{0.03\mathrm{cc}}$ to OARs without the need to estimate their nearest separation to the applicator surface. Our study revealed that adding IORT to EBRT led to a significant number of OARs exceeding dose constraints, a finding not identified in the current TARGIT clinical practice within the INTRAGO protocol. This discrepancy highlights the limitations of the current point-dose estimation approach and shows the importance of accurate 3D dose calculations in treatment planning.

The implementation of TG-43 or similar 3D dose calculation methods in clinical practice could significantly improve the accuracy of OAR dose estimation in IORT for glioblastoma. This would enable better adherence to dose constraints and potentially improve treatment outcomes by reducing the risk of exceeding OAR tolerance doses. Moreover, the more accurate dose calculations provided by the TG-43 formalism could play a valuable role in analyzing the results of the INTRAGO trial. By correlating actual delivered doses, calculated with higher accuracy, with clinical outcomes and toxicity data from the trial, this analysis could contribute to establishing more appropriate OAR dose constraints specifically derived from IORT treatments. Such IORT-specific constraints would be particularly valuable if the treatment modality becomes standard practice, as they would be based on actual clinical experience with low-energy X-rays rather than extrapolated from conventional radiotherapy data. Future studies should focus on validating these findings in larger patient cohorts and assessing the long-term clinical impact of more accurate IORT dose calculations.

6.7 Conclusion

This study demonstrates that while the TG-43 formalism provides a reasonable foundation for IORT dose calculations in glioblastoma treatment, more advanced models like MC_{het} may offer additional insights, particularly for OARs in heterogeneous tissue regions. The validation of TG-43 against MC_{w} simulations showed good overall agreement, with a high gamma pass rate of 98.0% using 1%/1mm criteria, supporting the use of TG-43 for clinical applications. However, observed discrepancies in low-dose regions and near tissue interfaces highlight the need for careful consideration of the TG-43 formalism's limitations in these areas.

Our findings demonstrate the potential benefits of implementing the TG-43 formalism or similar 3D dose calculation methods in clinical practice for IORT in glioblastoma treatment. The improved accuracy in OAR dose estimation, combined with the ability to generate full 3D dose distributions efficiently, could lead to better treatment planning and potentially improved patient outcomes. The TG-43 formalism not only provides reasonably accurate

dose calculations but also offers significant computational efficiency, with calculation times reduced from hours to less than a second compared to MC simulations. This combination of accuracy and speed makes TG-43 a practical choice for clinical IORT dose calculations in glioblastoma treatment.

The comparison of different dosimetry models reveals the complexities involved in accurately calculating doses for low-energy IORT treatments. While MC_{het} provides the most comprehensive account of tissue heterogeneity, the TG-43 formalism offers a practical compromise between accuracy and computational efficiency. The observed differences between models, particularly in regions near bony structures, highlight the need for careful consideration of tissue composition in dose calculations.

Our investigation provides insight into the dosimetric aspects of IORT in glioblastoma and emphasizes the importance of accurate 3D dose calculations in treatment planning. The implementation of more precise dosimetry methods, such as TG-43 or MC-based approaches, has the potential to improve the safety and efficacy of combined IORT and EBRT treatments for glioblastoma patients. Future research should focus on clinical validation of these findings in larger patient cohorts, exploration of their impact on long-term treatment outcomes, and investigation of the applicability of TG-43 in more heterogeneous anatomical sites.

Acknowledgements

D.S. Ayala Alvarez gratefully acknowledges the financial support received from the Fonds de recherche du Québec – Santé (FRQS, grant number 292924) throughout the duration of this research project. This work was supported in part by grants from the Canadian Institutes of Health Research (CIHR, Foundation Grant No. FDN-143257) and the Natural Sciences and Engineering Research Council of Canada (NSERC, Grant No. RGPIN-2019-06746). The authors extend their gratitude to Mathias Benker of Carl Zeiss for providing detailed specifications of the INTRABEAM spherical applicators, which were necessary for this study.

References

[1] R. Stupp *et al.*, "Radiotherapy plus concomitant and adjuvant temozolomide for glioblastoma," *New England journal of medicine*, vol. 352, no. 10, pp. 987–996, 2005.

[2] R. Stupp *et al.*, "Effects of radiotherapy with concomitant and adjuvant temozolomide versus radiotherapy alone on survival in glioblastoma in a randomised phase III study: 5-year analysis of the EORTC-NCIC trial," *The Lancet Oncology*, vol. 10, no. 5, pp. 459–466, 2009.

[3] J. S. Vaidya *et al.*, "Risk-adapted targeted intraoperative radiotherapy versus whole-breast radiotherapy for breast cancer: 5-year results for local control and overall survival from the TARGIT-A randomised trial," *The Lancet*, vol. 383, no. 9917, pp. 603–613, 2014.

[4] P. G. F. Watson, H. Bekerat, P. Papaconstadopoulos, S. Davis, and J. Seuntjens, "An investigation into the INTRABEAM miniature x-ray source dosimetry using ionization chamber and radiochromic film measurements," *Medical Physics*, vol. 45, no. 9, pp. 4274–4286, 2018.

[5] D. S. Ayala Alvarez *et al.*, "Evaluation of dosimetry formalisms in intraoperative radiation therapy of glioblastoma," *International Journal of Radiation Oncology, Biology, Physics*, vol. 117, no. 3, pp. 763–773, 2023.

[6] W. S. Culberson *et al.*, "Dose-rate considerations for the INTRABEAM electronic brachytherapy system: Report from the American association of physicists in medicine task group no. 292," *Medical Physics*, vol. 47, no. 8, e913–e919, 2020.

[7] M. Y. Shaikh, J. Burmeister, R. Scott, L. K. Kumaraswamy, A. Nalichowski, and M. C. Joiner, "Dosimetric evaluation of incorporating the revised V4.0 calibration protocol for breast intraoperative radiotherapy with the INTRABEAM system," *Journal of Applied Clinical Medical Physics*, vol. 21, no. 2, pp. 50–59, 2020.

[8] A. Abudra'a, B. Chauvenet, J. Gouriou, J. Plagnard, R. Itti, and I. Aubineau-Lanièce, "Dosimetry formalism and calibration procedure for electronic brachytherapy sources in terms of absorbed dose to water," *Physics in Medicine and Biology*, vol. 65, no. 14, p. 145 006, 2020.

[9] M. J. Rivard *et al.*, "Update of AAPM Task Group No. 43 Report: A revised AAPM protocol for brachytherapy dose calculations," *Medical Physics*, vol. 31, no. 3, pp. 633–674, 2004.

[10] D. S. Ayala Alvarez, P. G. F. Watson, M. Popovic, V. J. Heng, M. D. C. Evans, and J. Seuntjens, "Monte Carlo calculation of the relative TG-43 dosimetry parameters for the INTRABEAM electronic brachytherapy source," *Physics in Medicine and Biology*, vol. 65, no. 24, p. 245 041, 2020.

[11] D. S. Ayala Alvarez, P. G. F. Watson, M. Popovic, V. J. Heng, M. D. C. Evans, and J. Seuntjens, "Monte Carlo calculation of the TG-43 dosimetry parameters for the INTRABEAM source with spherical applicators," *Physics in Medicine & Biology*, vol. 66, no. 21, p. 215 017, 2021.

[12] F. A. Giordano *et al.*, "Intraoperative radiotherapy in newly diagnosed glioblastoma (INTRAGO): An open-label, dose-escalation phase I/II trial," *Neurosurgery*, vol. 84, no. 1, pp. 41–49, 2019.

[13] M. F. Valdivieso-Casique *et al.*, "RADIANCE—A planning software for intra-operative radiation therapy," *Translational Cancer Research*, vol. 4, no. 2, pp. 196–209, 2015.

[14] M. J. P. Chamberland, R. E. P. Taylor, D. W. O. Rogers, and R. M. Thomson, "Egs_brachy: A versatile and fast Monte Carlo code for brachytherapy," *Physics in Medicine & Biology*, vol. 61, no. 23, pp. 8214–8231, 2016.

[15] International Commission on Radiation Units and Measurements, *ICRU Report 44, Tissue substitutes in radiation dosimetry and measurement*. ICRU Publications, Bethesda, MD, 1989.

[16] International Commission on Radiation Units and Measurements, *ICRU Report 46, Photon, electron, proton and neutron interaction data for body tissues*. ICRU Publications, Bethesda, MD, 1992.

[17] J. Valentin, "Basic anatomical and physiological data for use in radiological protection: Reference values: ICRP Publication 89," *Annals of the ICRP*, vol. 32, no. 3-4, pp. 1–277, 2002.

[18] L. Beaulieu *et al.*, "Report of the Task Group 186 on model-based dose calculation methods in brachytherapy beyond the TG-43 formalism: Current status and recommendations for clinical implementation," *Medical physics*, vol. 39, no. 10, pp. 6208–6236, 2012.

[19] I. Sechopoulos *et al.*, "RECORDS: Improved reporting of montE CarlO RaDiation transport studies: Report of the AAPM research committee task group 268," *Medical physics*, vol. 45, no. 1, e1–e5, 2018.

[20] I. Kawrakow and D. W. O. Rogers, "The EGSnrc code system: Monte Carlo simulation of electron and photon transport," National Research Council Canada, Ottawa, Canada, Tech. Rep. PIRS-701, 2019.

[21] I. Kawrakow, E. Mainegra-Hing, F. Tessier, and B. R. B. Walters, "The egsnrc C++ class library, NRC report PIRS-898 (rev a)," National Research Council Canada, Ottawa, Canada, Tech. Rep., 2009.

[22] L. Sabbatucci and F. Salvat, "Theory and calculation of the atomic photoeffect," *Radiation Physics and Chemistry*, vol. 121, pp. 122–140, 2016.

[23] C. Valdes-Cortez *et al.*, "A study of Type B uncertainties associated with the photoelectric effect in low-energy Monte Carlo simulations," *Physics in Medicine & Biology*, vol. 66, no. 10, p. 105 014, 2021.

[24] D. Bote and F. Salvat, "Calculations of inner-shell ionization by electron impact with the distorted-wave and plane-wave Born approximations," *Physical Review A*, vol. 77, no. 4, p. 042 701, 2008.

[25] P. G. Watson and J. Seuntjens, "Effect of explicit M and N-shell atomic transitions on a low-energy x-ray source," *Medical physics*, vol. 43, no. 4, pp. 1760–1763, 2016.

[26] Varian Medical Systems, "Eclipse photon and electron algorithms reference guide," *Varian Medical Systems, Palo Alto, CA, USA*, 2015.

[27] A. Fogliata, G. Nicolini, E. Vanetti, A. Clivio, and L. Cozzi, "Dosimetric validation of the anisotropic analytical algorithm for photon dose calculation: Fundamental characterization in water," *Physics in Medicine & Biology*, vol. 51, no. 6, p. 1421, 2006.

[28] T. Knöös *et al.*, "Comparison of dose calculation algorithms for treatment planning in external photon beam therapy for clinical situations," *Physics in Medicine & Biology*, vol. 51, no. 22, p. 5785, 2006.

[29] L. Beaulieu *et al.*, "AAPM WGDCAB Report 372: A joint AAPM, ESTRO, ABG, and ABS report on commissioning of model-based dose calculation algorithms in brachytherapy," *Medical physics*, vol. 50, no. 8, e946–e960, 2023.

[30] International Commission on Radiation Units and Measurements, *ICRU Report 91, Prescribing, recording and reporting of stereotactic treatments with small photon beams*. ICRU Publications, 2014, vol. 14.

Chapter 7

Summary and future directions

7.1 Summary

This thesis has explored the dosimetry of the INTRABEAM system for intraoperative radiotherapy (IORT), with a particular focus on its application in the treatment of glioblastoma multiforme (GBM) within the context of the INTRAGO clinical trial. The research presented here addresses critical challenges in accurate dose calculation and treatment planning for low-energy X-ray sources used in IORT, contributing to the ongoing efforts to improve outcomes and reduce side effects in patients with this form of cancer.

7.1.1 Key findings

Our investigation began with a comprehensive characterization of the INTRABEAM bare probe using Monte Carlo (MC) simulations and experimental validation, as detailed in Chapter 3. This initial work provided the foundation for subsequent studies and highlighted the unique dosimetric challenges posed by the INTRABEAM system's low-energy X-ray spectrum and steep dose gradients. The derived TG-43 parameters for the bare probe offered valuable insights into the dosimetric properties of the source, revealing significant anisotropy and a radial dose function with a notably steeper gradient compared to conventional brachytherapy sources [1].

Building upon this foundation, Chapter 4 extended the TG-43 characterization to include the INTRABEAM system with spherical applicators, which are necessary for clinical applications. This work provided a comprehensive set of TG-43 parameters for all available applicator sizes, enabling more accurate 3D dose calculations within existing brachytherapy treatment planning frameworks. The results demonstrated the impact of applicator size and internal filtration on dose distributions, with larger applicators exhibiting increased anisotropy and the smallest applicators showing enhanced beam penetration due to internal aluminum filtration [2].

In Chapter 5, we conducted a critical evaluation of different dosimetry formalisms for IORT in GBM treatment. This study compared the current clinical standard (TARGIT method) with more accurate approaches, including the V4.0 calibration method, the C_Q method, and MC simulations in both water and heterogeneous media. Our findings revealed significant discrepancies between these methods, with the TARGIT approach consistently underestimating

doses to organs at risk (OARs). Notably, while the TARGIT method suggested no violations of OAR dose constraints for the IORT-only plans, the more accurate methods identified multiple instances where constraints were exceeded [3]. These results highlight the potential clinical impact of improved dosimetry methods and the limitations of current practice in ensuring safe and effective IORT treatments.

Finally, Chapter 6 presented a comprehensive evaluation of the TG-43 formalism for INTRABEAM IORT dosimetry in GBM treatment. This study compared TG-43 calculations with the TARGIT method and MC simulations in both water and heterogeneous media across a cohort of 20 patients from the INTRAGO trial. The results demonstrated good agreement between TG-43 and MC simulations in water, with a 98.0% gamma pass rate using 1%/1mm criteria. However, MC simulations in heterogeneous media revealed larger deviations, particularly near bony structures. This work highlighted the potential of the TG-43 formalism as a practical compromise between accuracy and computational efficiency for clinical IORT dose calculations.

Collectively, these findings represent significant advancements in our understanding of INTRABEAM dosimetry and its clinical implications. They demonstrate the limitations of current clinical practices and provide a strong foundation for improved treatment planning and dose delivery in IORT for GBM.

7.1.2 Implications for clinical practice

The research presented in this thesis has several important implications for clinical practice in IORT for GBM. The comprehensive TG-43 characterization of the INTRABEAM system with spherical applicators provides the necessary data for implementing more accurate 3D dose calculations within existing brachytherapy treatment planning systems. This could lead to improved treatment planning and more precise dose delivery in clinical settings. The demonstrated underestimation of OAR doses by the TARGIT method highlights the need for more accurate dosimetry in clinical practice. Implementing more sophisticated methods, such as the TG-43 formalism or MC-based approaches, could help ensure that OAR dose constraints are not inadvertently exceeded, potentially reducing treatment-related toxicities.

The comparison of different dosimetry formalisms emphasizes the importance of considering tissue heterogeneities in dose calculations, particularly for low-energy X-ray sources. While the TG-43 formalism offers a practical compromise for routine clinical use, the findings suggest that MC simulations in heterogeneous media may be necessary for cases where high precision is critical, such as when OARs are in close proximity to the treatment volume or when significant tissue density variations exist between the treatment area and OARs, particularly near bony structures or air cavities. The research highlights the potential benefits of integrating more advanced dosimetry methods into the clinical workflow for IORT in GBM treatment. This could involve the development of dedicated treatment planning systems that incorporate TG-43 or MC-based dose calculations, allowing for real-time optimization of treatment parameters.

Furthermore, the findings highlight the need for careful consideration of combined IORT and external beam radiotherapy (EBRT) doses when evaluating total OAR doses. The research suggests that current practices may underestimate the cumulative dose to OARs, emphasizing the importance of comprehensive treatment planning that accounts for both IORT and EBRT contributions. These implications collectively point towards the need for a shift in the standards in IORT dosimetry for GBM treatment, moving away from simplified methods towards more accurate, comprehensive approaches that can better ensure treatment safety and efficacy.

7.1.3 Limitations of the study

While this research has made significant contributions to the field of INTRABEAM dosimetry for IORT in GBM treatment, it is important to acknowledge several limitations. The Monte Carlo simulations, while highly accurate, rely on idealized models of the INTRABEAM source and applicators. Real-world variations in manufacturing and setup may introduce additional uncertainties that are not captured in these models. The TG-43 formalism, while offering improved accuracy over the TARGIT method, still assumes a homogeneous water medium. This simplification may lead to inaccuracies in dose calculations for heterogeneous anatomical sites like the brain.

A methodological limitation in the MC calculations of air-kerma rates should be noted. In our simulations, as described in Chapter 4, the air-kerma was calculated using an annular scoring volume at 50 cm without implementing specific collimation to exclude scattered radiation. This differs from the NIST standard approach for electronic brachytherapy sources, which uses a free-air chamber with collimation to limit the contribution from scattered photons. The inclusion of scattered radiation in our air-kerma calculations could lead to systematically higher air-kerma rates than would be measured using the NIST standard, potentially affecting our calculated dose-rate conversion coefficients. This effect could be particularly significant given the low-energy photon spectrum of the INTRABEAM system and its increased likelihood of scatter interactions. Future work should consider implementing explicit collimation in the MC simulations to more closely match the measurement conditions of the primary standard.

The clinical data used in this study was limited to a relatively small cohort of patients from the INTRAGO trial. A larger, more diverse patient population would be necessary to fully validate the findings and ensure their generalizability. Additionally, the research focused primarily on dosimetric aspects and did not directly assess clinical outcomes. While improved dosimetry is expected to lead to better treatment outcomes, this relationship needs to be established through long-term clinical studies. Furthermore, the study did not address the practical challenges of implementing more advanced dosimetry methods in real-time during IORT procedures. Issues such as computation time, equipment compatibility, and workflow integration need to be carefully considered for clinical translation.

An important limitation in the interpretation of IORT dose calculations relates to the anatomical representation used for dosimetry. In the INTRAGO protocol, patients undergo imaging at multiple time points: preoperative MRI for surgical guidance, early post-operative MRI within 24-48 hours after IORT to assess surgical results, and a planning CT several days later for EBRT treatment planning. While the planning target volume is defined based on the peritumoral edema visible in FLAIR sequences from the post-operative MRI co-registered to the planning CT, this anatomy may differ considerably from the surgical configuration during IORT delivery. The brain shift that occurs during surgery, the immediate post-surgical changes, and the evolution of peritumoral edema in the days following resection can all affect the actual geometric relationships between the treatment volume and surrounding structures. Furthermore, during IORT the patient's skull is open and the cavity is exposed, whereas during subsequent CT imaging the wound has been closed, potentially altering the local tissue configuration. These anatomical differences between the treatment-time configuration and the imaging used for dose calculations represent an inherent uncertainty in our dosimetric analysis that could not be fully addressed with current methodologies.

While this research made efforts to account for some radiobiological effects, it did not fully explore all the implications of the low-energy X-ray spectrum used in INTRABEAM IORT. In line with the INTRAGO protocol recommendations, we incorporated radiobiological considerations by converting IORT doses to equivalent 2 Gy fraction (EQD2) doses for comparison with EBRT, using an RBE of 1.5 for the INTRABEAM beam quality and

an α/β ratio of 2 for OARs in the brain. However, the study did not investigate the validity of these RBE and α/β values, nor did it explore the accuracy of the EQD2 model in this specific context. The research revealed that while IORT doses alone did not exceed OAR constraints, the combined IORT and EBRT doses often surpassed these limits. This finding raises questions about the appropriateness of the current OAR constraints and the accuracy of the EQD2 conversion for low-energy IORT.

A significant limitation in the interpretation of the results from Chapter 5 relates to the origin of the dose constraints used in the INTRAGO trial. These constraints were not derived from long-term IORT outcome studies, which are still lacking for glioblastoma treatment. Instead, they were established based on previous clinical experience with conventional external beam radiotherapy techniques, primarily single-fraction stereotactic radiosurgery and other high-dose-per-fraction treatments, with estimated RBE corrections to account for the low-energy x-ray spectrum of the INTRABEAM system. The biological response to low-energy X-rays, particularly in the complex environment of immediate post-surgical irradiation, may differ substantially from these established protocols. Furthermore, potential differences in biological response between IORT and conventional radiotherapy modalities beyond those accounted for by the RBE factor were not examined. These aspects, including the investigation of tissue-specific RBE values and the development of more sophisticated biological models for low-energy X-rays, represent important areas for future research to enhance the accuracy of dose interpretations and treatment planning in INTRABEAM IORT.

Lastly, the validation of MC simulations was primarily performed using measurements in water phantoms. While this provides a good foundation, it may not fully capture the complexities of dose deposition in heterogeneous patient anatomies. These limitations highlight areas for future research and development in the field of INTRABEAM dosimetry for IORT in GBM treatment.

7.2 Future research directions

Building upon this thesis's findings and limitations, several promising avenues for future research emerge. Long-term follow-up studies of patients treated with IORT using the INTRABEAM system are needed to correlate dosimetric improvements with clinical outcomes. This could involve retrospective analyses of INTRAGO trial data using the more accurate dosimetry methods developed in this thesis, as well as prospective studies implementing these methods in treatment planning.

7.2.1 Integration of imaging and treatment planning

The integration of intraoperative imaging modalities, such as CT, MRI, or ultrasound, could significantly enhance the accuracy of IORT dose calculations. Real-time imaging could provide patient-specific anatomical information, allowing for adaptive treatment planning and improved targeting. Collaboration with equipment manufacturers, such as Zeiss, could facilitate the development of integrated IORT systems with advanced imaging capabilities.

Building on the TG-43 parameters and MC simulation methods developed in this thesis, future work should focus on creating fast, accurate treatment planning systems for intraoperative use. This could involve the use of GPU-accelerated MC simulations to enable real-time dose calculations and plan optimization. Such systems would

need to balance computational efficiency with accuracy, potentially exploiting hybrid approaches that combine pre-calculated data with real-time adjustments based on intraoperative imaging.

7.2.2 Expansion of clinical applications and radiobiology studies

While this thesis focused on GBM treatment, the INTRABEAM system has potential applications in other areas, such as breast and rectal cancer. Future studies should investigate the dosimetric considerations and clinical outcomes for these additional indications, making use of the improved dosimetry methods developed here. This expansion could lead to a broader adoption of IORT techniques and potentially improve outcomes for a wider range of cancer patients.

In parallel, in-vitro and in-vivo studies are needed to better understand the radiobiological effects of low-energy X-rays used in INTRABEAM IORT. This research could help determine more accurate RBE values and biological modeling parameters, improving the translation between physical and biologically effective doses. Such studies would be particularly valuable in optimizing treatment protocols and understanding the potential combined effects between IORT and other treatment modalities, such as chemotherapy or immunotherapy.

7.2.3 Advanced modeling and quality assurance

Future research should focus on refining MC models to include more detailed representations of patient anatomy and tissue composition. This could involve the use of dual-energy CT for improved tissue segmentation or the incorporation of functional imaging data to account for tumor heterogeneity. MC simulations could also be used to investigate the impact of setup uncertainties and anatomical variations on dose distributions, leading to more robust treatment planning approaches.

Alternative dose calculation methods, such as deterministic solutions to the linear Boltzmann transport equation, could also be explored. The Varian Acuros BV algorithm [4], currently used in brachytherapy treatment planning systems, could potentially be adapted for electronic brachytherapy sources like INTRABEAM. These methods offer faster calculation times than full MC simulations while maintaining acceptable accuracy in heterogeneous media [5]. Investigation of such alternatives could help bridge the gap between the current clinical practice (based on simplified water measurements) and computationally intensive MC calculations, potentially enabling real-time adaptive planning during IORT procedures.

It is important to develop standardized quality assurance procedures and dosimetry protocols specifically designed for low-energy X-ray IORT. This would ensure consistent and accurate dose delivery across different clinical centers, particularly important for multi-center clinical trials. Such protocols should address the unique challenges of IORT dosimetry, including the steep dose gradients and the impact of tissue heterogeneities on dose distributions.

7.2.4 Comparative studies and treatment optimization

A comprehensive comparison between the dosimetry methods developed in this thesis and commercial treatment planning systems, such as Radiance TPS used with the INTRABEAM system, would be valuable. This could help identify areas for improvement in commercial systems and facilitate the clinical translation of advanced dosimetry

methods. Additionally, further research is needed to optimize the integration of IORT with other treatment modalities, such as EBRT. This could involve the development of biologically guided treatment planning systems that account for the unique radiobiological properties of IORT and its interactions with other therapies.

These future research directions aim to address the limitations identified in the current work and further advance the field of INTRABEAM dosimetry for IORT. By pursuing these avenues, we can work towards improving the accuracy, efficacy, and safety of IORT treatments for patients with GBM and potentially expand its applications to other oncological indications.

7.3 Conclusion

This thesis has made contributions to the field of INTRABEAM dosimetry for intraoperative radiotherapy, particularly in the context of glioblastoma multiforme treatment. Through a combination of Monte Carlo simulations, experimental validation, and clinical data analysis, we have developed and evaluated improved methods for dose calculation and treatment planning. The research has highlighted the limitations of current clinical practices and demonstrated the potential benefits of more sophisticated dosimetry approaches.

The comprehensive characterization of the INTRABEAM system using the TG-43 formalism provides a valuable resource for improving dose calculations within existing brachytherapy treatment planning frameworks. Comparing different dosimetry formalisms has revealed significant discrepancies in organ-at-risk dose estimates, emphasizing the need for more accurate methods in clinical practice. Evaluating the TG-43 formalism against Monte Carlo simulations has shown its potential as a practical compromise between accuracy and computational efficiency for routine clinical use.

While these findings represent important advancements, they also highlight the complexities involved in accurately calculating doses for low-energy IORT treatments. The research highlights the need for careful consideration of tissue heterogeneities, applicator design, and the integration of IORT with other treatment modalities. The limitations identified in this work point to several promising avenues for future research, including the development of real-time intraoperative treatment planning systems, the integration of intraoperative imaging, and further investigation of the radiobiological effects of low-energy X-rays.

Ultimately, the goal of this research is to improve patient outcomes by enabling more precise and effective IORT treatments. By advancing our understanding of INTRABEAM dosimetry and providing tools for more accurate dose calculation, this work contributes to the ongoing efforts to enhance the therapeutic potential of IORT in GBM treatment and potentially expand its applications to other oncological indications. By building on the foundation laid in this thesis and pursuing the identified future research directions, we can work towards realizing the full potential of INTRABEAM IORT in improving cancer treatment outcomes.

References

[1] D. S. Ayala Alvarez, P. G. F. Watson, M. Popovic, V. J. Heng, M. D. C. Evans, and J. Seuntjens, “Monte Carlo calculation of the relative TG-43 dosimetry parameters for the

INTRABEAM electronic brachytherapy source," *Physics in Medicine and Biology*, vol. 65, no. 24, p. 245 041, 2020.

[2] D. S. Ayala Alvarez, P. G. F. Watson, M. Popovic, V. J. Heng, M. D. C. Evans, and J. Seuntjens, "Monte Carlo calculation of the TG-43 dosimetry parameters for the INTRABEAM source with spherical applicators," *Physics in Medicine & Biology*, vol. 66, no. 21, p. 215 017, 2021.

[3] D. S. Ayala Alvarez *et al.*, "Evaluation of dosimetry formalisms in intraoperative radiation therapy of glioblastoma," *International Journal of Radiation Oncology, Biology, Physics*, vol. 117, no. 3, pp. 763–773, 2023.

[4] Acuros BV, "Algorithm reference guide," *Document ID B504878R01A, Revision A*, vol. 8, pp. 1–36, 2013.

[5] M. Sinnatamby, V. Nagarajan, S. Reddy K, G. Karunanidhi, and V. Singhavajala, "Dosimetric comparison of Acuros™ BV with AAPM TG43 dose calculation formalism in breast interstitial high-dose-rate brachytherapy with the use of metal catheters," *Journal of Contemporary Brachytherapy*, vol. 7, no. 4, pp. 273–279, 2015.